Karlsruhe Institute of Technology

Phenomenology of Axion Dark Matter

Zur Erlangung des akademischen Grades eines
Doktors der Naturwissenschaften (Dr. rer. nat.)

von der KIT-Fakultät für Physik des
Karlsruher Instituts für Technologie (KIT)
angenommene
Dissertation

von

Andreas Pargner

Mündliche Prüfung: 01.02.19

1. Referent: Prof. Dr. Thomas Schwetz-Mangold
2. Korreferent: Prof. Dr. Guido Drexlin

Erklärung

Ich versichere hiermit, dass ich die vorliegende Dissertation selbständig und unter Beachtung der Regeln zur Sicherung guter wissenschaftlicher Praxis im Karlsruher Institut für Technologie (KIT) in der aktuellen Fassung angefertigt habe. Ich habe keine anderen als die angegebenen Quellen und Hilfsmittel benutzt. Wörtlich oder inhaltlich übernommene Stellen sind als solche kenntlich gemacht.

Ort, Datum

Andreas Pargner

Für meinen Onkel ...

Abstract

The axion is a well-motivated dark matter (DM) candidate which has its origin in Peccei and Quinn's solution for the strong CP problem. In the present work, we study phenomenological implications of axion DM that mainly originate from its cosmological evolution.

We especially focus on scenarios where the Peccei-Quinn symmetry is broken after inflation. Here, we expect large isocurvature fluctuations in the axion energy density. These can eventually collapse into gravitationally bound objects, called miniclusters. By calculating the mass function of the axion miniclusters, we are for the first time able to give predictions on their distribution in mass and size. We find for a QCD axion with mass $m_a \sim \mu$eV, a typical minicluster mass of $\sim 10^{-13} M_\odot$ and size of $\sim 10^6$ km. The results of this study are also published in Ref. (a).

By numerically simulating the actual collapse of the axion overdensities after they decouple from the Hubble expansion, we also consider the equilibrium state of the axion miniclusters. Namely, a so far open question is if the miniclusters collapse into a static axion star configuration or rather form dilute virialized clouds. In fact, we find hints for the latter and it seems that after a short period of violent collapse the miniclusters take a quite dilute state which is characterized by an oscillating ratio of kinetic to potential energy.

In another part, we consider the effects of the axion isocurvature fluctuations on cosmological large-scale observables, like the cosmic microwave background (CMB). It turns out that these become only important for ultra-light axion-like particles (ULAs). Using observations of the CMB primary anisotropy spectrum we can show that due to these effects ULA DM with masses in a range 10^{-24} eV $- 10^{-15}$ eV can be strongly constrained (b).

Further, we also briefly review the experimental possibilities for axion detection experiments. For example, it is known that in a strong electromagnetic field, the DM axion background field can induce tiny electric and magnetic fields. In an appendix of the present work, we discuss a quantum field calculation of these induced fields with the main focus on the impact of the spatial size of the applied field in comparison to the axion Compton wavelength (c).

(a) J. Enander, A. Pargner, and T. Schwetz, "Axion minicluster power spectrum and mass function", JCAP 1712 no. 12, (2017) 038, arXiv:1708.04466.

(b) M. Feix, J. Frank, A. Pargner, R. Reischke, B. M. Schaefer, and T. Schwetz, "Testing post-inflation Axion Dark Matter using CMB Observations (Working Title)", *in preparation.*

(c) M. Beutter, A. Pargner, T. Schwetz, and E. Todarello "Axion-electrodynamics: a quantum field calculation", *prepared for the submission to JCAP*, arXiv:1812.05487.

Zusammenfassung

Ein guter Kandidat für die Dunkle Materie in unserem Universum ist das Axion. Es hat seinen Ursprung in der Lösung von Peccei und Quinn für das starke CP Problem. In der vorliegenden Arbeit, betrachten wir phenomenologische Konsequenzen von Axion-Dunkler-Materie, welche hauptsächliche durch die kosmologische Entwicklung des Axionfeldes hervorgerufen wird.

Unser Hauptaugenmerk liegt hierbei auf Szenarios in denen die Peccei-Quinn-Symmetry nach einer inflationären Phase gebrochen wird. Hier erwarten wir starke, so genannte isocurvature Fluktuationen in der Axionenergiedichte. Diese können schon in einer frühen Phase des Universums von der kosmologischen Expansion entkoppeln und in gravitativ gebundene Objekte kollabieren. Diese werden Axion-Minicluster genannt. Indem wir die Massenfunktion dieser Minicluster berechnen, können wir das erste mal Vorhersagen für ihre Verteilung bezüglich der Masse und der Größe machen. Für ein QCD Axion mit der Masse $m_a \sim \mu$eV finde wir zum Beispiel typische Miniclustermassen von $M_{\rm MC} \sim 10^{-13} M_\odot$ und Größen von etwa 10^6 km. Die Ergebnisse dieser Betrachtung wurden in Referenz (a) veröffentlicht.

Indem wir den eigentlich Kollaps der Minicluster numerisch simulieren, können wir auch deren Gleichgewichtszustand betrachten. Denn bis jetzt ist ungeklärt, ob die Minicluster in eine statische Axionstern-Konfiguration kollabieren oder ob sie eher den Zustand ähnlich einer dünnen, virialisierten Wolke annehmen. In der Tat zeigen unsere Simulation Hinweise für letzteres. Nach einer kurzen Phase des Kollapses scheint es als ob die Minicluster tatsächlich einer dünnen Wolke ähneln, die durch ein oszillierendes Verhältnis zwischen kinetischer und potentieller Energie gekennzeichnet ist.

In einem anderen Teil dieser Arbeit befassen wir uns mit den Effekten der isocurvature Fluktuation in der Axionenergiedichte für kosmologische Observablen, wie zum Beispiel dem kosmischem Mikrowellenhintergrund. Es stellt sich heraus, dass diese nur signifikant sind, falls das Axion extrem leicht ist. Indem wir die Daten von aktuellen Beobachtungen des kosmologischen Mikrowellenhintergrunds verwenden, können wir durch diese Effekte bereits einen großen Bereich, in dem extrem leichte Axionen die Dunkle Materie erklären können, ausschließen, nämlich Axionemassen von 10^{-24} eV $- 10^{-15}$ eV (b).

Ferner betrachten wir auch kurz die experimentellen Möglichkeiten zum Nachweis von Axion-Dunkler-Materie. Es ist bekannt, dass in einem starken elektromagnetischen Feld die Axion-Dunkle-Materie schwache elektrische und magnetische Felder induziert. In einem Anhang dieser Arbeit diskutieren wir eine quantenfeldtheoretische Berechnung dieser induzierten Felder. Insbsondere betrachten wir den Zusammenhang zwischen der Ausdehnung des elektromagnetischen Feldes und der Axion-Compton-Wellenlänge (c).

(a) J. Enander, A. Pargner, and T. Schwetz, "Axion minicluster power spectrum and mass function", JCAP 1712 no. 12, (2017) 038, arXiv:1708.04466.

(b) M. Feix, J. Frank, A. Pargner, R. Reischke, B. M. Schaefer, and T. Schwetz, "Testing post-inflation axion dark matter using CMB observations (working title)", *in preparation.*

(c) M. Beutter, A. Pargner, T. Schwetz, and E. Todarello "Axion-electrodynamics: a quantum field calculation", *prepared for the submission to JCAP*, arXiv:1812.05487.

Contents

I. Introduction **1**

II. Preliminaries **5**
II.1. The Strong CP Problem and the Axion 5
II.2. Axion-like Particles 9
II.3. Axion and ALP Interactions with the SM 10

III. Producing Relic Axions **13**
III.1. Thermal Production 13
III.2. Vacuum Realignment 14
III.3. Decay of Topological Defects 24

IV. Formation of Axion Miniclusters **27**
IV.1. Revisiting the Axion Field Evolution 30
IV.2. Power Spectrum of the Density Fluctuations 35
IV.3. Decoupling from the Hubble Flow 42
IV.4. Distribution of Axion Miniclusters 43
IV.5. ALP Miniclusters 51

V. Fate of Axion Miniclusters **53**
V.1. Scalar Cloud under Self-Gravity 53
V.2. Schrödinger-Poisson System for Minicluster Collapse 58

VI. Post-Inflation Realignment and Large-Scale Observables **73**
VI.1. Cosmological and Astrophysical Constraints on Ultra-light Axions 78
VI.2. Axion Isocurvature Fluctuations and the CMB 81
VI.3. Implications for Axion Properties 85

VII. Summary and Outlook **91**

A. Units **95**

B. Axion-electrodynamics for DM Detection **97**

C. Rewriting the Axion Evolution Equation in Terms of Temperature **101**

D. Non-relativistic Approximation of the Axion Field **103**

E. Numerical Approach for Solving the Schrödinger-Poisson System **107**

F. Madelung Transformation **119**

Literature **121**

Acknowledgments **136**

List of Figures

II.1. Parameter Space for ALP-Photon Coupling. 12

III.1. The Vacuum Realignment Mechanism. 15
III.2. Temperature dependent Axion Mass and the Hubble Rate. 22
III.3. Axion Properties explaining DM Abundance in the post-inflation Realignment Scenario. 23

IV.1. Vacuum Realignment in the post-inflationary Scenario. 28
IV.2. Evolution of the Axion Field Fourier Modes. 35
IV.3. Power Spectrum of the Realignment Density Fluctuations. 39
IV.4. Comparison with Results from Numerical Simulations in Vaquero et al. 41
IV.5. Smoothed Variance of the Density Fluctuations. 46
IV.6. Distribution of Axion Miniclusters in Mass and Size. 48
IV.7. Dimensionless Mass Function of Axion Miniclusters. 49

V.1. Minicluster Distribution and Dilute Axion Stars. 57
V.2. Evolution of a Scalar Cloud under Self-Gravity. 65
V.3. Evolution of the Current during the Scalar Cloud Collapse. 66
V.4. Ratio of Kinetic to Potential Energy during the Scalar Cloud Collapse. 67
V.5. Correlation of the Phase in the Scalar Cloud Collapse. 68
V.6. Evolution of the Wave Function in the Schrödinger-Poisson System. 70
V.7. Evolution of the Particle Current in the Schrödinger-Poisson System. 71

VI.1. Sketch of the primordial Power Spectrum for adiabatic and isocurvature Fluctuations in the Axion Energy Density. 76
VI.2. Post-inflation Peccei-Quinn Breaking and CMB Constraints I. 86
VI.3. Post-inflation Peccei-Quinn Breaking and CMB Constraints II. 88
VI.4. Post-inflation Peccei-Quinn Breaking and CMB Constraints III. 89

VII.1. Highlights of the present Work. 93

B.1. Feynman Diagram for Electron Interaction with an Axion Background Field and an external Photon Field. 98

E.1. A moving Gaussian Wave Packet in a Box. 110
E.2. A moving Gaussian Wave Packet in a Box with absorbing Boundaries. 111
E.3. Gravitational Potential of a Gaussian Wave Packet. 113
E.4. Evolution of Gaussian Wave Packet under the Schrödinger-Poisson System. . . 116

List of Tables

IV.1. Results for the Distribution of Axion Miniclusters in Mass and Size. 49

V.1. Definitions on the Nomenclature for the Discussion of the Minicluster Collapse. 60

VI.1. Definitions and Explanations for the Discussion of DM Density Fluctuations. . . 74
VI.2. Exclusion limits on ultra-light Axions. 80
VI.3. Paramters of the Cosmological Model for the post-inflation Realignment Scenario and their fiducial Values. 83

I. Introduction

The need for non-luminous Dark Matter (DM) in our Universe was realized already in the 1930's by observing the kinematics of galaxy clusters [1, 2]. Since then, more and more evidence for DM is accumulating [3]. However, almost a century after the first mention, its true nature is still one of the biggest puzzles in physics.

One might think that the missing invisible matter has an astrophysical or cosmological origin and hides in massive compact halo objects (MACHO) or primordial Black Holes (pBH) [4,5]. But searches for microlensing and other astrophysical signals of MACHOs and pBHs exclude large parts of the possible parameter space [6, 7]. Therefore, it is believed that neither MACHOs nor pBHs can explain all or even large parts of the observed DM [8]. Also, modifications of General Relativity are so far not successful in conclusively explaining all the evidences for DM [9, 10].

Therefore, we might have to look in another corner. Namely, a different possibility could be that the DM consists of particles which mainly interact gravitationally with the visible Universe. Since the Standard Model (SM) of particle physics does not include a suitable candidate, this calls for an explanation going beyond the known. Typically, the guiding principle for the search for physics beyond the SM (BSM) is explanations for shortcomings of it, like the unification of the gauge couplings at high scales or the hierarchy problem. From the 1980's on, the most popular explanation for these puzzles have been within supersymmetric (SUSY) models [11]. One advantage of SUSY is that it can provide excellent DM candidates. These would only weakly interact with the SM and are therefore called weakly interacting massive particles (WIMPs). An immense experimental effort was put forward to look for WIMPs in indirect and direct detection experiments [12]. Today, the latter reach unprecedented sensitivity and soon will be even able to detect the irreducible background of neutrino fluxes from the sun and other astrophysical sources. Despite this heroic effort, there is so far no conclusive observation of a detection signal [13, 14]. This non-observation in direct detection experiments and the null-results of SUSY searches at colliders [15] made the WIMP recently a less and less attractive solution to the DM puzzle [16].

That is why in the last years, another BSM particle regained popularty and is slowly developing into the most appealing DM candidate. Originally, it has appeared in Peccei and Quinn's solution of the strong CP problem [17]. In the late 1970's, they found an elegant explanation for why the strong interactions of the SM do not violate the CP symmetry. A byproduct of their solution is a pseudo-Nambu-Goldstone (pNG) boson, the axion [18, 19]. It was soon realized that also many other high energy extensions of the SM contain as well pNG bosons with similar properties as the axion. For this reason these particles are usually called axion-like particles (ALPs) [20, 21].

The Peccei-Quinn solution of the strong CP problem requires a new global chiral $U(1)$ symmetry which gets spontaneously broken at the energy scale f_a by the vacuum expectation value of a complex scalar field. The axion emerges as the phase degree of freedom of this complex scalar after the Peccei-Quinn symmetry is broken. A potential for the axion is provided via the mixing with the active mesons, giving it a mass inversely proportional to the breaking scale f_a. The mixing happens around the QCD phase transition when the quark condensates form. At higher energies, the axion is effectively massless. Also, the axion interaction with the SM particles is inversely proportional to f_a. In Peccei and Quinn's original proposal, f_a coincides with the electroweak breaking scale, leading to rather sizeable couplings. This scenario was soon ruled out by beam dump experiments [22]. However, in so-called invisible axion models,

f_a can be at very high scales, giving the axion very weak interactions and an extremely small mass [23–26].

Even though being very light, the axion can be an excellent cold DM (CDM) candidate, thanks to its non-thermal production via the vacuum realignment mechanism [27–30]. When the Peccei-Quinn symmetry is broken in the early Universe, at high temperatures $T \sim f_a$, the axion field is massless and since no specific field value is energetically favored, it simply takes some random one. At lower temperatures around the QCD phase transition, its potential becomes important which makes the axion field roll down to the CP conserving minimum and therefore realign with the vacuum. The energy stored in the coherent oscillations around this minimum behaves like collisionless matter and makes a good explanation for the DM in our Universe. A typical axion mass suitable to explain the observed DM density is $m_a \sim 10^{-5}$ eV [31].

However, there are two fundamentally different scenarios how this production mechanism could have been realized. Namely, whether the Peccei-Quinn symmetry breaking happens before or after an inflationary epoch. In the first scenario, the axion field takes one value in the whole observable universe and the axion energy density is proportional to this single value. But when the Peccei-Quinn symmetry breaking happens after inflation, the situation is more complicated. Here, the axion field takes different values in causally disconnected regions which leads to large isocurvature fluctuations in the axion energy density. This has some interesting phenomenological consequences for axion DM.

Namely, large overdensities can decouple from the Hubble flow already in the radiation dominated epoch and form gravitationally bound objects. These are called axion miniclusters [32]. When estimating the size of an axion minicluster via the horizon when the field oscillations commence, a typical minicluster mass is $M_{\rm MC} \sim 10^{-11}\ M_\odot$ for $m_a \sim 10^{-5}$ eV. If all or big parts of the axion DM would be clumped in miniclusters, this could have a variety of important implications. Foremost, it would lower the detection potential of typical axion DM haloscope experiments dramatically. Still, there might be ways of observing axion miniclusters themselves, for example via gravitational microlensing or as a source for fast radio bursts [33,34]. But before drawing definite conclusions it is essential to get a solid understanding of the formation history and the distribution of axion miniclusters.

Much of the present work is therefore dedicated to shedding light on this issues. By carefully following the axion field evolution in the post-inflation Peccei-Quinn symmetry breaking scenario, we are able to study the formation of axion miniclusters and calculate for the first time their distribution not only in mass but also in size. Using a semi-analytical approach and statistical methods allows for a transparent interpretation of the underlying physics and the dependence on the axion paramters like the mass m_a and the Peccei-Quinn breaking scale f_a. Our results give a useful estimate on the properties of the axion miniclusters and can serve as input for the study of their further evolution.

Namely, we can expect that after their formation, the miniclusters experience a period of collapse. An interesting question is if they decohere and settle in a virialized configuration or if they collapse into a coherent object, a so-called axion star [35]. A numerical investigation of this is also part of the present work.

We further consider the implications of post-inflation Peccei-Quinn breaking in the more general context of ALPs. It turns out that for ultra-light ALPs, also known as ULAs, the isocurvature fluctuations in the energy density can have a sizeable effect in cosmological large-scale observables. By looking at the implications for the anisotropy spectrum of fluctuations in the cosmic microwave background (CMB), we are able to constrain large parts of the parameter space where ULAs can be the DM.

This work is structured as follows. We start by briefly reviewing the strong CP problem, its solution by Peccei and Quinn, and the role of the axion therein, in Ch. II. There, we also discuss the more general case of ALPs and the interaction of axions with the SM particles. In App. B, we take a closer look at the axion-photon interaction and present results of a quantum field theoretical calclation of axion-induced electric and magnetic fields. We discuss the different

cosmological production mechanisms for DM axions in Ch. III with a special focus on the vacuum realignment mechanism for which we also derive very useful quantitative estimates for the relic axion abundance. In Ch. IV, we study the formation of axion miniclusters in the post-inflation vacuum realignment scenario in detail. Chapter V is dedicated to the fate of axion miniclusters meaning that we consider the subsequent collapse of axion overdensities after their decoupling from the Hubble flow. This way we can learn about the equilibrium configuration of axion miniclusters. In Ch. VI, we take a look at the effects of the axion isocurvature fluctuations in the post-inflation Peccei-Quinn breaking scenario on the CMB power spectrum and derive some strong limits on ULA DM. We finish in Ch. VII with a summary and an outlook. In App. A, we discuss the natural unit system and give some useful conversion relations. The appendices C to F provide further supplement material to the main text.

II. Preliminaries

To set the stage for the present work, we briefly introduce the strong CP problem and review the role of the axion in its solution. We also look at the more general case of axion-like particles (ALPs) and consider the various interactions of axions and ALPs with the SM.

The following short overview is far from comprehensive. There exists a plethora of great reviews on the strong CP problem [36–40] as well as on different aspects of axion phyiscs [41–47]. Many thoughts and arguments presented here are naturally inspired by these ever-helpful resources.

II.1. The Strong CP Problem and the Axion

A theory of massive quarks $\mathbf{q}$ and strong interactions[1]

$$\mathcal{L}_s = \frac{1}{4} G_{a\mu\nu} G^{a\mu\nu} - (\bar{\mathbf{q}}_L m_q \mathbf{q}_R + \text{h.c}) - \frac{\alpha_S}{8\pi} \theta G_{a\mu\nu} \tilde{G}^{a\mu\nu} \tag{II.1}$$

has two possible sources for violating parity (P), time reversal (T) and the combined transformation of charge conjugation and parity (CP). First via the quark masses m_q, which can be complex in general, and second via the term $\sim \theta G\tilde{G}$. When $SU_c(3)$ was first introduced as the theory of strong interactions, the second term was not present per choice of the designer. In this case, it was thought that the theory can easily be made CP symmetric and there was and is convincing experimental evidence that strong interactions do not violate CP.

So, assuming for a moment the $\theta G\tilde{G}$ therm would not be present then by writing the mass as $m_q = |m_q| \exp[\mathrm{i}\theta_q]$, it seems like a chiral transformation

$$q_L \;\rightarrow\; \mathrm{e}^{\mathrm{i}\theta_q/2} q_L \quad , \qquad q_R \;\rightarrow\; \mathrm{e}^{-\mathrm{i}\theta_q/2} q_R \tag{II.2}$$

would rotate away the phases and make them unphysical. But in fact this is not true since such a chiral transformation has an anomaly and is therefore not a real symmetry of the theory. This is also the reason why the only gauge invariant way of writing strong interactions is including the $\theta G\tilde{G}$ term, as it was shown by t'Hooft [48]. This is why the parameter θ can be understood as a phase $\in [-\pi, \pi]$ describing the choice of a specific gauge invariant vacuum [49].

However, for making the quark masses in the gauge invariant Lagrangian, Eq. (II.1), real we can still perform a chiral rotation, like in Eq. (II.2). But then the Lagrangian transforms like

$$\mathcal{L}_s \;\rightarrow\; \mathcal{L}_s' = \frac{1}{4} G_{a\mu\nu} G^{a\mu\nu} - |m_q| \left(\bar{\mathbf{q}}_L \mathbf{q}_R + \text{h.c}\right) - \frac{\alpha_S}{8\pi} \left(\theta + N_f \theta_q\right) G_{a\mu\nu} \tilde{G}^{a\mu\nu} \,. \tag{II.3}$$

and the modification of the $G\tilde{G}$ term results from the anomalous character of the transformation. Note that we consider now the general case of N_f different quark flavors and use a diagonal mass matrix. Since θ as well as $N_f\theta_q$ are completely arbitrary phases, we expect that $\bar{\theta} \equiv \theta + N_f\theta_q$ can easily be of $\mathcal{O}(1)$.

[1] It is $\tilde{G}_a^{\mu\nu} = \epsilon^{\mu\nu\rho\sigma} G_{a\rho\sigma}/2$ the dual of the gluon field strength tensor G and a is the color index.

From the theory of electroweak interactions we know that CP does not have to be a true symmetry of nature. Here, the irremovable phases in the quark mixing matrix cause flavor changing neutral currents which violate CP [50]. In fact, including the full electroweak sector of the SM with the gauge invariant strong interactions, as described above, leads to [37]

$$\bar{\theta} = \theta + \mathrm{ArgDet} M_q \tag{II.4}$$

being the really physically revlevant parameter. Here, M_q is the full quark mass matrix.

The presence of the CP violating $\bar{\theta} G\tilde{G}$ term has very profound consequences. Possibly the most notable one is that it induces an electric dipole moment for the neutron [39]

$$|d_n| \sim 5.2 \cdot 10^{-16}\ \bar{\theta}\ \mathrm{e} \cdot \mathrm{cm}\,. \tag{II.5}$$

But with stringent experimental constraints on d_n, namely $|d_n| < 0.3 \cdot 10^{-25}$ e $\cdot$ cm [51], the $\bar{\theta}$ parameter should be tiny, i.e. we must have $\bar{\theta} < 10^{-9}$. This is very surprising since, as we have argued, one would a priori not expect θ to be small, nor $\mathrm{ArgDet} M_q$. Even more unreasonable is to expect that these too completely unrelated parameters cancel in the needed precision. Hence, the strong CP problem is the puzzle why strong interactions do not violate CP, even though there is no fundamental reason for it.

A minimal solution to this problem, as we can see easily from Eq. (II.4), would be that one of the light quarks is massless. But this possibility is strongly disfavored by experiments as well as lattice calculations, see Ref. [52] and references therein. Another solution could be that a high energy completion of the SM is indeed CP symmetric and it is only broken spontaneously [53,54]. In this case, the $\theta G\tilde{G}$ term would not be there, to begin with, since here $\theta = 0$ would be the only gauge invariant CP conserving choice for the vacuum. The model building challenge of this mechanism is to still produce the observed phases of the quark mass matrix. In addition, the needed new degrees of freedom must be usually very heavy to not induce a sizeable $\bar{\theta}$ via loop effects. In this case, the low energy part of the theory often just reproduces the SM. Therefore, this type of models "lack a certain kind of predictivity" [55], cf. also Ref. [56].

The most appreciated method explaining the smallness of $\bar{\theta}$ is the solution provided by Peccei and Quinn [17]. Their main idea was promoting the static $\bar{\theta}$ parameter to a dynamical variable which should eventually settle in a CP conserving state. To do this, they exploited the very same source why the $G\tilde{G}$ term is physical to begin with. Namely, the anomalous character of a chiral $U(1)$ transformation. Thus, Peccei and Quinn introduced a new global chiral $U(1)$ symmetry in the strongly interacting sector. Such a symmetry is now known as Peccei-Quinn symmetry, abbreviated as $U(1)_{\mathrm{PQ}}$. But for making $\bar{\theta}$ dynamcial, also new degrees of freedom and therefore new fields must be added to the SM. In the most minimal and original attempt by Peccei and Quinn, it suffices to add one new complex scalar field. It basically acts as second Higgs doublet and it can spontaneously break the $U(1)_{\mathrm{PQ}}$ symmetry by acquiring a vacuum expectation value (vev). As usual, one of the two Higgs doublets couples to the down-type, the other to the up-type quarks. The potential for the Higgs fields is chosen such that the whole Lagrangian is symmetric under a chiral rotation of the quark fields[2]

$$\mathbf{u} \ \rightarrow\ \mathrm{e}^{\mathrm{i}\theta_u \gamma_5}\mathbf{u} \quad , \quad \mathbf{d} \ \rightarrow\ \mathrm{e}^{\mathrm{i}\theta_d \gamma_5}\mathbf{d}\,. \tag{II.6}$$

To make the gauge invariant Lagrangian truely symmetric under such a tranformation, one also has to shift the vacuum angle

$$\theta \ \rightarrow\ \theta - N_f\,(\theta_u + \theta_d) \tag{II.7}$$

because of the anomaly.

After the breaking of the electroweak symmetry, which in this case coincides with the $U(1)_{\mathrm{PQ}}$ symmetry breaking, the neutral components of the Higgs doublets acquire their vevs v_u and

[2] It is γ_5 the usual product of the Dirac matrices γ_i.

v_d with $\sqrt{v_u^2 + v_d^2} \simeq 250$ GeV and their phases become the Nambu-Goldstones. One linear combination will be eaten by the Z boson, as usual. But the orthogonal combination becomes a new massless field, namely the axion a. A kinetic term for a of the form

$$\mathcal{L}_{a,\mathrm{kin}} = \frac{1}{2} (\partial_\mu a) (\partial^\mu a) \tag{II.8}$$

follows from the kinetic terms of the Higgs fields. In this model, the axion has a remaining shift symmetry $a \to a + 2\pi n f_a$, with $f_a = v_u v_d / \sqrt{v_u^2 + v_d^2}$ and $n \in \mathbb{N}$ [43].

Axion couplings to the quarks arise from the mass terms. However, they can be removed by again performing a chiral rotation and this eventually leads to the desired coupling of the axion to gluons:

$$\mathcal{L}_{a,\mathrm{gl}} \sim -\frac{\alpha_S}{8\pi} \frac{a}{f_a} G_{a\mu\nu} \tilde{G}^{a\mu\nu} \,. \tag{II.9}$$

Now, using the remaining shift symmetry one can redefine the axion field to absorb the $\bar{\theta} G\tilde{G}$ vacuum term. Thus, the static $\bar{\theta}$ parameter was successfully promoted to the dynamical axion field $a(x)$, $\bar{\theta} \to a(x)/f_a$.

By removing the axion-quark coupling from the mass terms, more interactions for the axion arise. Since the quarks are electrically charged, interactions between the axion and the photon field of the form[3]

$$\mathcal{L}_{a,\mathrm{ph}} \sim \frac{\alpha}{8\pi} \frac{a}{f_a} F_{\mu\nu} \tilde{F}^{\mu\nu} \tag{II.10}$$

are induced. The kinetic terms of the quark field lead to the derivative couplings

$$\mathcal{L}_{a,\mathrm{qu}} \sim \frac{(\partial_\mu a)}{f_a} \bar{\mathbf{q}} \gamma^\mu \gamma_5 \mathbf{q} \,. \tag{II.11}$$

We will later discuss the interaction between the axions and the SM particles in more detail. But note that all couplings are suppressed by the Peccei-Quinn breaking scale f_a.

It remains to show that the axion field really solves the strong CP problem. Since the term in Eq. (II.9) causes potentially the same effects as the static $\bar{\theta} G\tilde{G}$ term. However, there exists a theorem by Vaffa and Witten which states that without other sources of CP violation, the QCD vacuum energy is minimized in a CP symmetric state [57]. Thus, QCD itself solves the strong CP problem by providing a potential for the axion field which guides it into a CP conserving minimum. This potential arises when after the QCD confinement the $aG\tilde{G}$ term leads to the mixing between the axion and the mesons. In chiral perturbation theory, the axion potential is calcuable at tree level. It has the form [52][4]

$$V_{\mathrm{cPT}}(a) = m_\pi^2 f_\pi^2 \left[1 - \sqrt{1 - \frac{4 m_u m_d}{(m_u^2 + m_d^2)} \sin^2 \left(\frac{a}{2 f_a} \right)} \right] , \tag{II.12}$$

which is indeed minimized at the CP conserving minimum, $a = 0 \bmod 2\pi f_a$. The potential can also be calculated by an effective instanton action which describes the non-perturbative effects of QCD. Using this technique, it is found that [58]:

$$V_{\mathrm{inst}}(a) = m_\pi^2 f_\pi^2 \frac{m_u m_d}{(m_u^2 + m_d^2)} \left[1 - \cos \left(\frac{a}{f_a} \right) \right] . \tag{II.13}$$

[3] Again, it is $\tilde{F}_{\mu\nu} = \epsilon_{\mu\nu\rho\sigma} F^{\rho\sigma}/2$ the dual of the usual field strength tensor F of the photon field.

[4] Be aware that we have applied a shift such that the minimum of the potential is at zero. Further note that to avoid any confusion at this point we set the number of degenerate minima N_{DW} in the interval $a/f_a \in [-\pi, \pi]$ to one. If $N_{\mathrm{DW}} \neq 1$, this has some interisting implications, especially in the comsological context. We will revisit this topic in Sec. III.3 when discussing topological defects. However, it should be mentioned that the original Peccei-Quinn model has $N_{\mathrm{DW}} = 3$.

Besides a slightly different parametric dependence, both results agree in the prediction for the axion mass:

$$m_a^2 = \frac{\partial^2 V}{\partial a^2}\Big|_{\min} = \frac{m_\pi^2 f_\pi^2}{f_a^2}\frac{m_u m_d}{(m_u + m_d)^2}\,. \tag{II.14}$$

This inverse proportionality of the mass m_a to the Peccei-Quinn breaking scale f_a is one of the defining features of the QCD axion. It makes phenomenological studies particularly compact since f_a, or equivalently m_a, is the only parameter describing virtually all axion properties.

The axion potential at any given temperature, also above the QCD confinement, can be related to the topological susceptibility of QCD, $\chi_{\rm QCD}$. It is

$$m_a^2 f_a^2 = \frac{\partial^2 V_{\rm QCD}}{\partial (a/f_a)^2} \equiv \chi_{\rm QCD}(T) \tag{II.15}$$

and $\chi_{\rm QCD}$ can be calculated either in an interacting instanton liquid model (IILM) [59], or, as it was recently done by Borsanyi et al in Ref. [60], with state of the art lattice methods. In Ref. [60] it was found that $\chi_{\rm QCD}(T \lesssim 100\,{\rm MeV}) \equiv \chi_{\rm QCD} \simeq (75.5\ {\rm MeV})^4$ which leads to the compact relation

$$m_a \simeq 5.7\ \mu{\rm eV}\ \left(\frac{10^{12}\ {\rm GeV}}{f_a}\right) \tag{II.16}$$

for the zero-temperature QCD axion mass. At high temperatures, well above the QCD phase transition, $\chi_{\rm QCD}(T)$ vanishes, making the axion massless. The temperature dependence of the axion mass will become important when we discuss the evolution of the cosmological axion field. With Eq. (II.15), it is

$$m_a(T) = \frac{\sqrt{\chi_{\rm QCD}(T)}}{f_a} \tag{II.17}$$

a general relation for the temperature dependent axion mass. In the IILM approach, a paramterization for $\chi(T)$ can be found. In Ref. [59] it is reported by Wantz and Shellard that

$$\chi_{\rm QCD}(T) = 1.68 \cdot 10^{-7}\ \Lambda^4 \left(\frac{\Lambda}{T}\right)^{6.68} \qquad \text{for } T > \Lambda \tag{II.18}$$

and they set $\Lambda = 400$ MeV. This means that the axion masse "switches on" with a power law $\sim (\Lambda_{\rm QCD}/T)^{3.34}$ for decreasing temperatures. At temperature below $T < 400$ MeV it approaches its zero temperature mass, where it settles around $T \approx T_{\rm QCD} \simeq 100$ MeV [59].

Let us come back to the original idea of Peccei and Quinn, where f_a is of the order of the electroweak breaking scale. This does not only lead to quite heavy axions, $m_a \sim$ keV, but more importantly to sizable couplings to the SM particles. Therefore, the original Peccei-Quinn model was quickly ruled out by beam dump and other experimental constraints [22].

But the basic idea of the Peccei-Quinn mechanism can easily be expanded by adding more new degrees of freedom. This allows for pushing the symmetry breaking scale to very high energies. The most prominent approaches of this kind are the DFSZ [23, 24] and the KSVZ models [25,26]. In the first, besides the second Higgs doublet, another complex SM singlet field is added. Whereas in the latter case, additional heavy SM singlet quarks are included. Since in both models f_a can be at virtually arbitrarily high scales, the axion does not only can be made extremly light, $m_a \sim \mu$eV, but also very weakly interacting. This is why the axion emerging in this models is called invisible.

To summarize this section we repeat the most important properties of the QCD axion. Its defining feature is the coupling to the gluons of the form (II.9). This interaction is model independent since it is eventually the reason why the axion solves the strong CP problem. Therefore, also the relation between the axion mass and the symmetry breaking scale, as in Eq. (II.14), is model independent. Model-dependent are the actual couplings to the other SM particles, i.e. photons, quarks, and leptons. A generic feature on the other hand is that all come with the suppression by f_a.

II.2. Axion-like Particles

When a global symmetry is spontaneously broken, Nambu-Goldstone (NG) bosons naturally arise and there exist many extensions of the SM where this happens. Examples are models where family or lepton-number symmetries are introduced. Here, the NGs are called familons respectively majorons [61]. But since new massless degrees of freedom are in general strongly constrained, these new scalar or pseudo-scalar particles should be massive. This rather makes them pseudo-NGs (pNGs). Their mass might be generated dynamically, like in the case of the QCD axion, or it can be there to begin with, for example by a small explicit symmetry breaking. We call such particles axion-like particles (ALPs). See e.g. Ref. [62] for a thorough review of ALPs.

In general, the biggest difference between the QCD axion and ALPs is that the latter do not have to have a specific relation between their mass m_A and the breaking scale f_A of the new global symmetry. Taking a model-independent approach, these two parameters are completely independent. Nevertheless, if we assume that a potential for the ALP A is generated by some exotic strongly interacting sector, we might write it as

$$V_{\mathrm{ALP}}(A) \sim \Lambda^4 \left[1 - \cos\left(\frac{A}{f_A}\right)\right] , \tag{II.19}$$

in analogy to the instanton potential of the QCD axions. This gives a relation for the ALP mass

$$m_A^2 f_A^2 = \frac{\partial^2 V_{\mathrm{ALP}}}{\partial (A/f_A)^2} = \Lambda^4 . \tag{II.20}$$

Thus, Λ^4 takes the role of the topological susceptibility as χ_{QCD} did in the QCD case. But note that this is just a reshuffling of the parameters since in most cases also Λ is unknown. So, the ALP can be characterized either by m_A and f_A or, assuming a certain mechanism for generating the the ALP potential, by f_A and Λ. Thus, there are only two independent parameters in the end.

Let us come to the interactions of ALPs and SM particles. In principle they have similar couplings as the QCD axion and the various coupling constants might be calculable in specific models [61]. In a model-independent approach, they can be treated as free parameters. However, due to their NG nature, the interactions are in general suppressed by the symmetry breaking scale f_A. Assuming a high f_A, this leads to very feeble interactions.

Since the ALP couplings to the photon and fermions are so similar to those in the case of the QCD axion, most of the experiments that are actually intended to detect the QCD axion are also sensitive to ALP interactions. This might seem like an advantage since the parameter space can be probed basically model independently. But on the other hand, a signal caused by the QCD axion or an ALP could virtually not be distinguished, leading to interesting challenges in case of an actual detection. In fact, we would need as many signals as possible, from as many different kinds of experiments, to be sure whether an ALP or the QCD axion was detected. This is also discussed in Ref. [43].

Finally, we note that ALPs also appear in more ambitious unified theories. For example, in SUSY theories or string theoretical models [62]. In the latter, scalar fields with axion-like properties come up in great numbers when the higher spacetime dimensions are compactified. Here, ALPs appear as Kaluza-Klein modes with a plethora of different masses. This phenomenon is often dubbed as axiverse [20], meaning that the universe should basically be full of ALPs with different kinds of roles.

II.3. Axion and ALP Interactions with the SM

At low energies, the important interactions of the axion with the SM are the ones with photons, nucleons, and electrons. We can write the phenomenologically most interesting interactions as

$$\mathcal{L}_{\text{int}} = -\frac{g_{a\gamma\gamma}}{4} a F^{\mu\nu}\tilde{F}_{\mu\nu} + \mathrm{i}\sum_{f=n,p,e}\frac{g_{af}}{2m_f}\left(\partial_\mu a\right)\bar{\mathbf{\Psi}}_f\gamma^\mu\gamma_5\mathbf{\Psi}_f - \mathrm{i}\sum_{f=p,n}\frac{g_{af\gamma}}{2m_f} a F^{\mu\nu}\bar{\mathbf{\Psi}}_f\sigma_{\mu\nu}\gamma_5\mathbf{\Psi}_f\,. \tag{II.21}$$

Note that for historical reasons $g_{a\gamma\gamma}$ and $g_{af\gamma}$ have mass dimension -1, whereas the coupling to fermions g_{af} is dimensionless [43].

As we have discussed before, in specific axion or ALP models the value of the coupling constants might be calculable and related to some other paramters. To express the couplings g in Eq. (II.21) via dimensionless coupling constants C, we can restore the $\sim 1/f_a$ dependence we have found in Eq. (II.10) and (II.11), by making the identifications

$$g_{a\gamma\gamma} \equiv \frac{\alpha}{2\pi}\frac{C_{a\gamma\gamma}}{f_a} \quad , \quad g_{af} \equiv \frac{C_{af}m_f}{f_a} \quad , \quad g_{af\gamma} \equiv \frac{C_{af\gamma}}{f_a}\,. \tag{II.22}$$

Let us take a brief look at the actual values for the coupling constants in the case of the KSVZ and DFSZ model for the QCD axion. To calculate the coupling with neutrons and protons, model independent contributions from the meson mixing are important. For that, careful QCD calculations are needed. In Ref. [52], Villadoro et al present results of an analysis using chiral perturbation theory. They report values for the coupling of axions to protons and neutrons in KSVZ-like models,

$$C_{ap}^{\text{KSVZ}} = -0.47(3) \quad , \quad C_{an}^{\text{KSVZ}} = -0.02(3) \tag{II.23}$$

and for DFSZ-like models

$$C_{ap}^{\text{DFSZ}} = -0.617 + 0.435\sin^2\beta \pm 0.025 \quad , \quad C_{an}^{\text{DFSZ}} = 0.254 - 0.414\sin^2\beta \pm 0.025\,. \tag{II.24}$$

The angle β is related to ratio of the Higgs vevs. Note that the uncertainty comes from using chiral perturbation theory for the low energy QCD calculations.

The axion-photon coupling [52]

$$C_{a\gamma\gamma} = \frac{E}{N} - 1.92(4) \tag{II.25}$$

has the same form for DFSZ and KSVZ models. But it depends on the ratio of the electromagnetic anomaly number E and the color anomaly number N. In hadronic axion models, a subclass of the KSVZ models, one usually has $E/N = 0$, whereas in classical DFSZ models $E/N = 8/3$. However, it was recently shown by Di Luzio et al in Ref. [63] that these might not be the only possible values for E/N in DFSZ or KSVZ models which solve the strong CP problem. This enlarges the possible parameter space for the axion-photon coupling quite a bit.

In the following, we want to give a brief overwiew on the observational implications of the different axion interactions with the SM particles.

Axion-Photon Coupling

The first term in Eq. (II.21) leads to the coupling of axions to two photons which makes in principle a decay of the axion into two photons possible. The photons resulting from the process $a \to 2\gamma$ would have a very clear signature with frequencies $\omega = m_a/2$ each. However, for large breaking scales, say $f_a \sim 10^{12}$ GeV, the lifetime of the axion is longer than the age of the

Universe. This makes it cosmologically stable, which is also necessary for being a DM contender by the way.

But the $g_{a\gamma\gamma}$ coupling also leads to the mixing of the axion and photons in strong electromagnetic fields. This is known as the Primakoff effect and is experimentally the most accessible axion detection channel. In a seminal work by Sikive [64], two experiments exploiting the Primakoff effect were proposed. In so-called light shining through a wall (LSW) experiments, a laser is directed through a strong magnetic field onto a wall. In the magnetic field photons from the laser can turn into axions. The very weakly interacting axions easily penetrate the wall. If behind the wall again a strong magnetic field is applied, the axions turn back into detectable photons. The currently best limits by a LSW experiment come from OSQAR at CERN, excluding $|g_{a\gamma\gamma}| > 10^{-7}$ GeV for $m_a < 10^{-4}$ eV [51].

Sikivie also proposed a setup to detect DM axions using the Primakoff effect. Assuming that the DM halo consists of axions permeating the Earth constantly, the idea is to use a microwave cavity with a strong magnetic field as a haloscope. In the cavity, axions could resonantly mix with the photons from the magnetic field and produce a microwave signal. The ADMX experiment (University of Washington) is the longest running axion DM haloscope using this technique [65]. Recently, first exclusion limits on the axion-photon coupling in a parameter range predicted by KSVZ as well as DFSZ models were reported [66]. In App. B we take a closer look at the axion-photon interaction. There we also present results of a quantum field calcuatlion for the induced electric and magnetic field caused by the interaction of an axion background field and a strong external magnetic field [67].

Finally, the Primakoff effect can be used to detect axions coming from astrophysical sources like the Sun [68, 69]. Assuming the axions are produced inside the Sun, be it via Primakoff or another interaction process, they could easily escape due to their weak interactions and travel to the Earth. The idea of a so-called axion helioscope is to point a strong magnetic field to the Sun and incoming axions could be turned into photons therein. The CAST experiment at CERN is the first of its kind, using discarded LHC prototype magnets [70]. Currently, an upgrade of the CAST setup, called IAXO, is in its first stages [71].

The axion-photon mixing also offers an anomalous cooling mechanism for stars. By observations of horizontal branch stars and their lifetime, severe contraints on the cooling via axions can be made [72]. This excludes couplings $|g_{a\gamma\gamma}| > 6.6 \cdot 10^{-11}$ GeV^{-1} for a wide mass range [51]. Also the analyis of the spectrum of cosmic gamma rays can be used to test the axion-photon mixing. Therefore, observations by the H.E.S.S. and the Fermi-LAT collaborations put further constraints on the coupling $g_{a\gamma\gamma}$ [73, 74].

Axion-Nucleon Coupling

From the second term in Eq. (II.21), we learn that the axion, even tough being very light, cannot transmit scalar long-range interactions between macroscopic bodies. Therefore, the axion evades usual fifth force constraints. Nevertheless, the pseudo-scalar axion coupling might lead to interactions between two polarized probes [75]. For now, the constraints coming from such experiments are much weaker than the ones from astrophyssical considerations [76].

Namely, the most important implication from the axion-nucleon coupling is that it leads to another anomalous cooling mechanism for hot stars and especially supernovae. Here, the crucial process is nucleon-Bremsstrahlung like $n + n \rightarrow n + n + a$. With the latest results from neutron star cooling observations it is found that it must be $g_{an}^2 < 6 \cdot 10^{-19}$ [77].

Despite the axion nucleon coupling being not as easy experimentally accessible as the coupling to photons, there were recently some interesting new concepts put up which could test it anyway. For example, the pseudo-scalar interaction of the DM axion background field with a spinning nucleon could have a similar effect as in nuclear magnetic resonance [78].

Interstingly, the last term in Eq. (II.21) has the very same consequences as for why the axion was brought up to begin with. Namely, it causes an electric dipole moment for the neutron. But now, the effect is highly suppressed by the coupling scale f_a. Still, there exist ideas for

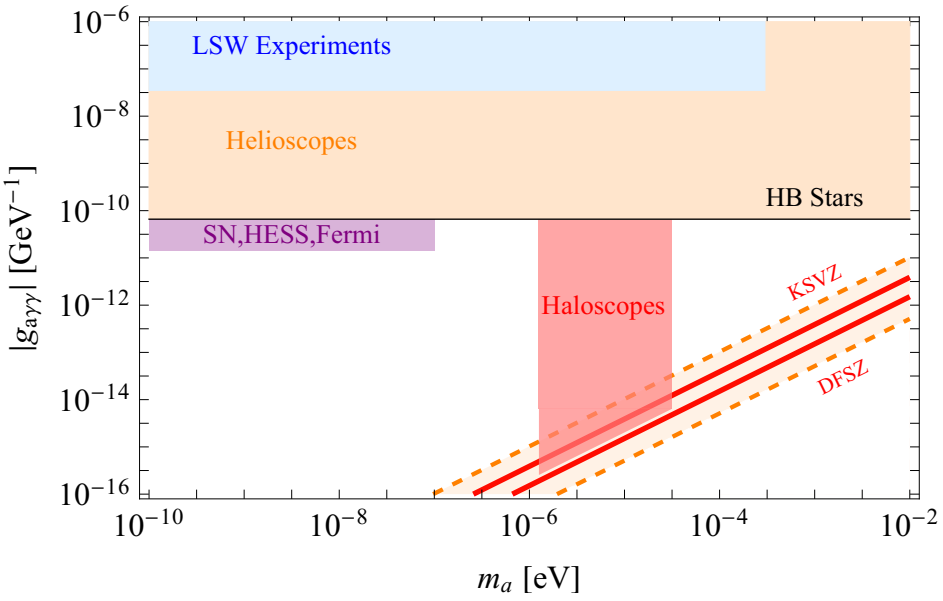

Figure II.1.: Parameter Space for ALP-Photon Coupling. The constraints (blue, orange, and purple regions) for the helioscope, light shining through a wall (LSW) experiments, and the astrophysical constraints (supernovae, H.E.S.S., FermiLAT) are extracted from Ref. [51], where similar plots can be found. The projection of the haloscope sensitivity (light red) is inspired by Ref. [43]. The red lines indicate the theory prediction for the photon coupling in case of KSVZ respectively DFSZ models, cf. Eq. (II.25). The band corresponds to variations of $C_{a\gamma\gamma}$ in different model setups.

experiments using this effect to detect effects of the DM axion field [78].

Axion Parameter Space

All the different couplings and interactions of the axion can be used to elucidate its properties. As an example, we show in Fig. II.1 a sketch of the $g_{a\gamma\gamma} - m_a$ parameter space with recent experimental constraints [51] and projections for future sensitivity of upcoming experiments [43]. We also add the DFSZ and KSVZ model predictions for the photon coupling of the QCD axion. We see that the various astrophysical as well as experimental observations test and constrain the parameter space already quite well. However, as we have stated in our introduction, the field of axion detection is very fastly growing. Thus, the picture in Fig. II.1 might change again soon. For an excellent review of the axion-SM interactions and the recent experimental efforts to detect the axion see Ref. [43].

III. Producing Relic Axions

In the previous chapter, we have discussed how the axion emerges as the Nambu-Goldstone, i.e. the phase degree of freedom, of a complex scalar field when the global $U(1)_{\rm PQ}$ symmetry is spontaneously broken. This happens at some high energy scale f_a. Put in the cosmological context, this means in the hot and early Universe.

There exist different cosmological production mechanisms for relic axions. Besides the usual thermal freeze-out, there are also very efficient non-thermal ones. These are the axion production via the so-called vacuum realignment mechanism and, in certain scenarios, via the decay of topological defects. In the following, we discuss the different sources for relic axions in some detail. The most attention is paid to the realignment mechanism, where we also derive useful quantitative estimates for the relic abundance of the QCD axion as well as for ALPs. We will see that the axions produced in this way are excellent candidates for explaining the observed DM in our Universe.

III.1. Thermal Production

Axions can be produced by different thermal processes in the SM plasma of the early Universe. After hadronization and at temperatures $T \lesssim 200$ MeV, the most important process is pion-axion conversion $\pi + N \;\leftrightarrow\; a + N$, with N being some nucleon. When the interaction rate of this process drops below the Hubble expansion, a number of relic axions freezes-out of the cosmological expansion. This is, for example, nicely discussed by Kolb and Turner in Ref. [79]. They estimate the number density of thermal relic axions to be

$$n_{a,\rm th} \simeq \frac{83\ \text{cm}^{-3}}{g_*(T_{\rm F})/10}\,, \tag{III.1}$$

which depends on the number of degrees of freedom g_* at time of freeze-out $T_{\rm F}$.

If the freeze-out happens at $T_{\rm F} > m_a$ the axions behave as dark radiation. As soon as the temperature drops below their mass, they evolve as non-relativistic matter. So, we note that thermal axions are not only produced in comparable numbers as massive neutrinos but also behave similarly. Hence, they would rather act as hot or warm DM than cold DM.

But for thermally producing axions in relevant numbers, the axion-SM interactions cannot be too weak. Recall that they scale inversely with f_a. It can be shown that we need $f_a \lesssim 10^{12}$ GeV to establish thermal equilibrium with the SM plasma, to begin with [44]. Otherwise, the thermal production is not possible or very inefficient. Furhter, in Ref. [79] it is shown that for having a relic abundance of thermally produced axions with $\Omega_{a,\rm th}h^2 \sim 0.1$, i.e. comparable with the observed amount of DM, the axion must be as heavy as $m_a \sim$ eV. Such heavy axions are not cosmologically stable and also strongly cosntrained from beam dump experiments [80]. For lighter axions, the contribution of thermally produced axions to the energy budget of the universe is completely negligible [44].

Therefore, we conclude that thermally produced axions are not a good candidate to explain the DM density in our Universe for various reasons. If they would be produced in large enough numbers, they would behave as hot DM which is strongly constrained by observations of large-scale structures [81] or they would not even be stable [80]. For masses $m_a \lesssim$ eV they will only

be a subdominant component of the relic axions since there are much more effective production mechanisms, as we will show in the following.

III.2. Vacuum Realignment

Vacuum realignment is a largely model-independent way of producing relic axions and it results basically only from the cosmological evolution of the axion field, as we will discuss now in some detail. A sketch of the situation is depicted in Fig. III.1. Reviews on the axion production via vacuum realignment can be found in Refs. [44, 79, 82]. Some of the original works on this topics are Refs. [27–30].

We start by considering the evolution of the axion field in an expanding universe. Its only interactions should be gravitational and all couplings with the SM particles are neglected. From our discussion considering the thermal production of axions, we know that this is a reasonable working assumption. The Lagrangian of the axion field is then simply

$$\mathcal{L}_a = -\frac{1}{2}\left(\partial_\mu a\right)\left(\partial^\mu a\right) - V(a)\,. \tag{III.2}$$

Following Eq. (II.19), we can write the potential as

$$V(a) = m_a^2 f_a^2 \left[1 - \cos\left(\frac{a}{f_a}\right)\right]\,. \tag{III.3}$$

It turns out to be convenient to work with the dimensionless field $\theta(x) \equiv a(x)/f_a$, which is often called the misalignment field. With Eq. (III.2), its Lagrangian is

$$\mathcal{L}_\theta = f_a^2 \left[-\frac{1}{2}\left(\partial_\mu \theta\right)\left(\partial^\mu \theta\right) - V(\theta)\right] \tag{III.4}$$

with the potential

$$V(\theta) = m_a^2\left(1 - \cos\theta\right)\,. \tag{III.5}$$

The geometry of the spacetime is defined via the metric $g^{\mu\nu}$ and we take it to be that of an expanding Friedman-Robertson-Walker universe. Assuming zero curvature, $g^{\mu\nu}$ is defined via the line element[1]

$$\mathrm{d}s^2 = -\mathrm{d}t^2 + R^2(t)\left(\mathrm{d}r^2 + \mathrm{d}\Omega^2\right)\,, \tag{III.6}$$

with R being the scale factor. Its evolution is determined by the Friedmann equation

$$H^2 = \frac{8\pi G}{3}\rho_\mathrm{c}\,, \tag{III.7}$$

where the Hubble rate H is defined as $H = \dot{R}/R$, and ρ_c is the energy density of the universe. As usual, dots denote derivatives with respect to time. Note that for now, we assume that the axion field only barely contributes to the overall energy density, i.e. it should not influence the evolution of H.

The equation governing the dynamics of θ can be derived by varying the action

$$S_\theta = \int \mathrm{d}^4x\ \sqrt{-g}\mathcal{L}_\theta\,. \tag{III.8}$$

With Eq. (III.3) and (III.6) we find the equation of motion:

$$\ddot{\theta} + 3H\dot{\theta} - \frac{1}{R^2}\nabla^2\theta + \frac{\mathrm{d}V}{\mathrm{d}\theta} = 0\,. \tag{III.9}$$

[1] Note that Eq. (III.6) implies that we are using the convention where $g_{\mu\nu}$ has mostly positive entries on its diagonal.

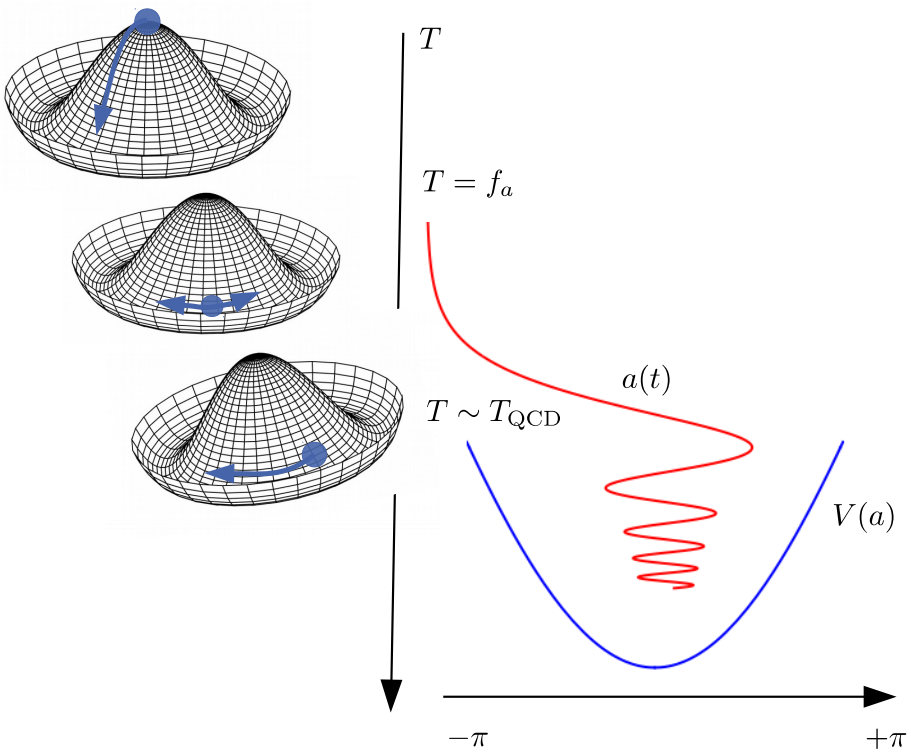

Figure III.1.: The Vacuum Realignment Mechanism. At temperatures $T = f_a$ the complex Peccei-Quinn scalar field develops its vacuum expectation value and breaks the global $U(1)_{\mathrm{PQ}}$ symmetry. This can be pictured as the complex scalar falling into the valley of its Mexican hat potential. It can fall basically in any given direction since none is energetically favored. We say the potential is flat in this direction. This means that the axion, which is identified as the phase of the complex scalar, is massless and can have any value in $a/f_a \in [-\pi, \pi]$. At high temperatures the axion field is essentially frozen at this value. But when the universe cools down to temperatures $T \sim T_{\mathrm{QCD}}$ around the QCD phase transition, a potential $V(a)$ and therefore a mass for the axion is generated. This can be pictured as the Mexican hat being slightly tilted. This implies that the axion field is driven away from its initial value and it has to realign with the CP conserving minimum of its potential, the vacuum state with the lowest energy. Therefore, as soon as it can overcome the so-called Hubble drag of the cosmological expansion, the axion field will start to roll down to the potential minimum. It will slightly overshoot it and start to oscillate around it. The energy stored in this coherent oscillations behaves as collisionless matter and can explain the observed DM energy density.

The axion energy density ρ_a, as well as the pressure P_a, can be calculated from the stress-energy tensor

$$T^{\mu\nu} = f_a^2 \partial^\mu\theta\partial^\nu\theta + g^{\mu\nu}\mathcal{L}_\theta \tag{III.10}$$

and we find with $\rho_a = T^0{}_0$ and $P_a = T^i{}_i$:

$$\rho_a = f_a^2\left[\frac{1}{2}\dot{\theta}^2 + \frac{1}{2R^2}(\nabla\theta)^2 + V(\theta)\right], \tag{III.11}$$

$$P_a = f_a^2\left[\frac{1}{2}\dot{\theta}^2 - \frac{1}{6R^2}(\nabla\theta)^2 - V(\theta)\right]. \tag{III.12}$$

Using the full cosine-potential of the axion makes the evolution equation of θ nonlinear and therefore difficult to study, at least analytically. However, we note that for small θ the potential becomes approximately harmonic, namely

$$V(\theta) \simeq \frac{1}{2}m_a^2\theta^2\,. \tag{III.13}$$

Using this harmonic approximation linearizes the evolution equation and simplifies things a lot. On the other hand, since θ can in principle have any value in $[-\pi,\pi]$, the assumption that θ is small might seem very ad hoc. Further, in the harmonic approximation the information that θ is in fact a periodic variable is completely lost and therefore potentially important effects for the field evolution are neglected. We will encounter this problem later, when we discuss toplogical defects in Sec. III.3. Nevertheless, the advantages of the harmonic approximation outweigh these shortcomings since it allows us to study the Eq. (III.9) analytically. This makes it possible to not only understand the axion field evolution qualitatively but also to derive robust quantitative estimates on the energy density of the axions produced thereby.

In the harmonic approximation the equation of motion is given by

$$\ddot{\theta} + 3H\dot{\theta} - \frac{1}{R^2}\nabla^2\theta + m_a^2\theta = 0\,, \tag{III.14}$$

which is similar to that of a damped harmonic oscillator, where H plays the role of the friction and the gradient term plus the mass term that of the frequency.

Recall that the axion mass is a function of temperature, $m_a = m_a(T)$. At early times, long before the QCD effects become important, we have $m_a(T) \sim 0$ and the axion is massless. This means that $H \gg m_a$ and the Hubble friction term in the evolution equation dominates. Thus for early times $T \gg T_{\mathrm{QCD}}$ and Eq. (III.14) becomes

$$\ddot{\theta} + 3H\dot{\theta} - \frac{1}{R^2}\nabla^2\theta = 0\,. \tag{III.15}$$

Rewriting this in terms of the Fourier transform $\theta_k = \int \mathrm{d}^3k/(2\pi)^3\theta(\vec{x})$, we see that the equations of the single modes k decouple and we have

$$\ddot{\theta}_k + 3H\dot{\theta}_k + \frac{k^2}{R^2}\theta_k = 0\,. \tag{III.16}$$

For now, we are mostly interested in gaining a qualitative understanding of the cosmological evolution of the axion field and calculating the energy density. For the latter, we see from Eq. (III.11) that the contribution from axions with $k \neq 0$ will be redshifted away quickly compared to the contribution of the zero-mode. Therefore, we focus for the moment on the evolution equation of the zero-mode only. However, in Sec. IV we will revisit the equation of motion of θ and include the gradient terms in a conclusive solution. We will see that in certain scenarios these are important for the acutal evolution of the field and lead to very interesting phenomenological consquences.

For $k = 0$, i.e. the homogeneous θ field, Eq. (III.15) becomes

$$\ddot{\theta} + 3H\dot{\theta} = 0 \quad \text{for } H > m_a \tag{III.17}$$

and therefore θ is frozen at is intial value $\theta = \theta_\mathrm{I}$, as we have already anticipated in our sketch in Fig. III.1.

But how do we chose θ_I? Recall that when the Peccei-Quinn symmetry is broken, the misalignment field can take some random value from $[-\pi, \pi]$ in causally disconnected regions. If this happens before an inflationary epoch of the universe, let us call this the pre-inflation scenario, one of these causal regions with uniform θ_I value is blown up by inflation and will eventually occupy the whole visible universe. Hence, after inflation the θ_I value of the axion field is the same everywhere and fixed at some random value. On the other hand, in a post-inflation Peccei-Quinn breaking scenario the situation is quite different. Here, the visible universe consists after Peccei-Quinn breaking of many patches with different θ_I values. But before discussing this interesting situation, let us start by considering the first and more simple scenario, where Peccei-Quinn breaking happens before the end of inflation.

Pre-Inflation Scenario

Before continuing, we note that as long as the field is frozen at $\theta = \theta_\mathrm{I}$, we have $\rho_a = -P_a$. Hence, it has the same equation of state, $w \equiv P/\rho = -1$, as dark energy. But as long as its contribution to the energy budget is negligible, it will not influence the overall cosmological evolution. However, if the axion field would be frozen at θ_I still in the late universe it could eventually become relevant compared to the radiation and matter energy contributions and therefore drive an accelerated expansion. For making this possible the axion must essentially be massless, such that $H \gg m_a$ holds also at late times or today where we indeed observe the accelerated expasion of our Universe. For the QCD axion this is basically impossible since Peccei-Quinn breaking scales f_a beyond the Planck scale would be needed, as a quick check with the value for the Hubble rate today $H_0 \sim 10^{-33}$ eV [83] and the relation for the zero-temperature axion mass m_a in Eq. II.16 shows. But even for ultra-light ALPs explaining the accelerated expansion of our Universe is rather difficult since other cosmological observations strongly constrain such light axions. In Sec. VI we take a closer look at the limits on the mass of ultra-light axions. See also, for example, Ref. [82] and references therein for a more in-depth discussion of possible axion explanations for the observed cosmological constant.

For the moment, we conclude that it is safe to expect that at some point in the cosmological evolution the mass term in

$$\ddot{\theta} + 3H(T)\dot{\theta} + m_a^2(T)\theta = 0 \tag{III.18}$$

eventually overcomes the Hubble friction. In our sketch of the axion field evolution in Fig. III.1 we have identified this as the time the field starts to roll down to the potential minimum. From Eq. (III.18) we see that as soon as $H(T) \lesssim m_a(T)$, the field will start to oscillate with a frequency given by $\sim m_a$. This motivates an ansatz of the WKB form:

$$\theta(t) = A(t)\mathrm{e}^{\mathrm{i}\Phi(t)}\,. \tag{III.19}$$

The functions $A(t)$, $\Phi(t)$ are real valued and we should keep in mind that θ is also real. Plugging this ansatz in Eq. (III.18), we find:

$$\frac{\ddot{A}}{A} - \dot{\Phi}^2 + 3H\frac{\dot{A}}{A} + m_a^2 = 0\,, \tag{III.20}$$

$$\dot{A} + A\left(\frac{3}{2}H + \frac{\ddot{\Phi}}{2\dot{\Phi}}\right) = 0\,. \tag{III.21}$$

As usual for the WKB approach, we assume that $A(t)$ is a slowly varying function relative to $\Phi(t)$ and the dynamics in $\Phi(t)$ are of the order of the frequency, i.e. m_a in our case. This means, we can use that $\ddot{A}/A, H\dot{A}/A \ll \dot{\Phi}_a^2, m_a^2$. Doing so, Eq. (III.20) becomes[2]

$$\dot{\Phi}^2 = m_a^2 \quad \Rightarrow \quad \Phi(t) = \int \mathrm{d}t'\, m_a(t') + \text{const}\,. \tag{III.22}$$

Using this intermediate result in Eq. (III.21), we find[3]

$$\dot{A} + A\left(\frac{3}{2}H + \frac{\dot{m}_a}{2m_a}\right) = 0\,, \tag{III.23}$$

which is solved by

$$A(t) = \frac{C}{R^{3/2}\sqrt{m_a(t)}} \tag{III.24}$$

and C is some real constant. Using these results in our ansatz and taking the real part, we find that $\theta(t)$ is of the form

$$\theta(t) = \frac{C}{R^{3/2}\sqrt{m_a(t)}} \cos \int_{t_0} \mathrm{d}t'\, m_a(t')\,, \tag{III.25}$$

where still the constant C must be determined by the initial conditions. For finding these let us take a look at the behavior of the energy density ρ_a. Before the field starts to oscillate, it is frozen at its initial value θ_I and ρ_a is constant. Therefore, we have

$$\rho_a(t) = \frac{1}{2} f_a^2 m_a^2(t) \theta_\mathrm{I}^2 \quad \text{for } H > m_a\,. \tag{III.26}$$

After the field starts to oscillate our solution for $\theta(t)$ in Eq. (III.25) should apply. It has a rapidly oscillating part, with the characteristic frequency $\sim m_a$, and a slowly evolving envelope. Taking the mean $\langle\cdot\rangle$ over the fast oscillations, we find for the energy density

$$\langle \rho_a(t) \rangle = \frac{C^2}{2m_a(t)} \frac{f_a^2 m_a^2(t)}{R^3} \quad \text{for } H < m_a\,. \tag{III.27}$$

These two limiting expressions for the energy density ρ_a should be patched together at the time the field starts to oscillate. Let us call this time $t = t_\mathrm{osc}$, which we can equivalently expressed by a temperature $T = T_\mathrm{osc}$. This temperature can be estimated by setting $3H(T_\mathrm{osc}) = m_a(T_\mathrm{osc})$, i.e. when Hubble friction and mass term become equally important. Equating (III.26) and (III.27) at $T = T_\mathrm{osc}$ gives

$$C^2 = m_a(T_\mathrm{osc}) R^3(T_\mathrm{osc}) \theta_\mathrm{I}^2 \tag{III.28}$$

and therefore the energy density at temperatures $T < T_\mathrm{osc}$ is

$$\rho_a(T) \simeq \frac{1}{2} f_a^2 m_a(T_\mathrm{osc}) m_a(T) \left(\frac{R(T_\mathrm{osc})}{R(T)}\right)^3 \theta_\mathrm{I}^2\,. \tag{III.29}$$

This result can of course only be an estimate since we bravely patched together the two limiting, very different behaviors of $\theta(t)$. In reality, there should be a smooth transition between the two. However, an important result is that the energy density behaves as $\rho_a \propto m_a(t)/R^3(t)$.

[2] Note that in fact $\dot{\Phi}^2 = m_a^2$ leads to two possible solutions. Without loss of generality we chose $\dot{\Phi} = m_a$. Using that m_a is a function growing in time, it can be easily shown that taking the minus sign instead leads to to the very same result in the end.

[3] Note that the axion mass should switch on adiabatically in the sense that $\dot{m}_a/m_a$ exists and is well behaved. A sudden switch on of the mass would imply that $\dot{m}_a \to \infty$ at some point. This corresponds to a first order phase transition. Such a scenario must be treated differently, see e.g. Ref. [84].

This means that the comoving number density of axions $n_a \equiv \rho_a/m_a \propto R^{-3}$ produced via this realignment mechanism is conserved, as soon as the field starts to oscillate.

Further, we can use our result for $\theta(t)$ to calculate the pressure and we find

$$\langle P_a(t) \rangle = 0\,, \tag{III.30}$$

where we took again the average over the fast oscillations. Thus, with the comoving number of axions n_a being conserved and an equation of state $w = 0$, we conclude that the realignment axions behave just as non-realtivistic matter, i.e. like CDM.

However, to complete this statement we should also show that the fluctuations in the axion energy density can explain the observed large-scale structures. This means that the fluctuations $\delta \equiv (\rho_a - \bar{\rho}_a)/\bar{\rho}_a$, $\bar{\rho}_a$ being the spatial mean of the axion energy density, should basically start to grow linearly after matter-radiation equality, as in the standard CDM lore. Noh et al gave a proof in a series of papers [85–88] that this is indeed the case. Still, it should be noted that the evolution equation of the linear axion fluctuations is slightly modified compared to usual CDM. Without going into too much detail, we simply quote the result for the equation governing the dynamics of δ in linear order cosmological perturbation theory [85]:

$$\ddot{\delta} + 2H\dot{\delta} - \left(4\pi G_N \bar{\rho}_a - \frac{1}{4}\frac{k^4}{m_a^2 R^2}\right)\delta = 0\,, \tag{III.31}$$

with G_N being Newton's constant. From this we see that the evolution equation contains an effective soundspeed $c_s^2 \neq 1$, depending on the scale k of the fluctuations. This defines the axion Jeans scale $k_J = (16\pi G \bar{\rho}_a m_a^2)^{1/4}$ and modes $k < k_J$ will grow linearly after matter-radiation equality, as standard CDM fluctuations do. On the other hand, modes with $k > k_J$ oscillate and therefore suppress structure formation on very small scales. However, for axion masses $m_a > 10^{-22} - 10^{-21}$ eV this scale is cosmologically completetly irrelevant. Hence, as long as the axion is heavy enough it reproduces the same behavior for the matter power spectrum as we woul expect for standard CDM. But for ultra-light axions with $m_a \sim 10^{-22}$ eV the suppression effect might become relevant and observable [89–91]. Again, we revisit the issue of ultra-light axions in Sec. VI. At this point, we conclude that as long as we consider axions with masses $m_a > 10^{-22}$ eV we can treat them as normal CDM.

Before moving to the post-inflation scenario, we want to point out that we learn from our result in Eq. (III.29) that the energy stored in the axion field oscillations depends on the initial misalignment angle θ_I. This is very intuitive since it simply means that the stored energy is sensitive to the point from where the field started to roll down to its potential minimum. Recall that in the pre-inflation scenario, θ_I is just some arbitrary value in $[-\pi, \pi]$. Allowing for some fine-tuning in this free parameter, one can set ρ_a to almost any desired value. One could argue that this makes the pre-inflation scenario rather less predictive, cf. Ref. [92] for a discussion of this topic and Ref. [93] for a very recent in-depth global analysis in view of the axion being the DM in a pre-inflation scenario. We will see that the ambiguity of choosing θ_I vanishes in the post-inflation Peccei-Quinn breaking scenario.

Post-Inflation Scenario

Recall that in the post-inflation scenario the universe after Peccei-Quinn symmetry breaking consists of many patches with different values for θ_I. The size of this patches is basically fixed by the causal horizon and therefore the Hubble rate $H(T)$. It turns out that this very inhomogeneous initial conditions for the axion field lead to large isocurvature fluctuations in the energy density, see e.g. Ref. [94].[4] Following the field evolution in this scenario and calculating ρ_a is very non-trivial. The so far neglected gradient terms and also the nonlinearity of the

[4] We will later, in Ch. VI, define more carefully what is meant by isocurvature fluctuations. Till then, we simply use this term to indicate that these are fluctuations in the axion component only.

potential have important consequences. We will discuss this interesting topics in more detail in Sec. III.3 and Ch. IV. But for now, let us focus on calculating the mean energy density

$$\overline{\rho}_a = \frac{1}{V}\int \mathrm{d}^3x\ \rho_a(\vec{x}) \tag{III.32}$$

of the axion energy density in the post-inflation scenario.

To get an estimate for it, let us assume that also at the time the oscillations commence, the axion field consists of many independent patches with different values for θ_I. Then, the energy density of every patch depends on its initial misalignment angle θ_I but else should be of the form as found Eq. (III.29). This means that taking the spatial mean of the energy density corresponds to summing over all the patches, which is in fact equivalent to summing over all the random draws of θ_I [79, 94].[5] Hence, the mean energy density is

$$\overline{\rho}_a(T) \simeq \frac{1}{2}f_a^2 m_a(T_\mathrm{osc})m_a(T)\left(\frac{R(T_\mathrm{osc})}{R(T)}\right)^3\overline{\theta}_\mathrm{I}^2 \tag{III.33}$$

with

$$\overline{\theta}_\mathrm{I}^2 = \int \mathrm{d}\theta\ \mathcal{F}(\theta)\theta^2 = \frac{\pi^2}{3} \tag{III.34}$$

being the variance of θ_I. To calculate this quantitiy, we have assumed a flat probability distribution function $\mathcal{F}(\theta) = 1/(2\pi)$ for θ. This is reasonable since no specific choice for θ_I in the interval $[-\pi, \pi]$ is preferred.

Thus, in contrast to the pre-inflation scenario the realignment axion energy density does not depend on a free parameter, but is essentially fixed by f_a and m_a. This makes the post-inflation scenario very predicitive, at first glance. Setting ρ_a to the observed DM density in principle fixes a specifc DM axion mass, at least for for the QCD scenario. However, unfortunately there is a remaining uncertainty in predicting ρ_a in the post-inflation scenario coming from the number of axions produced in the decay of topological defects, cf. Sec. III.3 for more details.

A Quantitative Estimate

Neglecting for a moment this uncertainties, we turn to a more quantitative estimate of the relic abundance of axions produced in the realignment mechanism. Since the form of ρ_a is basically the same in the pre- and post-inflation scenario we can cover both cases at once. Further, we will be as general as possible for assuming the actual relation of the axion mass m_a and Peccei-Quinn breaking scale f_a, such that our results also apply for ALPs.

For calculating the axion energy density today $\rho_{a0} \equiv \rho_a(T_0)$, it is convenient to express the ratio of $R(T_\mathrm{osc})/R(T_0)$ appearing in the expressions for ρ_a via the entropy conservation in the radiation component, i.e. we use $s(T_\mathrm{osc})R^3(T_\mathrm{osc}) = s(T_0)R^3(T_0)$. For the temperature dependence of the entropy density it holds that [79]

$$s(T) = \frac{2\pi^2}{45}g_{s*}(T)T^3\,, \tag{III.35}$$

where $g_{*s}(T)$ are the properly weighted relativistic degrees of freedom. With that we find

$$\rho_{a0} \equiv \rho_a(T_0) = \frac{1}{2}f_a^2 m_a(T_\mathrm{osc})m_a(T_0)\frac{g_{s*}(T_0)}{g_{s*}(T_\mathrm{osc})}\left(\frac{T_0}{T_\mathrm{osc}}\right)^3\begin{cases}\overline{\theta}_\mathrm{I}^2 = \frac{\pi^2}{3} & \text{post-inflation}\\ \theta_\mathrm{I}^2 \in [0,\pi^2] & \text{pre-inflation}\end{cases}. \tag{III.36}$$

For making further progress we obviously have to determine T_osc. To do so, we must specify an explicit temperature dependence for the axion mass m_a. For the QCD axion, this is set by the topological susceptibility of QCD $\chi_\mathrm{QCD}(T)$ which is only known numerically. But to also

[5] A sketch of the post-inflation realignment scenario can be found in Fig. IV.1 at the beginning of Ch. IV.

include the case of ALPs and to study the parametric dependence of $T_{\rm osc}$ and therefore ρ_a on the fundamental model parameters f_a and m_a, let us rather assume a power law for $m_a(T)$ which for low temperatures becomes constant and goes to the zero-temperature mass $m_a = \Lambda^2/f_a$. Recall that in the case of the QCD axion $\Lambda = \chi_{\rm QCD}^{1/4}(T \lesssim 100 \text{ MeV}) \approx 75.5$ MeV [60] and for ALPs Λ is a yet arbitrary scale. Thus, we use as a parameterization for the temperature dependent axion mass[6]

$$m_a(T) = \min\left[\frac{\Lambda^2}{f_a}, b\frac{\Lambda^2}{f_a}\left(\frac{\Lambda}{T}\right)^n\right] \tag{III.37}$$

$$= \begin{cases} b\frac{\Lambda^2}{f_a}\left(\frac{\Lambda}{T}\right)^n & , T \geq b^{1/n}\Lambda \\ \frac{\Lambda^2}{f_a} & , T < b^{1/n}\Lambda \end{cases}, \tag{III.38}$$

introducing the parameter $b \simeq 0.1 \ldots 10$ to take into account that the transition to the zero temperature mass might not be exactly at $T = \Lambda$. The parameter $n \in \mathbb{R}^+$ controls how sudden the mass is switched on.

Now, we are able to determine $T_{\rm osc}$ using its definition, $3H(T_{\rm osc}) = m_a(T_{\rm osc})$. For that we have to consider different cases: First, we have to distinguish if the oscillations start in a radiation or matter dominated epoch. Note that in the latter case, the axion cannot serve as the DM in our Universe since it has no time to provide the gravitational potential wells for the visible matter and therefore to explain structure formation in the usual way [95]. However, in the present work we are especially interested in scenarios where the axion can be the DM. Thus, we want to focus on scenarios where the oscillations start already in radiation dominated epoch, i.e. at temperatures $T > T_{\rm eq} \sim 9 \cdot 10^3$ K ~ 1 eV. This allows us to derive a lower bound on the axion mass for which it still can be the DM. Since $H(T_{\rm eq}) \sim 10^{-28}$ eV this constraint is $m_a \gtrsim 10^{-27}$ eV [82]. In the following we will always assume the axion to be heavier than this. Thus, with oscillations starting already at relatively high temperatures we can use the known relation for the Hubble rate $H(T)$ in a radiation dominated universe [79]

$$H(T) = \left[\frac{8\pi^3 g_*(T)}{90 M_{\rm Pl}^2}\right]^{1/2} T^2 \simeq 1.66\sqrt{g_*(T)}\frac{T^2}{M_{\rm Pl}}\,, \tag{III.39}$$

where the relativistic degrees of freedom are given by $g_*(T)$. For the explicit temperature dependence of $g_*(T > 100 \text{ MeV})$ as well as $g_{s*}(T > 100 \text{ MeV})$ we use the tabulated values from the recent lattice calculations by Borsanyi et al presented in Ref. [96] and apply an interpolation with the cubic spline method. Below $T = 100$ MeV we set $g_* = 3.36$ and $g_{s*} = 3.91$ to be constant [79].

The next distinction we have to make is if $T_{\rm osc}$ is before or after the mass reaches its zero temperature value. With our parameterization for m_a in Eq. (III.38) the first scenario means $T_{\rm osc} < b^{1/n}\Lambda$. This can be translated to a constraint on f_a:

$$\left(\frac{M_{\rm Pl}}{f_a}\right)^{1/2} \frac{1}{2.23\ g_*(T_{\rm osc})^{1/4}} < b^{1/n} \tag{III.40}$$

$$\Rightarrow \quad \left(\frac{M_{\rm pl}}{f_a}\right)^{1/2} \lesssim 1\,. \tag{III.41}$$

To get to the second line, we have assumed that $g_*(T_{\rm osc}) \sim 100$ and $b \sim 1$. So, as long as the Peccei-Quinn breaking scale is well below the Planck scale, i.e. $f_a < M_{\rm Pl}$, oscillations should always commence before the axion reaches its zero temperature value.

[6] See also Eq. (II.18) and for example the work by Visinelli and Gondolo in Ref. [31] for a similar parameterization of m_a in case of the QCD axion. But note that an important difference is that in this parameterization of Gondolo et al the zero-temperature mass is always reached at $T = \Lambda$, whereas in ours this happens at $T = b^{1/n}\Lambda$.

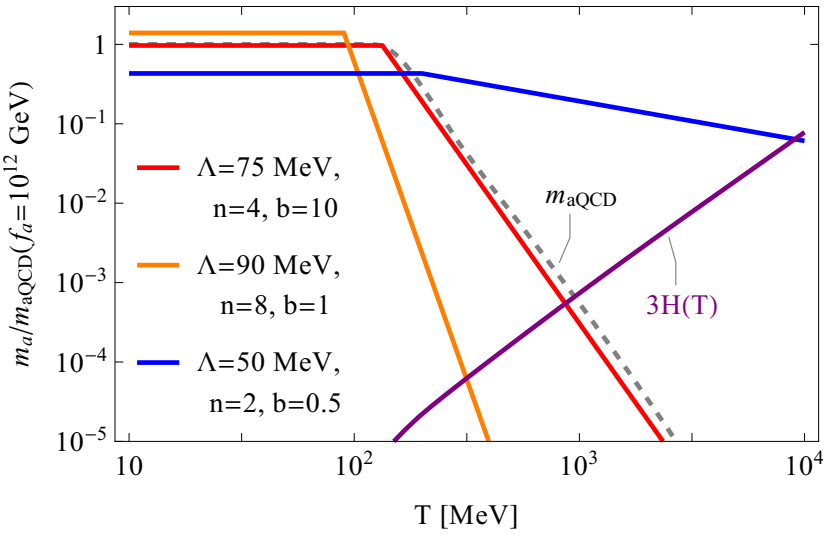

Figure III.2.: Temperature dependent Axion mass and the Hubble Rate. We use the parameterization in Eq. (III.38) for $m_a(T)$ and different values for Λ, b and n to show the temperature dependent axion mass. The Pecci-Quinn breaking scale is set to $f_a = 10^{12}$ GeV. We also show the evolution for the QCD axion $m_{a\rm QCD}(T) = \chi^{1/2}_{\rm QCD}(T)/f_a$, dashed gray line, using the result for the toplogical susceptibility from lattice calculations in Ref. [96]. We normalize m_a to the zero temperature QCD axion mass $m_{a\rm QCD} \simeq 5.6 \cdot 10^{-6}$ eV for a better comparison. The purple line shows the Hubble rate also normalized to $m_{a\rm QCD}$. At temperatures $T = T_{\rm osc}$, where $3H = m_a$, the axion field starts to oscillate.

Assuming that $f_a < M_{\rm Pl}$ and therefore $T_{\rm osc} > b^{1/n}\Lambda$, we find for the oscillation temperature:

$$T_{\rm osc} = b^{1/(2+n)}\Lambda\left(\frac{M_{\rm Pl}}{f_a}\right)^{1/(2+n)} \frac{1}{(4.98)^{1/(2+n)} g_*(T_{\rm osc})^{1/(4+2n)}} \tag{III.42}$$

$$= b^{1/(2+n)} m_a^{1/2} M_{\rm Pl}^{1/(2+n)} f_a^{n/(4+2n)} \frac{1}{(4.98)^{1/(2+n)} g_*(T_{\rm osc})^{1/(4+2n)}}\,, \tag{III.43}$$

which has still a very non-trivial dependence on the number of relativistic degrees of freedom $g_*(T)$. Therefore, $T_{\rm osc}$ can in general only be determined numerically. Note that in the second line we have expressed Λ by the zero temperature mass m_a via $\Lambda^2 = m_a f_a$.

In Fig. III.2, we show $m_a(T)$ for different choices of the parameters Λ, b, and n, while fixing $f_a = 10^{12}$ GeV. We also add the temperature dependent QCD axion mass $m_{a\rm QCD}(T) = \chi^{1/2}_{\rm QCD}(T)/f_a$ to the plot, using the lattice results from Ref. [96] for the temperature dependence of toplogical susceptibility. It turns out that when setting $\Lambda \simeq \chi^{1/4}_{\rm QCD}(T=0) \simeq 75.5$ MeV, $n = 4$, and $b = 10$ we are able to parmeterize the temperature dendence of the QCD axion mass quite well. By showing also the Hubble rate $H(T)$, using the expression Eq. (III.39), we can identify the intersection of the curves m_a and $3H$ at $T = T_{\rm osc}$. We see that this is indeed well before the mass becomes constant.

With the explicit form for $m_a(T_{\rm osc})$, we can write the energy density as

$$\rho_{a0} = \frac{b}{2}\Lambda^4\left(\frac{\Lambda}{T_{\rm osc}}\right)^n \frac{g_{s*}(T_0)}{g_{s*}(T_{\rm osc})}\left(\frac{T_0}{T_{\rm osc}}\right)^3 \begin{cases} \bar{\theta}_{\rm I}^2 = \frac{\pi^2}{3} & \text{post-inflation} \\ \theta_{\rm I}^2 \in [0,\pi^2] & \text{pre-inflation} \end{cases} \tag{III.44}$$

$$= \frac{b}{2}\frac{m_a^{(n+4)/2} f_a^{(n+4)/2}}{T_{\rm osc}^n} \frac{g_{s*}(T_0)}{g_{s*}(T_{\rm osc})}\left(\frac{T_0}{T_{\rm osc}}\right)^3 \begin{cases} \bar{\theta}_{\rm I}^2 = \frac{\pi^2}{3} & \text{post-inflation} \\ \theta_{\rm I}^2 \in [0,\pi^2] & \text{pre-inflation} \end{cases} \tag{III.45}$$

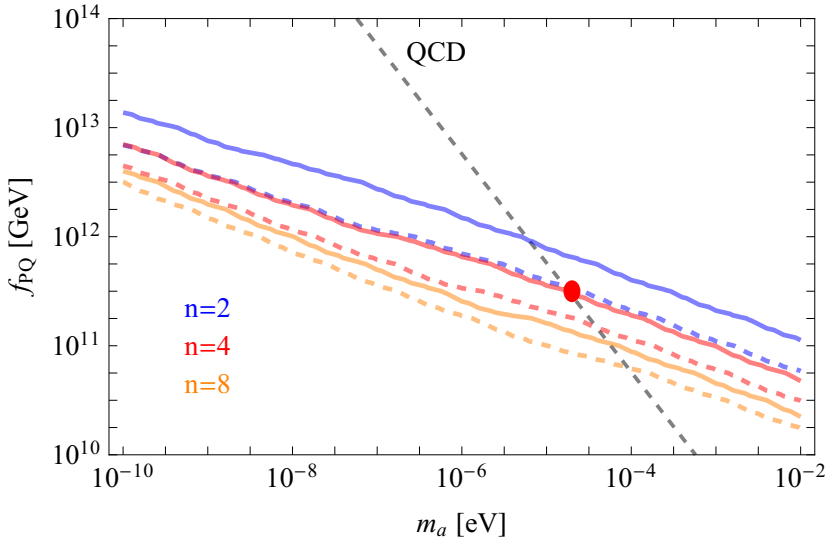

Figure III.3.: Axion Properties explaining DM Abundance in post-inflation Realignment Scenario. With the relation for the axion energy density ρ_a discussed in the text we calculate contours in the $m_a - f_a$ plane where $\Omega_a h^2 = 0.1$. To parameterize the temperature dependence of the axion mass we use Eq. (III.38) and set $n = 2, 4, 8$. The solid lines correspond to $b = 10$ and the dashed lines to $b = 0.1$. We also add the $f_a - m_a$ relation of the QCD axion. Since the parameter choice $n = 4$, $b = 10$, reproduces the temperature dependence of the QCD axion quite nicely, we identify the point where these two curves meet, indicated by the red circle, as the QCD axion explaining the DM in our Universe, i.e. for axion masses $m_a \sim 10^{-5}$ eV.

Note that in the first line, before using $\Lambda^2 = m_a f_a$, it becomes obvious that the Peccei-Quinn breaking scale f_a enters only implicitly via $T_{\rm osc}$. If we use our explicit relations for $T_{\rm osc}$, we arrive at the main result for ρ_{a0}:

$$\rho_{a0} = \frac{b^{-1/(n+2)}}{2} \Lambda T_0^3 \frac{g_{s*}(T_0)}{g_{*s}(T_{\rm osc})} \left[\frac{f_a \; 4.98 \; g_*^{1/2}(T_{\rm osc})}{M_{\rm Pl}}\right]^{(n+3)/(n+2)} \begin{cases} \overline{\theta}_{\rm I}^2 = \frac{\pi^2}{3} & \text{post-inflation} \\ \theta_{\rm I}^2 \in [0, \pi^2] & \text{pre-inflation} \end{cases} \tag{III.46}$$

$$= \frac{b^{-1/(n+2)}}{2} m_a^{1/2} f_a^{(3n+8)/(2n+4)} T_0^3 \frac{g_{s*}(T_0)}{g_{*s}(T_{\rm osc})} \cdot \left[\frac{4.98 \; g_*^{1/2}(T_{\rm osc})}{M_{\rm Pl}}\right]^{(n+3)/(n+2)} \begin{cases} \overline{\theta}_{\rm I}^2 = \frac{\pi^2}{3} & \text{post-inflation} \\ \theta_{\rm I}^2 \in [0, \pi^2] & \text{pre-inflation} \end{cases}, \tag{III.47}$$

which can be used to find the relic abundance $\Omega_a = \rho_{a0}/\rho_{\rm crit}$ depending on the scale f_a, m_a or Λ, and the parameters b and n. It is $\rho_{\rm crit} = 8\pi H_0^2 M_{\rm Pl}^2/3$, and $H_0 = h \; 100{\rm km}/({\rm Mpc} \cdot {\rm s})$ is the Hubble rate today. Recall that the observed amount of DM in our Universe today is $\Omega_{\rm CDM} h^2 \simeq 0.1$ [51].

In Fig. III.3, we show contours in the $m_a - f_a$ plane for the post-inflation Peccei-Quinn breaking scenario where the axion can explain all of the observed DM in our Universe, i.e. we set $\Omega_a h^2 = 0.1$ and $\overline{\theta}_{\rm I} = \pi^3/3$, and we consider different paramter choices b and n. Note that the lines can also be understood as exclusion limits on f_a since for larger f_a we would have $\Omega_a h^2 > 0.1$ and the the axion energy density would overclose the Universe.

The dashed line in Fig. III.3 marks the relation between the Peccei-Quinn breaking scale f_a and the zero temperature mass m_a for the QCD axion. As we have seen in Fig. III.2, a

parameterization with $b = 10$ and $n = 4$ fits the temperature evolution of the QCD axion mass quite well. Therefore, the point where the QCD $f_a - m_a$ relation and our curve for $b = 10$, $n = 4$ meet, can be understood as the QCD axion mass giving the correct DM abundance. Therefore, we find as an estimate for the DM QCD axion mass

$$m_{a\mathrm{QCD}} \sim 10^{-5} \text{ eV} \tag{III.48}$$

which corresponds to a Peccei-Quinn breaking scale

$$f_a \sim 10^{12} \text{ GeV} . \tag{III.49}$$

Finally, we note that with our result for ρ_a in Eq. (III.47), we can reproduce the known relation for the relic abundance of the QCD axion [31, 59, 97]

$$\Omega_a h^2 \simeq 0.1 \left(\frac{f_a}{10^{12} \text{ GeV}} \right)^{7/6} . \tag{III.50}$$

by again setting $\Lambda = \chi_{\mathrm{QCD}}^{1/4} \simeq 75.5$ MeV, $b = 10$, and $n = 4$. Therefore, this choice of paramters marks our QCD benchmark model.[7]

III.3. Decay of Topological Defects

In the harmonic approximation of the axion potential, important nonlinear effects are neglected. These become important in the cosmological evolution of the axion field in the post-inflation Peccei-Quinn scenario. In the following, we briefly discuss how this comes about.

Using the full nonlinear potential, it turns out that the field equation of the complex Peccei-Quinn scalar allows for stable classical string-type solutions, after the symmetry is spontaneously broken. Such classical stable field solutions are known as topological defects. See Refs. [99–101] for original works, thorough reviews of this topic and consequences for cosmology.

In terms of the axion field, we can understand the formation of cosmic strings the following way. As we have pointed out before, when the Peccei-Quinn symmetry gets spontaneously broken, the complex field can roll down in any direction in field space, see also our sketch in Fig. III.1. The direction in which the field rolls down and therefore the θ_{I} value of the axion field can be different from one causal horizon to another. However, there might exist points in space which are surrounded by the axion field wrapping around all values from $-\pi$ to π. At this specific point the complex scalar "does not know" in which direction it should roll down and we can picture it as being trapped at the top of its Mexican-hat potential. This field configuration is obviously different from the vacuum, which corresponds to the field sitting in the valley. However, it is stable as long as the axion is massles. In three spatial dimensions these points where the complex field still sits on top of the potential line up as the cosmic string. When the universe expands and cosmic strings cross, they can form loops which quickly lose their stored energy by radiating relativistic axions [100]. In this way the number of strings goes into a so-called scaling behavior and we expect about one long string per Hubble volume, cf. Ref. [102] for a recent discussion of this topic.

If the Peccei-Quinn breaking happens before or during inflation and one causal horizon with a specific θ_{I} is blown up, we expect only one string in the whole universe. Its contribution to the overall energy density can safely be neglected. However, in the post-inflation scenario the eventual decay of the strings leads to another important source for relic axions. Since in this

[7] Note that, for example, Visinelli and Gondolo in Ref. [31] or O. Mena et al in Ref. [98] choose a different choice of paramters for the temperature dependent QCD axion mass. They also set $n = 4$ but $b = 0.01$. However, the reason for that is, as was pointed out earlier, a slightly different parameterization for $m_a(T)$. Again, in their approach the zero-temperature mass is always reached at $T = \Lambda$. Therefore, their choice of $\Lambda \simeq 170$ MeV is approximately equivalent to $b^{1/n}\Lambda$, for our setup $b = 10$, $n = 4$, and $\Lambda \simeq 75.5$ MeV.

scenario the axion field after Peccei-Quinn symmetry breakings is very inhomogeneous and as we can picture it consisting of many patches with different field values, we also expect many strings. Soon as the axion mass becomes important, they become unstable and start to decay. In fact, they become the boundaries of so-called domains or domain walls. Recall that the axion field has values in $[-\pi, \pi]$ and is periodic, i.e. the endpoints of the interval might be identified. Thus, we can picture the decay of the string-wall system the following way. When the axion potential becomes important and the field starts to roll down to the minimum of the potential at $\theta = 0$, patches in space which have $\theta_{\mathrm{I}} = \pm\pi$ can choose a path from $-\pi$ along negative values to reach the minimum or along π and the positive values. This we can understand as creating two different domains in the universe. The strings, being the boundaries of these domain walls, start to "unzip" them when the axion field settles to its minimum everywhere and this leads eventually to the decay of the string-wall system [44].

Calculating the amount of axions produced in this decay of the topological defects is a long-standing issue. It can only be conclusively studied by numerical simulations of the evolution of the complex Peccei-Quinn scalar. However, the main problem is resolving the actual thickness of the strings [103]. As a matter of fact, it should be of the order of the Hubble horizon at the time of Peccei-Quinn breaking. But since the axion potential becomes only important much, much later, one would have to cover many of orders magnitude in time and therefore in space in a simulation following from the formation to the decay of the strings. This is virtually impossible and therefore approximations for the numerical simulations are unavoidable. Unfortunately, this leads to the fact that estimates on the number of axions produced in the string-wall decays cover almost four orders of magnitudes. Results in the classical literature for $\Omega_{a,\mathrm{str}}$ when compared to realignment production $\Omega_{a,\mathrm{re}}$ only are [82, 104–106]:

$$\Omega_{a,\mathrm{str}} h^2 = (0.15 \ \ldots \ 186)\, \Omega_{a,\mathrm{re}} h^2 \,. \tag{III.51}$$

The interested reader is referred to Refs. [102, 103, 107, 108] for recent discussions on this issue.

It seems that the community is still far away from a conclusive solution. However, if the uncertainty in understanding the decay of the string-wall system could finally be overcome, it would indeed be possible to give a concrete prediction for the DM axion mass in the post-inflation scenario, as we have pointed out before. Klaer and Moore for example suggest with the results of their simulations, including realignment axions and axions from the string-wall decay, a DM mass for the axion which is $m_a \simeq 26.2\ \mu$eV [103]. This is of the same order as our estimate in Eq. (III.48) with the realignment axions only.

However, a final word of caution for the post-inflation Peccei-Quinn breaking scenario is in order. Namely, the above described decay of strings and domain walls is only possible if there exists only one unique minimum of the axion potential in the intervall $[-\pi, \pi]$. As soon as there is a number $N_{\mathrm{DW}} \neq 1$ of degenerate minima, the domain walls are stable and they tend to quickly dominate the energy density leading to a very different universe than we observe. This is called the domain wall problem. Scenarios with stable domain walls are therefore basically ruled out [109]. Ways to circumvent this issue, besides a pre-inflation Peccei-Quinn breaking, are models in which $N_{\mathrm{DW}} = 1$ or models with a small explicit symmetry breaking which lifts the degeneracy between the N_{DW} minima [44].

IV. Formation of Axion Miniclusters

As was already pointed out in the previous chapter, the inhomogeneous initial conditions for the axion field in the post-inflation Peccei-Quinn breaking scenario cause large isocurvature fluctuations in the axion energy density [94]. A sketch of the situation is presented in Fig. IV.1.

The characteristic size L of the energy density fluctuations is of the order of the causal horizon when the field starts to oscillate and can therefore be related to the comoving Hubble volume at $T_{\rm osc}$, i.e. the characteristic comoving size is $L \sim 1/(H(T_{\rm osc})R(T_{\rm osc}))$. This corresponds to a physical size of these fluctuations today of $L_0 \sim R(T_0)/(R(T_{\rm osc})H(T_{\rm osc}))$.

Let us estimate L_0 with our result for $T_{\rm osc}$. In the following, we focus exclusively on the case of the QCD axion. ALP scenarios will be discussed in Sec. IV.5 and Ch. VI. Therefore, we use our benchmark values $b = 10$, $n = 4$, and $\Lambda = 75.5$ MeV for paramterizing the temperature dependence of the axion mass $m_a(T)$ via Eq. (III.38). With that, the oscillation temperature is given by

$$T_{\rm osc} \simeq 1.2 \text{ GeV } \frac{1}{g_*(T_{\rm osc})^{1/8}} \left(\frac{10^{12} \text{ GeV}}{f_a}\right)^{1/6} \tag{IV.1}$$

and the size of the fluctuations today can be estimated as

$$L_0 \sim 0.1 \text{ pc } \left(\frac{g_{s*}(T_{\rm osc})}{g_{s*}(T_0)}\right)^{1/3} \frac{1}{g_*(T_{\rm osc})} \left(\frac{f_a}{10^{12} \text{ GeV}}\right)^{1/6} \tag{IV.2}$$

$$\sim 0.05 \text{ pc } \left(\frac{f_a}{10^{12} \text{ GeV}}\right)^{1/6}, \tag{IV.3}$$

which is much smaller than any cosmological relevant scale if $f_a \sim 10^{12}$ GeV, as needed for the axion to explain the observed amount of DM in our Universe. In the second line we have approximated $g_{*,s*}(T_{\rm osc}) \sim 100$ and $g_{*s}(T_0) \sim 3$.

Even though, being not relevant on cosmological scales the isocurvature fluctuations in the axion energy density have other interesting phenomenological consequences for axion DM. Namely, the large overdensities can decouple from the Hubble expansion already at high redshifts and collapse very early into dense gravitationally bound objects, called axion miniclusters. This makes the DM a clumpy stew instead of the usually assumed homogeneous fluid which has very profound consequences, especially for direct detection experiments like axion DM haloscope, as we will shortly see.

We can estimate the size of a typical minicluster $R_{\rm MC}$ by assuming that it originates from a fluctuation which has collapsed around matter-radiation equality, i.e. we can assume $R_{\rm MC} \sim R(T_{\rm eq})/(R(T_{\rm osc})H(T_{\rm osc}))$. With an analogue calculation as in our estimate for L_0, we find

$$R_{\rm MC} \sim 10^6 \text{ km } \left(\frac{f_a}{10^{12} \text{ GeV}}\right)^{1/6}, \tag{IV.4}$$

which is comparable to the radii of the large planets in our solar system.

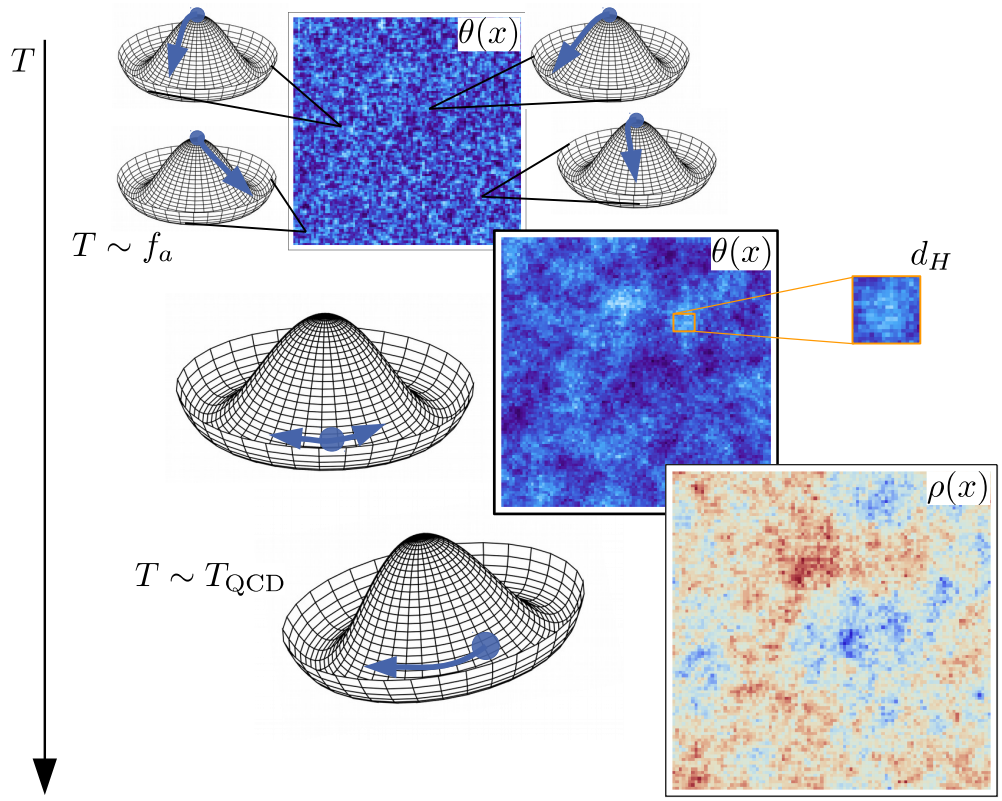

Figure IV.1.: Vacuum Realignment in the post-inflationary Scenario. When Peccei-Quinn symmetry breaking happens at temperatures $T \sim f_a$ the complex scalar develops its vacuum expectation value and it rolls down into the valley of the Mexican hat potential. The axion field, identified as the phase $\theta(x) = a(x)/f_a$ of the complex scalar, can take any value between $-\pi$ and π in causally disconnected regions since no specific value is energetically favored. This is sketched in the first picture. In the snapshot of $\theta(x)$, the dark blue colors might correspond to negative values and the light blue colors to positive. However, it should simply highlight that the axion field after Peccei-Quinn symmetry breaking basically looks like white noise since its field values are completely uncorrelated from one horizon to another. As long as the field is massless, at temperatures $T > T_{\mathrm{QCD}}$, this picture does not change too much. While the universe keeps expanding and cooling, the gradient terms in the evolution equation of $\theta(x)$ will always smooth the field on scales of the Hubble horizon d_H. This is shown in the second picture. Around the QCD phase transition, at temperatures $T \sim T_{\mathrm{QCD}}$, the axion potential is generated and it will make the field roll down to the CP conserving minimum. The energy stored in the oscillations around the minimum locally depends on the value from which the field started to roll down. Hence, the inhomogeneous field leaves its imprint as large fluctuations in the energy density $\rho(x)$. This is depicted in the bottom panel. Here, red colors might correspond to high density and blue color to low density regions. The large overdensities can decouple very early from the Hubble expansion to form gravitationally bound axion miniclusters.

The mass of a minicluster $M_{\rm MC}$ is provided by the energy density of the axions inside a Hubble patch at $T_{\rm osc}$. We can therefore estimate a typical mass via $M_{\rm MC} \sim \frac{4}{3}\pi\overline{\rho}_a(T_{\rm osc})(\pi/H(T_{\rm osc}))^3$. With our results for the mean energy density $\overline{\rho}$ we find[1]

$$M_{\rm MC} \sim 2\pi^6 \frac{f_a^2}{m_a(T_{\rm osc})} \tag{IV.5}$$

$$\sim 10^{-11}\ M_\odot \left(\frac{f_a}{10^{12}\ \text{GeV}}\right)^{7/3}, \tag{IV.6}$$

which is about the mass of an asteroid [110]. It might seem like a surprising result that higher Peccei-Quinn breaking scales and therefore lighter axions, lead to heavier miniclusters. But recall that the lighter the axions the later the field starts to oscillate since the oscillation temperature is set by the equality $3H(T_{\rm osc}) = m(T_{\rm osc})$. This means that smaller m lead to a smaller Hubble rate at $T_{\rm osc}$, and therefore to larger fluctuations $\sim 1/H(T_{\rm osc})$ which eventually lead to more massive miniclusters.

With the estimate for the mass and the size of the miniclusters, we can calculate the escape velocity $v_{\rm esc} = \sqrt{GM/R}$ for axions gravitationally bound inside such an object. Plugging in the numbers, we find $v_{\rm esc} \ll 1$, suggesting that the axions inside a minicluster are non-relativistic. Hence, we can calculate the particle density n_a inside a minicluser simply via $n_a = \rho_a/m_a$. With our estimates for $M_{\rm MC}$ and $R_{\rm MC}$, we find that n_a inside a minicluster is huge:

$$n_a \sim 10^{28}\ \text{cm}^{-3} \left(\frac{f_a}{10^{12}\ \text{GeV}}\right)^3. \tag{IV.7}$$

This means that in case of a direct encounter of the earth with a minicluster, the signal in a DM haloscope, being sensitive to n_a, would by highly enhanced. However, an event like this is incredibly rare, unfortunately. Namely, we can estimate the encounter rate of the earth with a minicluster assuming that a fraction $f_{\rm MC}$ of the DM is bound in objects with mass $M_{\rm MC} \sim 10^{-11} M_\odot$. The number density $n_{\rm MC}$ of miniclusters in our local neighberhood can then be calculated with the value for the local DM energy density $\rho_{\rm DM} \simeq 0.01\ M_\odot\ \text{pc}^{-3}$ [111] and we expect $n_{\rm MC} \sim (0.01 \cdot f_{\rm MC})/\text{AU}$.[2] Adopting the predictions of the DM flux of a 100 GeV WIMP, $\Phi_{\rm WIMP} \sim 6.6 \cdot 10^4\ \text{cm}^{-2}\ \text{s}^{-1}$ [111], to a $M_{\rm MC} \sim 10^{-11}\ M_\odot$ minicluster, we find a flux at earth $\Phi_{\rm MC} \sim f_{\rm MC}\ 10^{-40}\ \text{cm}^{-2}\ \text{s}^{-1}$. With that the encounter rate $\nu_{\rm MC} = \Phi_{\rm MC} R_{\rm MC}^2$ is given by

$$\nu_{\rm MC} \sim 0.01 \frac{f_{\rm MC}}{\tau_{\rm univ}} \left(\frac{R_{\rm MC}}{10^6\ \text{km}}\right)^2 \tag{IV.8}$$

and $\tau_{\rm univ} \simeq 4.1 \cdot 10^{17}$ s is the lifetime of the Universe. This means that if the axion DM would be mainly bound in miniclusters, the idea of direct detection with conventional haloscopes would be virtually doomed and we might have to think about novel techniques to find axion DM or try to observe the miniclusters themselves.

A naive attempt for minicluster detection might be to use them as graviational lenses. However, with our estimates for the mass and size it is obvious that they cannot act as strong lenses since they are too dillute. Namely, their Einstein radius

$$R_{\rm E} \sim 4.3 \cdot 10^4\ \text{km} \left(\frac{M_{\rm MC}}{10^{-11}\ M_\odot}\right)^{1/2} \left(\frac{D}{\text{Mpc}}\right) \tag{IV.9}$$

[1] Note that there is some discrepancy in the literature on how to define the size d_H corresponding to a Hubble patch. A definition of $d_H = 1/H$ instead of $d_H = \pi/H$ might only lead to small differences for d_H itself but as severe impacts on the mass of the miniclusters, in fact it changes about π^3 which is about a factor 30. Note that the factor π appears when relating $k = aH$, the comoving wave number corresponding to the Hubble horizon, with the size d_H. A wavelength λ can be expressed via a wavenumber k as $k = 2\pi/\lambda$. Then, the radius of the Hubble horizon d_H might be identified as half the wavelength, i.e. $k = \pi/d_H$.

[2] AU stands for astronomical unit and it is approximately the distance between the sun and the earth, 1 AU = $1.496 \cdot 10^8$ km.

is well inside their phsyical radius; D being the distance between observer and source. However, they might serve as pico- or microlenses, as suggested in Ref. [33]. More recently, in Ref. [112,113] Fairbairn et al even claim that already with existing data from lensing surveys, like the one presented in Ref. [114], limits on $f_{\rm MC}$ can be derived. But to do so they have to make some ad hoc assumptions for the formation and especially the evolution of the miniclusters.

But there might be further observable implications of axion miniclusters. For example, in Ref. [34] it is speculated that axion miniclusters could be sources for fast radio bursts and in Ref. [115] it is discussed that if the clumps are tidally disrupted during galaxy formation, remnant axion streams might increase again the chance for a direct detection in haloscope experiment. Very recently the interest in more exotic objects, called axion stars, revived, cf. Refs. [35, 116–119] and it is discussed if the axion miniclusters could give the proper soil for forming these coherent axion states [120, 121].

However, for all these proposals a solid understanding of the formation history and especially the distribution of axion miniclusters is essential. The estimates for $R_{\rm MC}$ and $M_{\rm MC}$, found above, can only provide an intuition for the typical minicluster properties. In fact, it is natural to expect a variety of miniclusters with different masses and sizes. Deriving their distribution will be the main goal of this chapter and is one of the major outcomes of the present work.

A first in-depth study of minicluster formation was done by Kolb and Tkachev [122, 123] in the early 90's. They have solved the evolution equation of the real axion field numerically in an expanding background including the full nonlinear potential. A similar analysis was later repeated by Zurek et al [124]. Both groups observed in their simulation besides the formation of typical miniclusters even denser objects, they called axitons. These can be understood as pseudo-soliton solutions of the nonlinear field equations, see our discussion in Ch. V. However, it turns out that they are not stable and decay quickly into semi-relativistic axions [125, 126]. Since the simulations by Kolb and Tkachev, as well as Zurek et al, were limited to the real axion field only, the effect of the strings and the domain walls is neglected. A conclusive analysis of the minicluster formation including the topological defects can be only done by numerically following the evolution of the complex Peccei-Quinn scalar from the moment of symmetry breaking till around matter-radiation equality. Very recently, a first attempt for this was done by Vaquero et al in Ref. [108]. Still, the authors had to use some ad hoc approximations to overcome the issue of the huge discrepancy between the scales of the string thickness and the size of the Hubble horizon at $T_{\rm QCD}$.

In the present work, we take a different approach and investigate the formation of miniclusters in a semi-analytic way. The idea is that in the harmonic approximation for the potential the evolution equation of the axion field linearizes which allows us to use statistical methods to derive the power spectrum of the energy density fluctuations. The power spectrum can then be used in a Press & Schechter-like approach for calculating the minicluster mass function.

The results of this study are published in Ref. [127]. Here, we focus on discussing the intricacies of the calculations which have not been discussed in detail in this reference. For points that have already been elaborated exhaustively in Ref. [127], we reserve our right to refer the reader to the discussion therein.

IV.1. Revisiting the Axion Field Evolution

In the harmonic approximation for the axion potential, i.e. $V(\theta) \simeq m_a^2\theta^2/2$, the evolution equation of the misalignment field $\theta(x)$ is given by

$$\ddot{\theta} + 3H(T)\dot{\theta} - \frac{1}{R^2}\nabla^2\theta + m_a^2(T)\theta = 0\,. \tag{IV.10}$$

Now we want to include the gradient terms to correctly capture the effect of the inhomogeneous initital conditions on the field evolution and the impact on the energy density.

Recall that in the harmonic approximation it turns out that a decomposition of $\theta(x)$ in terms of Fourier modes[3]

$$\theta_k = \int \mathrm{d}^3x\ \theta(\vec{x})\mathrm{e}^{\mathrm{i}\vec{k}\vec{x}} \quad \Leftrightarrow \quad \theta(\vec{x}) = \int \frac{\mathrm{d}^3k}{(2\pi)^3}\ \theta_k \mathrm{e}^{-\mathrm{i}\vec{k}\vec{x}} \tag{IV.11}$$

is useful since the evolution equations of the θ_k's decouple and we have

$$\ddot{\theta}_k + 3H(T)\dot{\theta} + \frac{k^2}{R^2}\theta_k + m_a^2(T)\theta_k = 0\,, \tag{IV.12}$$

which can be solved mode by mode. This motivates an ansatz for θ_k of the form

$$\theta_k(t) = \theta_k f_k(t)\,, \tag{IV.13}$$

where the information on the initial conditions can be encoded in $\theta_k \equiv \theta_k(t_i)$, $t = t_i$ being the initial time, and the function $f_k(t)$ acts as transfer function, describing the time evolution of the k-th mode. Note that f_k can in prinicple be a complex valued function. However, choosing real initial conditions or to be explicit, $f_k(t_i) = 1$ for all k, then f_k is real also at late times.

Choosing the proper initial Conditions

After the Peccei-Quinn symmetry breaking, the misalignment field $\theta(x)$ can be understood as random field with a value picked from the interval $[-\pi, \pi]$ and distributed in the different Hubble patches. We can try to describe this situation using statistical methods. I.e. we try to characterize $\theta(x)$ by its statistical moments. Assuming a flat probability distribution function $\mathcal{F}(\theta) = 1/(2\pi)$ for θ in $[-\pi, \pi]$, we can calculate its mean[4]

$$\langle\theta(x)\rangle = \int_{-\pi}^{\pi} \mathrm{d}\theta\ \mathcal{F}(\theta)\theta = 0\,, \tag{IV.14}$$

the first moment, and its variance

$$\langle\theta(x)^2\rangle = \int_{-\pi}^{\pi} \mathrm{d}\theta\ \mathcal{F}(\theta)\theta^2 = \frac{\pi^2}{3}\,, \tag{IV.15}$$

the second moment.

Further insight on the properties of $\theta(x)$ can be found by calculating the two-point correlation function $\xi(\vec{x}, \vec{y}) = \langle\theta(\vec{x})\theta(\vec{y})\rangle$, where $\langle\cdot\rangle$ can be understood as a spatial or statistical mean. In our case this is equivalent. If we assume isotropy, ξ should be a function of the distance $|\vec{x} - \vec{y}|$ between the two points only. This has important implications for the statistics of the Fourier modes θ_k. Namely, if

$$\langle\theta(x)\theta(y)\rangle = \xi(|\vec{x} - \vec{y}|) \tag{IV.16}$$

it is easy to show that for the Fourier modes θ_k it must hold that

$$\langle\theta_k\theta^*_{k'}\rangle = (2\pi)^3\delta^3(k - k')P_\theta(k)\,, \tag{IV.17}$$

with $P_\theta(k)$ being the Fourier transform of the two-point correlator. The function $P_\theta(k)$ is known as the power spectrum of the Fourier modes.

[3]The integrals are taken over comoving coordinates $\vec{x}$ and wave vectors $\vec{k}$. Since $\theta(x)$ is a real field, we have the constraint $\theta_k = \theta^*_{-k}$ for the Fourier modes.

[4]In Ref. [127] it was noted that when choosing $\theta \in [-\pi, \pi]$ we already encounter the first subtle consequence of the harmonic approximation. Indeed the misalignment field θ should be a periodic variable. So any interval of length 2π should be equally appropriate to describe the physics. But when approximating $V(\theta) \simeq m_a^2\theta/2$ and therefore giving up the periodicity, the only reasonable choice for θ is the interval sweeping over $\theta = 0$, i.e. the minimum of the potential.

We know that the initial misalignment field should resemble white noise, at least on scales larger than the Hubble horizon. For perfect white noise the two-point correlator is a delta-function, meaning that the values of two neighboring points are completely uncorrelated. Note that a delta-shaped correlator leads to a constant power spectrum. For our initial misalignment field, on the other hand, we expect only white noise beyond the scales of the causal horizon, but a complete correlation on scales smaller than that, i.e. on these scales ξ should be constant. A constant correlation function yields a power spectrum which is a delta-pulse. Combining these two different behaviors for the initial misalignmet field motivates an ansatz for $P_\theta(k)$ of a top-hat form

$$P_\theta(k) = C\Theta(K-k)\,, \tag{IV.18}$$

with $\Theta(\cdot)$ being the Heaviside function and K is a cut-off scale defined by the comoving size of the Hubble horizon

$$K \equiv R(t_i)H(t_i)\,, \tag{IV.19}$$

where $t = t_i$ is again the time where the initial conditions are set. With this ansatz the power spectrum is flat for large scales, $k < K$, and drops to zero for $k > K$.

The normalization constant C can be determined via the variance of θ. Using $\langle\theta^2\rangle = \pi^2/3$, we find $C = 2\pi^4/K^3$ and therefore

$$P_\theta^{\mathrm{TH}}(k) = \frac{2\pi^4}{K^3}\Theta(K-k)\,. \tag{IV.20}$$

A disadvantage of this ansatz is that the two-point correlator $\xi(|\vec{x}-\vec{y}|)$ in fact takes the form

$$\xi(|\vec{x}-\vec{y}|) \sim \frac{\sin\left(K|\vec{x}-\vec{y}|\right) - K|\vec{x}-\vec{y}|\cos\left(K|\vec{x}-\vec{y}|\right)}{K^3|\vec{x}-\vec{y}|^3}\,, \tag{IV.21}$$

which has long range correlations beyond scales of the Hubble horizon $1/K$ only dropping off like one over the distance squared.

As an alternative we use a Gaussian ansatz for the power spectrum

$$P_\theta^{\mathrm{G}}(k) = \frac{8\pi^4}{3\sqrt{\pi}K^3}\exp\left(-\frac{k^2}{K^2}\right)\,, \tag{IV.22}$$

where again the normalization is determined via the variance of θ. Using this power spectrum for the Fourier modes, the long range correlations in the two-point correlation function are exponentially suppressed. Thus, this might be the more physically appropriate choice and we use it as our standard setup. However, whenever it turns out to be helpful we also consider the top-hat power spectrum since it lets us nicely keep track of the impact of the cut-off scale K in our calculations.

Another important aspect in our approach is choosing the inital time $t = t_i$. Optimally it should be at the time of Peccei-Quinn symmetry breaking. But the problem is that in the harmonic approximation we do not include the effects of the strings, which are essential for the early evolution of the axion field [99]. However, according to Kibble's seminal work in Ref. [99] we can expect that the gradient terms in the evolution equation of θ will always smooth the field on scales of the causal horizon, as long as it is massless. Beyond the Hubble horizon, the values should still be uncorrelated, see also our sketch in Fig. IV.1. Following this reasoning we conclude that our ansatz for describing the white noise character of $\theta(x)$ should also hold at any time after Peccei-Quinn symmetry breaking, as long as the mass can still be neglected. Therefore, we choose as an initial time for our calculations a time slightly before the field starts to oscillate, i.e. $t_i < t_{\mathrm{osc}}$ or equivalently we can define an initial temperature for our calculations $T_i > T_{\mathrm{osc}}$. Again, we should set T_i not too large due to our ignorance of the string effects.

Therefore, as our standard setup we fix $T_i = 3T_{\rm osc}$, to properly cover on the one hand the time where the field starts to oscillate, and on the other hand to be as insensitive to the nonlinear effects as possible. The actual value for $T_{\rm osc}$ depends on the chosen breaking scale f_a and we can estimate it via Eq. (IV.1). But it is roughly of the order $T_{\rm osc} \sim 1$ GeV. We will later study the impact of choosing different T_i's and how this affects our results.

Solving the Evolution Equation

With the initial power spectrum $P_\theta(k)$ of the Fourier modes fixed, we can now turn to solving the actual evolution equation. The dynamics of the Fourier modes is determined by the evolution of the f_k's which follows from

$$\ddot{f}_k + 3H(T)\dot{f} + \frac{k^2}{R^2} f_k + m_a^2(T) f_k = 0\,. \tag{IV.23}$$

Instead of using time as the independet variable, we can equivalently choose the temperature T. After this change of variables, Eq. (IV.23) becomes

$$\frac{\mathrm{d}^2 f_k}{\mathrm{d}T^2} + \left(3H(T)\frac{\mathrm{d}t}{\mathrm{d}T} - \frac{\mathrm{d}^2 t}{\mathrm{d}T^2}\Big/\frac{\mathrm{d}t}{\mathrm{d}T}\right)\frac{\mathrm{d}f_k}{\mathrm{d}T} + \left(\frac{k^2}{R^2(T)} + m_a^2(T)\right)\left(\frac{\mathrm{d}t}{\mathrm{d}T}\right)^2 f_k = 0 \tag{IV.24}$$

and $\mathrm{d}t/\mathrm{d}T$ can be determined via the Friedman equations. We find:

$$\frac{\mathrm{d}t}{\mathrm{d}T} = -M_{\rm Pl}\sqrt{\frac{45}{64\pi^3}}\frac{1}{T^3 g_{s*}\sqrt{g_*}}\left(4g_* + \frac{\mathrm{d}g_*}{\mathrm{d}T}T\right)\,. \tag{IV.25}$$

The Friedman equations also relate the evolution of the scale factor to the temperature

$$\frac{\mathrm{d}R}{\mathrm{d}T} = -\frac{1}{4}\frac{1}{g_{s*}T}\left(4g_* + \frac{\mathrm{d}g_*}{\mathrm{d}T}T\right)R \tag{IV.26}$$

and the Hubble rate as a function of temperature is given by $H(T) = 1/R(\mathrm{d}R/\mathrm{d}T)(\mathrm{d}T/\mathrm{d}t)$. Details on deriving the expressions in Eqs. (IV.24)-(IV.26) can be found in App. C.

For getting continous functions for the relativistic degrees of freedom $g_*(T)$ and $g_{s*}(T)$ we again use the values given in Ref. [96] and apply a cubic spline interpolation method. For the evolution of the mass $m_a(T)$ we do not use our own parameterization but rather implement the numerical results from the lattice calculations of $\chi_{\rm QCD}(T)$ in Ref. [96] for using the more realistic evolution of the axion mass. Making use of these exact relations, Eq. (IV.24) can be solved only numerically.

Before doing so, we should make the equation for the f_k's dimensionless by expressing the wave numbers with respect to some reference scale. It turns out that a reasonable choice is the comoving wave number

$$K_1 \equiv RH(T = 1\ \mathrm{GeV})\,, \tag{IV.27}$$

which is about the scale of the Hubble horizon at $T = T_{\rm osc}$. When expressed in terms of K_1 all wave numbers of interest are of order one. For example, as a rule of thumb for the cut-off scale K we find:

$$\frac{K}{K_1} = \frac{RH(T = 3T_{\rm osc})}{RH(T = 1\ \mathrm{GeV})} \simeq 3\ \left(\frac{T_{\rm osc}}{1\ \mathrm{GeV}}\right)\,. \tag{IV.28}$$

To arrive at this estimate we have used the approximations $R \propto T^{-1}$ and $H(T) \propto T^2$ in a radiation dominated universe.

The evolution equation in terms of the dimensionless wavenumbers $\tilde{k} \equiv k/K_1$ takes the form

$$\frac{\mathrm{d}^2 f_{\tilde{k}}}{\mathrm{d}T^2} + \left(3H(T)\frac{\mathrm{d}t}{\mathrm{d}T} - \frac{\mathrm{d}^2 t}{\mathrm{d}T^2}\Big/\frac{\mathrm{d}t}{\mathrm{d}T}\right)\frac{\mathrm{d}f_{\tilde{k}}}{\mathrm{d}T} + \left(\frac{\tilde{k}^2}{R^2(T)}K_1^2 + m_a^2(T)\right)\left(\frac{\mathrm{d}t}{\mathrm{d}T}\right)^2 f_{\tilde{k}} = 0\,. \tag{IV.29}$$

$$\Leftrightarrow \quad f_{\tilde{k}}'' + 3\bar{H}(T) f_{\tilde{k}}' + \bar{\omega}_k^2(T) f_{\tilde{k}} = 0\,. \tag{IV.30}$$

The primes denote derivatives with respect to temperature and in the second line we have introduced abbreviations for an effective Hubble rate $\bar{H}$ and frequency $\bar{\omega}_{\tilde{k}}$.

We can now try to solve this equation mode by mode for a large number of $\tilde{k}$. However, it turns out that soon after the mass term becomes important, the rapid oscillations in $f_{\tilde{k}}$ cause numerical problems. We find that a workaround for this issue is using the following hybrid approach of a numerical and a semi-analytical method. At high temperatures between $T_i = 3T_{\rm osc}$ and $T \sim T_{\rm osc}$ we can use straightforward numerical methods to solve Eq. (IV.30). To circumvent the problem of the rapid oscillations, we use that at temperatures $T < T_{\rm osc}$ we are effectively dealing with the equation of an underdamped harmonic oscillator, since $m_a > \overline{H}$. Hence, we can proceed similar as in Sec. III.2, by making a WKB ansatz for $f_{\tilde{k}}$ of the form

$$f_{\tilde{k}}(T) = 2A_{\tilde{k}}(T)\cos\Phi_{\tilde{k}}(T) \quad \text{for } T < T_{\rm osc}\,. \tag{IV.31}$$

The functions $A_{\tilde{k}}$ and $\Phi_{\tilde{k}}$ are determined by

$$A'_{\tilde{k}} + \frac{1}{2}\left(\bar{H} + \frac{\bar{\omega}'_{\tilde{k}}}{\bar{\omega}_{\tilde{k}}}\right) = 0 \tag{IV.32}$$

and

$$\Phi'^2_{\tilde{k}} - \omega^2_{\tilde{k}} = 0 \tag{IV.33}$$

and the initial conditions for these equations must be found by matching the WKB ansatz and its derivative to the full numerical solution. Let us call the time of matching $T_{\rm WKB}$. The values for $A_{\tilde{k}}(T_{\rm WKB})$ and $\Phi_{\tilde{k}}(T_{\rm WKB})$ are determined by

$$2A_{\tilde{k}}(T_{\rm WKB})\cos\Phi_{\tilde{k}}(T_{\rm WKB}) = f_{\tilde{k}}(T_{\rm WKB})\,, \tag{IV.34}$$

$$2A_{\tilde{k}}(T_{\rm WKB})\sin\Phi_{\tilde{k}}(T_{\rm WKB}) = \frac{f'_{\tilde{k}}(T_{\rm WKB})}{\bar{\omega}_{\tilde{k}}(T_{\rm WKB})}\,. \tag{IV.35}$$

To arrive at the second equation we made use of the WKB condition $A'/A < \omega$.

Hence, the algorithm for finding the time evolution of $f_{\tilde{k}}$ can be summarized as follows:

1. Solve Eq. (IV.30) for a given $\tilde{k}$ numerically, starting at $T_i = 3T_{\rm osc}$ down to $T = T_{\rm WKB} < T_{\rm osc}$.
2. At $T = T_{\rm WKB}$ solve the system of equations (IV.34)-(IV.35) to find $A_{\tilde{k}}(T_{\rm WKB})$ and $\Phi_{\tilde{k}}(T_{\rm WKB})$.
3. Use $A_{\tilde{k}}(T_{\rm WKB})$ and $\Phi_{\tilde{k}}(T_{\rm WKB})$ as the initial conditions for solving Eq. (IV.32) and (IV.33) numerically. Then, determine $f_{\tilde{k}}(T) = 2A_{\tilde{k}}(T)\cos\Phi_{\tilde{k}}(T)$ for $T < T_{\rm WKB}$.

It turns out that by choosing $T_{\rm WKB} = 0.5T_{\rm osc}$ we achieve very good numerical stabilty and an excellent fit to a full numerical approach. In Fig IV.2 we show $f_{\tilde{k}}$ as a function of temperature, for the modes $\tilde{k} = 0$ and $\tilde{k} = 3$. The Peccei-Quinn breaking scale is fixed at $f_a = 10^{12}$ GeV, i.e. $T_{\rm osc} \sim 1$ GeV and the dimensionless cut-off wavenumber is $\tilde{K} \sim 3$. We observe that the WKB approximation nicely matches to the numerical solution at $T \sim 0.5T_{\rm osc}$. Further, we see that the high $\tilde{k}$ mode begins to oscillate already before $T_{\rm osc}$. At this point the period of the oscillations is not yet set by the mass only but also depends on $\tilde{k}$. Obviously, the earlier a mode starts to oscillate, the more the amplitude is damped compared to the zero-mode. Of course, this does not hold for arbitrary high $\tilde{k}$. But note that the modes beyond the cut-off scale will be further suppressed by the power spectrum P_θ. As soon as the mass reaches its zero temperature value, all modes will eventually oscillate with the same frequency $\sim m_a$.

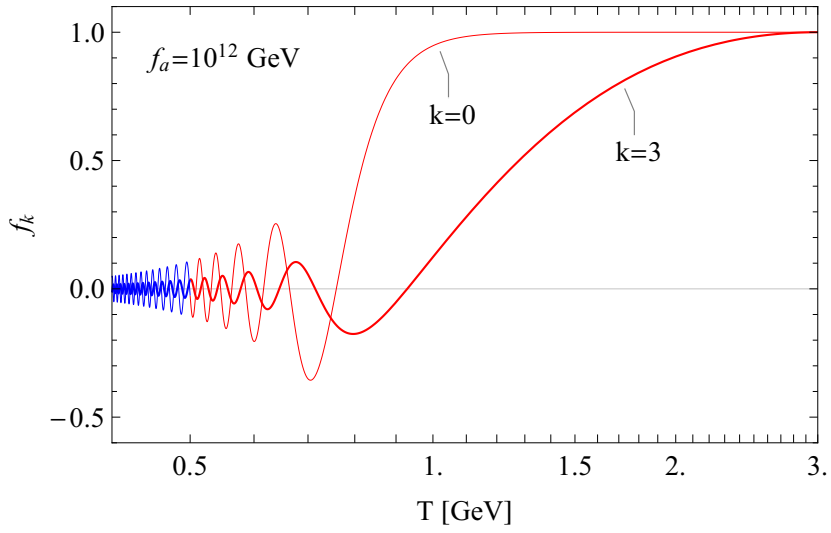

Figure IV.2.: Evolution of the Axion Field Fourier Modes. The zero mode (thin line) starts to oscillate as soon as the mass term becomes dominant, around $T_{\rm osc} \sim 1$ GeV. The higher modes on the other hand, oscillate already before $T_{\rm osc}$. Therefore, their amplitude is suppressed compared to the zero-mode. As an example, we show the evolution of the mode with $\tilde{k} = k/K_1 = 3$. Soon after the rapid oscillations commence we apply a WKB approximation for temperatures $T < T_{\rm WKB} = 500$ MeV. The WKB solution is shown in blue. We see that it nicely matches to the numerical solution, shown in red. Details on the technicalities of the matching are given in the text.

IV.2. Power Spectrum of the Density Fluctuations

We can use our results for the evolution of the Fourier modes to calculate the energy density ρ of the axion misalignment field and its evolution. It is

$$\rho(x) = \frac{1}{2}\dot{\theta}^2 + \frac{1}{2R^2}\left(\nabla\theta\right)^2 + \frac{1}{2}m_a^2(T)\theta^2 \tag{IV.36}$$

$$\Leftrightarrow \quad \rho(x) = \frac{f_a^2}{2}\int \frac{\mathrm{d}^3k}{(2\pi)^3}\frac{\mathrm{d}^3k'}{(2\pi)^3}\,\theta_k\theta^*_{k'}F(k,k')\mathrm{e}^{-\mathrm{i}(\vec{k}-\vec{k}')\vec{x}} \tag{IV.37}$$

$$\text{with} \quad F(k,k') = \dot{f}_k\dot{f}_{k'} + \left(\frac{\vec{k}\cdot\vec{k}'}{R^2} + m_a^2\right) f_k f_{k'}\,, \tag{IV.38}$$

where we made use of the relation $\theta_k = \theta^*_{-k}$. We note that Fourier transform of the energy density can be written as

$$\rho_q = \frac{f_a^2}{2}\int \frac{\mathrm{d}^3k}{(2\pi)^3}\theta_k\theta^*_{k-Q}F(k,k-Q)\,, \tag{IV.39}$$

which will be useful when we consider the density fluctuations. But first let us start by calculating the mean energy density $\overline{\rho}$.

Mean Energy Density

Since taking the spatial average of the energy density $\overline{\rho}_a$ is equivalent to calulating the statistical mean $\langle\cdot\rangle$ of $\rho_a(x)$, it follows from Eq. (IV.37) that

$$\overline{\rho} = \langle\rho(x)\rangle = \frac{f_a^2}{2}\int \mathrm{d}^3k\ P_\theta(k)F(k,k)\,. \tag{IV.40}$$

Hence, the mean energy density is determined by the power spectrum of the Fourier modes $P_\theta(k)$ and its evolution via $F(k,k)$.

For times $T < T_{\mathrm{osc}}$, we can express f_k via the WKB ansatz and bring the expression for $\overline{\rho}$ in an even more familiar form. As we can see from Fig. IV.2, f_k rapidly oscillates at late times with the frequency $\sim m_a$ and has an envelope that scales as $R^{-3/2}$, cf. also the disucssion in Sec. III.2. We can factor this overall scaling of f_k out of $F(k,k)$ and further make it dimensionless by dividing through the zero temperature mass. Thus, we define the dimensionless quantitiy $\tilde{F} \equiv (R(T)/R(T_*))^3 F/m_a^2$ and T_* is an a priori arbitrary temperature scale below T_{osc}. For convenience we chose $T_* = 100$ MeV since here the mass reaches its zero temperature value and the evolution of $\tilde{F}$ should therefore approach a constant behavior. This is confirmed by explicit numerical calculations for $\tilde{F}$ as a function of temperature. Introducing $\tilde{F}$, we can rewrite the mean energy density as

$$\overline{\rho} = \frac{1}{2}f_a^2 m_a^2 \left(\frac{R(T_*)}{R(T)}\right)^3 \int \mathrm{d}^3k\ P_\theta(k)\tilde{F}(k,k)\,, \tag{IV.41}$$

Now, using the power spectrum P_θ of the top-hat form from Eq. (IV.20) the integral is cut off at $k = K$ and we find

$$\overline{\rho} = \frac{1}{2}f_a^2 m_a^2 \left(\frac{R(T_*)}{R(T)}\right)^3 \pi^2 \int_0^1 \mathrm{d}\tilde{k}\ \tilde{k}^2 F(\tilde{k},\tilde{k})\,, \tag{IV.42}$$

where the factor $1/K^3$ in the normalization of P_θ was absorbed in the integration measure to make the integral over the Fourier modes dimensionless. It is $\tilde{k} = k/K$ for this instance.

The result for $\overline{\rho}$ in Eq. (IV.42) has the same parametric dependence as our previous expression in Eq. (III.33). However, the variance of the misalignment angle $\langle\theta_{\mathrm{I}}^2\rangle = \pi^2/3$ from before is now replaced by the proper weighted contribution of the non-zero k modes via the integral over $\tilde{F}(\tilde{k},\tilde{k})$.

Doing the calculation for different Peccei-Quinn breaking scales f_a, we are also able to reproduce the relation for the relic abundance

$$\Omega_a h^2 \simeq 0.1 \left(\frac{f_a}{10^{12}\ \mathrm{GeV}}\right)^{7/6}\,. \tag{IV.43}$$

However, it turns out that in our approach the numerical factor somewhat dependends on the initial time T_i. When choosing $T_i = 2T_{\mathrm{osc}}$ instead of the default assumption $T_i = 3T_{\mathrm{osc}}$, the energy density is about a factor two larger. This can be understood as the high k modes not having enough time to red-shift away before the mass becomes constant and the evolution of $\tilde{F}$ is frozen. Thus, their contribution to the energy density is still large compared to the zero-mode which should actually make up the main contribution to $\overline{\rho}$. We also note that another shortcoming of our method is that the result for $\Omega_a h^2$ differs about 30% depending on the chosen initial power spectrum, top-hat or Gaussian.

Energy Density Fluctuations

Recall that the fluctuations in the energy density are definded as

$$\delta(x) \equiv \frac{\rho(x) - \overline{\rho}}{\overline{\rho}}\,, \tag{IV.44}$$

i.e. as the local variation of the energy density compared to its mean. The Fourier transform of $\delta(x)$ reads

$$\delta_q = \frac{\rho_q}{\overline{\rho}} \quad \text{for } Q \neq 0 \tag{IV.45}$$

and it can be related to the power specturm $P(q)$ of the fluctuations [128]. With a similar calculation as for the power spectrum of the field modes, we find:

$$\langle \delta_q \delta^*_{q'} \rangle = (2\pi)^3 \, \delta\left(\vec{q} - \vec{q}'\right) P(q) \tag{IV.46}$$

and therefore it is

$$P(q) = \langle |\delta_q|^2 \rangle / V \, . \tag{IV.47}$$

Note that evaluating the Dirac distribution at zero can be done by using its definition

$$(2\pi)^3 \delta^3(\vec{k}) = \int_V \mathrm{d}^3 x \; \mathrm{e}^{\mathrm{i}\vec{k}\vec{x}} \, . \tag{IV.48}$$

With this, we have

$$\delta(\vec{k} = 0) = \frac{V}{(2\pi)^3} \, , \tag{IV.49}$$

where V is some large volume.

The interpretation of the power spectrum $P(q)$ is that it tells us how much power sits in fluctuations of a given mode. It has the dimensions of a volume. A quantity with a more transparent meaning is the dimensionless power spectrum [128]

$$\Delta^2 = \frac{q^3}{2\pi^2} P(q) \, . \tag{IV.50}$$

Values of $\Delta^2(q) \sim 1$ indicate that fluctuations are of $\mathcal{O}(1)$ at the given scale q. We will shortly see that the power spectrum of the density fluctuations is a necessary input for deriving the miniclusters mass function.

With our results for ρ_q and $\overline{\rho}$, we can determine $P(q)$ via

$$P(q) = \frac{1}{V} \frac{\langle |\rho_q|^2 \rangle}{\overline{\rho}} \, . \tag{IV.51}$$

But first we note that

$$\langle |\rho_q|^2 \rangle = \frac{f_a^2}{4} \int \frac{\mathrm{d}^3 k}{(2\pi)^3} \frac{\mathrm{d}^3 k'}{(2\pi)^3} \langle \theta_k \theta^*_{k-Q} \theta^*_{k'} \theta_{k'-Q} \rangle F(k, k-Q) F(k', k'-Q) \tag{IV.52}$$

can be evaluated using Wick's theorem [129]. Namely, by applying this theorem the expectation value under the integral can be written as

$$\langle \theta_k \theta^*_{k-Q} \theta^*_{k'} \theta_{k'-Q} \rangle = \langle \theta_k \theta^*_{k-Q} \rangle \langle \theta^*_{k'} \theta_{k'-Q} \rangle + \langle \theta_k \theta^*_{k'} \rangle \langle \theta^*_{k-Q} \theta_{k'-Q} \rangle + \langle \theta_k \theta_{k'-Q} \rangle \langle \theta^*_{k-Q} \theta^*_{k'} \rangle \, , \tag{IV.53}$$

i.e. a sum of products which each can be evaluated via the relation $\langle \theta_k \theta^*_{k'} \rangle = (2\pi)^3 \delta(\vec{k} - \vec{k}') P_\theta(q)$ and using the power spectrum $P_\theta(q)$ of the Fourier modes of the misalignment field.

We note that the last term in Eq. (IV.53) drops when using $q \neq 0$ and as an intermediate result we have

$$\langle \theta_k \theta^*_{k-Q} \theta^*_{k'} \theta_{k'-Q} \rangle = (2\pi)^6 P_\theta(|\vec{k}|) P_\theta(|\vec{k} - \vec{q}|) \left\{ \left[\delta^3(\vec{k} - \vec{k}') \right]^2 + \left[\delta^3(\vec{k} + \vec{k}' - \vec{q}') \right]^2 \right\} . \tag{IV.54}$$

When performing the integral, the first term gives $|F(k, k-q)|^2$ and the square of a Dirac distribution can be evaluated with the relation in Eq. (IV.49). The second term yields $|F(q-k, -k)|^2$. With the realness condition for $\theta(x)$, we have $f_k = f_{-k}$ and therefore $|F(q-k,-k)|^2 = |F(k, q-k)|^2$ using the definition of F. Hence, both terms give the same result when eventually plugged into $\langle|\rho_q|^2\rangle$. With this, we find the following expression for the power spectrum of the energy density fluctuations

$$P(q) = 2(2\pi)^3 \frac{\int \mathrm{d}^3k \; P_\theta(|\vec{k}|) P_\theta(|\vec{k}-\vec{q}|)\, F(k, k-q)^2}{\left[\int \mathrm{d}^3k \; P_\theta(k) F(k,k)\right]^2} \,. \tag{IV.55}$$

Before showing actual results for $P(q)$, let us summarize the main features of our approach. By using statistical methods to describe the physical situation of the misalignment field, we were able to express the energy density as well as the fluctuations therein via the power spectrum of the field modes. Their dynamics is encoded in the effective factor $F(k, k')$ which is derived by solving the evolution equation with a hybrid method of a full numerical and a WKB approach. As soon as the mass reaches its zero-temperature value, F will scale as R^{-3}. This is independent of k and therefore the evolution in the nominator and the denominator in our expression for $P(q)$ cancel. Thus, the power spectrum is frozen for temperaturs $T < 100$ MeV.

However, note that since we are using the harmonic approximation for the axion potential we do not expect to observe the very high density fluctuations with $\delta \gg 1$ which have been seen in full numerical simulations with the nonlinear potential [108,122–124]. Also by not including the effect of the topological defects, we are not able start our calculations at arbitrary high scales. Rather, we had to make an educated guess for the acutal form of the power spectrum P_θ at temperatures briefly before the field starts to oscillate. Further, note that for normalizing the power spectrum we use the mean energy density $\overline{\rho}$ from our calculations, i.e. we include only the axions from the realignment mechanism. Thus, additional axion production channels might suppress the relative fluctuations, if they do not add additional power themselves. The possible shortcomings of our approach are also discussed in more detail in Ref. [127].

Results

In the upper panels of Fig. IV.3 we show the power spectrum $P(q)$ (left) and the dimensionless power spectrum $\Delta^2(q)$ (right) of the energy density fluctuations for three different choices of the Peccei-Quinn breaking scale, $f_a = 10^{10}, 10^{11}, 10^{12}$ GeV, at a time $T < 100$ MeV where the axion mass has reached its zero-temperature value and therefore $P(q)$, as well Δ^2, are frozen. For our choices of f_a, the realignment axions make up $\sim 1 - 100\%$ of the observed DM density, respectively, cf. Eq. (IV.43). As a reference scale for the wave numbers in our plots we use K_1, cf. Eq. (IV.27) for the definition. Further, note that for calculating $P(q)$ and therefore $\Delta^2(q)$, we use the Gaussian power spectrum P_θ^{G} from Eq. (IV.22) for the field modes.

Figure IV.3 corresponds to Fig. 2 and 3 in Ref. [127] where the important aspects of the power spectrum are already discussed in detail. Here, we want to repeat some of the main observations. Obviously, $P(q)$ shows the characteristic constant behavior of white noise on large scales, i.e. small q. This means fluctuations for each mode are equally likely. However, for larger q the power spectrum has a very sharp drop-off at some charatcteristic scale which is different for the different choices of the symmetry breaking scale f_a. Looking at the plot of Δ^2 we learn that this scale corresponds to the position of the peak and therefore to the characteristic size of the fluctuations.

Let us study the position of the peak in Δ^2 more carefully. For the breaking scale $f_a = 10^{12}$ GeV, we know that $T_{\mathrm{osc}} \sim 1$ GeV. This means that in this case the position of the peak at $\sim 4K_1$ corresponds to a scale about four times smaller than the Hubble horizon at the time the oscillations commence. Therefore, the characterstic size of the fluctuations in the axion energy density should be about $L \sim 1/(4R(T_{\mathrm{osc}})H(T_{\mathrm{osc}}))$. This is in contrast to what we have assumed in our estimates for the typical fluctuation size at the very beginning of this chapter. There,

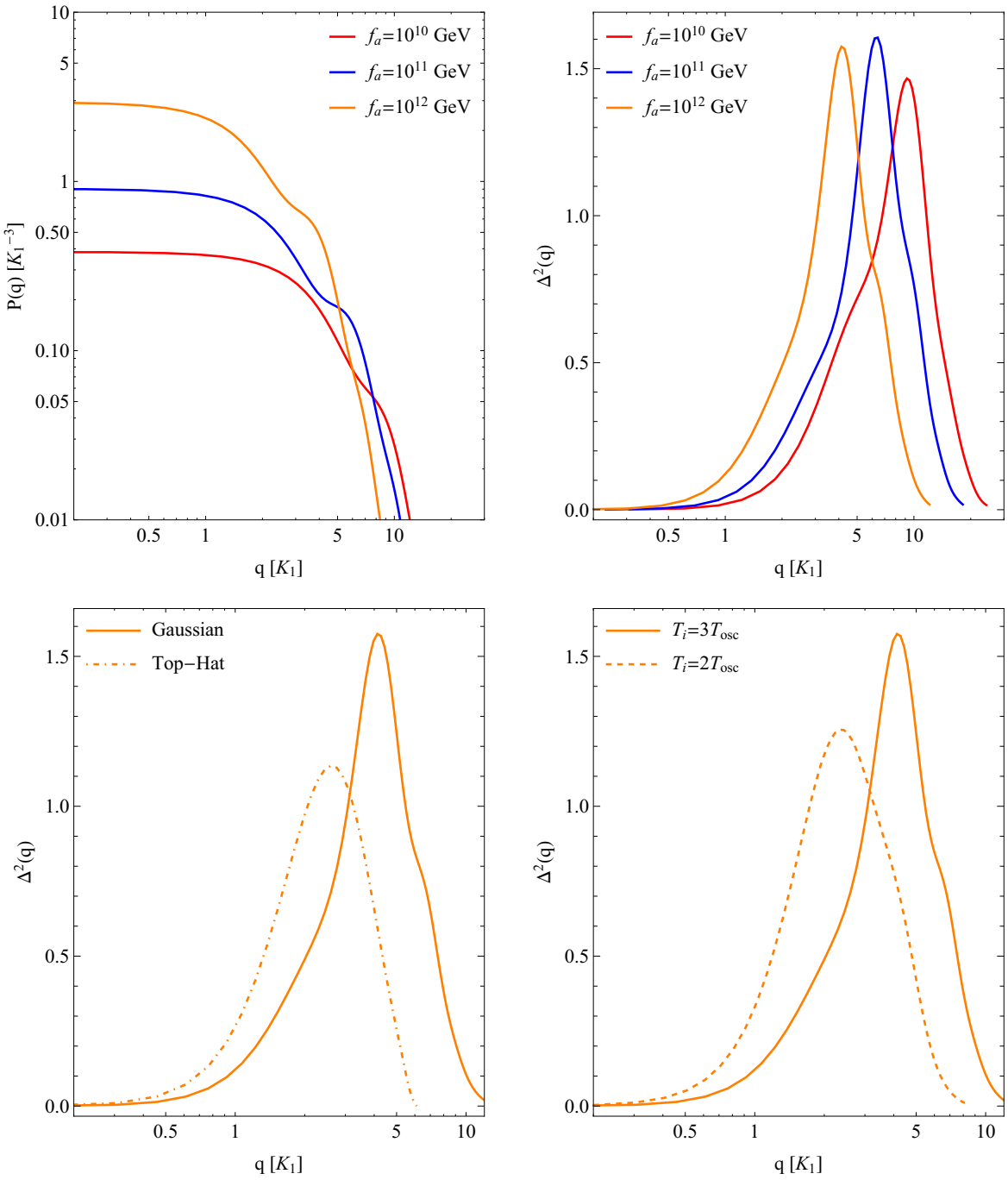

Figure IV.3.: Power Spectrum of the Realignment Density Fluctuations. This figure corresponds to Fig. 2 respectively 3 in Ref. [127]. The upper left panel shows the power spectrum $P(q)$ of the energy density fluctuations for different choices of f_a. The constant behavior for large scales (small q) is typical for white noise. The sharp drop-off in the power spectrum happens at the characteristic size of the fluctuations. This scales also correspond to the positon of the peaks in the dimensionless power spectrum Δ^2 (upper right panel). The height of the peak indicates that the fluctuations in the axion energy density are of $\mathcal{O}(1)$. In the lower panels we study the impact of choosing different power spectra for the Fourier modes, top-hat versus Gaussian, and the influence of the initial time T_i. Details can be found in the text. As reference scale for the wavenumber we use $K_1 = RH(T = 1\text{ GeV})$.

we naively expected that the horizon at $T_{\rm osc}$ defines the characteristic size of the fluctuations. However, our calculations show that they are somewhat smaller. This effect must be accounted to the correct treatment of the gradient terms in our calculation of the evolution equation of the axion field. Note that for the other choices, $f_a = 10^{10}, 10^{11}$ GeV, the oscillation temperature is higher, i.e. $T_{\rm osc} > 1$ GeV, which means that the horizon at the time the oscillation commence is smaller and therefore the peak of Δ^2 is shifted to higher q's.

We now turn to the low q behavior of the power spectrum $P(q)$ and Δ^2. Recall that low q mean large spatial scales. A numerical fit shows that for very low $q \ll K_1$ the dimensionless power spectrum Δ^2 can be paramerized via

$$\Delta^2 \sim [0.12, 0.39, 1.2] \cdot 10^{-1} \left(\frac{q}{K_1}\right)^3 \quad \text{for} \quad f_a = [10^{10}, 10^{11}, 10^{12}] \text{ GeV} \,. \tag{IV.56}$$

This underlines that $P(q) \propto \Delta^2/q^3$ becomes indeed constant for large scales. It turns out that when getting closer to the peak, the shape of Δ^2 is better fit by a parabola. From the height of the peak in Δ^2 we learn that the fluctuations are about $\mathcal{O}(1)$.

Note that if the fluctuations would be exactly of the size of the comoving Hubble horizon at $T_{\rm osc}$, we would expect the dimensionless power spectrum to be $\Delta^2 = (k/K_{\rm osc})^3$. However, our fit in Eq. (IV.56) shows again that the actual sizes of the fluctuations is smaller than that. This can be nicely seen for the choice $f_a = 10^{12}$ GeV, where $K_{\rm osc} \sim K_1$. With our result $\Delta^2 < (q/K_{\rm osc})^3$, we find that the characteristic mode q of the fluctuations is larger than $K_{\rm osc}$.

With the plots in the lower panels of Fig. IV.3 we can study the influence of the choice of P_θ (left), as well as the initial time (right), on Δ^2 while fixing $f_a = 10^{12}$ GeV. Note that a change of the initial time also influences the cut-off K. Therefore, we observe the expected shift of Δ^2 towards lower q in the lower left right, when setting $T_i = 2T_{\rm osc}$ instead of the default assumption $T_i = 3T_{\rm osc}$. Looking at the influence of P_θ in the lower left panel, we see that when choosing the top-hat power spectrum $P_\theta^{\rm TH}$ for the field modes, Δ^2 quickly goes to zero at around $q = 6K_1$. Recall that $P_\theta^{\rm TH}(k) \propto \Theta(k-K)$ and therefore our result for Δ^2 implies that even though we have no power in high modes $q > K \sim 3K_1$ in the Fourier coefficients θ_q of the field, we do so in the spectrum of the density fluctuations. This must be an effect of the gradient terms which appear squared in the expression for the energy density. Note that for the Gaussian power spectrum this cut-off is smeared out.

Comparison with Results from numerical Simulations of Vaquero et al [108]

In the following, we compare our results to the outcome of the recent numerical simulations by Vaquero et al in Ref. [108] where the complex Peccei-Quinn scalar with the full nonlinear potential was considered. This means that in the simulations from Vaquero et al effects of the strings as well as the nonlinearities in the axion potential are included. In Fig. IV.4 we reproduce Fig. 11 from Ref. [108], where the dimensionless power spectrum Δ^2 from both, our semi-analytic approach as well as the full numerical result is shown.

It turns out that for the low wavenumber region, both results are roughly consistent. Especially, the position of the first peak and also the rise of Δ^2 are comparable. Thus, Vaquero et al confirm our observation that the size of the fluctuations is smaller than naively expected. They also find the same white noise behavior of the power spectrum for large scales. Namely, they report a fit for Δ^2 in the low q region [108]

$$\Delta^2_{\rm string} \sim 0.3 \cdot 10^{-1} \left(\frac{q}{K_1}\right)^3 \quad \text{for } f_a = 10^{12} \text{ GeV} \,, \tag{IV.57}$$

which parametically agrees with our result in Eq. (IV.56). However, the numerical factor is about four times smaller.

Looking at Fig. IV.4, it becomes clear that for higher q values, beyond the first peak in Δ^2, the two results start differ notably. Where our result for Δ^2 quickly drops to zero, the full

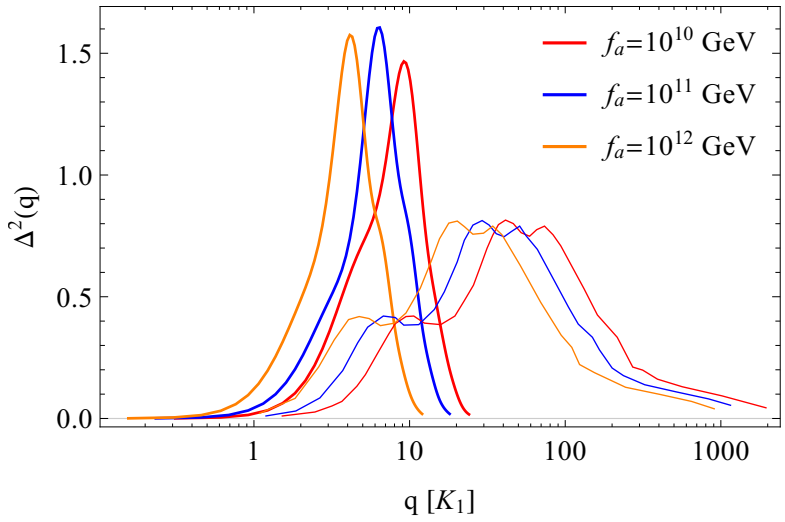

Figure IV.4.: Comparison with Results from Numerical Simulations in Vaquero et al. [108]. The thin lines correspond to the results from Ref. [108] and the thick lines to the results from our calculations. We observe that for low q's our semi-analytic and the numerical results roughly agree in position of the first beak and the cubic growth. For higher modes on the other hand, the numerical results have a much more richer structure due to including the string effects. We see that these also lead to less power in the modes and an overall reduction of the height of Δ^2. Note that this figure is a reproduction of Fig. 11 in Ref. [108]. As reference scale for the wavenumber we chose $K_1 = RH(T = 1\text{ GeV})$.

numerical simulations lead to a much richer structure, which must be an effect of the strings and the nonlineartiy of the axion potential. Another important difference is that the overall height of Δ^2 is significantly lower for the full numerical results compared to our approach. The reason for this seems to be that by using the white noise initial conditions for the misalignment field, we have overestimated the power in the high modes, close to our cut-off scale K. In fact, it looks like the strings, actually acting as the boundaries of the inhomogeneous patches of the misalignment field, reduce the power on the smallest scales, as can also be seen in Fig. 6 in Ref. [108]. However, also the overall normalization of the power spectrum should play a role, as we have already pointed out before. Recall that we use only the realignment axions for normalizing the fluctuations δ, whereas Vaquero et al automatically include the axions from the string and domain wall decays.

Another interesting observation from the results of the full numerical simluations is that even though Vaquero et al do observe the formation of the high density axitons with $\delta \gg 1$, they find that the power spectrum of the energy density is dominated by the mild $\delta \sim 1$ fluctuations, cf. especially Fig. 7 in Ref. [108]. Interestingly, this is somewhat in contrast to the results of Kolb & Tkachev in Ref. [33], where they speculate that the $\delta \gg 1$ overdensities might lead to very dense miniclusters, possibly observable as graviational femtolenses. The results by Vaquero et al, on the other hand, rather suggest that the typical miniclusters should mainly arise from the $\mathcal{O}(1)$ fluctuations.

Thus, we conclude that despite the indisputable importance of the nonlinear effects of the axion potential, we can capture with our harmonic approximation the dominant part of the power spectrum, namely the low wavenumber region, and therefore the important part responsible for the minicluster formation.

IV.3. Decoupling from the Hubble Flow

So far, when studying the evolution of the axion field we have neglected all gravitational effects besides the expansion of the universe. However, as soon as the power spectrum is frozen the overdense regions in the axion energy density can decouple from the Hubble flow and start to collapse. From our results for the power sepectrum in the previous section, we have learned that the fluctuations in the axion energy density are not small and therefore should not be treated perturbatively. Further, when considering the collapse of the axion overdensities we have to take into account that they can decouple already very early, i.e in the radiation dominated epoch. Recall that the power spectrum becomes constant already at $T \sim 100$ MeV.

To study the actual decoupling of axion density fluctuations, we can use results presented by Kolb and Tkachev in Ref. [130] where they have developed a spherical collapse model for arbitrary large overdensities which holds in matter as well as radiation dominated universes. In the following, we briefly recap their approach and reproduce the results which are most important for us.

We start by considering the evolution of a sphere with physical size r which includes the DM mass M in an expanding universe. If the size of the sphere is equal to or smaller than the Hubble horizon, we can assume the radiation encapsuled is homogeneous. The equation of motion for the radius r is simply

$$\ddot{r} = -\frac{8\pi G}{3}\rho_{\mathrm{rad}} r - \frac{GM}{r^2}\,, \tag{IV.58}$$

i.e. the sum of the pressure in the relativistic component and the attractive Newtonian force. We can assume that the mass M stays constant during the decoupling from the Hubble flow.

The radius r might be written as

$$r = a b_\zeta \zeta\,, \tag{IV.59}$$

where for now, a is the scale factor[5], ζ is the initial comoving coordinate, and b_ζ is the so-called deceleration parameter. It denotes the deviation of the evolution of r from the overall Hubble flow.

We are interested in the time a fluctuation δ corresponding to a given mass M and size R starts to collapse. For a spherically symmetric fluctuation, the relation between M, R, and δ is

$$M = \frac{4}{3}\pi\overline{\rho}(1+\delta)R^3(t_i)\zeta^3\,, \tag{IV.60}$$

where t_i is an initial time where we start to consider the collapse and $R = R(t_i)$ is the initial comoving size. Note that for small fluctuations $\delta \ll 1$, we find that $M \propto R^3$, i.e. there is a one-to-one relation between the mass and the size. For the axion density fluctuations we can not draw this conclusion, since δ is of $\mathcal{O}(1)$ and it cannot be neglected. This will become important later, when we want to calculate the minicluster mass function.

The start of the collapse of a fluctuation δ can be identified with the time when the radius decouples from the Hubble expansion and starts to turn around, i.e. when $\dot{r} = 0$. Using the scale factor $x \equiv a/a_{\mathrm{eq}}$ instead of time as the independent variable, the relation defining the time of turnaround becomes

$$b + x\frac{\mathrm{d}b}{\mathrm{d}x} = 0\,. \tag{IV.61}$$

Note that we dropped the subscript ζ.

[5]Note to avoid confusion with variables describing spatial sizes, we denote in the following the scale factor with a instead of R, as we have done so far.

Rewriting the equation of motion in Eq. (IV.58) in terms of the deceleration parameter b as a function of x, we find:

$$x(x+1)\frac{\mathrm{d}^2 b}{\mathrm{d}x^2} + \left(1+\frac{3}{2}x\right)\frac{\mathrm{d}b}{\mathrm{d}x} + \frac{1}{2}\left(\frac{\delta+1}{b^2} - b\right) = 0\,. \tag{IV.62}$$

This equation can be solved numerically for different δ. As initial conditions we can chose for example $b(x_i) = 1$ and $b'(x_i) = 0$. However, it turns out that the result is not very sensitive the actual choice of the initial condtions. Nevertheless, it must be noted that the initial time has to be $x_i \ll 1$ to produce the correct behavior of $b(x)$. For our purposes, this means that the exact initial time we start considering the decoupling of the axion overdensities should not matter too much, as long as it is well before matter-radiation equality. For convenience we take $T_* = 100$ MeV. Recall that at this temperature the axion reaches its zero temperature value and hence the power spectrum is frozen. This means that from this time on, only the gravitational interactions should dictate the evolution of the density fluctuations.

With the result for $b(x)$ in terms of a given δ we can determine the time of turnaround x_{ta} via Eq. (IV.61). With our numerical results, we can confirm the approximate relation

$$x_{\mathrm{ta}} \approx \frac{0.7}{\delta} \tag{IV.63}$$

already found by Kolb and Tkachev in Ref. [130].

For considering the axion overdensities, we interpret this result the following way. At a given time x all fluctuations larger than a critical value

$$\delta_{\mathrm{c}} \approx \frac{0.7}{x} \tag{IV.64}$$

should have started to collapse and a fluctuation δ can be characterised by a mass M and a radius R via

$$\delta(R, M) = \frac{3M}{4\pi R^3 \overline{\rho}} - 1 \tag{IV.65}$$

which is just a reformulation of Eq. (IV.60). It is important to note that R is the comoving size of the fluctuation at t_i. Thus, in our case at $T = 100$ MeV. We want to point out again that Eq. (IV.65) does not give one-to-one relation between M and R. This implies that there exist different tupels (M, R) which lead to the same δ. Together with our result for the power spectrum of the fluctuations, Eq. (IV.64) and (IV.65) are the main incredients for deriving the mass function of the miniclusters.

Note that it is not advisable to describe the evolution of a minicluster after the time of turnaround with Eq. (IV.62). Because it does not contain a term which can stop the collpase, the late time solution will always be a collapse into a singulartiy. Kolb and Tkachev speculate that the collapse should stop at about half the turnaround radius due to virialization [130]. However, it is questionable if this is the case for axion overdensities. We postpone a more in-depth discussion of the evolution of the axion miniclusters after their decoupling from the Hubble flow to Ch. V.

IV.4. Distribution of Axion Miniclusters

In the standard DM matter scenario, the Press & Schechter method [131] and similar approaches [132, 133] can be used to calculate the mass distribution of collapsed objects, the so-called mass function. See, for example, Refs. [128, 134] for thorough reviews of this topic. The Press & Schechter method provides an analytic handle on predicting the distribution of DM halos using a spherical collapse model as input. Even though, N-body simulations [135] show

that the actual collapse might be far from spherical [134], the analytic approaches succeed in reproducing the correct DM halo mass functions, at least qualitatively. In the following, we discuss how we can apply and modify the Press & Schechter method for calulating the distribution of axion miniclusters. We start by briefly reviewing the basic features of the original approach and pointing out what modifications are needed in the case of the axion miniclusters.

According to Ref. [128], the mass function can be written as

$$\frac{\mathrm{d}n}{\mathrm{d}M} = f(\delta_c, \sigma_R)\frac{\overline{\rho}}{M^2}\left|\frac{\mathrm{d}\log\sigma_R}{\mathrm{d}M}\right| , \tag{IV.66}$$

where $n(M)$ is the comoving number density of objects with mass M. We can interpret Eq. (IV.66) as a relation for the distribution of the number density of callapsed objects in the intervall $\mathrm{d}M$. On the right hand side of Eq. (IV.66), we have, besides the mean energy density $\overline{\rho}$, the quantitiy

$$\sigma_R^2 \equiv \langle \delta_R^2(x)\rangle = \frac{1}{2\pi^2}\int \mathrm{d}k\; k^2 P(k)|\tilde{W}_R(k)|^2 , \tag{IV.67}$$

which is the variance of the density fluctuations smoothed over some scale R [127, 128]. The smoothing is done by applying a window function $W_R(x)$ and $\tilde{W}_R(k)$ is its Fourier transform. Different shapes can be used for the window function. A natural choice would be a sphere in real space, but it turns out that it is often more convenient to use a top-hat in k space, $\tilde{W}_R(k) = \Theta(1-kR)$. We will comment on the reason and the implications of this specific choice later. Together with the window function comes a smoothing volume V_R depending on the scale R and the actual shape of the window function. Usually, for small fluctuations, the scale R is directly identified with the mass contained in the volume the fluctuations were smoothed over, i.e. $M_R = V_R\overline{\rho}$. This makes M and R basically equivalent. However, this relation does not hold in the case of the axion density fluctions which are expected to be large, following our results from before. Therefore, we have to stick to the general expression in Eq. (IV.60) for a relation between the fluctuations δ and M and R.

Coming back to the definition of $\mathrm{d}n/\mathrm{d}M$ in Eq. (IV.66), the function $f(\delta_c, \sigma_R)$ is included to represent the probability for finding a fluctuation in the smoothed fluctuation field which is larger or equal than a critical height δ_c. Assuming that δ is a Gaussian random variable, Press & Schechter used the form[6]

$$f(\delta_c, \sigma_R) = \sqrt{\frac{2}{\pi}}\frac{\delta_c}{\sigma_R}\exp\left[-\frac{\delta_c^2}{2\sigma_R^2}\right] . \tag{IV.68}$$

In the standard spherical collapse model where the fluctuations are treated perturbatively and the collapse only happens after matter-radiaton equality, it is found that the critical density is $\delta_c \simeq 1.686$ and δ_c can be related to the redshift via the usual growth factor [134]. However, for our purposes, where we have to consider the collapse of nonlinear fluctuations in matter as well as radiation dominated eras, we should replace the usual expression for δ_c by our result from before, namely $\delta_c(x) \approx 0.7/x$.

Before going into the further details of the mass function for the axion miniclusters, we want to comment on some general features of the mass function in the usual CDM scenario. It should be noted that in the Press & Schechter approach an overdensity identified with mass M is understood as collapsed as soon as its corresponding smoothed variance $\sigma_R = \sigma(M) \geq \delta_c$. This means that there is at any time a characteristic mass scale, let us call it M_c, at which $\sigma(M_c) = \delta_c$ holds [128] and for masses larger than M_c the mass function will be suppressed due to the form of $f(\delta_c, \sigma_R)$. This large M suppression is more or less independent of the underlying power

[6] In fact $f(\delta_c, \sigma_R)$ should not be mistaken with a proper probability distribution function since it is not normalized correctly. Note that there is an issue of a missing factor two which was put in by hand in the original work by Press & Schechter. This is known as the cloud-in-cloud problem, see for example Ref. [128] for a discussion of this issue and solutions for it.

spectrum and the shape of σ_R. For small masses, on the other hand, we find that the mass function diverges as $1/M^2$ if $|\mathrm{d}\log\sigma_R/\mathrm{d}M|$ in Eq. (IV.66) does not go to zero fast enough. So, the small M behavior of the mass function does depend on the shape of σ_R. However, it turns out that for usual CDM, the mass function still diverges for $M \to 0$. We will shortly see that this changes in the case of axion miniclusters.

A modified Press & Schechter Method for the Minicluster Mass Function

Let us repeat the necessary modifciations of the standard Press & Schechter method when we want to calculate the minicluster mass function in a similar approach. First, we should not use the one-to-one relation between smoothing scale and mass since we are dealing with nonlinear fluctuations. This implies that the minicluster mass function should in fact be a distribution in mass and size. Second, we have to use our results from Sec. IV.3 to describe the critical density $\delta_c(x)$. The actual derivation of the double differential axion minicluster mass function is presented in great detail in Ref. [127]. At this point, we only want to briefly summarize the most important steps.

As in the standard Press & Schechter approach, we start with the asssumption that the smoothed density fluctuation δ_R is a Gaussian random variable with the variance σ_R as defined in Eq. (IV.67). The probability distribution function (PDF) of δ_R is then given by

$$f_{\mathrm{sm}}(\delta_R; R) = \frac{1}{\sqrt{2\pi}}\frac{1}{\sigma_R}\exp\left[-\frac{\delta_R^2}{2\sigma_R^2}\right] . \tag{IV.69}$$

Note that δ_R is understood as the smoothed fluctuation identified with one specific smoothing scale R.

Let us take a step back and determine the joint distribution $f(\delta, r)$ for fluctuations of height δ and some size r. Equation (IV.69) suggests that only fluctuations with $r > R$ contribute to the smoothed PDF. This motivates the ansatz [127]

$$g(R) f_{\mathrm{sm}}(\delta, R) = \int_R^\infty \mathrm{d}r \; f(\delta, r) \tag{IV.70}$$

for deriving $f(\delta, r)$. The function $g(R)$ is introduced such that $f(\delta, r)$ can be normalized correctly. For that it should hold that:

$$g(R) = \int \mathrm{d}\delta \int_R^\infty \mathrm{d}r \; f(\delta, r) , \quad g(0) = 1 . \tag{IV.71}$$

Equation (IV.70) together with (IV.71) provides a non-trivial system of equations for deriving $g(R)$ and therefore $f(\delta, R)$. In Ref. [127] it was shown that by differentiating Eq. (IV.70), we arrive at the equation

$$f_{\mathrm{sm}}(\delta; R)\left[\frac{\mathrm{d}g(R)}{\mathrm{d}R} - \frac{\mathrm{d}\log\sigma_R}{\mathrm{d}R}\left(1 - \frac{\delta^2}{\sigma_R^2}\right) g(R)\right] = -f(\delta, R) \tag{IV.72}$$

which is solved by $g(R) = \sigma_R/\sigma_0$ with $\sigma_0 \equiv \sigma_{R=0}$ is the variance without smoothing. Therefore, the joint distribution function is given by

$$f(\delta, R) = -\frac{1}{\sigma_0}\frac{\mathrm{d}\sigma_R}{\mathrm{d}R}\frac{\delta^2}{\sigma_R^2} f_{\mathrm{sm}}(\delta; R) . \tag{IV.73}$$

The physical interpretation of this result and the relation between f and $\mathrm{d}\sigma_R/\mathrm{d}R$ is the following. If σ_R is constant, this means that there are no fluctuations of this size and therefore $f(\delta, R)$ vanishes.

In Fig. IV.5 we show the results for σ_R as well as the normalized derivative $1/\sigma_0(\mathrm{d}\sigma_R/\mathrm{d}R)$ using the power spectra $P(q)$ presented in the previous section. As a reference scale we introduce

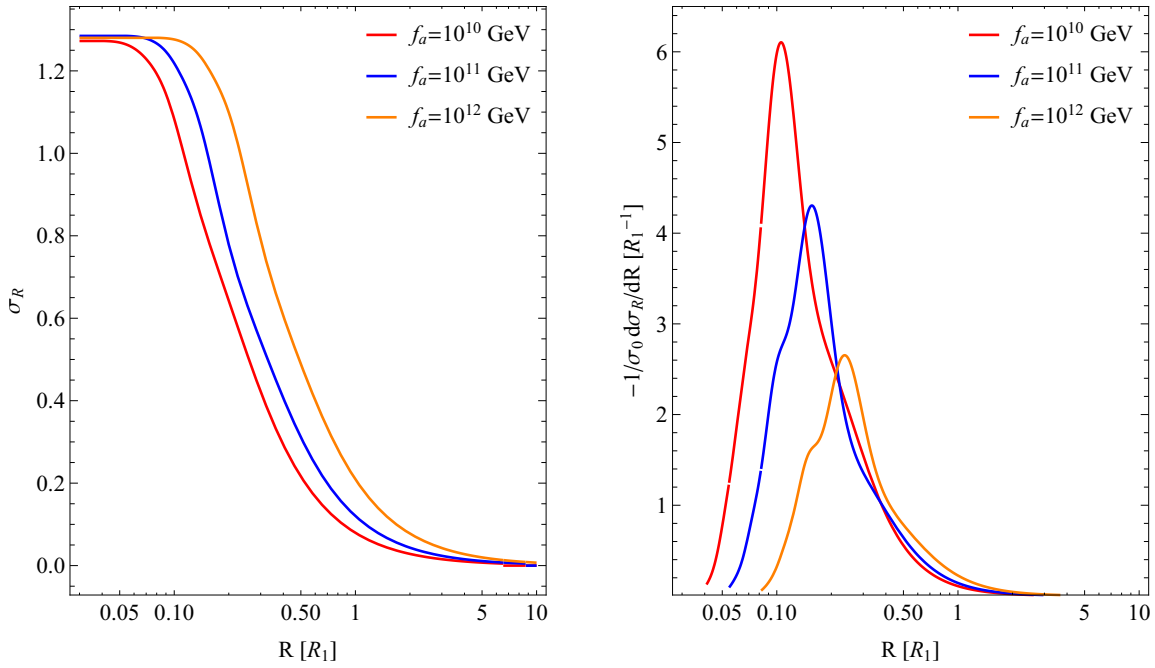

Figure IV.5.: Smoothed Variance of the Density Fluctuations. The left panel shows the variance σ_R as a function of the smoothing scale R and the right panel its derivative normalized to the variance without smoothing. The latter is an important input for deriving the mass function of axion miniclusters via the modified Press & Schechter method presented in the text. This figure corresponds to Fig. 4 in [127].

the comoving size $R_1 \equiv 1/(aH(T = 1\text{ GeV}))$. We see that the derivative peaks roughly at the characteristic scale of the fluctuations, which we have identified before, and qickly goes to zero for small R. In fact, this should provide a low R cut-off for $f(\delta, R)$.

Our results for the variance σ_R might be compared with the work by Fairbairn et al presented in Ref. [113] where the standard Press & Schechter method and some ad hoc assumptions for the power spectrum of the axion density fluctuations are used to determine an estimate for the axion minicluster mass function. They find a similar constant behavior σ_R when $R \to 0$, cf. Fig. 4 in Ref. [113]. We will later compare our results for the axion minicluster mass function with that of Fairbarin et al in more detail.

With the probability function $f(\delta, R)$ at hand, we can determine the number density n of collapsed miniclusters similar as in the standard approach. We find

$$\frac{\mathrm{d}n}{\mathrm{d}R\mathrm{d}M} = \frac{3}{2\pi M R^3} f(\delta, R)\Theta(\delta - \delta_c(x))\,, \tag{IV.74}$$

where δ is now understood as a function of M and R via the relation Eq. (IV.65) and the Heaviside function makes sure that only fluctuations larger than the critical value $\delta_c = 0.7/x$ are taken into account.

By integrating over R we can find an analogous expression to the usual one-dimensional mass function:

$$\frac{\mathrm{d}n}{\mathrm{d}M} = \frac{3}{2\pi M} \int_0^{R_c(M)} \mathrm{d}R\ \frac{1}{R^3} f(\delta, R)\,. \tag{IV.75}$$

The critical radius $R_c(M)$ is determined via setting $\delta = \delta_c$ in Eq. (IV.65).

Before presenting numerical results, we want to discuss the qualitative behavior of the mass function in our modified setup and compare it to the standard Press & Schechter result. For

high masses, we still expect an exponential suppression of $n(M)$, for the same reasons as before. However, since $f(\delta, R)$ drops quickly for $R \to 0$, meaning that fluctuations smaller than some characteristic size are strongly suppressed, we can expect a different behavior for small masses. Namley, if $f(\delta, R)$ goes to zero fast enough, i.e. faster than $1/(MR^3)$ does, the mass function should have a cut-off at some low M. Our results show that this is indeed the case. However, it turns out that the cut-off is only visible if we choose the k space top-hat window function. For other choices, e.g. a sphere in real space or a Gaussian window function, we have checked that the mass function still diverges. This unwanted remnant of the choice of the window function is a known issue of the Press & Schechter method [136]. This problem was also recently discussed by Fairbairn et al in Ref. [113] in view of the minicluster mass function.

Results

In the following, we present results for the double differential minicluster mass function defined in Eq. (IV.74). Recall that it was defined as the comoving number density of collapsed objects at a time $x = a/a_{\rm eq}$ and it is a function of the initial comoving size R and the inital mass M of the overdensity. Note that we can assume that the mass stays constant during the decoupling process. However, the size definetly changes. Hence, a quantity which might be of greater interest than R is actually the physical size of the fluctuation at the time of turnaround. Let us call it $r_{\rm ta}$. We can determine $r_{\rm ta}$ as a function of R from the spherical collapse model described in Sec. IV.3. With $r_{\rm ta} = a_{\rm ta} b_{\rm ta} R$ and using the approximate result $b(x) \approx 1 + \delta x/2$ from Ref. [130] together with $\delta x_{\rm ta} = 0.7$, we find:

$$r_{\rm ta} = 0.4 \frac{a_{\rm eq}}{\delta} R \,. \tag{IV.76}$$

Expressing δ via the comoving reference scale R_1 and a reference mass scale $M_1 \equiv 4\pi\overline{\rho}(T = 1\ \text{GeV}) H^{-3}(T = 1\ \text{GeV})$, we find the useful relation [127]:

$$r_{\rm ta} \simeq 1.4 \cdot 10^9\ \text{km} \left(\frac{R}{R_1}\right)^4 \left(\frac{M_1}{M}\right) . \tag{IV.77}$$

With our numerical results for $\overline{\rho}(T = 1\ \text{GeV})$, a neat conversion rule from R to $r_{\rm ta}$ is given by

$$r_{\rm ta} \sim [2, 25, 360] \cdot 10^{10}\ \text{km} \left(\frac{R}{R_1}\right)^4 \left(\frac{10^{-14} M_\odot}{M}\right) \quad \text{for} \quad f_a = [10^{10}, 10^{11}, 10^{12}]\ \text{GeV} \,, \tag{IV.78}$$

which we can use to express R in $\mathrm{d}n/(\mathrm{d}M\mathrm{d}R)$ in terms of $r_{\rm ta}$.

For a better visualization of our results for the minicluster mass function, it is useful to introduce the dimensionless quantitites

$$X_{MR} = \frac{M}{\overline{\rho}} \frac{\mathrm{d}n}{\mathrm{d}\log M \mathrm{d}\log R} \tag{IV.79}$$

and

$$X_M = \frac{M}{\overline{\rho}} \frac{\mathrm{d}n}{\mathrm{d}\log M} \,, \tag{IV.80}$$

which give the contribution of collapsed objects per interval M and R respectively only M to the mean energy density $\overline{\rho}$. Recall that we use $\overline{\rho}$ of the realignment axions only. Hence, including other sources for relic axions might again change the normalization. However, we focus in our discussion mainly on the shape of mass function anyway.

In Fig. IV.6, we show results for the double differential axion minicluster mass function X_{MR} at the time of matter-radiation equality, using the above described methods and the results from the previous sections as input. We observe that the distributions are nicely peaked around a characteristic minicluster mass and size.

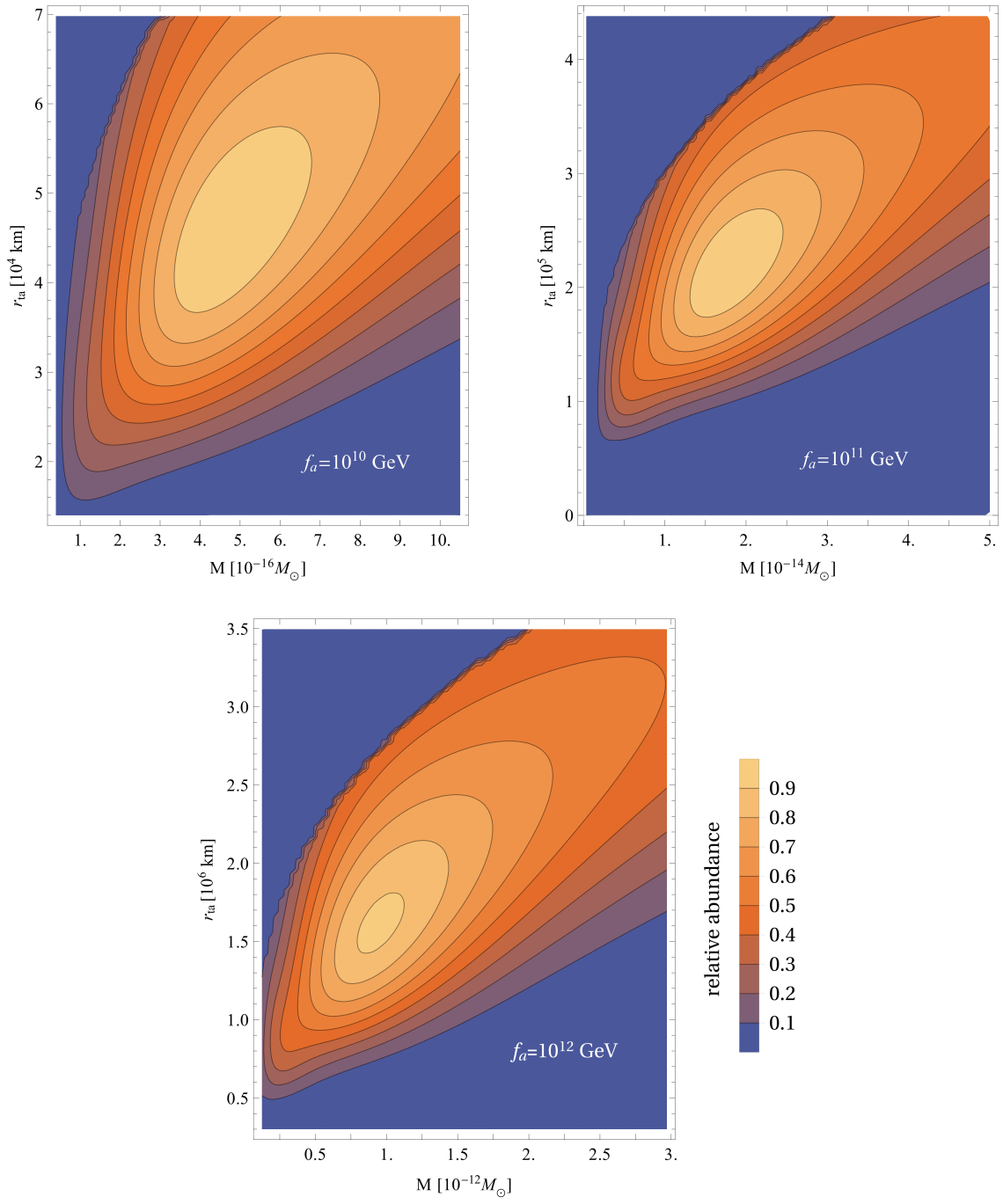

Figure IV.6.: Distribution of Axion Miniclusters in Mass and Size. Using the double differential mass function described in the text we calculate the relative abundance of miniclusters as a function of mass and turnaround radius for different Peccei-Quinn breaking scales $f_a = 10^{10}, 10^{11}, 10^{12}$ GeV. We observe that the distributions are peaked around a characteristic mass and characteristic radius. In Tab. IV.1 we summarize numerical results. Similar plots are shown in Fig. 5 of Ref. [127].

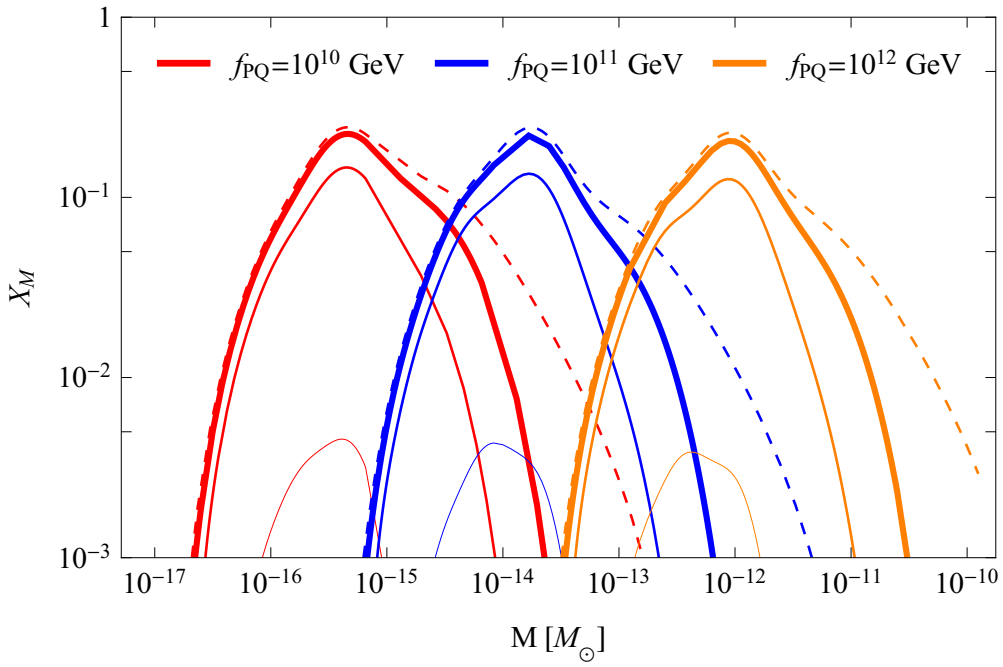

Figure IV.7.: Dimensionless Mass Function of Axion Miniclusters. The different linewidths, from thin to thick, correspond to different instances in time $x = 0.2, 0.5, 1$ with $x = a/a_{\rm eq}$. For the dashed line we chose $x = 5$, a time where the mass function already became almost time independent. This result corresponds to Fig. 6 of Ref. [127].

Figure. IV.7 shows the evolution of the integrated mass function X_M. Since with the definition of X_M we have factored out the overall expansion of the universe, the evolution of X_M therefore shows how the number density of collapsed objects per comoving volume grows. The distribution starts to peak around the characterstic mass and grows till around matter-radiation equality, i.e. $x \simeq 1$. After that only the large mass tail keeps evolving. We can intepret this as almost all fluctuations collapsing before $x = 1$. Note that with the relation $\delta_c = 0.7/x$ for the critical height, all fluctuaions eventually collapse when $x \to \infty$. Further, we observe the already anticipated exponential suppression of the mass function at high masses and the cut-off at low masses.

With our results for X_{MR} and X_M, we can extract the peak values for the characteristic turn-around radius $r_{\rm ta}^{\rm peak}$, as well as the characteristic minicluster mass $M_{\rm MC}^{\rm peak}$, for the miniclusters depending on the chosen Peccei-Quinn breaking scale. We can also define typical intervals for

f_a [GeV]	$M_{\rm MC}^{\rm peak}$ [$M_\odot$]	$M_{\rm MC}$ range [$M_\odot$]	$r_{\rm ta}^{\rm peak}$ [km]	$r_{\rm ta}$ range [km]
10^{10}	$4 \cdot 10^{-16}$	$[2 \cdot 10^{-17}, 1 \cdot 10^{-14}]$	$4 \cdot 10^4$	$[2 \cdot 10^4, 2 \cdot 10^5]$
10^{11}	$2 \cdot 10^{-14}$	$[5 \cdot 10^{-16}, 3 \cdot 10^{-13}]$	$2 \cdot 10^5$	$[4 \cdot 10^4, 7 \cdot 10^5]$
10^{12}	$8 \cdot 10^{-13}$	$[6 \cdot 10^{-14}, 2 \cdot 10^{-11}]$	$2 \cdot 10^6$	$[7 \cdot 10^5, 7 \cdot 10^6]$

Table IV.1.: Results for the Distribution of Axion Miniclusters in Mass and Size as presented in Ref. [127]. From the distrubtions X_M as well as X_{MR}, cf. Fig. IV.6 respectively IV.7, we can extract peak values for the characteristic minicluster mass $M_{\rm MC}$ and turnaround radius $r_{\rm ta}$. We also extract the intervals for $r_{\rm ta}$ and $M_{\rm MC}$ where their contribution is about 1% of the peak value of the distribution, giving typical ranges.

mass and turnaround radii of the miniclusters. This we do by extracting the values for $r_{\rm ta}$ and $M_{\rm MC}$ where X_{MR} is larger than 1% of the peak value. The outcome is summarized in Tab. IV.1. We note that the characteristic turnaround radii span about one order of magnitude, whereas the miniclusters masses cover almost three. This property is in good approximation independent of the Peccei-Quinn breaking scale.

We also note that the minicluster masses we find are smaller than expected with our naive estimate at the very beginning of this chapter, cf. Eq. (IV.6). However, this was to be expected since we have already found that the characteristic size of the fluctuations is smaller than the Hubble horizon at $T_{\rm osc}$ which was used to derive the estimate for $M_{\rm MC}$, to begin with. Note that the fluctuation size enters the minicluster mass cubed. This means that with the actual fluctuation size being about a quarter of what we expected, this explains the two orders of magnitude difference for $M_{\rm MC}$.

With our results we can also try to find a relation between f_a and $M_{\rm MC}$. Fitting the peak values to a function of f_a we find

$$M_{\rm MC} \sim 8 \cdot 10^{-13} M_\odot \left(\frac{f_{\rm PQ}}{10^{12}\ {\rm GeV}}\right)^{1.6} . \tag{IV.81}$$

It should of course be noted that with only three different values for f_a, we have very poor statistics and cannot give a conclusive statement on the actual scaling behavior. However, it is interesting that we find a somewhat shallower increase with f_a when compared to our estimate in Eq. (IV.6). There, we have found $M_{\rm MC} \propto f_a^{7/6}$. This could very well be due to an effect of the parameterization for the temperature dependent axion mass when deriving this estimate.

Our results for the turn around radius suggest a relation between $r_{\rm ta}$ and f_a like

$$r_{\rm ta} \sim 2 \cdot 10^6\ {\rm km} \left(\frac{f_a}{10^{12}\ {\rm GeV}}\right) , \tag{IV.82}$$

which is also very different than our naive estimate. Again this could be related to differences in the temperature dependence of the axion mass. But it could also be an actual effect of the gradient terms. For a conclusive answer a study of wider range of f_a's would be necessaray. However, recall that for the QCD axion only breaking scales f_a in the range between $10^{10} - 10^{13}$ GeV are really cosmologically relevant in the sense that it can explain a notable amount or all of the observed DM.

Finally, we want to point out that the turnaround radius we have found should not be mistaken with the actual size of the miniclusters today. So far, we have only considered the process of the decoupling from the Hubble flow, but not yet the subsequent collapse. Here, our results for the minicluster mass function can serve as valubale input for further studies. We ourselves turn to this topic in the Ch. V, when we consider the fate of the miniclusters. But assuming that the miniclusters end up in some kind of dilute and virialized state, their size today should be comparable to $r_{\rm ta}$.

Comparison with Results from Fairbairn et al [112, 113]

Before moving on, we want to compare our results for the axion minicluster mass function with the outcome of the study by Fairbairn et al in Refs. [112, 113]. For that, we first have to briefly review their approach. The big difference to our work is that Fairbairn et al do not consider the evolution of the axion field itself but focus only on the dynamics of the density fluctuations δ. For that, they assume similar initial conditions on the power spectrum of δ as we do for the power spectrum of the Fourier modes of the misalignment field. Namely, they also try to model the expected white noise behavior. But again, they assume the white noise for the fluctuations whereas we do that for the misalignment field itself. Doing so, we were able to derive the power spectrum of the density fluctuations from first principle and did not make any assumptions for it. Nevertheless, as we see from our results for $P(q)$ in Fig. IV.3, assuming a white noise behavior also for the density fluctuations and therefore approximating $P(q)$ via a top-hat or a Gaussian

as Fairbairn et al did was not a bad guess. Still, a problem of their study is that they have missed that the characterstic size of the fluctuations does not correspond to the Hubble horizon at $T_{\rm osc}$. This they have used as input for defining the power spectrum of the fluctuations. Recall that we were only able to see that the fluctuations are actually smaller because we followed the field evolution and properly included the gradient terms.

Further, to derive the mass function for the axion minicluster, Fairbairn et al use the power spectrum of the density fluctuations in a standard Press & Schechter approach. Hence, they do not consider the distribution in mass and size, but mass only.

Despite the shortcomings of their approach we find that their minicluster mass function qualitatively agrees with our results and the intervals of the characterstic minicluster masses span similar orders magnitude. The peak values however are not as easy to compare due to the issue of using different characteristic sizes of the fluctuations. Nevertheless, we conclude that our study and that of Fairbairn et al in Refs. [112, 113] still lead to comparable results for the axion minicluster mass function.

IV.5. ALP Miniclusters

So far, we have concentrated exclusively on the formation of miniclusters in the QCD axion scenario. However, when the realignment of a scalar field happens after inflation, large isocurvature fluctuations in the energy density generically occur. Therefore, we expect minicluster formation also for ALPs. See also Ref. [84] for a more in-depth study of this topic.

Our above-described method to derive the minicluster mass function can readily be applied to any other axion scenario than the QCD one. The only difference is that instead of temperature dependent QCD axion mass, a more general parameterization of $m_a(T)$, as for example presented Sec. III.2, should be used. This implies that for ALPs, the minicluster distribution will not only depend on the symmerty breaking scale, but also on the ALP mass m_a and details of its temperature dependence, $m_a(T)$. This widens the range for possible minicluster masses and sizes immensly. An application of our method to various ALP scenarios is presented in Ref. [137]. Here, we only want to give a very brief overwiew on the general properties of ALP miniclusters.

To get an estimate for the mass and size of ALP miniclusters, we proceed in analogy to the considerations at the very beginning of this chapter. Even though, the actual size of the fluctuations in the energy density might be smaller than the Hubble horizon at $T_{\rm osc}$, it should at least be of the same order. Hence, as a first guess we again assume for the characterstic size L of the fluctuations in the energy density are of the order $L \sim 1/(RH(T_{\rm osc}))$.

With our general parameterization of the temperature dependent axion mass in Eq. (III.38), we find that the oscillation temparature $T_{\rm osc}$ can be written as

$$T_{\rm osc} \sim \left[\frac{b}{4.98 g_*^{1/2}(T_{\rm osc})}\right]^{1/(2+n)} \cdot 10^{-(n-5)/(n+2)}\ {\rm GeV}\ \left(\frac{m_a}{10^{-5}\ {\rm eV}}\right)^{1/2} \left(\frac{f_a}{10^{12}\ {\rm GeV}}\right)^{n/(4+2n)} \tag{IV.83}$$

which might look a little convoluted due to the complicated dependence on the paramters b and n. But still it turns out that this a very useful relation for the following calculations.

For example, we can use it to estimate the size of the fluctuations today and we find[7]

$$L_0 \sim b^{-1} \left[\frac{b}{4.98 g_*^{1/2}(T_{\rm osc})}\right]^{n/n+2} \cdot 10^{2(n-5)/(n+2)}\ {\rm pc}\ \left(\frac{10^{-5}\ {\rm eV}}{m_a}\right)^{1/2} \left(\frac{10^{12}\ {\rm GeV}}{f_a}\right)^{n/(2n+4)} . \tag{IV.84}$$

[7] Note that the inverse proportionality to f_a might be somewhat puzzeling since for the QCD axion we found $L_0 \propto f_a^{1/6}$. But using $m_a \propto f_a^{-1}$ for the QCD axion and our benchmark value $n = 4$, we reproduce the QCD relation.

Hence, we see that L_0 can be quite large and even cosmologically relevant if the axion is extremely light. Recall that smaller m_a mean that the equality $m_a(T) = 3H(T)$ is met at lower temperatures and therefore at larger Hubble horizons.

A similar relation holds for the ALP minicluster size:

$$R_{\rm MC} \sim b^{-1} \left[\frac{b}{4.98 g_*^{1/2}(T_{\rm osc})}\right]^{n/n+2} \cdot 10^{2(6n+5)/(n+2)}\ {\rm km} \left(\frac{10^{-5}\ {\rm eV}}{m_a}\right)^{1/2} \left(\frac{10^{12}\ {\rm GeV}}{f_a}\right)^{n/(2n+4)} . \tag{IV.85}$$

Again smaller m_a produce larger miniclusters. Also the stiffness of the switch-on of the mass, i.e. the paramter n, has a non-trivial impact on the size. It has also great importance for the minicluster mass:

$$M_{\rm MC} \sim b^{-1} \left[\frac{b}{4.98 g_*^{1/2}(T_{\rm osc})}\right]^{n/n+2} 10^{-(9n+32)/(n+2)} M_\odot \left(\frac{10^{-5}\ {\rm eV}}{m_a}\right) \left(\frac{f_a}{10^{12}\ {\rm GeV}}\right)^{(n+4)/(n+2)} . \tag{IV.86}$$

This measn that for very light ALPs, the miniclusters can be as heavy as $M_{\rm MC} \sim M_\odot$. Note that the heavier the miniclusters the easier they might be observable in astrophysical observations like lensing surveys, cf. Ref. [113].

However, a word of caution is in order when considering very light axions in the context of miniclusters. First, if we stick to the zero-temperature relation $m_a = \Lambda^2/f_a$, light axions call for either very low Λ or very high f_a. It can be argued that Λ should not be too low, when put in the cosmological context. If we understand Λ as a scale of some strongly interacting dark sector and its confinement happens at $\Lambda \lesssim 1$ MeV, it might spoil the usual big bang nucleosynthesis (BBN) [84]. However, this problem can be easily overcome if it is possible that the dark sector and the visible sector are not in thermal equilibrium [138].

But, on the other hand, the breaking scale f_a can indeed not be arbitrary high, at least in our case of post-inflation symmetry breaking. Here, f_a should at least be smaller than the reheating temperature $T_{\rm RH}$. With CMB observations, estimates on the scale of inflation and therefore $T_{\rm RH}$ can be made. In Ref. [139], Abbot and Wise have used the large-scale isotropy of the CMB to derive a model-independent upper bound on the reheating temperature and they find $T_{\rm RH} \lesssim 10^{17}$ GeV. This translates into an upper bound on f_a in the post-inflation scenario, $f_a \lesssim 10^{17}$ GeV. Still, there might exist scenarios where the mass is generated differently and can therefore evade such constraints.

However, another perhaps even more important contstraint for very light ALPs in the post-inflation scenario occurs when they are supposed to explain all the DM. Since for the energy density we have $\rho_a \propto m_a m_a(T_{\rm osc}) f_a^2$, we find that extremly small masses call for very high f_a if we fix $\rho_a = \rho_{\rm DM}$. Therefore, the upper bound on f_a in the post-inflation scenario leads ot a lower bound on m_a. This issue is discussed in more detail in Ch. VI where we look at more general implications of the post-inflation realignment scenario for cosmological large-scale observables. At this point, we simply conclude that also for very lights ALPs it is difficult to make the miniclusters arbitrarily heavy or large. Again, more on this topic can be found in Ref. [137].

V. Fate of Axion Miniclusters

In the previous chapter, we have studied the evolution of the axion density fluctuations from the onset of the field oscillations till they decoupe from the Hubble flow and start to form the gravitationally bound miniclusters. However, their evolution should not stop there. Rather, we can expect the miniclusters to collapse under their own gravity once turned around from the Hubble expansion and eventually they should settle in some kind of equilibrium state. In Ref. [130], Kolb and Tkachev state that, after large DM fluctuations decouple from the Hubble flow, they will virialize at a size about half their turnaround radius. But in case of the axion, the process of "virialization" might be very non-trivial, if it happens at all. Recall that the virial theorem and the process of virialization is formulated for a gas or fluid consisting of a large number of particles. But so far, for our purposes we have described the axion field as a classical field and not as an ensemble of particles. Thus, it is not clear if the standard lore of virialization really applies for the collapse of axion density fluctuations.

In the following, we want to address the question of the dynamical collapse of axion miniclusters after they decouple from the Hubble flow in some detail. As initial conditions, we can use our results for the minicluster mass function. Note that this is an ongoing project and the results presented here are only preliminary. A conclusive discussion of the minicluster collapse will be presented elsewhere [140].

V.1. Scalar Cloud under Self-Gravity

We start with describing the localized overdensity of the axion field a, let us call it a scalar cloud, via the action

$$S = \int \mathrm{d}^4x \, \sqrt{-g} \left[-\frac{1}{2} g_{\mu\nu} \partial^\mu a \partial^\nu a - V(a) + \frac{\mathcal{R}}{16\pi G_N} \right] . \tag{V.1}$$

The impact of gravity is included as usual via the Ricci scalar $\mathcal{R}$ [141]. $\mathcal{R}$ depends on the metric $g_{\mu\nu}$ and $G_N = 1/(8\pi M_{\mathrm{Pl}}^2)$ is Newton's constant. Varying the action gives the equation of motions for a as well as $g_{\mu\nu}$. We find

$$\frac{1}{\sqrt{g}} \partial_\mu \left[\sqrt{-g} g^{\mu\nu} \partial_\nu \right] a + V'(a) = 0 \, , \tag{V.2}$$

$$R^{\mu\nu} - \frac{1}{2} g^{\mu\nu} = 8\pi G_N T_a^{\mu\nu} \, , \tag{V.3}$$

which are the Klein-Gordon equation for a scalar field a in a potential $V(a)$ and the Einstein equation sourced by the axion field itself. The Einstein equation will determine the geometry of the spacetime. The stress-energy tensor $T_a^{\mu\nu}$ was already defined in Eq. (III.10). In the harmonic approximation of the axion potential, we recover the Klein-Gordon equation of a free scalar field with mass m. But for studying the collapse of the scalar cloud, we want to include the so far neglected next-to-leading order term in the axion potential, i.e. we use

$$V(a) = m_a^2 f_a^2 \left(1 - \cos \frac{a}{f_a} \right) \simeq \frac{1}{2} m_a^2 a^2 - \frac{1}{4!} \frac{m_a^2}{f_a^2} a^4 \, . \tag{V.4}$$

The second term describes the quartic self-interactions of the axion field. The reason why we include it is that it might become dynamically important during the collapse. We will shortly investigate under what circumstances this could be the case.

Solving the coupled Einstein-Klein-Gordon (EKG) system is a difficult task and can only be done numerically, as was recently the case in the studies presented in Refs. [142–144]. However, we will argue in the following that for describing the gravitational collapse of the axion miniclusters, it should be sufficient to use a non-relativistic approximation of the EKG system.

As already mentioned in the very beginning of Ch. IV, we can estimate the escape velocitiy $v_{\rm esc}$ for the miniclusters given their mass $M_{\rm MC}$ and their size $R_{\rm MC}$. Naively, we have said that axions gravitationally bound in the miniclusters have velocities less than $v_{\rm esc}$. But as it turned out speaking about particles is in fact inconsistent with the axion field being described via a classical scalar. Therefore, we rather say that the classical field should have no modes with wavenumbers greater than $k_{\rm esc}$. For the typical miniclusters $v_{\rm esc} \ll 1$. This implies for the modes k that $k \ll k_{\rm esc} \equiv m v_{\rm esc}$. Hence, instead of treating the axion particles as non-realativistic, we can assume a non-relativistic approximation for the axion field itself.

It is known that a classical real scalar field in the non-relativistic limit can be described via a complex wave function ϕ as [145, 146]

$$a = \frac{1}{\sqrt{2m}} \left(\phi \mathrm{e}^{-\mathrm{i}mt} + \phi^* \mathrm{e}^{\mathrm{i}mt} \right) \tag{V.5}$$

with $\dot{\phi} \ll m\phi$ and $\ddot{\phi} \ll m^2\phi$, such that m is the largest energy scale in the problem. To gain some intuition for the phyiscal meaning of the wave function ϕ, let us consider the 00 component of the stress energy tensor T_a. This is nothing but the energy density ρ_a of the axion field, i.e.

$$T_a^{00} = \rho_a \approx \frac{1}{2}\dot{a}^2 + \frac{1}{2}m^2 a \,, \tag{V.6}$$

where we have neglected the gradient terms. This is in line with the non-relativistic approximation in the sense that we assume a hierarchy $k^2a^2 \ll \dot{a}^2 \sim m^2a^2$. Expressing a via the wave function ϕ and dropping fast oscillating terms, we find:

$$\rho_a = m\phi\phi^* \quad \Leftrightarrow \quad \phi\phi^* = \rho_a/m \equiv n_a \,. \tag{V.7}$$

We see that $|\phi|^2$ might be interpreted as the "number density" n_a of particles with mass m associated with the scalar field a. Again, this interpretation should be taken with a grain of salt. Namely, a justification for describing the actual quantum field $\hat{a}$ with a classical field is that it is in a so-called coherent state, let us call it $|a\rangle$, with a macroscopic particle density [147]. Usually, the assumption is then that the expectation value $\langle a|\hat{a}|a\rangle$ behaves as the classical field a would do. However, it must be noted that the coherent state $|a\rangle$ is not an eigenstate of the number operator, call it $\hat{N}$, and therefore the actual number N of particles making the state $|a\rangle$ is indefinite. Indeed, it has only a precisely defined phase. Hence, the real scalar we describe might be pictured a condensate of an indefinite but large number of axions. At this point, we do not want to go deeper into the interesting discussion of the proper description of the cosmological axion field. For a more in-depth look at this topic see Refs. [148–150]. We will briefly revisit this issue when discussing if quantum effects might become important during the collapse.

Still, for our purposes it turns out that "number density" interpretation of $|\phi|^2$ provides a good physical intuition for some of the important quantities. For example, we can calculate the mass M of a localized scalar cloud in terms of ϕ and we find that

$$M = \int \mathrm{d}^3r \; \rho_a = m \int \mathrm{d}^3r \; |\phi|^2 \,. \tag{V.8}$$

With the identification $|\phi|^2 = n_a$, this simply means that the complete mass M of the scalar cloud is made up of all particles $N_a \equiv \int \mathrm{d}^3r \; n_a$ with mass m.

Besides the non-relativistic approximation of the field, we can simplify the EKG system even further. It turns out that with the typical masses and turnaround radii of the miniclusters, we find for the Newtonian potential Φ_N that $\Phi_N \sim G_N M_{\rm MC}/R_{\rm MC} \ll 1$. Thus, it should be sufficient to consider the weak gravity limit for the minicluster collapse. Here, we can express the metric as [141]

$$g_{00} = -\left(1+2\Phi_N\right), \quad g_{i0} = 0, \quad g_{ij} = \left(1-2\Phi_N\right)\delta_{ij}, \tag{V.9}$$

and $\sqrt{-g} \simeq 1 - 2\Phi_N$.

With this ansatz and the non-relativstic approximation for the field, the action in Eq. (V.1) becomes

$$S = \int d^4x \left[\frac{(\nabla\Phi_N)^2}{8\pi G_N} - m\Phi_N\phi\phi^* + \frac{\mathrm{i}}{2}\left(\dot{\phi}\phi^* - \phi\dot{\phi}^*\right) - \frac{(\nabla\phi)\cdot(\nabla\phi^*)}{2m} + \frac{1}{16 f_a^2}\left(\phi\phi^*\right)^2\right], \tag{V.10}$$

cf. Ref. [116] and App. D for details of the derivation. Then, the equations of motion read

$$\mathrm{i}\partial_t\phi = -\frac{\Delta\phi}{2m} + m\Phi_N\phi + \frac{1}{8f_a^2}\phi^*\phi^2, \tag{V.11}$$

$$\Delta\Phi_N = 4\pi G_N m\phi\phi^*. \tag{V.12}$$

The first equation is of the form of the Gross-Pitaevskii (GP) equation which is best known in condensed matter physics describing Bose-Einstein condensation [151]. The second equation is simply the Poisson equation for the Newtonian potential with the axion energy density as the source.

Note that the first equation has some formal similarities with the quantum mechanical Schrödinger equation. However, in our case it it is in fact a classical field equation. See Ref. [116] for a very clear explanation. Nevertheless, our classical form of the GP equation shares an important property with the Schrödinger equation. Namely, that the absolute value of the wave function $|\phi|^2$ is conserved. With our identification $|\phi|^2 = n_a$, this can be interpreted as the number of particles being conserved, as it should be in the non-relativistic limit.

Still, we can wonder if at some point quantum effects might become dynamically important during the collapse and the description of the actual quantum axion field via its classical analogoue would be no longer valid. But in Ref. [152] it was argued by Dvali et al that the time it takes till the classical field description of the cosmological axion field breaks down is longer than the lifetime of our Universe. This they showed by comparing the timescale of the non-linear interactions in the classical field equations, the so-called classical break-time, with the corresponding timescale in the quantum mechanical equations, the quantum breaktime, see also Ref. [153]. Hence, we can use the result by Dvali et al not only as an a posteriori justification for describing the evolution of the axion miniclusters using the classical field equations, but also it tells us that we do not have to worry about quantum effects becoming dynamically important during the collapse.

The classical Gross-Pitaevskii-Poisson (GPP) system is usually not studied as a dynamical problem but in the context of finding static solutions of the scalar cloud. Such solutions are often called axion stars. These are the eigensolution of the GPP system with a definite eigenenergy E and a time evolution

$$\phi_s(\vec{r},t) = \phi_s(\vec{r})\mathrm{e}^{-\mathrm{i}Et}. \tag{V.13}$$

Recently, there has been an increased interest in finding these types of solutions, see Refs. [116–119] and for a very recent review Ref. [154]. Before turning to the dynamical collapse of the miniclusters, we briefly want to discuss the main features of the axion star solutions. In doing so, we realize that we cannot expect miniclusters to collapse directly into a static axion star configuration.

It is known that there exist two types of eigensolutions for the time-independent GPP system. In Ref. [117], Visinelli et al call them the dilute and the dense axion stars. For the dilute stars, it turns out that gravity dominates over the self-interactions. It can be shown that an approximate relation between the size R_s and the mass M_s of the stable star is of the form

$$R_s \sim \frac{M_{\rm Pl}^2}{m^2 M_s}\,. \tag{V.14}$$

To understand the properties of the axion star solutions and the GPP system a little better, we want to derive this result with a brief, heuristic analysis, adopting the variational method from Ref. [118]. See also Refs. [155, 156] for similar approaches.

Looking at the action $S = \int \mathrm{d}^4x\, \mathcal{L}$ in Eq. (V.10), we can rewrite the Lagrangian via a Legendre transformation as a Hamiltonian with a kinetic, gravitational, and self-interaction part, i.e.

$$H = H_{\rm kin} + H_{\rm grav} + H_{\rm self}\,. \tag{V.15}$$

Assuming spherical symmetry for the wave function ϕ_s and $\phi_s \to 0$ for $r \to \infty$, as it should for a localized configuration, we find

$$H_{\rm kin} = \frac{1}{2m}\int \mathrm{d}^3r\ (\nabla\phi_s)\cdot(\nabla\phi_s^*) = -\frac{4\pi}{2m}\int \mathrm{d}r\ \phi_s \frac{\partial}{\partial r}\left(r^2\frac{\partial}{\partial r}\phi_s^*\right)\,, \tag{V.16}$$

$$H_{\rm grav} = -\frac{1}{2}\int \mathrm{d}^3r\ m\Phi_N\phi_s\phi_s^* = -\frac{4\pi m}{2}\int dr\, r^2\Phi_N|\phi_s|^2\,, \tag{V.17}$$

$$H_{\rm self} = -\int \mathrm{d}^3r\ \frac{1}{16 f_a^2}\,(\phi_s\phi_s^*)^2 = -\frac{4\pi}{16 f_a^2}\int \mathrm{d}r\ r^2|\phi_s|^4\,. \tag{V.18}$$

The idea of the variational method is to guess a form for the wave function ϕ_s in terms of the mass M_s and the size R_s of the star and let one of these act as the variational parameter which should extremize the Hamiltonian [118]. It is convenient to choose R_s as this free parameter.

As an ansatz for ϕ_s, we can take a Gaussian of the form

$$\phi_s(r) = \frac{3^{3/2}}{\pi^{3/4}}\frac{M_s^{1/2}}{m^{1/2}R_s^{3/2}}\exp\left[-\frac{9}{2}\frac{r^2}{R_s^2}\right]\,, \tag{V.19}$$

where the normalization is determined via $M_s = m\int \mathrm{d}^3r|\phi_s|^2$ and we chose R_s as the radius which contains 99.9% of the mass. With this ansatz, the Newtonian potential can be determined directly from the Poisson equation. It turns out that $\Phi_N \simeq -GM_s/R_s$, and we can calculate the Hamiltonian analytically. We find

$$H(R_s) \simeq 0.7\frac{M_s}{m^2R_s^2} - 0.1\frac{M_s^2}{M_{\rm Pl}^2R_s} - \frac{M_s^2}{f_a^2m^2R_s^3}\,. \tag{V.20}$$

Details on the calculation are presented in App. D.

It is obvious that for large stars with $R_sM_s \gg 1$, hence dilute configurations, the self-interaction can be neglected. When extremizing $H(R_s)$ in this limit, we recover the relation between R_s and M_s in Eq. (V.14), namely $R_s \propto 1/M_s$.

Let us also take a look at small configurations with $R_sM_s \ll 1$. Here, we find a linear depenence between mass and size:

$$R_s \sim \frac{M_s}{f_a^2}\,. \tag{V.21}$$

This is the dense axion star branch. However, as it was noted in Ref. [117], the case of dense stars must in fact be treated relativistically since it turns out that these configurations have only a very limited lifetime and quickly evaporate into relativistic axions. Therefore, these are only quasi-stable solutions. In fact, the dense star configurations might be indentified with the axitons observed in the numerical simulations in Refs. [108, 122–124].

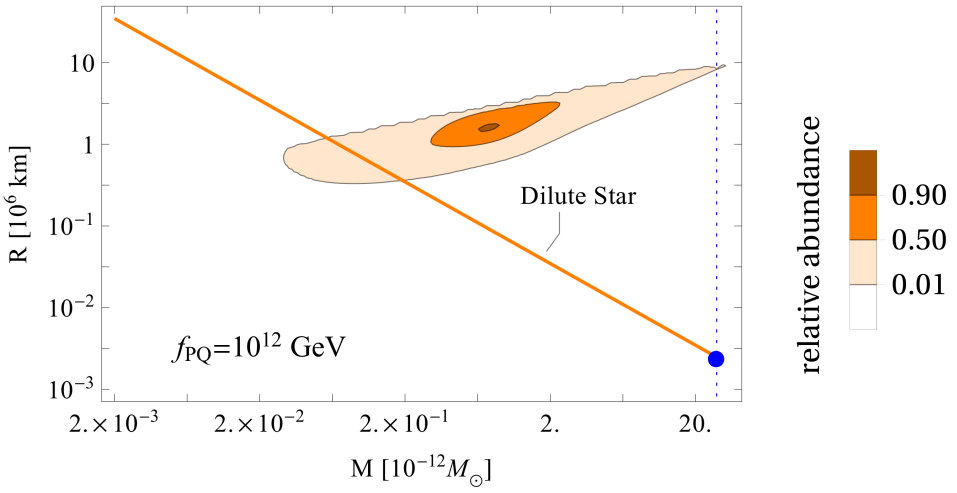

Figure V.1.: Minicluster Distribution and Dilute Axion Stars. The orange line indicates the dilute axion star solutions. The colored area shows our result for the distribution of miniclusters as function of turnaround radius and mass. The Peccei-Quinn breaking scale is set to $f_a = 10^{12}$ GeV. For masses beyond the blue dotted line, there exist no static axion star solutions.

Another interesting property of the static solutions of the GPP system is that there exists an upper mass for the stars. Above that, no stable or quasi-stable static solutions can be found. We can understand this, by trying to extremize the full Hamiltonian in Eq. (V.20) in terms of R_s. Namely, we find a quadratic equation which solutions are real only if

$$M_s < \frac{M_{\rm Pl} f_a}{m^2} \,. \tag{V.22}$$

This limits the maximum mass for an axion star for a given axion mass m and breaking scale f_a. However, we want to stress that this does not immediately imply that there cannot exist stable axion clouds with masses larger than this. For example, in the case of a QCD axion with the Peccei-Quinn breaking scale $f_a \sim 10^{12}$ GeV and a mass $m_a \sim \mu$eV, the maximum mass for axion stars is about $10^{-11} M_\odot$. However, if the QCD axion is supposed to be the DM it should also explain the DM halos around galaxies. Taking for example the Milky Way, this means halo masses of about $10^{12} M_\odot$ [157]. Without going into the details of halo formation in the case of axion DM, which is far beyond the reach of the present work, we simply want to point out that the maximum axion star mass only limits the static configurations. It should not be mistaken with a limit on other kinds of stable solution for the axion cloud bound under its self-gravitiy. These might be equilibrium solutions of the GPP system which are not characterized by a static eigenenergy. We will shortly define more precisely what we mean with static and equilibrium configurations.

But before doing so, we compare in Fig. V.1 our results for the distribution of axion miniclusters with the dilute star solutions for the QCD axion with a Peccei-Quinn breaking scale $f_a \sim 10^{12}$ GeV. We see that the miniclusters sit, for the most part, well above the axion star branch. It can be shown that the dilute branch acts as an attractor for configurations which are only slightly perturbed [118]. But in our case, it is clear that the miniclusters cannot be treated as such small perturbations. Therefore, we cannot expect a direct collapse into an axion star. Rather, we have to study the collapse as a dynamical problem to see if they might reach an equilibrium before even getting close to the axion star branch.

Another important observation from Fig. V.1 is that the miniclusters are in an area where $R_{\rm MC} M_{\rm MC} \gg 1$. Therefore, it is a well motivated working-assumption that gravity dominates the dynamics and the self-interactions should play a minor role. Since even if the miniclusters

would collapse all the way down into the dilute star configuration we have learned that even there self-interactions can be neglected. Doing so, simplifies the equations of motion of the scalar cloud drastically. We find

$$\mathrm{i}\partial_t\phi = -\frac{\Delta\phi}{2m} + m\Phi_N\phi\,, \tag{V.23}$$

$$\Delta\Phi_N = 4\pi G_N m\phi\phi^*\,, \tag{V.24}$$

which is known as the Schrödinger-Poisson (SP) system.

V.2. Schrödinger-Poisson System for Minicluster Collapse

It exists plenty of literature on solutions for the SP system, for the static [158–161], as well as the dynamical problem [162–167]. But since it is a nonlinear system, studying the dynamics of a certain initial configuration is only possible by a numerical simulation. This means that, if we want to learn about the fate of our axion miniclusters it is difficult to use known results. We rather have to set up our own calculations. The details of the actual numerics are presented in App. E. At this point, we want to make some general remarks on the SP system and discuss it rather from an analytical side. At the end of this section, we present first results of a simulation of a scalar cloud collapse and argue that the findings can be generalized to the case of the minicluster evolution.

Initial Wave Function and Definitions

Let us start by considering the initial conditions for the SP system. First, we have to define an initial wave function ϕ_i. It should describe the minicluster at the time it starts to collapse. A natural choice is a spherically symmetric Gaussian, as already used in Eq. (V.19). This means we assume

$$\phi_i(r) = \frac{3^{3/2}}{\pi^{3/4}}\frac{M_0^{1/2}}{m^{1/2}R_0^{3/2}}\exp\left[-\frac{9}{2}\frac{r^2}{R_0^2}\right]\,, \tag{V.25}$$

with M_0 and R_0 being the initial mass and size. But we have to keep in mind that the configuration we want to describe should already be gravitationally bound. Since this is precisely how we have defined the minicluster at the time of turnaround, namely as an overdensity which has decoupled from the Hubble flow due to its own gravity. Thus, we have to make sure that ϕ_i has no modes with $k > mv_{\mathrm{esc}}$, which would correspond to parts which are not gravitationally bound. Fourier transforming the Gaussian ansatz yields:

$$\phi_i(k) = \frac{1}{\pi^{3/4}3^{1/2}}\frac{M_0^{1/2}R_0^{3/2}}{m^{1/2}}\exp\left[-\frac{1}{2}\frac{k^2R_0^2}{9}\right]\,. \tag{V.26}$$

This means that 99.9% of all modes are smaller than $k_{99} \equiv 9/R_0$. It turns out that demanding $k_{99} < mv_{\mathrm{esc}}$ leads to the constraint $1 \ll G_N m^2 R_0 M_0$ on the initial mass M_0 and size R_0 for a given axion mass m. We find that this inequality is fulfilled for the vast majority of minicluster configurations in our distributions. For example, if we use $M_0 = 10^{-12}M_\odot$, $R_0 = 10^6$ km, and $m = 10^{-6}$ eV, we have $Gm^2R_0M_0 \sim 10^5$ which is indeed much bigger than one. Therefore, we conclude that with the Gaussian initial wave function in Eq. (V.25) we can describe a gravitationally bound minicluster.

However, it should be noted that this does not mean that the configuration cannot lose mass during the collapse, for example via some violent gravitational cooling [162, 163]. Only the initial configuration is gravitaionally bound. During the collpase, parts of the cloud might

become accelerated to velocities faster than $v_{\rm esc}$ and be ejected. We will see in the results of our simulations that this can be indeed the case for the minicluster collapse.

Another important point we have to address is the phase of the initial wave function. So far, without further motivation, we have assumed the wave function to be real. But in general it might as well be complex. Recall that the mass M_0 only fixes the absolute value of the wave function, via $M_0 = m \int \mathrm{d}^3 r \ |\phi|^2$, it does not give any information about the phase of the wave function. This means we have to make some physically motivated assumptions to fix it for our initial configuration.

Before doing so, let us try to develop an understanding for the physical meaning of the phase. For that, we take a look at the continuity equation

$$\partial_t |\phi|^2 + \nabla \cdot \mathbf{j} = 0 \,, \tag{V.27}$$

where the current $\mathbf{j}$ is defnied as

$$\mathbf{j} = \frac{1}{2m\mathrm{i}} \left(\phi^* \nabla \phi - \phi \nabla \phi^* \right) . \tag{V.28}$$

For the minicluster at the exact time of turnaround, we can expect that $\partial_t |\phi_i|^2 = \partial_t n_a = 0$, i.e. the "particle number" inside any given volume should not change. In an hydrodynamic interpretation of the continuity equation, this means that the minicluster behaves as an incompressible fluid. This implies for the current

$$\nabla \cdot \mathbf{j} = 0 \,. \tag{V.29}$$

If we write the wave function as

$$\phi_i = \alpha \mathrm{e}^{\mathrm{i}\beta} \,, \tag{V.30}$$

the current becomes

$$\mathbf{j} = \alpha^2 \frac{\nabla \beta}{m} = n_a \mathbf{u} \,. \tag{V.31}$$

In the second equality we used $\alpha^2 = |\phi_i|^2 = n_a$ and defined $\mathbf{u} \equiv \nabla\beta/m$. The interpretation of $\mathbf{u}$ is that of a bulk velocity with which the particle density flows.

For an incompressible fluid we have

$$\nabla \mathbf{j} = 0 \quad \Rightarrow \ \nabla \left(n_a \mathbf{u} \right) \tag{V.32}$$

$$\Leftrightarrow \quad \frac{1}{m} \left(2\alpha \nabla\alpha \nabla\beta + \alpha^2 \Delta\beta \right) = 0 \,, \tag{V.33}$$

The last equality can be solved if $\nabla\beta = 0$ and therefore $\beta = const$ for the whole wave function. This means we are free to choose $\beta = 0$ for our initial wave function and therefore make it real, without loss of generality. The physical interpretation is that at the beginning of the collapse the initial bulk velocity is set to zero.

The insights on the meaning of the phase of the wave function can be used to make some important definitions to fix the nomenclature for the subsequent discussions. For later reference they are also summarized in Tab. V.1. First, we define a scalar cloud to be in a "coherent configuration" when the phase of its wave function is the same everywhere. This holds for the miniclusters at the time of turnaround, as well as for the static axion star solutions. For example, Davidson and Schwetz found in Ref. [116] that the ground state of a stable axion star can be described by a real wave function. This implies that we can understand the axion star configuration as an incompressible fluid, which makes a lot of sense since it is already a static eigensolution and therefore it cannot or does not have to be further compressed to minimize its energy. On the other hand, a "virialized configuration" might be characterized as an equilibrium state that has a non-trivial phase, i.e. $\nabla\beta \neq 0$ over the size of the object. If on top, the actual

Static Solution	The time evolution of the wave function $\phi(\vec{r},t)$ is entirely described by $\phi(\vec{r},t) = \phi(\vec{r})\exp[-\mathrm{i}Et]$ and E is a time-independent energy.
Equlibrium Solution	Equilibrium for a given configuration is reached if the ratio of kinetic and potential energy stays constant when averaged over some long period of time. This implies that the size of the configuartion can still change, for example it can oscillate.
Coherent Configuration	The wave function of a coherent configuration has the same phase over its complete size. This holds for axion stars and the minicluster at the time of turnaround.
Virialized Configuration	We call a configuration virialized if it is in equilibrium and its wave function has a non-trivial phase in the sense that it is not correlated over the whole object.

Table V.1.: Definitions on the Nomenclature for the Discussion of the Minicluster Collapse.

phase of the wave function is uncorrelated on scales larger than some characterstic length scale, we can understand a virialized configuration, as opposed to a coherent one, as a state made up of several independently-moving wave packages. Note that this picture is in line with a virialized cloud of particles where the particles move independently of each other with some virial velocity. We should expect something similar for the virialized classical field. In Tab. V.1 we also add our definitions for the static and the equilibrium configurations.

It turns out that the two-point correlator $\zeta(r)$ of the phase of the scalar cloud wave function is an appropriate quantitiy to determine whether a configuration is coherent or not. For a spherical symmetric configuration, we define it as

$$\zeta(r) = \langle\beta(r_1)\beta(r_1+r)\rangle = \frac{1}{R}\int_0^R \mathrm{d}r_1\ \beta(r_1)\beta(r_1+r)\,, \tag{V.34}$$

with R being some scale larger than the size of the cloud. Note that for a coherent configuration we should have $\zeta = const$, since the phase is the same everywhere. On the other hand, for a non-coherent configuration, where the phase might only be correlated on small scales, $\zeta(r)$ should give us information precisely on that characteristic correlation length, call it L. In that case, we can expect $\zeta(r)$ to be nonzero only for $r < L$, and than drop quickly to zero for $r > L$. Equipped with the appropriate initial conditions and tools to analyze the scalar cloud during the collapse, we can now turn to discussing the actual equations governing the dynamics.

Schrödinger Equation and the Problem of Scales

The Schrödinger equation has an inherent scale, namely the mass m, which leads to a characteristic size and time $\sim 1/m$ for the evolution of the wave function. Hence, if we want to make the SP system dimensionless we can start by introducing $x = mr$ and $\tau = mt$ as the new independent dimensionless variables. But actually counting the dimensions in the SP system, we find besides $[r] = [t] = -1$ and $[\Phi_N] = 0$ that $[\phi] = 3/2$. Recall that $m|\phi|^2$ is the energy density and therefore the dimension of the wave function is clear. Further, we have $[G_N] = -2$ and $[m] = 1$. This means for writing the SP system in a dimensionless form, we also have to rescale the wave funtion. We find that with the redefinitions

$$\tau = mt\,, \quad x = mr\,, \quad \tilde{\phi} = \sqrt{\frac{4\pi G_N}{m}}\phi\,, \quad \tilde{\Phi}_N = \Phi_N\,, \tag{V.35}$$

the SP system can be brought into the dimensionless form

$$\mathrm{i}\partial_\tau \tilde{\phi} = -\frac{1}{2x}\frac{\partial^2}{\partial x^2}\tilde{\phi} + \tilde{\Phi}_N \tilde{\phi}\,, \tag{V.36}$$

$$\frac{1}{x}\frac{\partial^2}{\partial x^2}\tilde{\Phi}_N = 4\pi \tilde{\phi}\tilde{\phi}^*\,. \tag{V.37}$$

Interestingly, it turns out that the SP system has a remaining degree of freedom which allows us to redefine the dimensionless quantities with a real parameter λ. To be concrete this means that if we have found a solution $(\tilde{\phi}, \tilde{\Phi}_N)$, then a whole family of solutions is given via the rescaling

$$\left(\tau, x, \tilde{\phi}, \tilde{\Phi}_N\right) \longrightarrow \left(\lambda\tau, \lambda^{1/2}x, \lambda^{-1}\tilde{\phi}, \lambda^{-1}\tilde{\Phi}_N\right)\,. \tag{V.38}$$

A similar behavior was found in, for example, Refs. [164, 166].

However, for the case of the miniclusters the inherent scale of the SP system poses some severe problems which, as it turns out, also cannot be overcome with the help of the freedom of rescaling. The reason for this is the huge difference between the characteristic length scale of the Schrödinger equation $1/m$ and the size of the minicluster. Take for example the axion mass $m_a \sim \mu$eV, then the characteristic length scale of the Schrödinger equation is $\sim$ m. On the other hand, the miniclusters at the time of turnaround have a size of about 10^6 km. This is a whopping difference of nine orders of magnitude. Obviously, this huge difference is prohibitive for any attempt of a numerical simulation. As we have already mentioned, despite all our efforts, we have not been able to solve this problem even using the freedom of rescaling.

A possible way out of this misery could be to rewrite the Schrödinger equation in terms of scale-free fluid equations. This can be done via a Madelung transformation [168]. Unfortunately, we will shortly see that this also leads to some difficulties, again of numerical nature.

Fluid Description

Since the seminal work by Madelung in 1927 it is known that the Schrödinger equation can be interpreted in terms of hydrodynamic quantities [168]. This is also true for the combined system of Poisson and Schrödinger equation. We can show this by expressing the wave function as $\phi = \alpha \exp[\mathrm{i}\beta]$ with α and β being real functions. Doing so, the SP system can be written as

$$\nabla(\rho\mathbf{u}) + \partial_t \rho = 0\,, \tag{V.39}$$

$$\partial_t \mathbf{u} + (\mathbf{u}\cdot\nabla)\,\mathbf{u} = -\nabla\left(\Phi_N - \frac{\Delta\sqrt{\rho}}{2m^2\sqrt{\rho}}\right)\,, \tag{V.40}$$

$$\Delta\Phi_N = 4\pi G\rho\,, \tag{V.41}$$

where again $\rho = m|\alpha|^2$ is the density and $\mathbf{u} = \nabla\beta/m$ can be indentified with a bulk velocity. See App. F for details on the derivation.

The first two equations are of a similar form as the Euler and the continuity equation of a perfect fluid, the third is again the Poisson equation for the Newtonian potential. Therefore, this system of equations is known as the Euler-Poisson (EP) system.

On the right-hand side of the second equation, we can identify the inward pressure due to the Newtonian potential and the outward directed so-called quantum pressure $P_Q \propto \Delta\sqrt{\rho}/\sqrt{\rho}$. The latter forbids a collapse into a singularity. However, it is also this term which causes trouble in the fluid picture. Namely, P_Q becomes divergent whenever the density vanishes locally which is identified as the shell-crossing. In contrast to the SP system, the EP system is therefore not valid at all times but only until the first shell-crossing occurs [169]. The shell-crossing is an effect which reveals the true underlying wave nature of the scalar field. It can be understood as an interference effect. If we picture the wave function like an onion made up of different shells, then during the collapse it can happen that a shell falling inwards interferes with another shell traveling outwards. This leads to nods or zeros in the wave function and therefore to $\rho \to 0$.

Nevertheless, we find that this shortcoming of the fluid picture can be overcome in the case of extreme dilute configurations. Namely, approximating the density via $\rho \sim M/R^3$ and plugging this into Eq. (V.40), we see that for very large configurations we can in fact neglect the quantum pressure term against the gravity contribution. Doing so, the EP system simply describes the classical evolution of a fluid under self-gravity. In the cosmological context, this form of the EP system without quantum pressure is ususally used to describe the evolution of fluctuations in the DM fluid. If the overdensities are linear, the equations can be solved analytically [79]. Otherwise, they must be studied using, for example, N-body simulations [135]. This means the fluid is expressed via a large ensemble of particles. Interestingly, it is precisely the equivalence between the SP and EP system that is sometimes used to bypass N-body simulations and describe the collapse process rather via wave functions [170, 171]. This may already indicate that it is not necessarily easier to solve the EP system instead of the SP system.

However, we can try to combine the advantages of both, fluid and wave function description, to conclusively describe the minicluster collapse. Namely, a possible approach could be the following. To circumvent the problem of scales in the Schrödinger equation, we could start with describing the initial configuration rather via the EP system. But since it is very dilute it is well motivated to neglect the quantum pressure term. Doing so, we can expect a more or less simple inward collapse reducing the size of the initial configuration. But as soon as the quantum pressure term becomes important, we should switch back to the description via the SP system to capture the true wave nature of the problem. Note that a similar procedure is used by Niemeyer et al in Ref. [121] to study the halo formation of ultralight axions in numerical simulations.

However, it turns out that for our purposes, even though the EP system is scale-free, in the sense that the characteristic scale m was absorbed in the definition of the bulk velocity $\mathbf{u}$, it is far from trivial to solve it numerically. As pointed out before, advanced numerical methods like N-body simulations are needed to resolve the nonlinearity in the evolution equation of $\mathbf{u}$ even when neglecting the quantum pressure. Setting up a full-fledged N-body code goes beyond what we actually want to achieve. Recall that the initial question was to find out how or if a minicluster collapses into a virialized equilibrium configuration.

So, instead of using a combined approach of EP and SP system description, we rather try to answer this question by using as a toy model replacement for the actual minicluster. The setup of the toy model should be such that it reflects the important properties of the miniclusters but still can be studied via the SP system. We will shortly discuss what this means in detail. The idea is then that the result of a toy model simulation can be generalized to understand also the evolution of the miniclusters.

Toy Model

An appropriate toy model for an axion minicluster should describe a gravitationally bound and very dilute scalar cloud. We have already found that both of these characteristics are encoded in the inequality

$$M_0 R_0 m^2 G_N \gg 1\,. \tag{V.42}$$

Let us see how this constraint translates into the dimensionless SP system. Recall that in the spherical symmetric case the mass M_0 is determined via

$$M_0 = 4\pi m \int \mathrm{d}r\; r^2 |\phi|^2 \tag{V.43}$$

and therefore it fixes the normalization of the initial wave function. Expressing this relation via the dimensionless quantities x and $\tilde{\phi}$, as defined above, we find that

$$\tilde{M}_0 \equiv M_0 m G_N \tag{V.44}$$

is a useful dimensionless analogue to the initial mass M_0. Then, the initial dimensionless wave function is given by

$$\tilde{\phi}_i = \frac{\tilde{M}_0^{1/2}}{\pi^{3/4} X^{3/2}} \exp\left[-\frac{x^2}{2X^2}\right], \tag{V.45}$$

where we have defined the dimensionless length X via

$$X = \frac{R_0 m}{3}, \tag{V.46}$$

with R_0 being the initial size of the cloud.

With the definitions for X and $\tilde{M}_0$ the inequality in Eq. (V.42) can be rewritten as

$$X\tilde{M}_0 \gg 1. \tag{V.47}$$

This means, if we want to adequately describe the situation of the minicluster via a toy model characterized by $\tilde{M}_0$ and X, we should choose X and M such that $X\tilde{M}_0 \gg 1$.

But this is not the only requirement we have on our parameters. In fact, equally important is that $X \gg 1$ meaning that the initial configuration covers many times the characteristic length scale of the Schrödinger equation. Recall that in the actual minicluster case we speak of nine orders of magnitudes.

On the other hand, translating typical minicluster values $M_0 = 10^{-12} M_\odot$ and $m = 1\ \mu$eV, to $\tilde{M}_0$ we have $M_0 m G_N \sim 10^{-4}$ which implies that we should not set $\tilde{M}$ too large. Hence, we conclude that a good toy model for the minicluster should have $X \gg 1$, $\tilde{M}_0 \ll 1$, and $X\tilde{M}_0 \gg 1$. Still, it should circumvent the problem of scales, i.e. X cannot and should not be chosen arbitrarily large.

When setting up toy models fulfilling all these requirements, we find in our numerical simulations that the larger we choose X compared to $\tilde{M}_0$, the longer the simulations need to show any interesting effects. In fact, if $X_0 \ggg \tilde{M}_0$, basically nothing happens for a very long time. But this has an interesting physical interpretation, as we will see in the following. Namely, when $X \ggg \tilde{M}$, this simply means that the gravitational potential is very small, i.e. $\Phi_N \ll 1$ as it should for weak gravity and as it is the case of the miniclusters. So far so good. However, a very weak gravitational potential has profound consequences for the evolution of the wave function. This we can understand when looking at the Schrödinger equation in Eq. (V.23). For the very dilute configurations we are considering, we can neglect the kinetic energy compared to gravitational potential, at least for the initial configuration. Such that Eq. (V.23) simply becomes

$$\mathrm{i}\partial_t \phi \simeq -m\Phi_N \phi. \tag{V.48}$$

This should give us a crude estimate on the initial evolution of ϕ. Using again the ansatz $\phi = \alpha \exp[\mathrm{i}\beta]$ for the wave function, we find that $\alpha = const$ and for the phase we have

$$\dot{\beta} = m\Phi_N \quad \Leftrightarrow \quad \beta(t) = \Phi_N m t, \tag{V.49}$$

where we chose $\beta(t = t_i) = 0$. Thus, it takes the time $T = (\Phi_N m)^{-1}$, or in terms of our dimensionless coordinate $T_\tau = \Phi_N^{-1}$, till the phase starts to significantly differ from its initial value. We note that this time might also be identified with the onset of the collapse. This is because we can relate β to the current $\mathbf{j} \propto \nabla\beta$ and this means only if $\nabla\beta$ becomes nonzero, a current $\mathbf{j}$ develops and parts of the initial configuration can start to collapse. After that, the evolution of the phase will make the wave function start to oscillate and neglecting the kinetic terms is no longer a good assumption. Hence, our result in Eq. (V.49) must be understood as valid only at first moments of the evolution of the wave function. However, it does not only tell us that if $\Phi_N \lll 1$, it will take very long $\propto \Phi_N^{-1}$ till we see the phase and therefore

the wave function start to evolve, but also it gives us the very general result that every dilute configuration with $\beta = const$ which is not yet an eigenstate of the SP system, will eventually develop a non-trivial phase and starts to collapse, however long this may take. Note that very long in terms of the dimensionless $\tau = mt$, does not directly imply long in terms of physical time.

Hence, we conclude from this discussion on the properties of the toy model two important things. First, we cannot choose the parameters X and $\tilde{M}$ in a way that Φ_N is arbitrarily small. Otherwise, our simulations will take too long. Second, we have learned that we should be able to generalize the outcome of a toy model with only mild choices for X and $\tilde{M}_0$, meaning especially that $\tilde{M}_0$ does not need to be extremely small, to more extreme configurations like the actual axion miniclusters. Again, the reason for this is that for the latter it might simply take longer to start to collapse but as soon as they do so, the behavior should be similar to that of the toy model.

Preliminary Results and Discussion

In the following, we present and discuss the results of a simulation of the SP system with the numerical methods described in App. E. As our setup for the initial wave function we choose

$$\tilde{M} = 15 \quad \text{and} \quad X = 20\,. \tag{V.50}$$

These values are of course much different than what we would expect for the miniclusters. However, they should fulfill the requirements for an appropriate toy model, we have found above. Namely, it has a weak gravitational potential $\tilde{M}/X < 1$ and still it holds that the gravitational energy dominates the kinetic energy, i.e. $X\tilde{M} > 1$. The mass however is extremely different than that of a minicluster. But recall this just means that that the collapse will start earlier in our simulations. In fact, it turns out that with this values for X and $\tilde{M}$ we observe that the cloud seems to approach an equilibrium state in a reasonable computation time.

In our simulation, the spatial domain has the size $X_N = 150$, i.e. 7.5 times larger than the initial cloud, and is divided 600 grid-points. We run our simulations till $T = 600$ with 2400 timesteps. Note that this results in a resolution $\Delta x = \Delta\tau = 0.25$. For more detailed studies, a finer grid should be used to reduce the numerical errors. However, to get a first impression for the scalar cloud collapse, this should be good enough for our needs. We have also checked that with this setup we have a good numerical stability.

At the very end of this section, in Fig. V.6, we show snapshots of the evolution of the rescaled wave function $u = r\phi$. However, we strongly recommend taking a look at a movie of the simulation which can be found here [172]. Figure V.2 shows a projection of the evolution of the absolute value $|u|$ in the $r - t$ plane, which also gives a nice picture for the dynamics of the scalar cloud collapse.

Let us summarize some of the most important observations of our simulation. It seems that in a first period, up to $\tau \sim 100$, the absolute value of the rescaled wave function stays almost constant. However, the real and imaginary part start to show an oscillatory behavior already very early. This is in line with Φ_N being quite sizeable for the configuration we choose, cf. our discussion above. Around $\tau \sim 150 - 200$ some drastic events happen and we observe a rapid infall of parts of the wave. After that, the configuration starts to develop a sharp peak close to its center. This is also the time where the density develops its first zero, which corresponds to the first shell-crossing. Then it seems that parts of the wave which have been accelerated during the infall are ejected and escape the gravitational potential. Note that to avoid unphysical reflections of the outwards travelling waves, we have implemented absorbing boundary conditions. Details on this can be found in App. E. Still, it looks like some parts of the ejected waves slow down and turn around to the center, leading to another period of infall. At times $\tau > 300$, the configuration seems settled and we only observe some oscillations of the peak close to zero.

To support these observations, we take a look at the evolution of the current $\mathbf{j}$ which was defined in Eq. (V.28). Recall that $\mathbf{j}$ tells us how the particle density flows. In our spherically

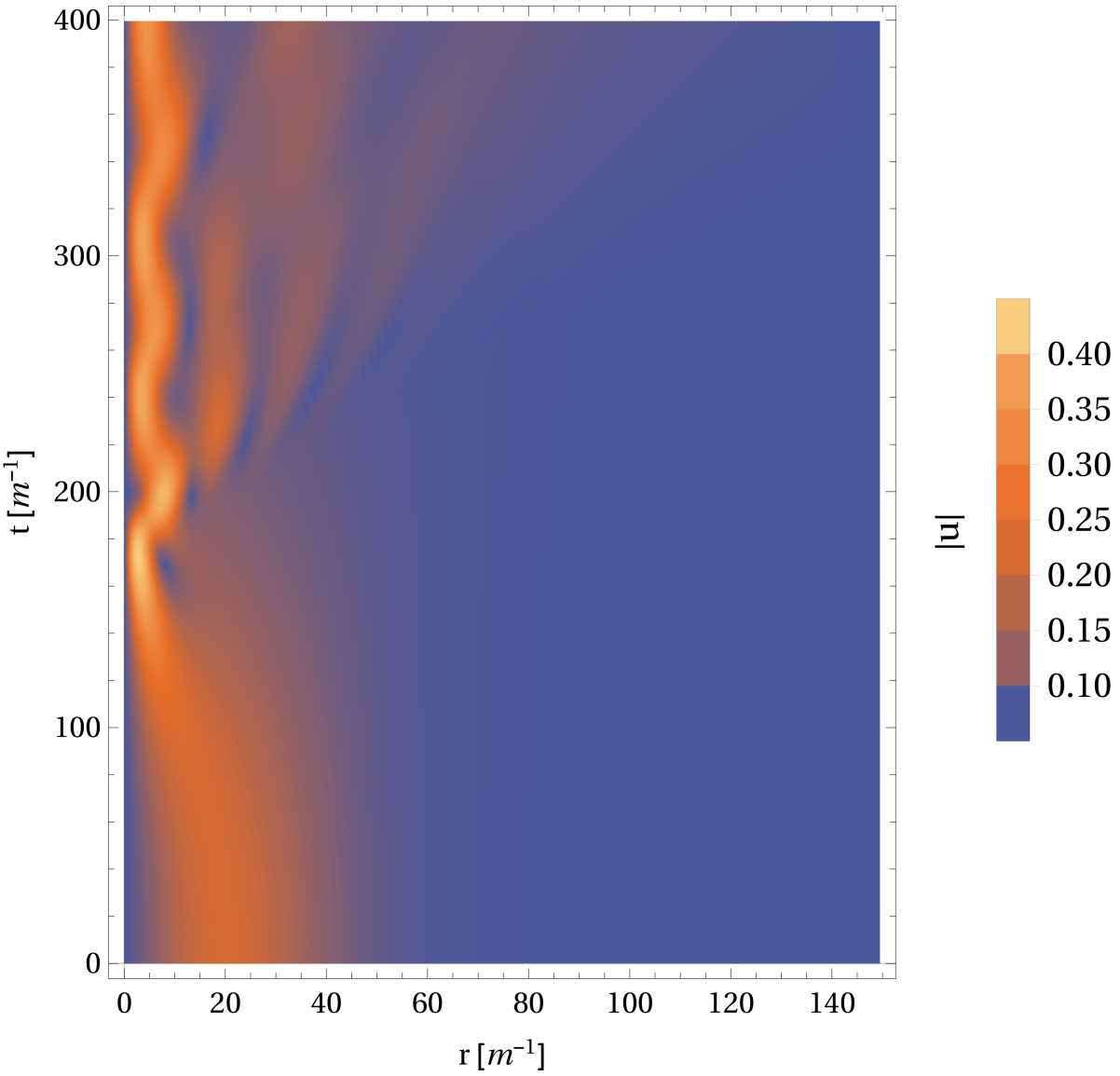

Figure V.2.: Evolution of a Scalar Cloud under Self-Gravity. We show the evolution of the absolute value $|u|$ of the rescaled wave function $u = r\phi$ in the $r - t$ plane. Time as well as size are given in terms of the inverse scalar field mass m. A detailed discussion of this plot can be found in the text.

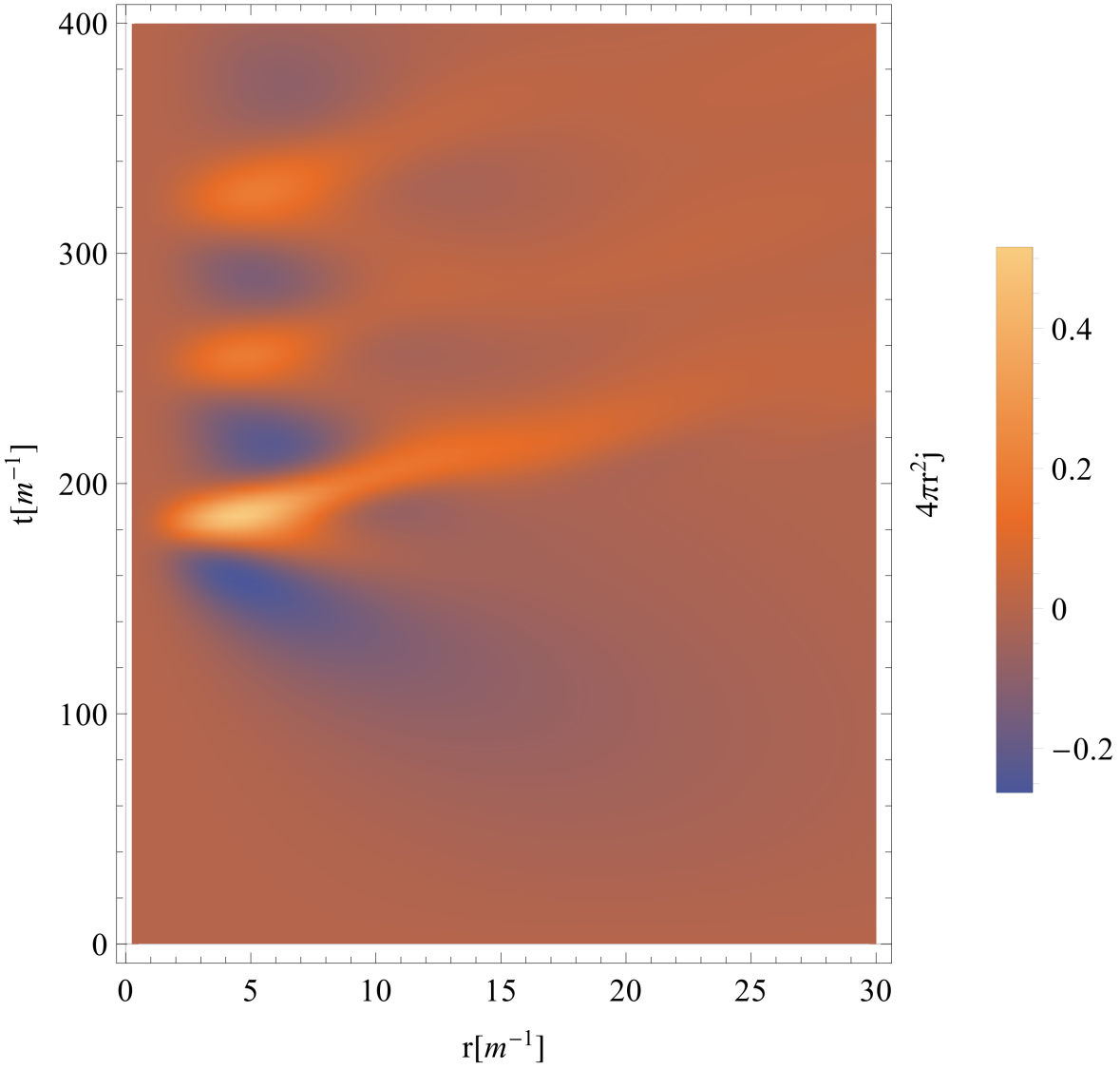

Figure V.3.: Evolution of the Current during the Scalar Cloud Collapse. The quantity $4\pi r^2 j$ gives to the particle current through the surface of a sphere with radius r, see Eq. (V.28) for the definition of j. Negative values indicate an infall of matter and positive value to an ejection. In this plot, we show the projection of the rescaled particle current in the $r - t$ plane corresponding to the evolution of the wavefunction shown in Fig. V.2. Note that this is a zoom-in into the range from $x = 0 \ldots 30$. Time as well as radius are given in terms of the inverse scalar field mass m.

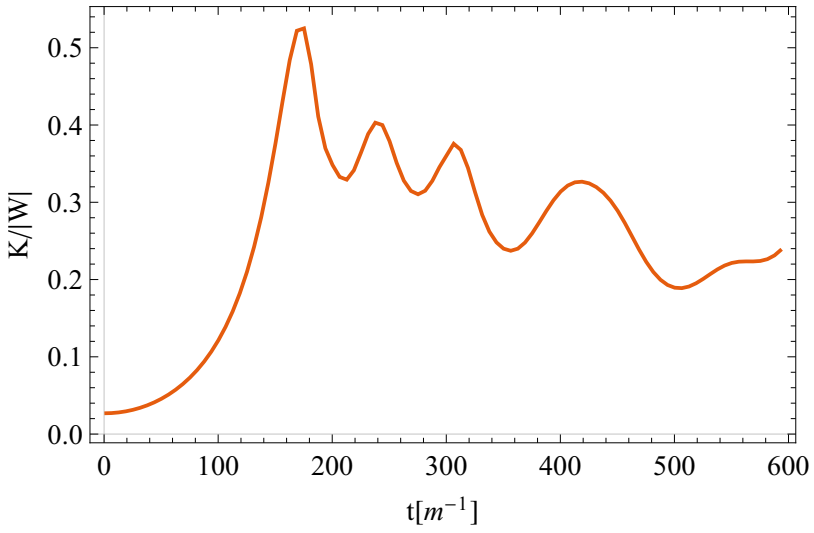

Figure V.4.: Ratio of Kinetic to Potential Energy during the Scalar Cloud Collapse. For the initial configuration we have $K/|W| \ll 1$ since the potential energy dominates over the kinetic energy. In the first moments of our simulation the ratio does not change much. But as soon as the first shell-crossing occurs, a lot of kinetic energy is gained and $K/|W|$ becomes larger. Then, the ratio starts oscillates back and forth around an almost constant value.

symmetrics case $\mathbf{j} = j\hat{e}_r$ and negative values correspond to an infall towards the center, whereas positive j indicate an ejection of material. For our purposes it turns out to be useful to look at the rescaled current $4\pi r^2 j$ which gives the current through the surface of sphere with radius r. We present snapshots of the simulation in Fig. V.7, at the end of this section. A movie of the evolution of the current $4\pi r^2 j$ can be found here [173]. In Fig. V.3 we show a projection of the evolution of $4\pi r^2 j$ in the $r - t$ plane.

We clearly see that in the beginning of our simulation, a negative current builds up at the outward boundary of the configuration. This corresponds to parts of the wave starting to collapse. The current grows further and further, till at a sudden point it switches its sign. This is precisely the time of the first shell-crossing. It also underlines our observation from before that the first collapse is followed by an explosive ejection of matter. After the first phase of infall and ejection, we see some smaller eruptions, indicated by the oscillation of j. This we can again understand as the crossing between shells moving in different directions. Far away from the center, we see a small positive current travel towards infinity. This corresponds to the ejected material.

To see if the configuartion approaches an equilibrium according to our definition in Tab. V.1, we also calculate the ratio of the kinetic energy K and the potential energy W with Eq. (V.16) and (V.17). In terms of the dimensionless variable x and the dimensionless wave function $\tilde{\phi}$, these become

$$K = \frac{1}{2mG_N} \int \mathrm{d}x \; x^2 \left(\frac{\partial \tilde{\phi}}{\partial x}\right) \left(\frac{\partial \tilde{\phi}^*}{\partial x}\right) . \tag{V.51}$$

for the kintetic energy and

$$W = -\frac{1}{2mG_N} \int \mathrm{d}x \; x^2 \Phi_N \tilde{\phi}\tilde{\phi}^* \tag{V.52}$$

for the potential.

The evolution of $K/|W|$ is given in Fig. V.4. Per construction, the potential energy is larger than the kinetic for the initial configuration. We see that ratio stays almost constant, as long

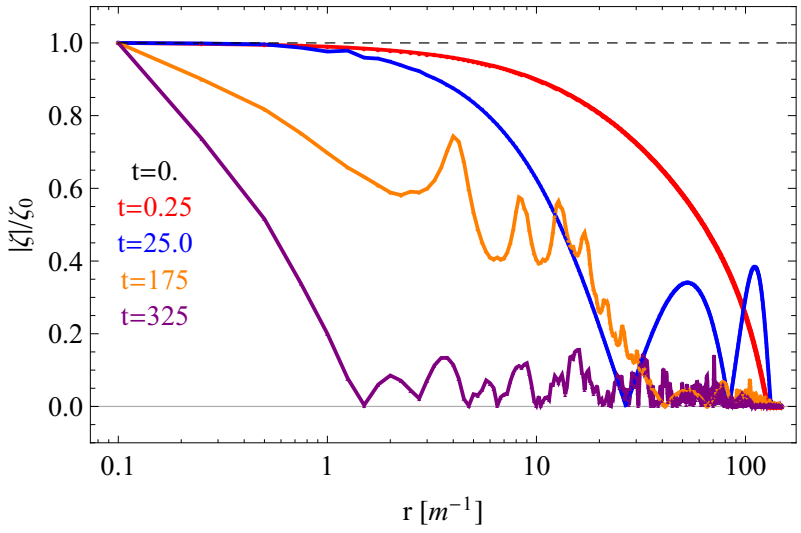

Figure V.5.: Correlation of the Phase in the Scalar Cloud Collapse. The quantity ζ measures the correlation of the phase of the wave function and it is defined in Eq. (V.34). At the beginning, at $t = 0$, the phase of the initial wave function is fully correlated per definition. But soon after we start evolving, it starts to decohere and the phase becomes uncorrelated on scalers larger than $\sim 1/m$. At later times, interference patterns in the collapse due to the wave nature of the scalar field emerge. This leaves its impact in oscillations in the correlator.

the density is almost unchanged, i.e. till $\tau \sim 100$. But as soon as the collapse happens at $\tau \sim 150 - 200$, this suddenly changes. This means that kinetic energy is gained during the period of infall, and the potential energy becomes smaller. After the first infall, we see that the ratio oscillates back and forth with a smaller and smaller amplitude. It seems that $K/|W|$ tends towards a constant value $0.3 - 0.2$ at late times. This would speak for reaching an equilibrium as we have defined it in Tab. V.1. However, to be sure about that a longer simulation time is needed. Nevertheless, it is interesting that the configuration seems to approach a ratio different than $K/|W| \sim 0.5$, which we would expect for a potential $W \propto 1/r$. A ratio $K/|W| < 0.5$ might indicate that the potential is somewhat shallower than the simple $1/r$ behavior.

To learn if the configuration does not only evolve towards an equilibrium but also virializes, we study the evolution of the correlator $\zeta(r)$ of the phase of the wave function, as defined in Eq. (V.34). For better comparison of the correlation at different times, it is useful to normalize it to the value at zero displacement $\zeta_0 \equiv \zeta(r = 0)$. The evolution of $|\zeta(r)|/\zeta_0$ is shown in Fig. V.5. For $t = 0$, when we begin our simulations, $\zeta = 1$ per definition. Immediately after we start evolving, the phase becomes uncorrelated for large displacement, implying that the correlation length becomes smaller till it seems to settle at a length $\sim 1/m$. However, we still observe some long range oscillations in the correlation function. We assign this to an effect of the actual wave nature of the scalar field. Namely, in Fig. V.6 we observe some interference patterns in the late stages of the simulation which might cause this long range correlations in the phase.

Based on our observations of the evolution of $\zeta(r)$ and $K/|W|$, we are tempted to conclude that the scalar cloud we have considered in our simulation indeed collapses into an equilibrium state. We also note that the size of the final configuration is not much smaller than the initial one. In our special case, it is about a quarter of the initial size, i.e. the same order of magnitude. Further, we have checked that it seems to have lost only very little of its mass during the collapse. Even tough, we saw that some parts were ejected, cf. especially Fig. V.2.

Assuming that we can generalize the behavior of our toy model to the collapse of the axion miniclusters, our findings should also apply to them. This means, looking back at Fig. V.1, that

the distribution of the miniclusters after their collapse should also be far above the axion star branch and indeed they rather settle in an equilibrium configuration than directly collapse into a static star solution. This also implies that since their mass and size should change only little during the collapse, the results for the miniclusters mass function we have found in Ch. IV also gives a good estimate for the distribution of the miniclusters today.

However, it must be noted that these results and conclusions are still preliminary. The project of studying the actual equilibrium configuration is still work in progress. More simulations, a finer grid and especially longer running times are needed. Further, the question about the actual virialization is not yet satisfactory answered. Even though, we have found that the phase of the wave function becomes uncorrelated during the collapse it is not clear if this truely indicates virialization. Also it can be questioned if the correlator we have defined is the proper quantity to study the actual effects of virialization. From looking at the final moments of our simulation, one could also get the impression that the equilibrium state close to the center is still quite coherent and argue that the inital cloud has only shrinked to a smaller size, settling in some kind of breathing mode, cf. Ref. [174]. Also it is debatable if, by limiting ourselves to the spherically symmetric case, we are even able to see a randomization of the phase in our simulations. Recall that uncorrelated phases was one of the attributes of the virialized configuration following from our discussion before. Hence, we conclude that there are still some open questions before we can make conclusive statements about the fate of axion minicluster. Still, the methods and findings presented here can be extremely valuable for doing so.

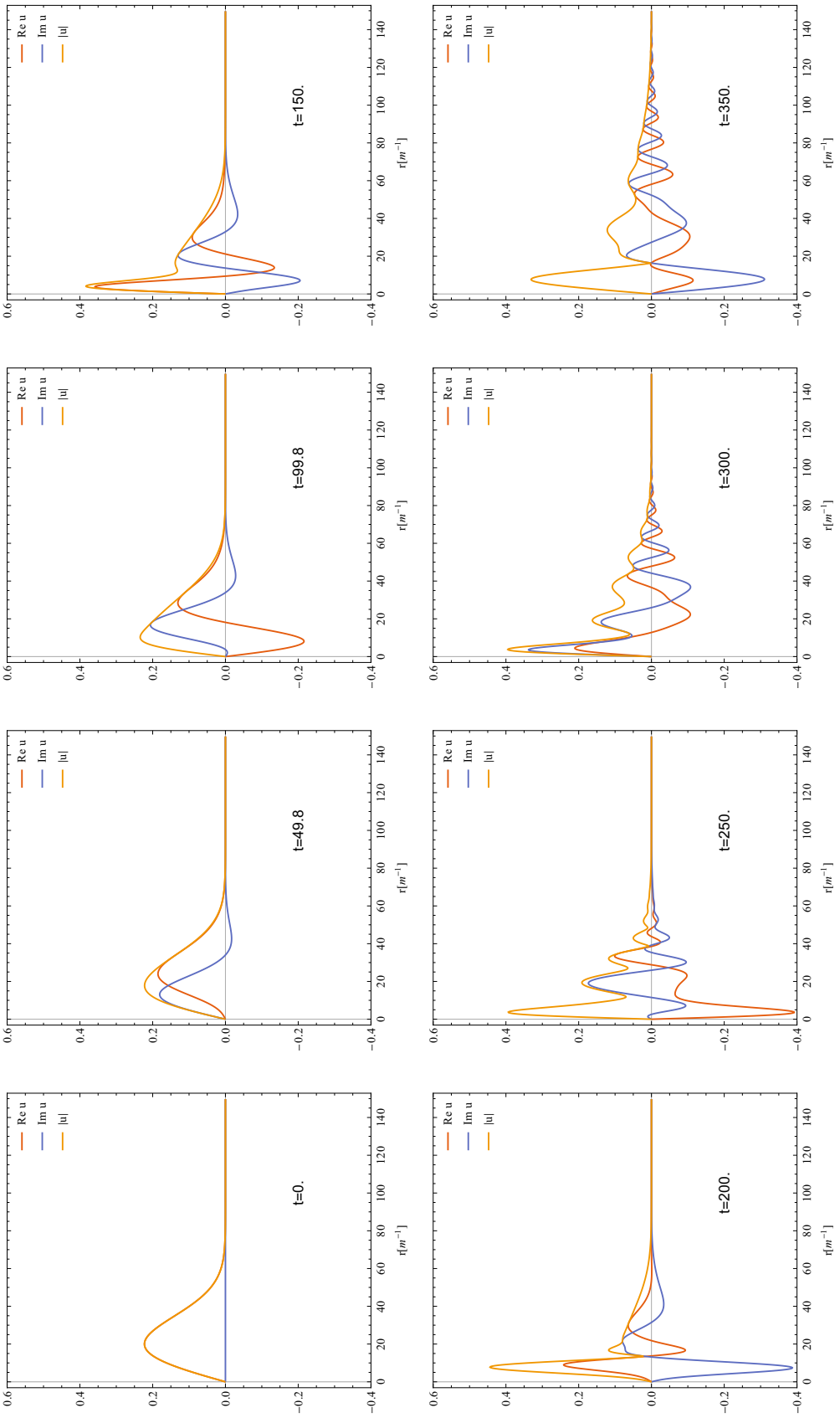

Figure V.6.: Evolution of the Wave Function in the Schrödinger-Poisson System. We show different snapshots of our simulations of the Schrödinger-Poisson system. The orange curves correspond to the absolute value $|u|$ of the rescaled wave function $u = r\phi$, the red to the real and blue to the imaginary part of u.

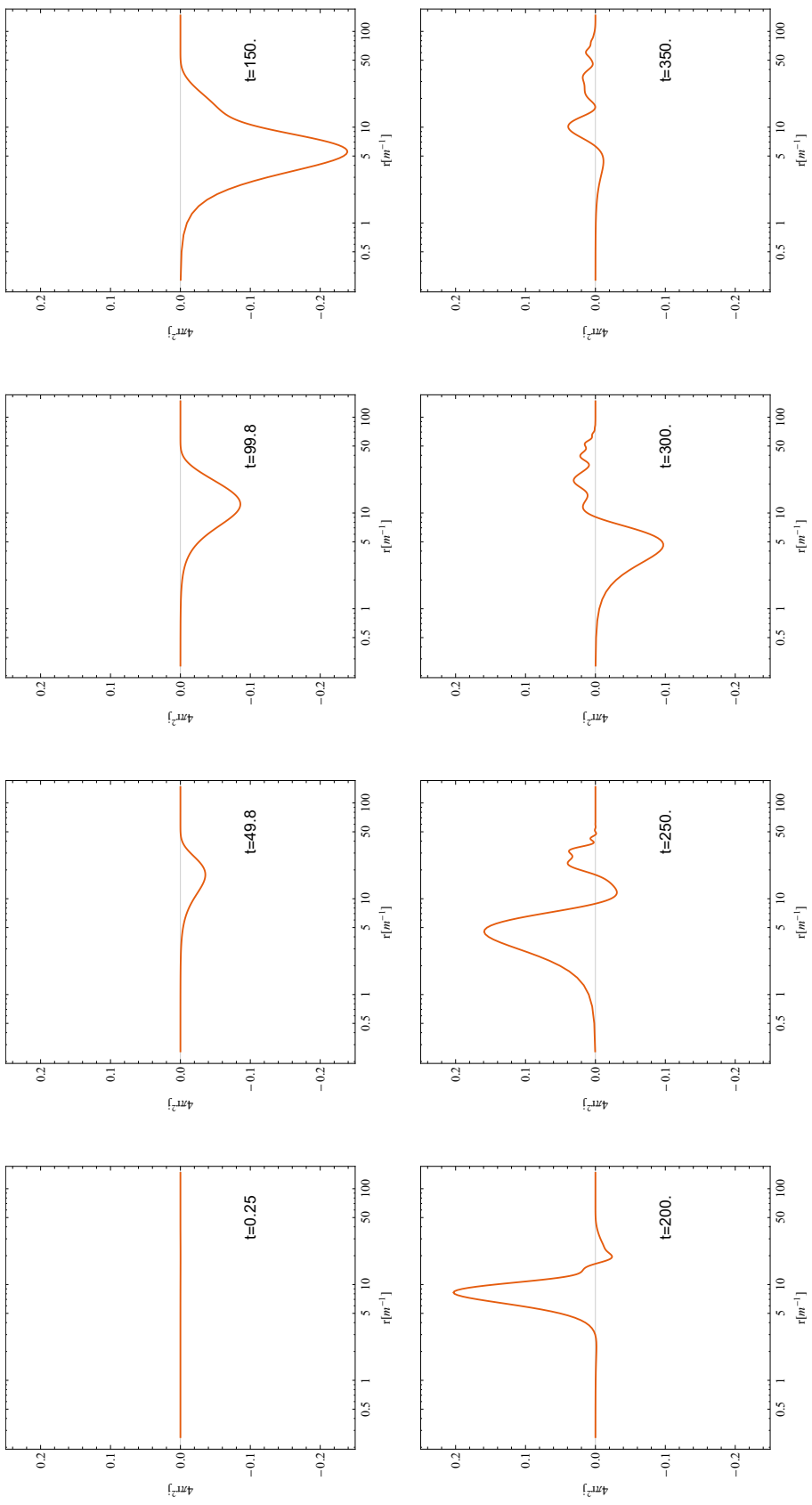

Figure V.7.: Evolution of the Particle Current in the Schrödinger-Poisson System. The quantity $\mathbf{j}$ was defined Eq. (V.28). Its interpretations is that of a current with which the particle density flows.

VI. Post-Inflation Realignment and Large-Scale Observables

In this chapter, we study how the post-inflation vacuum realignment of the axion field impacts cosmological large-scale observables. We especially focus on the effects in the spectrum of the primary anisotropies of the cosmic microwave background (CMB).

So far, we have mainly considered the QCD axion scenario where the spatial size of the isocurvature density fluctuations in the post-inflation Peccei-Quinn breaking scenario are extremely small compared to cosmological scales, cf. our discussion at the beginning of Ch. IV. The formation of miniclusters with sizes of $\sim 10^6$ km and masses of $\sim 10^{-13} M_\odot$ will leave the cosmological evolution on large scales virtually untouched. Rather, the adiabatic fluctuations in the axion energy density inherited from inflation will be dominant for shaping, for example, the CMB spectrum. However, we will show in the following that for very light ALPs with masses $\sim 10^{-24} - 10^{-15}$ eV, the impact of the iscorvuature fluctuations coming from a post-inflation realignment are not negligible. Further, we note that CMB observations and other cosmological observables can be sensitive to it. The results of this study will be presented in Ref. [175].

Before we consider the isocurvature fluctuations in the axion energy density in detail, let us recall some of the basics for discussing energy density fluctuations in the cosmological context. See, for example, the textbooks Refs. [79, 141, 177, 178] for more details. In Tab. VI.1 we also summarize some of the most important points.

In general, we can assume that the energy density fluctuations $\delta_{\rm DM}$ in the DM component consist of adiabatic and isocurvature fluctuations, i.e.

$$\delta_{\rm DM} = \delta^{\rm ad}_{\rm DM} + \delta^{\rm iso}_{\rm DM} \,. \tag{VI.1}$$

The adiabatic fluctuations are identified as fluctuations in the spatial curvature seen by a comoving observer. This means that it affects the energy density fluctuations of all species in the universe, DM, baryons, and photons, more or less the same and we have $\delta\rho \neq 0$ in total. For describing super-horizon modes of the adiabatic fluctuations it is convenient to introduce the gauge-invariant quantity $\mathcal{R} \equiv \delta_{\mathcal{K}}$ indicating the fluctuations in the local curvature $\mathcal{K}$.[1]

In a radiation dominated universe the following relation between the adiabatic energy density fluctuations in the different species, DM, baryons b, and photons γ, and $\mathcal{R}$ holds [178]:

$$\delta^{\rm ad}_{\rm DM} = \delta_{\rm b} = \frac{3}{4}\delta_\gamma = \mathcal{R} \,. \tag{VI.2}$$

Further, it turns out that $\mathcal{R}$ is constant in time. This implies that also the super-horizon fluctuations in, for example, the DM energy density are frozen as long as the universe is radiation dominated.

Usually, it is assumed that the adiabatic fluctuations are inherited from the quantum fluctuations in the inflaton field. After inflation and reheating they leave their imprint as fluctuations

[1] Note that for super-horizon modes the subtelties of choosing a specific gauge which in the context of General Realtivity means choosing a specific coordinate system become important. See, for example, Ref. [177] for more details.

Power Spectrum	The power spectrum $P(k)$ is related to the density fluctuations $\delta(x) = (\rho(x) - \overline{\rho})/\overline{\rho}$, $\overline{\rho}$ being the mean energy density, via the Fourier transform of the two-point correlation function $\zeta(x-x') = \langle\delta(x)\delta(x')\rangle$. The dimensionless power spectrum $\Delta^2 = k^3P(k)/(2\pi^2)$ indicates the fluctuation power in the mode k.
Super- and Sub-Horizon Modes	The scale of a fluctuation in the energy density might be identified with a wave number λ or equivalently with a mode $k \sim \lambda^{-1}$. Fluctuations with a size λ larger than the causal horizon (super-horizon), i.e. $\lambda > d_H \sim H^{-1}$ or equivalently $k < H$, despite a decaying solution, do not evolve and therefore stay constant with time. It is said, they are frozen. On the other hand, for sub-horizon modes with $k > H$, causal processes become important and this, for example, can lead to the well-known linear growth of the sub-horizon density fluctuations after matter-radiation equality.
Adiabatic Fluctuations	Adiabatic fluctuations can be identified with local fluctuations in the spatial curvature as seen by a comoving observer. Since fluctuations in the gravitational potential affect all particle species the same, this means that for adiabatic fluctuations a fractional increase in the number density in one component leads to the same increase in the other. The name adiabatic results from the fact that since also radiation participates in this kind of fluctuations, the particle density in a comoving volume stays constant. Thus, no heat is transferred.
Isocurvature Fluctuations	Isocurvature fluctuations cannot be produced via an adiabatic process. This means foremost that they cannot be identified with fluctuations in the local curvature, hence the name isocurvature. But if the curvature should not be affected by say the fluctuation of the energy density in one component, it means that it must be compensated by the others such that $\delta\rho = 0$ overall. The consequence of this is that as soon as an isocurvature fluctuation enters the horizon, energy must be reshuffled between the different particle species. This is precisely the effect why, for example, isocurvature fluctuations in the DM leave their imprint the the radiation component and therefore eventually in the CMB, cf. Ref. [176]. Note that the distinction between isocurvature and adiabatic fluctuations is only meaningful for super-horizon modes.

Table VI.1.: Definitions and Explanations for the Discussion of DM Density Fluctuations. See also, for example, Ref. [79].

in the local curvature. Since quantum fluctuations are in general assumed to be scale-invariant, one usually sets for the spectrum of $\mathcal{R}$ [177]

$$\Delta^2_{\mathcal{R}} = A_s \left(\frac{k}{k_*}\right)^{n_s-1} \tag{VI.3}$$

with k_* being some pivot scale, $n_s \simeq 1$ is the so-called spectral index and A_s is the amplitude of the adiabatic fluctuations. Both A_s and n_s can be related to the properties of the inflaton field in specific inflation models, we will turn to this later at the beginning of Sec. VI.2. Note that Eqs. (VI.2) and (VI.3) imply that also for the adiabatic DM fluctuations we have $\Delta^{\rm ad}_{\rm DM} \simeq A_s$ for $n_s \simeq 1$ and this in turn means that the power spectrum $P^{\rm ad}_{\rm DM}(k) \propto k^{-3}$ for the super-horizon modes.

Isocurvature fluctuations, on the other hand, occurr as fluctuations in the number density n_i of only one of the species i in the universe. Hence, they cannot by identified with fluctuations in the local curvature. Rather, we must have for isocurvature fluctuations that the overall energy density fluctuations vanish locally, i.e. this translate into the constraint that $\delta\rho = 0$ in total [79].

To compare isocurvature and adiabatic fluctuations it is convenient to introduce again a gauge-invariant quantity, in this case often called $\mathcal{S}_i$ and i denotes the the species in which the isocurvature fluctuations sit. Let us focus on the DM component. Then, it is [177]

$$\mathcal{S}_{\rm DM} \equiv \frac{\delta(n_{\rm DM}/n_\gamma)}{(n_{\rm DM}/n_\gamma)} = \frac{\delta n_{\rm DM}}{n_{\rm DM}} - \frac{\delta n_\gamma}{n_\gamma} \tag{VI.4}$$

which in radiation domination simplifies to

$$\mathcal{S}_{\rm DM} = \delta_{\rm DM} - \frac{3}{4}\delta_\gamma \,. \tag{VI.5}$$

Now, using Eqs. (VI.1) and (VI.2) we find in this case

$$\mathcal{S}_{\rm DM} = \delta^{\rm iso}_{\rm DM} \,. \tag{VI.6}$$

This means that the spectrum of the isocurvature fluctuations $\mathcal{S}_{\rm DM}$ is equal to the spectrum of the DM isocurvature energy density fluctuations, i.e.

$$\Delta^2_{\mathcal{S}} = \Delta^2_{\rm DM,iso} \,. \tag{VI.7}$$

To compare the impact of the isocurvature in relation to the adiabatic fluctuations at the some scale k_* we introduce the quantitiy

$$f^2_{\rm iso} \equiv \left.\frac{\Delta^2_{\mathcal{S}}}{\Delta^2_{\mathcal{R}}}\right|_{k=k_*} \tag{VI.8}$$

which for the DM isocurvature fluctuations and when focusing on super-horizon modes is identical to using

$$f^2_{\rm iso} = \left.\frac{\Delta^2_{\rm DM,iso}}{\Delta^2_{\rm DM,ad}}\right|_{k=k_*} . \tag{VI.9}$$

Let us now turn to the specific case of the axion isocurvature fluctuations in the post-inflation Peccei-Quinn breaking scenario. For that we have found in Ch. IV what kind of power spectrum we can expect. Namely, it is constant on large scales and exponentially suppressed on scales smaller than the comoving Hubble horizon at the time the field starts to oscillate, i.e. at high modes $k > RH(T = T_{\rm osc})$; R being the scale factor and H the Hubble rate. This reflects the white noise behavior of the initial fluctuations with a characteristic cut-off length, cf. Fig. IV.1 for a reminder of the situation in the post-inflation Peccei-Quinn breaking scenario. With our

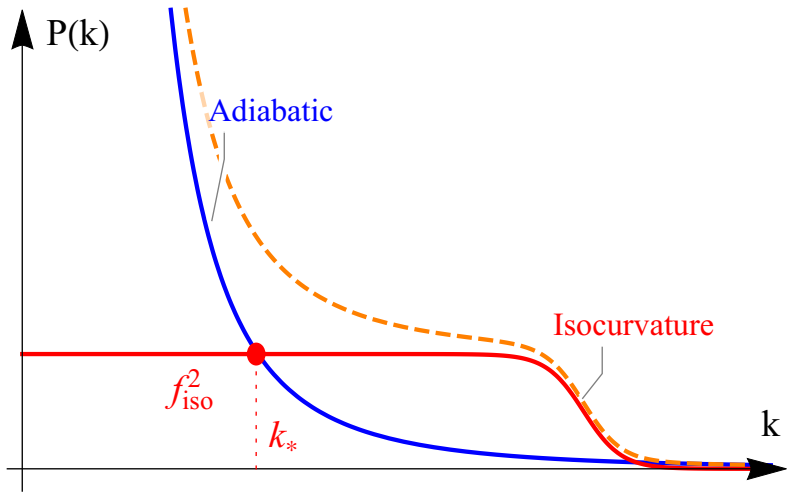

Figure VI.1.: Sketch of the primordial Power Spectrum for adiabatic and isocurvature Fluctuations in the Axion Energy Density. The power spectrum of the isocurvature fluctuations (red) is constant for low k modes and exponentially suppressed above scales $k > K$, where K corresponds to scales of the comoving Hubble horizon when the field oscillations commence, cf. the discussion in Sec. IV. The scales of the fluctuations around the cut-off K are far too small to be accesible with cosmological observations. The adiabatice power spectrum (blue) behaves as k^{-3} for super-horizon modes. We define a scale k_* where the relative amplitude of the isocurvature power spectrum with respect to the adiabatic power spectrum is $f^2_{\rm iso}$. Note that the power spectra are given in the conformal Newtonian gauge.

results in Sec. IV.2, we have found that in the low k region the dimensionless power spectrum of the isocurvature fluctuations behaves as

$$\Delta^2_{\rm iso} = C \left(\frac{k}{K}\right)^3 , \tag{VI.10}$$

with $K = RH(T_{\rm osc})$ and the constant of proportionality C must be determined by numerically following the axion field evolution. Our results, as well as the results from Vaquero et al in Ref. [108], indicate that $C = 0.01 \ldots 0.1$ and the exact value depends on the actual Peccei-Quinn breaking scale and details on the explicit temperature dependence of the axion mass. See Ref. [137] for a more in-depth discussion of this topic also including the general case of ALPs. Recall that $C = 1$ can be interpreted as the scale of the fluctutaions being equal to Hubble horizon at $T_{\rm osc}$ and smaller C suggest smaller characteristic scales for the fluctuations. With Δ^2 for low k modes given in Eq. (VI.10), we may write the power spectrum of the isocurvature fluctuations symbolically as

$$P_{\rm iso}(k) = \begin{cases} 2\pi^2 K^3 & \text{for } k < K \\ \text{exp. suppressed} & \text{for } k > K \end{cases} . \tag{VI.11}$$

Note that at $T = T_{\rm osc}$, K marks the transition from sub- to super-horizon modes.

Since the power spectrum of the adiabatic density fluctuations is generated long before matter-radiation equality it usually called primordial [177]. In our case where we on top expect the

discussed isocurvature fluctuations arising at the time the field starts to oscillate, the spectrum of the DM fluctuations before matter-radiation equality is in fact composed of $P_{\rm ad}(k)$ and $P_{\rm iso}(k)$ and as long as there is no correlation between the two, the complete spectrum is simply their sum. Thus, in our case the primordial spectrum describes the spectrum consisting of the early generated adiabatic as well as the isocurvature fluctuations arising after the axion field starts to oscillate.

In Fig. VI.1 we sketch $P_{\rm ad}(k)$, $P_{\rm iso}(k)$, as well as $P_{\rm ad}(k) + P_{\rm iso}(k)$, at an early time, after the field has started to oscillate, but before matter-radiation equality. Cosmologically relevant is foremost the region to the very left, i.e. the low k modes. The part on the right is usually far beyond the reach of any cosmological observable, as we will see in the following.

The scale K where the exponential suppression of the isocurvature power spectrum becomes important can be calculated with our result in Eq. (IV.84). We find as an estimate for the comoving scale K today, with $R(T_0) = 1$,

$$K \sim b \left[\frac{b}{4.98 g_*^{1/2}(T_{\rm osc})}\right]^{-n/n+2} \cdot 10^{(4n+22)/(n+2)}\ {\rm Mpc}^{-1} \left(\frac{m_a}{10^{-5}\ {\rm eV}}\right)^{1/2} \left(\frac{f_a}{10^{12}\ {\rm GeV}}\right)^{n/(2n+4)}, \tag{VI.12}$$

where we have used the parameterization for the temperature dependent axion mass, introduced in Sec. III.2:

$$m_a(T) = \begin{cases} b m_a \left(\frac{\Lambda}{T}\right)^n & , T \geq b^{1/n}\Lambda \\ m_a & , T < b^{1/n}\Lambda \end{cases}. \tag{VI.13}$$

The energy scale Λ can be related to zero temperature mass m_a and the Peccei-Quinn breaking scale f_a via $\Lambda = m_a^{1/2} f_a^{1/2}$. Recall that for ALPs, m_a and f_a are independent parameters, whereas for the QCD axion they are equivalent. The parameters b and n control how the mass dynamically switches on via a power law with decreasing temperature.

We see that for a typical QCD DM axion mass, $m_a \sim 10^{-5}$, the values for the cut-off K are much larger than what can be observed with either large-scale structure (LSS) surverys of the matter power spectrum, which are roughly sensitive to scales down to $k \sim 0.1 - 1\ {\rm Mpc}^{-1}$ or CMB observations, where already modes with $k \gtrsim 0.01 - 0.1\ {\rm Mpc}^{-1}$ are suppressed by Silk damping [179].

From our estimate in Eq. (VI.12), it follows that large n are advantageous for getting a small and therefore observable K. In the large n limit we have

$$K \sim 10^4\ {\rm Mpc}^{-1} \left(\frac{m_a}{10^{-5}\ {\rm eV}}\right)^{1/2} \left(\frac{f_a}{10^{12}\ {\rm GeV}}\right)^{1/2}. \tag{VI.14}$$

On the other hand, if we want the axion to explain all the DM in the Universe, we find that the product $m_a f_a$ is essentially fixed. Namely, with our relation for ρ_{a0} in Eq. (III.47), we find

$$\rho_{a0} \sim \frac{1}{2}\frac{\pi^2}{3} m_a^{1/2} f_a^{1/2} \left(\frac{f_a}{M_{\rm Pl}}\right) T_0^3 \tag{VI.15}$$

for large n and therefore

$$K \propto \frac{1}{f_a}. \tag{VI.16}$$

This means, the larger the f_a, the smaller the cut-off mode K and this in turn corresponds to larger fluctuation sizes, which may become cosmologically relevant. Note that due to the relation between f_a and m_a via the energy density, exremely large f_a imply very small m_a when fixing $\rho_{a0} = \rho_{\rm DM}$.

However, we have to keep in mind that we are considering a scenario where Peccei-Quinn breaking happens after inflation. Hence, f_a should be smaller than the reheating temperature $T_{\rm RH}$ which forbids arbitrary large f_a. This was already briefly mentioned in our discussion of the ALP miniclusters in Sec. IV.5. There, we noted that a reasonable estimate for the reheating temperature after inflation is $T_{\rm RH} \lesssim 10^{17}$ GeV, following Ref. [139].

But even though the scales $\sim K^{-1}$, where the isocurvature power spectrum dominates over the adiabatic, might be difficult to observe or even only if f_a is extremely high, we can still try to study the impact of the isocurvature fluctuations on scales larger than K^{-1}. For that, we can consider its relative contribution in the power spectrum compared to the adiabatic fluctuations at some low $k_* \ll K$. This is also indicated in Fig. VI.1. But it should be notetd that k_* does not need to be at the intersection of $P_{\rm iso}$ and $P_{\rm ad}$. For convenience, we set $k_* = 0.05$ Mpc^{-1}.

Using the explicit forms for the adiabatic, cf. Eq. (VI.3), as well as the isocurvature fluctuations, Eq. (VI.10), in our definition for $f_{\rm iso}$, Eq. (VI.9), we find.

$$f_{\rm iso} = \frac{C^{1/2} k_*^{3/2}}{A_S^{1/2} K^{3/2}} \,, \tag{VI.17}$$

The idea is that if it is possible to constrain $f_{\rm iso}$ via, say CMB observations, this will in turn give a limit on K and therefore on the axion properties like m_a, f_a, and details on its temperature dependent mass.

VI.1. Cosmological and Astrophysical Constraints on Ultra-light Axions

To put our work in the context of the current state of research, we briefly review some existing cosmological and astrophysical constraints on the axion mass. We focus especially on the case of ultra-light axions (ULAs) since we have understood that for small m_a we can expect the strongest effects of the isocurvature fluctuations, cf. Eq. (VI.16). Most of the constraints we will discuss in the following are independent of any specific ALP model and rely mainly on the comsological evolution of the axion field, which we have discussed in Sec. III.2, or its gravitational interactions.

Let us start with the low mass end. In Ref. [95], Hlozek et al showed that ULAs with masses in the range 10^{-32} eV $< m_a < 10^{-25.5}$ eV can be basically ruled out looking at precision data from CMB measurements and LSS surveys. To come to this conclusion, Hlozek et al used the effect that ULAs change the height of the accoustic peaks in the multipole spectrum of the CMB primary anisotropies if they give a sizeable contribution to the energy density of the universe. Recall that the peaks are proportional to the matter-to-radiation ratio. Extremely light axions will only start to oscillate comparably late in the cosmological history and therefore behave quite long as a dark energy (DE) component. For details, see our discussion in Sec. III.2. In fact, the longer the axion acts as DE and does not contribute to the matter component, the more it modifies the matter-to-radiation ratio, i.e. the lighter the ULA the stronger this effect. Recall that for $m_a < 10^{-27}$ eV, the axion cannot explain the observed DM in our Universe since field oscillations commence only after matter-radiation equality.

Hlozek et al considered also modifications of the matter power spectrum for the case of ULA DM. Recall that the evolution equation of the linear fluctuations in the axion energy density are changed by an effective sound speed which suppresses fluctuations on scales smaller than axion Jeans scale $k_J \sim 1/m_a$, cf. Eq. (III.31). For ULAs with $m_a < 10^{-25}$ this becomes important in the sense that it notably suppresses the high k end of the matter power spectrum, similar to warm DM. Now, the predictions for the matter power spectrum in an ULA DM scenario can be compared to actual results from galaxy surveys like WiggleZ [180], to see if ULA DM is compatible with our obeservations.

Combining the results from CMB and LSS data, Hlozek et al find the already mentioned exclusion limit for ULA masses in the range 10^{-32} eV $< m_a < 10^{-25.5}$ eV. No less important, they conclude that axions with masses $m_a > 10^{-24}$ are virtually indistinguishable from standard CDM looking at the observables they choose. For similar studies see Refs. [181–184].

Moving to slightly higher masses, it turns out that ULAs with masses $m_a \sim 10^{-22} - 10^{-20}$ eV are exceptionally appealing DM candidates since they might provide a solution to some small-scale problems of CDM, especially to the so-called cusp-core problem [89]. Axions or more general scalar DM in this mass range is often called fuzzy DM (FDM) [90]. The reason why FDM can help to solve the cusp-core problem is that its de Broglie wavelength $\sim 1/(m_a v)$ can be comparable to the core size of galaxy halos. The suppression of fluctuations on these scales leads to a smooth central halo region which can be compared to the cuspy profile observed in numerical simulations of halo formation with standard CDM [185]. It turns out that a cored DM halo is preferred by measurements of stellar dynamics in dwarf galaxies [186].

However, as we have already mentioned before, ULA DM modifies the matter power spectrum on scales $k > k_J$ and observations of the Lyman-α lines of the neutral hydrogen in the inter-galactic medium, the so-called Lyman-α forest, can be used as to test this smallest scales. The Lyman-α observerations are senstitive to much higher k's in the matter power spectrum than what is accessible with, for example, galaxy surveys. To predict the matter power spectrum in an FMD scenario, hydrodynamical simulations are needed and, as it turns out, the results do not agree with the observed Lyman-α flux power spectrum [187,188]. Therefore, it is concluded that axions with masses $m_a \lesssim 10^{-21}$ eV can be ruled out as the main component of DM and therefore might be of no help in solving the cusp-core problem [189].

Very recently, Marsh and Niemeyer showed in Ref. [190] that it might be possible to constrain FDM even stronger. For that, they study the effect of oscillating soliton-like cores in FDM halos on the heating of star clusters. Comparing the heating rate under the assumption that star clusters are embedded in an FDM halo, Marsh and Niemeyer used observations on the size and the lifetime of a star cluster in the center of the dwarf galaxy Eridanus II to set a lower limit on the axion mass $m_a > 10^{-19}$ eV. They conclude that for lighter axions, the heating of the star cluster via the soliton-like cores would be too strong or prohibit the formation of Eridanus II at all. A similar result was found in Ref. [191]. However, it must be noted that these constraints heavily rely on the assumption that soliton-like cores form inside the FDM halo. This was so far only observed in simulations for dwarf galaxy halos with axion masses $m_a \sim 10^{-22}$ eV [185] and only in Ref. [121] it was observed that the cores are actually oscillating. For larger axion masses, the formation time of the solitonic cores becomes longer and it is questionable if they form at all, as was also noted in Ref. [190] by Marsh and Niemeyer themselves. Thus, the constraints from the observations of Eridanus II should be taken with some caution till results for halo simulations with axion masses $m_a \sim 10^{-19}$ eV exist and the formation of the oscillating soliton-like cores is confirmed.

For heavier axions, it turns out that observations of spinning black holes can be used to test the allowed mass range. The reason for this is that the scattering of a massive scalar field on a rotating BH can lead to a so-called superradiant instability and therefore to a spin-down of the BH. Without going into too much detail, we briefly want to sketch how this works. Recall that as soon as a particle crosses the event horizon of a BH it will be unavoidably swallowed. Thus, a BH acts as a perfect absorber for any particle, i.e. also for the axion. Now, it was realized by Zel'Dovich in the 1970's that if an absorber is spinning it can actually instead of absorb, reflect and even amplify an incoming wave [192].[2] This is possible by extracting rotational energy. If the wave or particle can be confined around the absorber by, say a mirror, it is possible that this process is repeated again and again, till all the rotational energy is extracted and the absorber spins down. This is called a superradiant instability. It can be shown that this effect also occurs for the scattering of a massive scalar field on a spinning BH [193]. Here, the confinement is provided by the gravitational potential of the BH itself. By repeatedly scattering, the axion

[2]Since this is a classical effect, we speak of waves rather than of particles.

Mass Range [eV]	Source and Comment
$10^{-33} < m_a < 10^{-25.5}$	Height of accoustic peaks in the CMB and observations on the matter power spectrum, e.g. Ref. [200]. Note that axions with $m_a \lesssim 10^{-27}$ eV cannot serve as DM.
$m_a < 10^{-21}$	Observations of the small scale matter power spectrum via the Lyman-α forrest and comparison with hydrodynamic simulations of FDM, e.g. Ref. [187].
$m_a < 10^{-19}$	Observations of dwarf galaxy Eridanus II [190]. Relies on the formation of oscillating solitonic cores in the DM halo.
$10^{-19} < m_a < 10^{-14}$	Spin-down of super-massive black holes via superradiant instability, e.g. Ref. [195]. Limits only appy if self-interactions are neglected. For $f_a \lesssim 10^{16}$ GeV self-interactions become important and make a bosenove more likely than a spin-down, see Ref. [196].

Table VI.2.: Exclusion limits on ultra-light Axions.

field is amplified and forms a cloud around the BH similar to the electron cloud in the Hydrogen atom and eventually will spin down the BH [194]. However, a superradiant scattering of axions on BHs is only possible if the mass m_a and the spin Ω of the BH satify a certain relation, roughly $m_a < \Omega$. See, for example, Ref. [193] for more details on the exact relation. This means that certain BHs can be used to test a certain mass range m_a. In Ref. [195], Stott and Marsh used observations on the lifetimes of super-massive BHs with $M_{\rm BH} \sim 10^5 - 10^9 M_\odot$ to exclude axion masses in the range 10^{-19} eV $< m_a < 10^{-14}$ eV. See also Refs. [196, 197] for similar studies and results.

However, it should be noted that for deriving these limits, self-interactions of the axion field are neglected. Namely, it turns out that if self-interactions are included, the extremely high particle densities in the axion cloud around the BH allow for a bosenova to occur before extracting the complete rotational energy of the BH and therefore no spin-down would be observable [198]. A bosenova happens in a Bose-Einstein condensate when the particle density is so high that nonlinear effects switch attractive interactions to repulsive ones. Assuming that we can treat the axion cloud around the BH as Bose-Einstein condensate, we can heuristically understand this effect by looking at the cosine-potential of the axion field and using our insights from the discussion in Sec. V.1. Expanding the axion potential $V(a) = m_a^2 f_a^2[1 - \cos(a/f_a)]$ in powers (a/f_a), gives $V(a) \sim m^2a^2 - m^2a^4/f_a^2 + m^2a^6/f_a^4 - \ldots$, where we do not care about numerical factors for the moment. So, we note that the self-interaction alternates between attractive and repulsive. Now, in Sec. V.1 we have learned that a^2 is proportional to the number density of axions. Therefore, it is obvious that with increasing particle densities the self-interactions become more and more important and even can change their sign from attractive to repulsive. In the axion cloud around the BH where the particle density is steadily increased by the superradiant scattering, this can lead to an explosive bosenova when some critical density is reached. See also Ref. [199] for more details. From our brief analysis it is immediately clear that this effect depends on f_a since the lower f_a, the stronger the self-interactions and the more likely it is that a bosenova occurs before the spin-down of the BH. In Refs. [199] and [196] the same cosine-ansatz for the axion potential is used to show that for $f_a \lesssim 10^{16}$ GeV, self-interactions cannot be neglected and naive SR limits from super-massive BHs do not apply. It turns out that this limit is in good approximation insensitive to the axion mass m_a since the self-interactions, as well as the superradiance effect, depend in such a way on m_a that the dependence cancels.

For later reference, we collect the various exclusion limits on the ULA masses in Tab. VI.2.

VI.2. Axion Isocurvature Fluctuations and the CMB

Pre-inflation Peccei-Quinn Symmetry Breaking

Before discussing how we use CMB data to constrain the axion isocurvature fluctuations for the post-inflation realignment scenario, let us briefly review how CMB observations are usually used to study the pre-inflation scenario, see for example Refs. [201–204].

When Peccei-Quinn breaking happens before or during an inflationary period, the quantum fluctuations of the massless axion field lead to isocurvature fluctuations in the energy density [205]. In this case, as for the fluctuations in the inflaton field, one can assume a scale-invariant spectrum. But since these kind of flucuations are related to the quantum fluctuations in the de Sitter vacuum during inflation, the power spectrum should be proportional to the scale of inflation. Hence, for the QCD axion it is assumed that [79]

$$\Delta^2_{\text{iso,pre}} = \frac{(H_I/2\pi)^2}{f_a^2\theta_i^2}\,, \tag{VI.18}$$

where H_I is the Hubble rate during inflation and θ_i is the initial misalignment angle. This means that in the pre-inflation Peccei-Quinn breaking scenario, the power spectrum of the adiabatic and the isocurvature fluctuations have the same form. This is a much different situation than for post-inflation realignment.

A general feature of DM isocurvature fluctuations is that they lead to a tilt of the angular power spectrum of the CMB such that it gets suppressed at small angular separations [176, 201, 206]. Without going into details of the actual derivation, we simply quote the result of the Planck collaboration for the limit on uncorrelated scale-free isocurvature contributions in the CDM component [202]:

$$\frac{\Delta^2_{\text{iso,pre}}}{\Delta^2_{\text{ad}}} < 0.038 \tag{VI.19}$$

at a pivot scale $k_* = 0.05\ \text{Mpc}^{-1}$. Since $\Delta^2_{\text{iso,pre}}$, as well as the adiabatic fluctuations Δ^2_{ad}, depend on the scale of inflation, the constraint in Eq. (VI.19) leads to an interesting relation between H_I and f_a. Let us briefly outline how this comes about.

In slow-roll single field inflation models the amplitude A_s and H_I^2 are proportional and it is [82]

$$A_s = \frac{1}{2\epsilon}\left(\frac{H_I}{2\pi M_{\text{Pl}}}\right)^2\,, \tag{VI.20}$$

with ϵ being the so-called slow roll parameter. With the measured value $A_s = 2.97 \cdot 10^{-9}$ [207] we can express ϵ via $(H_I/2\pi)^2$, such that with Eq. (VI.19) we have

$$H_I < 1.5 \cdot 10^6\ \text{GeV}\ \theta_i \left(\frac{f_a}{10^{12}\ \text{GeV}}\right)\,. \tag{VI.21}$$

The initial misalignment angle θ_i of the axion field, as well as the breaking scale f_a, are in principle unknown. But if the axion is meant to explain all the DM then θ_i can be fixed with respect to a given f_a. For finding this relation, we generalize our estimate for the relic abundance $\Omega_a h^2$ for the QCD axion in the post-inflation scenario in Eq. (III.50) to the pre-inflation scenario. It is

$$\Omega_a h^2 \simeq 0.1 \left(\frac{f_a}{10^{12}\ \text{GeV}}\right)\left(\frac{\theta_i^2}{\pi^2/3}\right)\,. \tag{VI.22}$$

Fixing $\Omega_a h^2 = 0.1$ and expressing θ_i via f_a, we find

$$H_I < 2.7 \cdot 10^6 \text{ GeV } \left(\frac{f_a}{10^{12} \text{ GeV}}\right)^{0.42} , \tag{VI.23}$$

which agrees with the relation given by the Planck collaboration in Ref. [202] and the original references, for example by Lyth [208] and Seckel and Turner [209].

The relation between H_I and f_a in Eq. (VI.23) opens up the possibility for testing single field low scale inflation via axion isocurvature perturbations. Namely, one can use the tensor-to-scalar ratio r_T as an independent probe of the scale of inflation H_I and combine this with the constraint Eq. (VI.23). For single field inflation it is $r_T = 16\epsilon$ [82]. A quick check shows that if Eq. (VI.23) holds, then $r_T \lll 1$ and the pre-inflation Peccei-Quinn breaking axion scenario is incompatible with observable values for r_T, as for example $r_T \sim 10^{-3}$ which is the sensitivity goal of a planned CMB stage IV mission [210]. Thus, an actual observation of a comparably large r_T could rule out a combination of single field inflation and pre-inflation Peccei-Quinn breaking with the axion being the DM. See also Ref. [203] for a more detailed discussion.

However, these constraints can be easily circumvented in more sophisticated inflation models. Further, note that we have limited our discussion to the QCD axion. For ALPs the situation is more complicated due to the independence of m_a and f_a, see for example Ref. [211]. See also Ref. [92] for a different approach which gets rid of the isocurvature bounds on the pre-inflation scenario completely.

Post-inflation Peccei-Quinn Symmetry Breaking

Our goal is to test f_{iso}, as defined in Eq. (VI.17), with the measurement of the power spectrum of CMB primary fluctuations. The procedure is similar to what is done in pre-inflation scenario and technical details of our study are presented in Ref. [175]. Here, we want to outline the most important steps for deriving the consraints in a rather pedagogical way.

The standard method for testing whether a cosmological model is able to correctly reproduce or predict our observations can be summarized as follows. First, of course, a cosmological model must be set up. It consists of a certain number of cosmological parameters. In the so-called cosmological standard model, a flat Friedmann-Robertson-Walker universe, i.e. $\Omega_{\text{tot}} = 1$, a cosmological constant Λ with the equation of state $w = -1$, and an energy component Ω_{DM} which behaves like CDM is assumed. This is often called the cosmological standard or ΛCDM model. The free parameters in this model are usually the Hubble rate H_0, the baryon density Ω_b, the total matter density Ω_{m}, the spectral index n_s, the amplitude of the adiabatic fluctations A_s, and the optical depth τ at time of reionization. In the most minimal model, the sum of the massive neutrinos $\sum m_\nu$ is fixed, as well as the running of the spectral index. The latter parameterizes a dependence of n_s on the scale k of the fluctuations. It can be expressed via $\alpha_s \equiv \mathrm{d}n_s/\mathrm{d}\log k$. See for example the corresponding review article in Ref. [51] for a more in-depth discussion of the cosmological standard model.

The ΛCDM model is very successful in predicting the observed CMB anisotropies as well as the matter power spectrum [207]. However, it can be extended by further cosmological parameters to check if also other models can do the job. In our case the additional parameter is obviously f_{iso}. Further, we let $\sum m_\nu$ as well as α_s be free parameters for being sensitive to possible correlations. In Tab. VI.3 we summarize the parameters of our model of the post-inflation Peccei-Quinn breaking scenario. Their fiducial values are taken from the recent Planck data [207].

After setting up a model, the next step is to calculate the actual predictions it makes for the cosmological observables. This is done by solving the evolution equations of the linear density fluctuations for specific parameter values. See, for example, Ref. [141] for an introduction to this topic. Solving the necessary Boltzmann equations to determine the evolution of the linear fluctuations can be automatized and there exist a handful of excellent public codes doing this

Parameter	Fiducial Value	Meaning
h	0.678	Today's Hubble rate paramterized via $H_0 = h\ 100$ km/(s Mpc).
Ω_m	0.314	Total matter densiy.
Ω_b	0.0486	Baryon density.
A_s	$2.92 \cdot 10^{-9}$	Amplitude of the adiabatic fluctuations.
n_s	0.963	Spectral index.
α_s	0	Running of the spectral index.
τ	0.089	Optical depth.
$\sum m_\nu$	0.05 eV	Sum of the neutrino masses.
f_iso	0	Strength of the isocurvature fluctuations at the pivot scale $k_* = 0.05$ Mpc^{-1}, cf. Eq. (VI.17).

Table VI.3.: Paramters of the Cosmological Model for the post-inflation Realignment Scenario and their fiducial Values. The latter are taken from the Planck data [207].

task. Among the most common are CAMB [212] and CLASS [213]. For our studies, we use the latter.

To solve the Boltzmann equations we have to set initial conditions for the flucutations at a time after inflation and long before matter-radiation equality. This is usually done by specifying their power spectrum. The exact time where the initial conditions are set does not matter too much, as long as all fluctuation modes k of interest are still outside of the horizon. Recall that in our model we allow for additional isocurvature fluctuations of strength f_iso in the DM component at the pivot scale k_*. But strictly speaking, the axion will only behave as DM after the field oscillations commence at T_osc. At early times and $T \gg T_\mathrm{osc}$, as we have discussed before, it rather behaves like dark energy. However, if we restrict our study to axions with masses $m_a > 10^{-24}$ eV, the dynamical change of the equation of state has virtually no impact on the CMB power spectrum, as was concluded in Ref. [95]. Thus, treating the axion energy like normal CDM right from the get-go makes no difference for our study. Also note that in principle we should modify the evolution equation of the axion density fluctuations to include the axion Jeans scale, see Eq. (III.31). However, as we have learned from our discussion in Sec. VI.1, this becomes only important for axions with masses $m_a < 10^{-21}$ eV and when studying the matter power spectrum. In our study we want to focus on the CMB spectrum and axions with $m_a < 10^{-21}$ eV are anyway already strongly constrained by the Lyman-α observations [189].

We should also point out that when implementing the isocurvature power in the CDM component in our Boltzmann solver, we do not include the actual cut-off K, but rather we take it to be flat all the way. The reason for this is that the CMB is anyway only sensitive to the low k region where the isocurvature power spectrum is constant, as we have discussed above. However, we have checked that including the cut-off properly, does not modify our results. An exception would be, of course, if the cut-off would be close to our pivot scale $k_* = 0.05$ Mpc^{-1} or even $K < k_*$. Even though, our estimate in Eq. (VI.16) suggests that for very light axions this could be the case, we will later see that for the scenarios of interest we always have $K > k_*$ or even $K \gg k_*$. Also note that around the cut-off the fluctuations can in fact not be treated perturbatively and therefore here the linear evolution equations would not be valid.

After evolving the initial fluctuations, we can compare the prediction of our cosmological models for the CMB multipole spectrum with the actual data. For sampling the parameter space we use a Markov Chain Monte-Carlo (MCMC) approach. See for example Ref. [214] for an automated application of this method for CMB data and other cosmological observables. In our study, we use the publicly available code emcee [215]. Via the MCMC sampling we can not

only extract the best-fit points for our cosmological model, which is not of too much interest in our study, but also estimate the sensitivity of the CMB data on a single parameter. With that we can extract a constraint of the recent Planck data [83] on the isocurvature contribution. We find the limit

$$f_{\rm iso}^{\rm Planck} < 0.3\,. \tag{VI.24}$$

Further, it turns out that there is an interesting correlation between $f_{\rm iso}$ and α_s and also $\sum m_\nu$. The reason for this is that these parameters have a similar effect on the power spectrum of the CMB anisotropies. However, this degeneracy might be broken when we would include other cosmological observables, like the measurements of baryonic acoustic oscillations (BAO) in LSS. But this is beyond the scope of the present work. An extensive discussion of the correlations of $f_{\rm iso}$ with the other cosmological parameters can be found in Ref. [175].

Recall that the angular power spectrum of the CMB can be decomposed into the modes C_ℓ where l corresponds to the multipole expansion in terms of spherical harmonics. As we have already mentioned at the beginning of this section, the isocurvature fluctuations lead to a tilt of the angular CMB power spectrum and therefore to a suppression of power at high ℓ. Also our caclulations show that the CMB multipole spectrum is most sensitive to $f_{\rm iso}$ at high ℓ. This is also clear since the high ℓ in CMB anisotropy spectrum are related to small angular displacements, i.e. small scales. Here, we expect the biggest influence of the isocurvature fluctuations of the form as in Eq. (VI.10). However, for high ℓ the instrumental noise in the CMB observations starts to dominate the data which means a lower sensitivity on the cosmological parameters. But in the planned Stage IV CMB missions it is expected that the noise level can be significantly reduced, especially for high frequencies [210]. This motivates us to estimate the sensitivity on $f_{\rm iso}$ that could be reached in future CMB Stage IV observations. To do this we use the so-called Fisher matrix formalism. See, for example, Ref. [216] for a thorough review of this method in view of its application for forecasting the precission with which specific cosmological parameters can be tested in CMB observations. The technical details for our specific Fisher analysis are reported in Ref. [175]. Here, we only want to briefly summarize the main ideas of this method. For that we follow closely the explanations in Ref. [216].

Let us assume that we have a model consisting of the model paramters $\mathbf{\Theta} = (\theta_1, \theta_2, \ldots)$ with which we can predict a measurement consisting of the datapoints $\mathbf{x} = (x_1, x_2, \ldots)$. Thinking of $\mathbf{x}$ as a random variable then we say that $L(\mathbf{x}; \mathbf{\Theta})$ gives the probability distribution of $\mathbf{x}$ in terms of a fixed parameter point $\mathbf{\Theta}$. If, on the other hand, we have a given data set $\mathbf{x}$ from a measurement then $L(\mathbf{x}; \mathbf{\Theta})$ gives the likelihood function for $\mathbf{\Theta}$ [216]. The best fit value, call it $\hat{\mathbf{\Theta}}$, is the point in the paramter space which maximizes the logarithmic-likelihood $\mathcal{L} = -\log L$ for this given data set. The Fisher matrix F is defined as $F_{ij} = \partial^2 \mathcal{L} / \partial\theta_i \partial\theta_j$ evaluated at the best fit point, i.e. it gives the curvature of $\mathcal{L}$ at $\hat{\mathbf{\Theta}}$. It can be shown that if a Gaussian probability distribution is assumed, F takes a very simple form. This allows, for example, in the case of a CMB angular power spectrum given in terms of C_ℓ's and known instrumental noise, for an easy computation of F, again see Ref. [175] for details. The inverse of the Fisher matrix is the covariance matrix T of the parameters θ_i and there exists a theorem by Cramér and Rao that says that for the diagonal entries of T it holds that $\Delta\theta_i \geq \sqrt{T_{ii}}$, $\Delta\theta_i$ being the variance of the model parameter θ_i. This means by calculating the Fisher matrix and from that the covariance matrix we can find a lower bound on the expected error bar on θ_i given a specific data set. With known noise properties for future CMB observation, we are therefore able to predict the sensitiviy on specific model paramters.

Applying this method to our case for constraining or testing $f_{\rm iso}$ with a CMB Stage IV observation, we find a sensitivity on values

$$f_{\rm iso}^{\rm S4,sens} > 0.1\,. \tag{VI.25}$$

VI.3. Implications for Axion Properties

Recall that the isocurvature contribution in the axion energy density, quantified via $f_{\rm iso}$, depends on $K = RH(T_{\rm osc})$, where the oscillation temperature $T_{\rm osc}$ is a function m_a, f_a, and depends on the explicit temperature dependence of the axion mass, cf. Eq. (III.43). Therefore, a limit on $f_{\rm iso}$ can be translated to constraints on the axion properties via Eq. (VI.17). Our procedure to extract these is the following. First, we choose a specific setup for the temperature dependent axion mass in terms of the paramters n and b, cf. Eq. (VI.13). Then, demanding that the axion should be all the DM allows us to fix the combination f_a and m_a via the relation $\rho_{a0} = \rho_{\rm DM}$ and the axion energy density today ρ_{a0} can be calculated via Eq. (III.47). This relation defines the DM axion mass. Given the fixed pairs (f_a, m_a) that yield $\Omega_a h^2 = 0.1$, we can determine the oscillation temperature $T_{\rm osc}$ and with that the size of the horizon $H(T_{\rm osc})$. This determines $f_{\rm iso}$ as a function of the DM axion mass m_a.

In our expressions for $T_{\rm osc}$, as well as for ρ_{a0}, the relativistic degrees of freedom as a function of temperature, $g_*(T)$ and $g_{s*}(T)$, enter. So far, when dealing with the QCD axion, it was always $T_{\rm osc} > 100$ MeV and we could use the results provided by Borsanyi et al's lattice calculations in Ref. [60] which apply for these temperatures. But for low mass axions the oscillation temperature might be below 100 MeV. For having $g_*(T)$ and $g_{s*}(T)$ also for temperatures down to $T \sim 1$ eV, we take the results from Ref. [217] and use a cubic spline interpolation for the tabulated values therein to get continous functions. Still, we have to keep in mind that $T_{\rm osc}$ must be above the temperature at matter-radiation-equality, ~ 1 eV, for the axion being the DM. But we will see that for the scenarios we are looking at, this is always the case.

For post-inflation symmetry breaking, the natural upper limit for f_a is the reaheating $T_{\rm RH}$, as discussed before. For the reheating temperature we use again the estimate $T_{\rm RH} < 10^{17}$ GeV from Abbott and Preskill in Ref. [139] as an upper limit. Note that by fixing the axion energy density to the present DM density, the upper limit on f_a implies a lower limit on the axion mass m_a.

Taking all this into account, we can calculate $f_{\rm iso}$ via Eq. (VI.17) as a function of the zero temperature DM axion mass m_a. To include the theoretical uncertainty on the explicit power spectrum of the isocurvature fluctuations we vary the constant C between 0.01 and 1. The results are given in Fig. VI.2, VI.3, and VI.4 where we indicate also the limit extracted from the Planck CMB data, as well as a projection for the sensitivity of future Stage IV obseravtions.

To understand how to read this plots let us take, for example, the parameter choice $b = 10$ and $n = 4$ in Fig. VI.2 and start with the lower left panel. All of the red line which lies above the Planck limit (dotted) can be ruled out for giving a too large isocurvature contribution. In this specific case, this translate to the limit on the axion mass in the range $m_a \lesssim 10^{-17}$ eV ($m_a \lesssim 10^{-19\ \rm eV}$) for $C = 1$ ($C = 0.01$). From the red curve in the upper left panel of Fig. VI.2 we can read off which breaking scale f_a corresponds to a given mass m_a, for giving the right energy density to explain DM. We see that for very low masses, high f_a are needed to still fulfill $\Omega_a h^2 = 0.1$. With $f_a < 10^{17}$ GeV, we find that a lower bound for our limits on the axion mass is $m_a \sim 10^{-24}$ eV. Hence, we conclude that for this choice of parameters, we can exclude axion masses in a range 10^{-24} eV $\lesssim m_a \lesssim 10^{-17}(10^{-19})$ eV when setting $C = 1$ ($C = 0.01$). This means our limits cover five to seven orders in magnitude, with the Planck data alone. Looking at the intersection of the red curve with the indicated line of the CMB Stage IV sensitivity (dashed), we see that these limits could be increased about at least one order of magnitude in the forseeable future.

The plots in the other two panels in Fig. VI.2 underline that for our choice of parameters, the oscillation temperature, shown on the top right, is always well above the temperature at matter-radiation equality, $T \sim$ eV and also K is always bigger than our pivot scale $k_* = 0.05$ Mpc. This means that the axion does not only has the right amount for being the DM but also that it behaves accordingly, i.e. it starts to oscillate before matter-radiation equality. Knowing that $K > k_*$ gives an a posteriori justification that we have assumed an all-the-way flat power

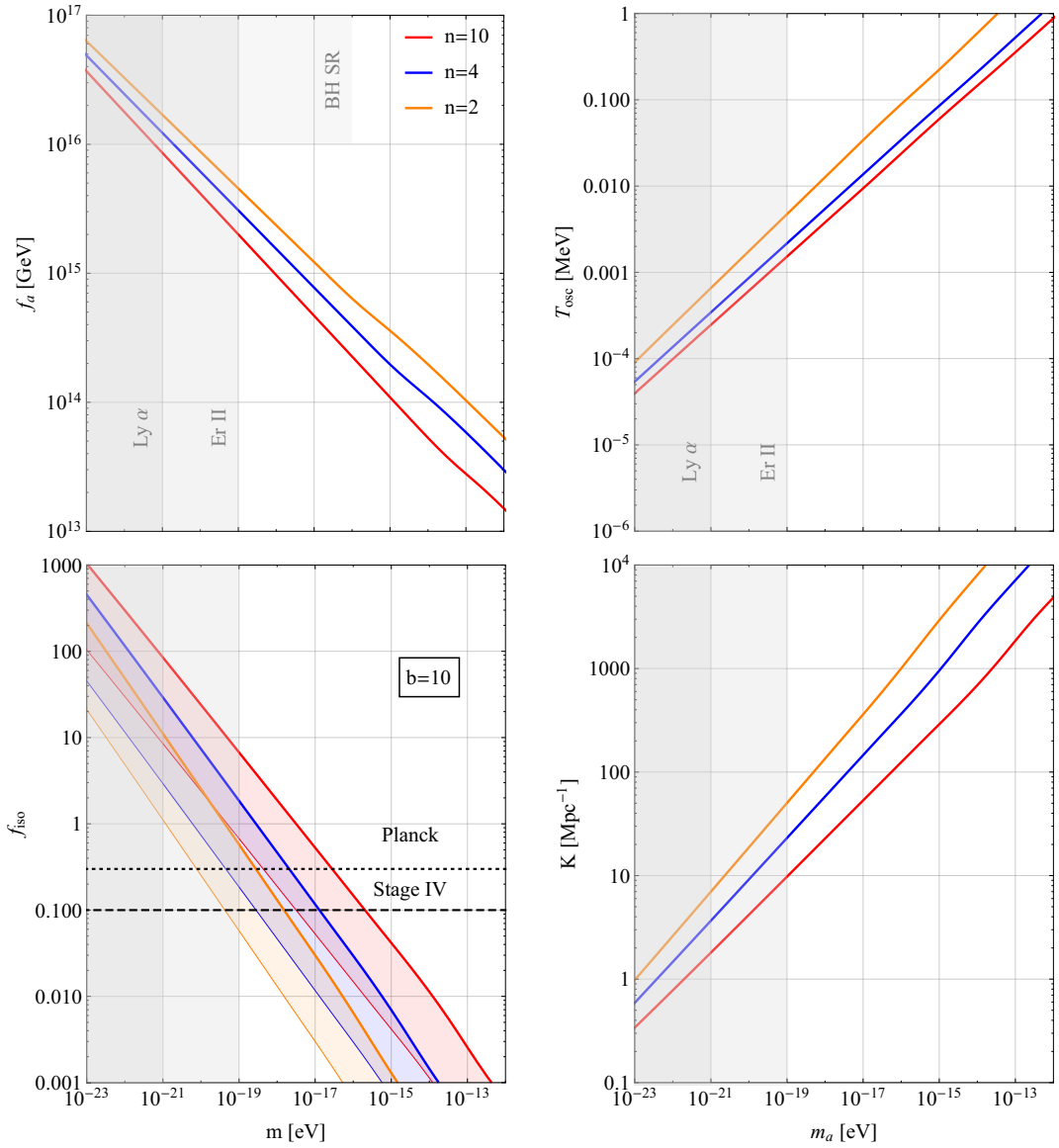

Figure VI.2.: Post-inflation Peccei-Quinn Breaking and CMB Constraints I. The upper left panel shows the relation between the zero temperature axion mass m_a and the Peccei-Quinn breaking scale f_a when fixing the axion energy density to the observed DM density in our Universe. We choose different parmeters for the temperature dependent axion mass, cf. Eq. (VI.13). For all curves we fix $b = 10$ and vary $n = 10, 4, 2$ (red, blue, orange). The temperature $T_{\rm osc}$ where the field starts to oscillates and begins to behave as DM is shown in the upper right panel. This is always well before matter-radiation equality where $T \sim$ eV. In the lower left panel we present the contribution of the isocurvature fluctuations with respect to the adiabtic fluctuation at the comoving scale $k_* = 0.05$ Mpc^{-1} in terms of the parameter $f_{\rm iso}$, cf. Eq. (VI.17) for its definition. Thick lines corrspond to setting $C = 1$ and thin lines $C = 0.01$. We also indicate the limit on $f_{\rm iso}$ coming from Planck observations and a projection of the sensitivity of future Stage IV observations. The lower right panel shows the comoving scale K of the cuf-off in the isocurvature power spectrum to underline that it is always $K \gg k_*$. The shaded areas correspond to possible constraints on the axion mass coming from Lyman α (Ly α), Eridanus II (Er II), and BH superradiance (BH SR).

spectrum for the isocurvature fluctuations and did not include the actual cut-off, when setting the initial conditions for solving the Boltzmann equations, see our discussion in the previous section.

In the plots we also include the existing constraints on ULA masses which we have reviewed in Sec. VI.1. We see that a large part of the limits we find lies in a region which is already strongly constrained from the Lyman-α observation. Here, we should in fact inlcude the axion Jeans scale in the evolution equation of the density fluctuations. However, as discussed before, it will mainly affect the matter-power spectrum and not the CMB anisotropies. We expect that our findings that the axion produces too large isocurvature fluctuations in this mass range will not be affected. Further, there is an overlap with the recent results from the study of the star cluster heating in Eridanus II caused by FDM halo cores. Again, in our opinion these results have yet to be confirmed. Here, our limits give an independent constraint on the ULA mass. Including also the constraints from BH SR we observe that for our setup f_a is always below $\sim 10^{16}$ GeV. Recall that this marks a lower limit on f_a for the SR limits since for $f_a < 10^{16}$ GeV the self-interactions of the axion field can spoil the BH spin-down. This means that in our case the SR constraints on m_a do not apply and here we are able to constrain ULA masses in a so far untouched region.

Looking at the other two curves in Fig. VI.2 as well as at Fig. VI.3 and VI.4, we find that also for other parameter choices large parts of the low mass end of the parameter space can be tested or already exluded with our study. The strongest limits are found for choices of low b and high n, as already anticipated with our estimate in Eq. (VI.12). For $n = 10$ and $b = 0.01$ we find that between eight and ten orders of magnitude for the axion mass can be excluded, this means the mass range 10^{-25} eV $\lesssim m_a \lesssim 10^{-15}(10^{-17})$ eV for $C = 1$ ($C = 0.01$).

The parameter choice $b = 1$ and $n = 0$ might be understood as the most conservative scenario since it gives the weakest constraints. Note that in this scenario the mass is not generated dynamically, but is assumed to be constant. By the weakest constraint we mean that the least of the axion mass paramter space is excluded. However, these limits include the contstraints on the models where the mass is generated dynamically. From this we can conclude that a model-indepedent, most conservative exclusion limit on the axion mass, from our study on the isocurvature fluctuations and its impact on the CMB can be set to

$$10^{-24}\ \text{eV} \lesssim m_a \lesssim 10^{-21} - 10^{-19}\ \text{eV} \tag{VI.26}$$

with the recent Planck data, including the theoretical uncertainty on the actual amplitude of the isocurvature power spectrum. With our projected sensitiv for future Stage IV sensitivity, we find that the limit might become

$$10^{-24}\ \text{eV} \lesssim m_a \lesssim 10^{-20} - 10^{-18}\ \text{eV} \tag{VI.27}$$

in the foreseeable future.

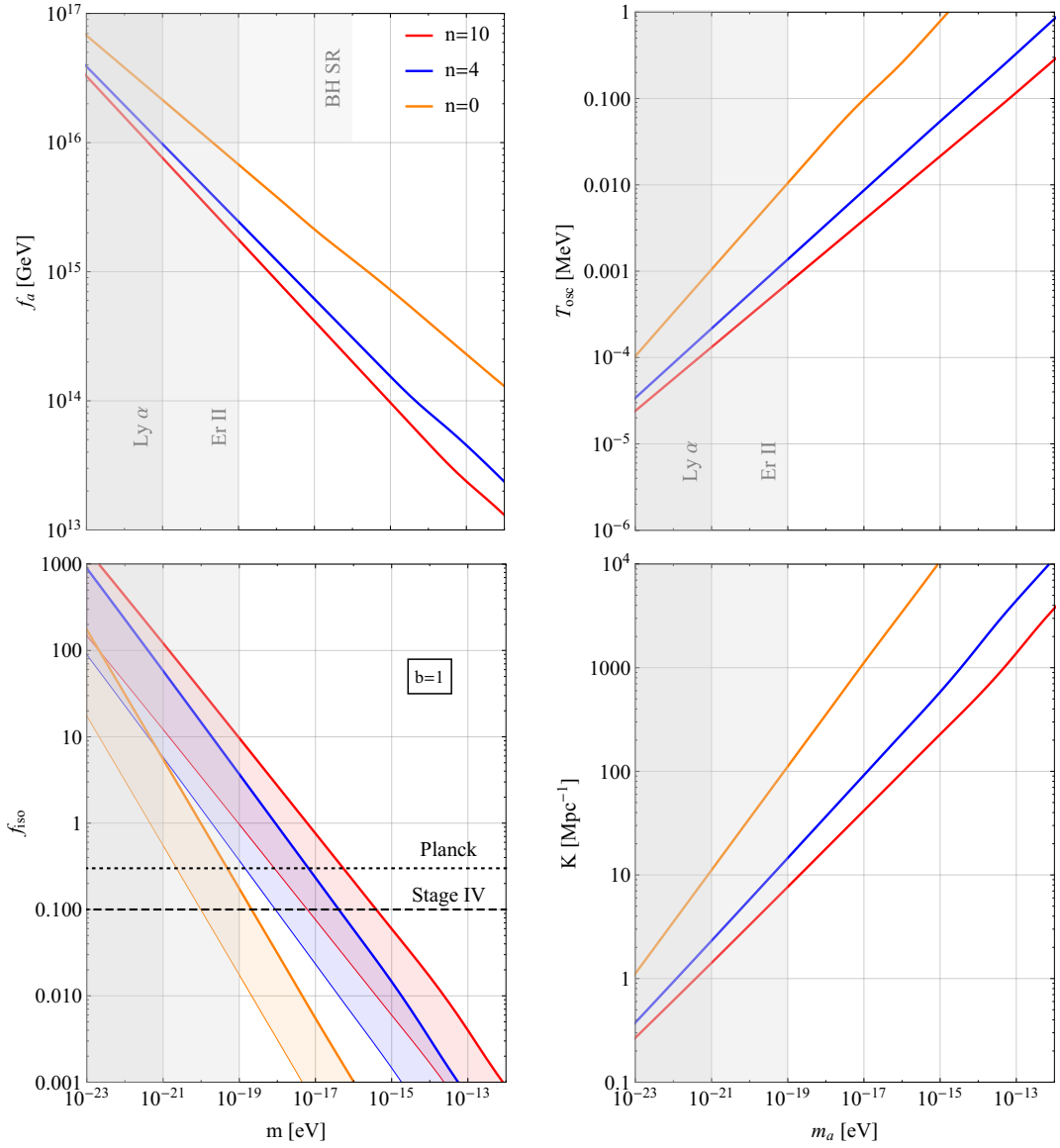

Figure VI.3.: Post-inflation Peccei-Quinn Breaking and CMB Constraints II. The information given in the caption of Fig. VI.2 applies also to these plots. The only difference is that we choose different paramters for the temperature dependent axion mass. Note that $b = 1$ and $n = 0$ corresponds to a constant axion mass.

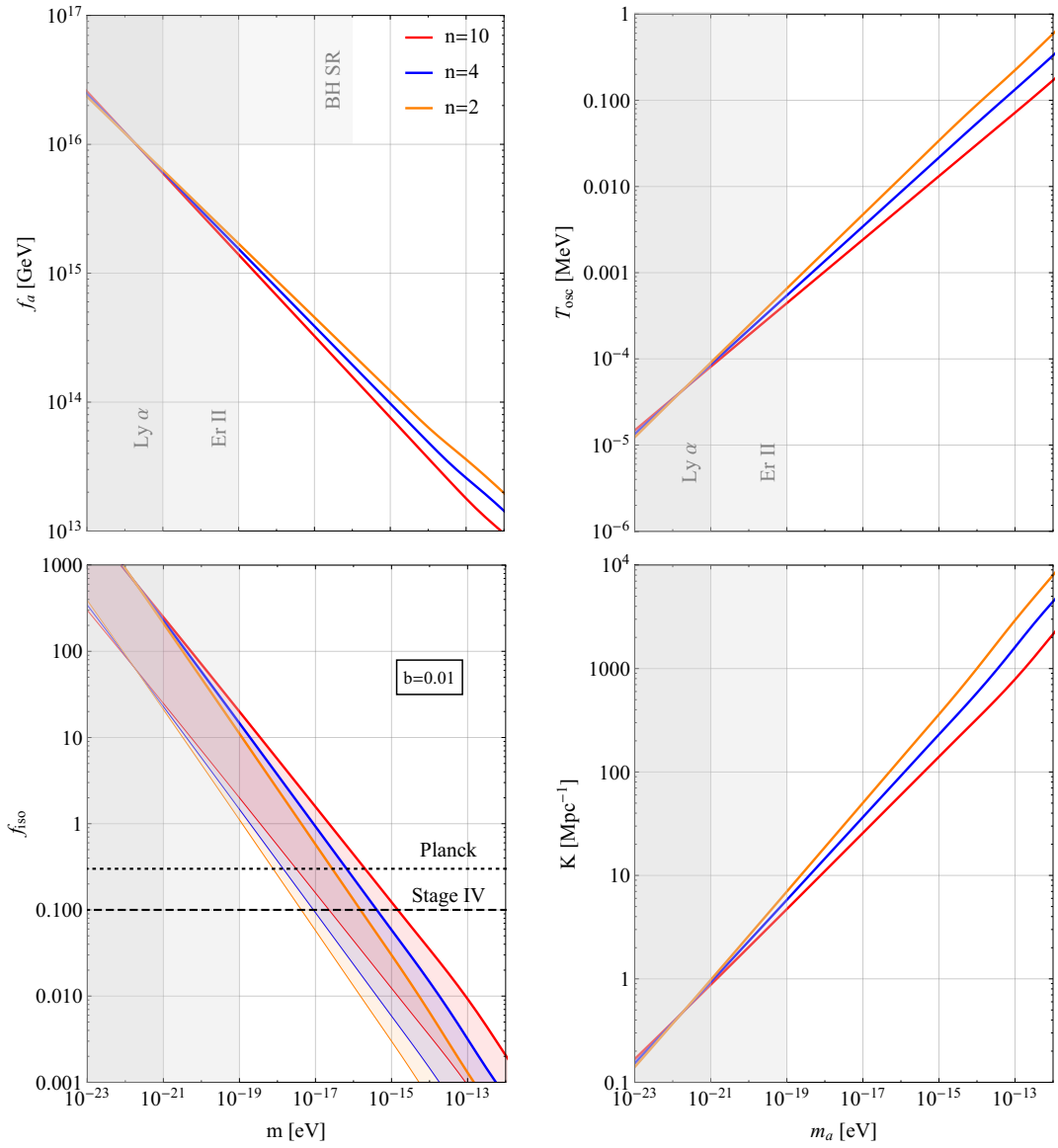

Figure VI.4.: Post-inflation Peccei-Quinn Breaking and CMB Constraints III. The information given in the caption of Fig. VI.2 applies also to these plots. The only difference is that we choose different paramters for the temperature dependent axion mass.

VII. Summary and Outlook

In the present work, we have focused on discussing phenomenological implications for the axion DM being produced by the vacuum realignment mechanism in a post-inflation Peccei-Quinn breaking scenario. Figure VII.1 summarizes the main ideas and shows some of the highlights of the studies we have presented.

After reviewing the Peccei-Quinn solution of the strong CP problem and the origin of the QCD axion, we have considered the cosmological production mechanisms of axion DM in some detail with an emphasis on the vacuum realignment. For that, we have derived useful quantitative estimates for the axion DM abundance valid for the QCD case, as well as for ALPs.

Much of this dissertation is dedicated to the study of the formation of axion miniclusters. These occur when large isocurvature fluctuations in the axion energy density decouple from the Hubble flow and collapse into gravitationally bound objects. This is a very generic effect, expected to happen as long as the Peccei-Quinn symmetry is broken after inflation. By a semi-analytic solution of the evolution equations of the QCD axion field and by applying statistical methods, we were able to calculate the power spectrum of the axion energy density fluctuations in this scenario. Our result for the power spectrum shows the typical characteristics of a white noise random field on large scales. On smaller scales it has a correlation length a little smaller than the comoving Hubble horizon at the time the field starts to oscillate. The power spectrum was used as input for a calculation of the axion minicluster mass function for which we have derived a modified Press & Schechter method. This has allowed us to not only calculate the minicluster distribution in mass but also in size. We have found that the two-dimensional mass function is nicely peaked around a characteristic miniclusters mass and size. For example, setting the Peccei-Quinn breaking scale at $f_a = 10^{12}$ GeV, the characteristic minicluster mass is $M_{\rm MC} \sim 10^{-13} M_\odot$ and a typical size is about 10^6 km. Note that we find that the typical minicluster mass is somewhat smaller than naively expected [32].

For deriving the power spectrum of the axion energy density fluctuations we had to make some physically motivated assumptions on the initial conditions of the axion field. Since we have used the harmonic approximation of the axion potential all nonlinear effects in the field evolution have been neglected. By comparing our results with the outcome of Ref. [108] where recently numerical simulations of the full nonlinear axion field evolution were performed we could identify some shortcomings of our approach. However, we have concluded that with our method we are able to describe the part of the power spectrum predominantly responsible for the formation of axion miniclusters well enough and avoid natural drawbacks of numerical simulations. Still, it would be interesting to use the power spectrum found in Ref. [108] in our modified Press & Schechter method and calculate the resulting minicluster distribution, to compare the outcome with our results.

We have also briefly commented on the possibility of applying our method for deriving the minicluster mass function to the more general case of ALPs. This is easily possible by just assuming a different temperature dependence for the axion mass than in the QCD case. We can expect a much larger variety of possible minicluster masses and sizes. For very light ALPs it could even be that the miniclusters are as heavy as $M_\odot$, opening up the possibility for direct detection via for example gravitational lensing. More detailed studies of ALP miniclusters will be presented in Ref. [137].

Another hitherto unanswered question was whether axion miniclusters can collapse into an

axion star, or whether they are more likely to enter an incoherent, virialized state after decoupling from the Hubble expansion. We have tried to solve this puzzle by numerically simulating the evolution of an axion overdensity under its own gravity. Since it turned out to be numerically prohibitive to use the actual properties of the miniclusters we have found before, we have rather considered a toy model of a scalar cloud, which should serve as a good approximation for the miniclusters. We have found that a dilute initial cloud eventually collapses into an equilibrium state which could be characterized by an oscillating ratio of kinetic to potential energy, similar to what we would expect for a virialized cloud. Thus, our results hint for the miniclusters not collapsing into a static axion star but indeed rather taking some virialized equilibrium state. However, the results are not yet conclusive and more simulations are needed. Still, our findings and especially the methods derived in the present work will be very useful for this.

In the last part of this dissertation, we have discussed the implications of the isocurvature fluctuations arising in the in post-inflation Peccei-Quinn breaking scenario for the more general case of ALPs. We have found that for ultra-light ALPs (ULAs) they can have sizeable effects in cosmological large-scale observables, like the CMB. Using the white noise power spectrum as input for the axion isocurvature fluctuations we have solved the cosmological Boltzmann equations and therefore were able to study their impact on the CMB anisotropy spectrum. It turned out that with the recent Planck data their contribution f_{iso} with respect to the adiabatic fluctuations in the DM component can already be strongly constrained. We find $f_{\mathrm{iso}} < 0.3$. Translating the limit on f_{iso} to the properties of the axion DM, we find that we can exclude ALP DM masses in a range 10^{-24} eV $- 10^{-15}$ eV. Where the low mass end is already strongly constrained by other astrophysical and cosmological observations, the limits on axion masses $m_a \gtrsim 10^{-20}$ eV provide new insights.

We can sum up that, with the work presented here, we have made an important contribution to better understanding the true nature of the DM. Assuming that it is composed of QCD axions, the formation of miniclusters is a very likely effect and a solid comprehension of their formation history is essential, especially for interpreting the results of direct detection experiments or for coming up with new experimental avenues. If, on the other hand, the DM would occur in the form of very light ALPs, we were able to show that large-scale observables can be used to put strong constraints on the allowed ALP DM masses.

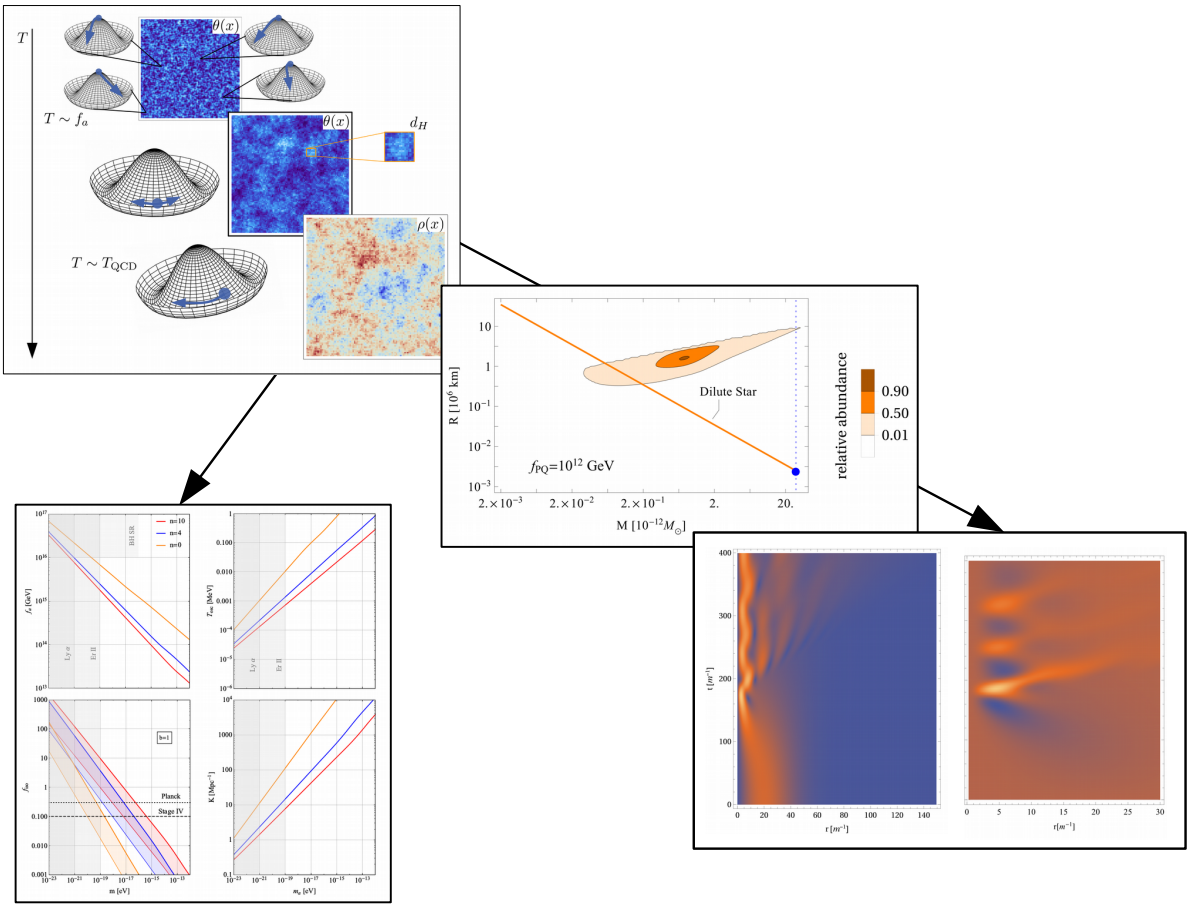

Figure VII.1.: Highlights of the present Work. This sketch summarizes the main ideas and outcomes of the present work. The first panel (cf. Fig. IV.1) sketches the vacuum realignment of the axion field in a post-inflation Peccei-Quinn breaking scenario which leads to large isocurvature fluctuations in the axion energy densitiy ρ. In the following large panels on the right branch, we show the implications in the QCD scenario where the isocurvature fluctuations are very small in the cosmological context. Here, the most interesting effect is the formation of dense axion miniclusters. The calculation of their distribution in mass and size is one of the major outcomes of the present work. The result can be compared with the static axion star configurations. This is indicated in the second panel (cf. Fig. V.1) on the right-hand side. Since we have realized that the miniclusters sit far above the axion star branch, we have considered the dynamical collapse of the miniclusters in numerical simulations for studying what kind of equilibrium configuration they take after decoupling from the Hubble expansion. The evolution of the minicluster density and the particle current during the collapse are shown in the last panel on the right (cf. Fig. V.2 and V.3). In the left branch, we indicate that for ultra-light ALPs the isocurvature fluctuations have other phenomenological implications. Namely, we have found that they lead to modifications of the CMB spectrum. We have used this effect to find some strong constraints on the allowed ALP DM mass. As teased in the panel on the lower left side (cf. Fig. VI.3). All the plots can be found in full-size in the corresponding chapters as indicated in the brackets.

Appendix A.
Units

In this appendix, we discuss the units used in the present work and give some useful relations.

If not stated otherwise, we work in natural units: $c = \hbar = k_{\mathrm{B}} = 1$. In this system there is only one fundamental dimension, namely energy.

With $c = 3.0 \cdot 10^8$ m/s, $\hbar = h/2\pi = 1.05 \cdot 10^{-34}$ kg $\cdot$ m^2/s $= 6.6 \cdot 10^{25}$ GeV $\cdot$ s, and $k_B = 8.6 \cdot 10^{-14}$ GeV$/K$ this implies the conversion rules

$$1 \text{ s} = 1.5 \cdot 10^{24} \text{ GeV}^{-1}\,, \tag{A.1}$$

$$1 \text{ m} = 5.0 \cdot 10^{15} \text{ GeV}^{-1}\,, \tag{A.2}$$

$$1 \text{ K} = 8.6 \cdot 10^{-14} \text{ GeV}\,, \tag{A.3}$$

between the SI system and natural units. Recall that 1 eV $= 1.6 \cdot 10^{-19}$ kg $\cdot$ m^2/s^2 and therefore

$$1 \text{ kg} = 5.63 \cdot 10^{26} \text{ GeV}\,. \tag{A.4}$$

The Planck mass is defined as

$$M_{\mathrm{Pl}} = \sqrt{\frac{c\hbar}{G_N}}\,, \tag{A.5}$$

where $G_N = 6.67 \cdot 10^{-11}$ m^{3}kg^{-2}s^{-2} is Newton's gravitational constant. In natural units it is

$$M_{\mathrm{Pl}} = 1.22 \cdot 10^{19} \text{ GeV}\,. \tag{A.6}$$

Spatial distances in astrophysics or cosmology are often measured in parsec, abbreviated with pc. In SI units, it is

$$1 \text{ pc} = 3.1 \cdot 10^{16} \text{ m}\,. \tag{A.7}$$

In natural units, we can express a parsec via an inverse energy, and the following conversion rule holds:

$$1 \text{ Mpc} = 1.55 \cdot 10^{38} \text{ GeV}^{-1}\,. \tag{A.8}$$

A handy measure for masses of astrophysical objects is the mass of our sun $M_\odot$. The solar mass is about

$$M_\odot \simeq 1.99 \cdot 10^{30} \text{ kg} \tag{A.9}$$

or equivalently

$$M_\odot \simeq 1.11 \cdot 10^{57} \text{ GeV}\,. \tag{A.10}$$

Appendix B.

Axion-electrodynamics for DM Detection

In this appendix, we discuss the axion-photon interactions, given in the Lagrangian in Eq. (II.21), in a little more detail. Thereby, we present results of a quantum field theoretical calculation of the induced electric and magnetic fields caused by the interaction of the axion DM field with a strong electromagnetic field. The outcome of this study is published in Ref. [67].

First, we notice that the axion-photon interactions of the form $\propto g_{a\gamma\gamma} F\tilde{F}$ lead to the modified Maxwell equations:

$$\vec{\nabla} \cdot \vec{E} = \rho_e - g_{a\gamma\gamma} \vec{B} \cdot \vec{\nabla} a \,, \tag{B.1}$$

$$\vec{\nabla} \times \vec{B} - \frac{\partial \vec{E}}{\partial t} = \vec{j}_e - g_{a\gamma\gamma} \left(\vec{E} \times \vec{\nabla} a - \vec{B} \frac{\partial a}{\partial t} \right) , \tag{B.2}$$

where ρ_e and $\vec{j}_e$ are the usual electric charge and current density. Assuming a homogeneous axion field, we see that the axion interaction with an external magnetic field, call it $\vec{B}^{\text{ext}}$, leads to an electric field

$$\vec{E}^{\text{ind}} = -g_{a\gamma\gamma} a \vec{B}^{\text{ext}} \,. \tag{B.3}$$

If the axion field a is the DM field, we can make the following simplified ansatz:

$$a = a_0 \cos m_a t \tag{B.4}$$

where the normalization a_0 is fixed by setting ρ_a to the local DM energy density $\rho_{\text{DM}} = 0.3\ \text{GeV/cm}^3$. Note that in this case, in a 7 T magnetic field we can expect an induced electric field with an amplitude of about 10^{-14} V/m if the axion has a mass of $m_a \sim 10^{-5}$ eV and a coupling $g_{a\gamma\gamma} \sim 10^{-10}$ GeV. This is an extremely tiny elctric field. But still it is the idea of the usual DM haloscopes to make this tiny field visible, usually by some kind of resonance effects [43].

The reason why deal with this topic is that in another project, where general interactions of SM particles with an axion background field are considered, the idea of using a Penning trap as an axion DM haloscope was brought up, see Ref. [218] for more details. In short, a Penning trap is a device with a strong homgeneous magnetic field and an elecrtric quadrupole field which allows to trap charged particles on a complicated spiral-like trajectory which is characterized by three different circular frequencies. See Ref. [219] for a comprehensive review of Penning traps. It turns out that if one of the frequencies is in resonance with the frequency of the axion background field, i.e. m_a, the trapped particle becomes sensitive to the axion-induced electric field. Using typical circular frequencies of a Penning trap, we have found that an axion mass of $m_a \sim 10^{-10} - 10^{-7}$ eV could lead to a resonant response of the trapped particle.

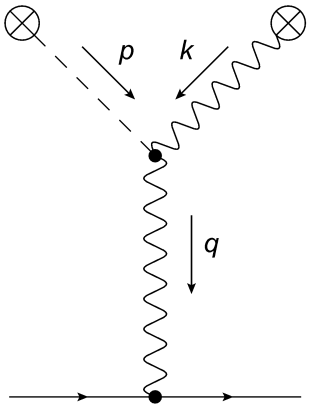

Figure B.1.: Feynman Diagram for Electron Interaction with an Axion Background Field and an external Photon Field. Corresponds to Fig. 1 in Ref. [67].

However, recently there has been a debate about how large the axion-induced electromagnetic fields actually are in case that the spatial dimension R of the external magnetic field is smaller than the Compton wavelength λ of the axion, cf. Refs. [220–222]. Ouellet and Bogorad in Ref. [220], as well as Kim et al in Ref. [221], argue by solving the modified Maxwell equations with the appropriate boundary conditions that the induced electric field is in fact suppressed by the small number $(R/\lambda)^2$. Tobar et al, on the other hand, claim in Ref. [222] that the induced field should not be suppressed, relying on an earlier work by J.E. Kim [223]. Note that with the axion Compton wavelength given by

$$\lambda = \frac{2\pi}{m_a} \approx 12\,\mathrm{m}\left(\frac{10^{-7}\,\mathrm{eV}}{m_a}\right) \tag{B.5}$$

this effect becomes important for masses $m_a < 10^{-7}$ eV and therefore also for our idea of detecting DM axions with a Penning trap where the magnetic field has dimensions of about $R \sim$ cm.

To add to this discussion and to understand if the axion-induced fields are suppressed or not, we try to study the axion-photon interactions from a quantum field point of view. Note that similar calculations were done by Hill in Refs. [224, 225] for calculating an induced oscillating dipole moment by axion interactions. All details of our study can be found in Ref. [67]. At this point, we outline the applied method and discuss the main result.

For understanding the effective field an electron sees that travels through an axion as well as photon background field, we look at the Feynman diagram shown in Fig. B.1. It turns out that by using standard quantum field techniques, we can write the transition amplitude $\mathcal{A}$ for the proccess $e \to e'$ shown in Fig. B.1 as

$$\mathcal{A} = -\mathrm{i}\int \mathrm{d}^4x J^\mu(x) A_\mu^{\mathrm{ind}}(x)\,, \tag{B.6}$$

where $j^\mu = e\bar{\psi}\gamma^\mu\psi$ is the usual electromagnetic current and

$$A_\mu^{\mathrm{ind}}(x) = \mathrm{i}g_{a\gamma\gamma}\int \mathrm{d}^4y D_{\mu\nu}(x-y)\partial_\rho a(y)\tilde{F}^{\rho\nu}(y)\,. \tag{B.7}$$

is the effective vector potential induced by the interaction of the external axion and the photon field. The photon propagator in the Feynman gauge is given by

$$D_{\mu\nu}(x-y) = \int \frac{\mathrm{d}^4q}{(2\pi)^4}\frac{-\mathrm{i}g_{\mu\nu}}{q^2+\mathrm{i}\epsilon}e^{-iq(x-y)}\,. \tag{B.8}$$

In case of our simple ansatz for the DM axion field in Eq. (B.4) and an external static magnetic field, we find that this vector potential leads to induced electric and magnetic fields of the form:

$$\vec{E}^{\text{ind}}(x) = -\frac{\partial \vec{A}^{\text{ind}}}{\partial t} = -g_{a\gamma\gamma} a_0 m_a^2 \, \mathrm{e}^{-\mathrm{i}m_a t} \int \frac{\mathrm{d}^3 q}{(2\pi)^3} \, \frac{\mathrm{e}^{\mathrm{i}\vec{q}\cdot\vec{x}}}{m_a^2 - \vec{q}^{\,2} + \mathrm{i}\epsilon} \vec{B}^{\text{ext}}(\vec{q}) \,, \tag{B.9}$$

$$\vec{B}^{\text{ind}}(x) = \vec{\nabla} \times \vec{A}^{\text{ind}} = -g_{a\gamma\gamma} a_0 m_a \, e^{-i m_a t} \int \frac{\mathrm{d}^3 q}{(2\pi)^3} \, \frac{\mathrm{e}^{\mathrm{i}\vec{q}\cdot\vec{x}}}{m_a^2 - \vec{q}^{\,2} + \mathrm{i}\epsilon} \vec{q} \times \vec{B}^{\text{ext}}(\vec{q}) \,. \tag{B.10}$$

We see that E^{ind} and B^{ind} depend on the geometry of the external magnetic field which is encoded in its Fourier transform $B^{\text{ext}}(q)$.

We can now look the at two extreme cases $R \gg \lambda$ and $R \ll \lambda$. In the first case, $B(\vec{q})$ will be dominated by the low q modes and we have $m_a^2 \gg q^2$ in the denominator of the integral. Thus, we recover for E^{ind} the form already given in Eq. (B.3). However, for $R \ll \lambda$, we have to properly evaluate the integral, also taking care of the poles. We find that

$$\vec{E}^{\text{ind}}(x) \simeq -g_{a\gamma\gamma} a_0 \, \vec{B}_0 \mathrm{e}^{-\mathrm{i}m_a t} (R m_a)^2 \,. \tag{B.11}$$

I.e. the induced field is indeed suppressed if the size of the magnetic field is smaller than the Compton wavelength of the axion. Hence, we agree rather with the findings in Refs. [220, 221] than the ones in Ref. [222]. Our ansatz allows for a neat interpretation of this suppression effect in terms of the momentum the external magnetic field can provide depending on its geometry.

Appendix C.

Rewriting the Axion Evolution Equation in Terms of Temperature

In the following, we give some details on deriving Eq. (IV.23), i.e. on rewriting the evolution equation of f_k,

$$\ddot{f}_k + 3H(T)\dot{f} + \frac{k^2}{R^2} f_k + m_a^2(T) f_k = 0\,, \tag{C.1}$$

in terms of temperature being the independent variable instead of time. First we note that

$$\frac{\mathrm{d}f_k}{\mathrm{d}t} = \frac{\mathrm{d}f_k}{\mathrm{d}T}\frac{\mathrm{d}T}{\mathrm{d}t} \tag{C.2}$$

and

$$\frac{\mathrm{d}^2 f_k}{\mathrm{d}t^2} = \frac{\mathrm{d}}{\mathrm{d}t}\left(\frac{\mathrm{d}f_k}{\mathrm{d}T}\frac{\mathrm{d}T}{\mathrm{d}t}\right) \tag{C.3}$$

$$= \frac{\mathrm{d}f_k}{\mathrm{d}T}\frac{\mathrm{d}^2 T}{\mathrm{d}t^2} + \frac{\mathrm{d}T}{\mathrm{d}t}\frac{\mathrm{d}}{\mathrm{d}t}\frac{\mathrm{d}f_k}{\mathrm{d}T}\,. \tag{C.4}$$

With

$$\frac{\mathrm{d}}{\mathrm{d}t}\frac{\mathrm{d}f_k}{\mathrm{d}T} = \frac{\mathrm{d}}{\mathrm{d}T}\frac{\mathrm{d}f_k}{\mathrm{d}t} = \frac{\mathrm{d}}{\mathrm{d}T}\left(\frac{\mathrm{d}f_k}{\mathrm{d}T}\frac{\mathrm{d}T}{\mathrm{d}t}\right) = \frac{\mathrm{d}^2 f_k}{\mathrm{d}T^2}\frac{\mathrm{d}T}{\mathrm{d}t} \tag{C.5}$$

it follows that

$$\frac{\mathrm{d}^2 f_k}{\mathrm{d}t^2} = \frac{\mathrm{d}f_k}{\mathrm{d}T}\frac{\mathrm{d}^2 T}{\mathrm{d}t^2} + \left(\frac{\mathrm{d}T}{\mathrm{d}t}\right)^2 \frac{\mathrm{d}^2 f_k}{\mathrm{d}T^2}\,. \tag{C.6}$$

Plugging this into the evolution equation, leads to

$$\frac{\mathrm{d}^2 f_k}{\mathrm{d}T^2} + \left(3H(T)\frac{\mathrm{d}t}{\mathrm{d}T} + \frac{\mathrm{d}^2 T}{\mathrm{d}t^2}\Big/\frac{\mathrm{d}T}{\mathrm{d}t}\right)\frac{\mathrm{d}f_k}{\mathrm{d}T} + \left(\frac{k^2}{a^2} + m_a^2(T)\right)\left(\frac{\mathrm{d}t}{\mathrm{d}T}\right)^2 f_k = 0\,. \tag{C.7}$$

Eventually we note that

$$\frac{\mathrm{d}^2 T}{\mathrm{d}t^2}\Big/\frac{\mathrm{d}T}{\mathrm{d}t} = \frac{\mathrm{d}^2 T}{\mathrm{d}t^2}\frac{\mathrm{d}t}{\mathrm{d}T} \tag{C.8}$$

$$= \underbrace{\frac{\mathrm{d}}{\mathrm{d}t}\left[\frac{\mathrm{d}T}{\mathrm{d}t}\frac{\mathrm{d}t}{\mathrm{d}T}\right]}_{=0} - \frac{\mathrm{d}T}{\mathrm{d}t}\frac{\mathrm{d}}{\mathrm{d}t}\left(\frac{\mathrm{d}t}{\mathrm{d}T}\right) \tag{C.9}$$

$$= -\frac{\mathrm{d}T}{\mathrm{d}t}\frac{\mathrm{d}^2 t}{\mathrm{d}T^2} = -\frac{\mathrm{d}^2 t}{\mathrm{d}T^2}\Big/\frac{\mathrm{d}t}{\mathrm{d}T}\,. \tag{C.10}$$

With that we arrive at the result given in Eq. (IV.24). Note that a similar relation is used in Ref. [96].

For deriving $\mathrm{d}t/\mathrm{d}T$ in Eq. (IV.25) we first recall that the Friedman equations in a radiation dominated universe can be written as:

$$\left(\frac{\dot{R}}{R}\right)^2 = \frac{8\pi}{3}\frac{\rho}{M_{\mathrm{Pl}}^2}\,, \tag{C.11}$$

$$\dot{\rho} = -3H(\rho + p) = -3HsT\,. \tag{C.12}$$

Note that the equation in the second line, namely using $s = (\rho + p)/T$, only holds if all relativistic particle species are in equilibrium, i.e. only for temperatures $T \gtrsim 1$ MeV before $e^+ - e^-$ annihiliation. But since we are focussing on temperatures $T > 100$ MeV, this does not affect our studies for the QCD axion. However, this can become important when considering the cosmological evolution of the ALP field, see also Ref. [137].

The expressions for the energy density of radiation reads

$$\rho = \frac{\pi^2}{30} g_* T^4 \tag{C.13}$$

and for the entropy density

$$s = \frac{2\pi^2}{45} g_{s*} T^3 \tag{C.14}$$

which can be found for example in classical textbooks like Ref. [79]. Using Eq. (C.13), (C.14), and (C.11) in the second Friedmann equation (C.12), one can show that the time as function of temperature is determined via

$$\frac{\mathrm{d}t}{\mathrm{d}T} = -M_{\mathrm{Pl}}\sqrt{\frac{45}{64\pi^3}}\frac{1}{T^3 g_{s*}\sqrt{g_*}}\left(4g_* + \frac{\mathrm{d}g_*}{\mathrm{d}T}T\right)\,. \tag{C.15}$$

Using this result together with Eq. (C.13) in the first Friedmann equation Eq. (C.11) gives

$$\frac{\mathrm{d}R}{\mathrm{d}T} = -\frac{1}{4}\frac{1}{g_{s*}T}\left(4g_* + \frac{\mathrm{d}g_*}{\mathrm{d}T}T\right)R\,. \tag{C.16}$$

Appendix D.

Non-relativistic Approximation of the Axion Field

Starting from the general action

$$S = \int \mathrm{d}^4x \, \sqrt{-g} \left[-\frac{1}{2} g_{\mu\nu} \partial^\mu a \partial^\nu a - V(a) + \frac{\mathcal{R}}{16\pi G_N} \right] \tag{D.1}$$

of a localized scalar cloud, we want to derive the Gross-Pitaevskii-Poisson system in Eq. (V.11) and (V.12) using the weak gravity limit $\Phi_N \ll 1$ and the non-relativistic limit for the field a.

In the weak gravitiy limit, we can write the metric $g_{\mu\nu}$ as [141]:

$$g_{00} = -\left(1 + 2\Phi_N\right) \quad \text{and} \quad g_{ij} = \left(1 - 2\Phi_N\right) \delta_{ij} \, . \tag{D.2}$$

Therefore, the determinant of the metric becomes

$$\sqrt{-g} = \sqrt{\left(1 + 2\Phi_N\right) \left(1 - 2\Phi_N\right)^3} \simeq 1 - 2\Phi_N \, . \tag{D.3}$$

The Ricci scalar in the weak gravity limit reads [141]

$$\mathcal{R} \simeq 2 \left(\nabla \Phi_N\right)^2 \, . \tag{D.4}$$

Using this in Eq. (D.1) we find:

$$S = \int \mathrm{d}^4x \, \left[\frac{\left(\nabla \Phi_N\right)^2}{8\pi G_N} + \frac{1 - 4\Phi_N}{2} \dot{a}^2 - \frac{\left(\nabla a\right)^2}{2} - \left(1 - 2\Phi_N\right) V(a) \right] \, . \tag{D.5}$$

In the non-relativistic limit, we express the axion field as

$$a = \frac{1}{\sqrt{2m}} \left(\phi \mathrm{e}^{\mathrm{i}mt} + \phi^* \mathrm{e}^{-\mathrm{i}mt} \right) \, . \tag{D.6}$$

with $\dot{\phi} \ll m$, $\ddot{\phi} \ll m^2$.

Using this ansatz we note that

$$\dot{a}^2 \simeq m\phi\phi^* + \mathrm{i} \left(\phi\dot{\phi}^* - \dot{\phi}\phi^* \right) \, , \tag{D.7}$$

$$\left(\nabla a\right)^2 \simeq \frac{\left(\nabla\phi\right)\left(\nabla\phi^*\right)}{m} \, , \tag{D.8}$$

$$a^2 \simeq \frac{1}{m} \phi\phi^* \, , \tag{D.9}$$

$$a^4 \simeq \frac{3\phi^2\phi^{*2}}{2m^2} \, . \tag{D.10}$$

Plugging this back into Eq. (D.5) we end with S given in Eq. (V.10). Varying the action S with respect to Φ_N gives the Poisson equation and varying S with respect to ϕ^* the Gross-Pitaevskii equation.

Introducing the canonical momenta $\pi_\phi = \partial\mathcal{L}/\partial\dot{\phi} = \mathrm{i}\phi^*/2$ and $\pi_{\phi^*} = \partial\mathcal{L}/\partial\dot{\phi}^* = -\mathrm{i}\phi/2$ for the fields ϕ and ϕ^*, we can perofrm a Legendre transformation of the Lagrangian $\mathcal{L} = \mathcal{L}(\phi, \dot{\phi}, \phi^*, \dot{\phi}^*, \Phi_N)$ density and simply read off the Hamiltonian from Eq. (V.10). Recall that it has the three contributions:

$$H_{\mathrm{kin}} = \frac{1}{2m}\int \mathrm{d}^3r\ (\nabla\phi)\cdot(\nabla\phi^*)\,, \tag{D.11}$$

$$H_{\mathrm{grav}} = -\frac{1}{2}\int \mathrm{d}^3r\ m\Phi_N\phi\phi^*\,, \tag{D.12}$$

$$H_{\mathrm{self}} = -\int \mathrm{d}^3r\ \frac{1}{16f_a^2}\,(\phi\phi^*)^2\ . \tag{D.13}$$

Next, we want to show how we find the estimate for $H = H_{\mathrm{kin}} + H_{\mathrm{grav}} + H_{\mathrm{self}}$ in Eq. (V.20). For a localized scalar cloud, a reasonable ansatz for the wave function ϕ is of a Gaussian form

$$\phi_i(r) = \frac{\phi_0}{\sqrt{4\pi}\sigma^{3/2}}\mathrm{e}^{-r^2/2\sigma^2}\,, \tag{D.14}$$

where the normalization ϕ_0 as well as the width σ should be determined via the mass M_0 and size R_0 of the cloud. The mass is given by

$$M_0 = 4\pi m\int_0^\infty dr\, r^2|\phi_i|^2\,. \tag{D.15}$$

and therefore

$$\phi_0 = \frac{2M^{1/2}}{\pi^{1/4}m^{1/2}}\,. \tag{D.16}$$

By choosing the Gaussian profile we can only include all the mass M_0 when we extend the integration to infinity. However, we can choose σ such that most of the mass is included in a region of size R_0. This we can accomplish in the following way. It is

$$M(R_0) = 4\pi m\int_0^{R_0} dr\, r^2|\phi|^2 \tag{D.17}$$

$$\underset{z=r/\sigma}{=} 4\pi\frac{M_0}{\pi^{3/2}}\int_0^{R_0/\sigma} dz\, z^2\mathrm{e}^{-z^2}\,. \tag{D.18}$$

Now choosing $R_0/\sigma = 3$ we find

$$\frac{M(R_0)}{M_0} = 0.99956\,, \tag{D.19}$$

i.e. 99.9% of the mass is included in the spherical region with size R_0 which is sufficient for our needs. Hence, as the profile for a spherical symmetric scalar cloud we chose

$$\phi_i(r) = \frac{3^{3/2}}{\pi^{3/4}}\frac{M_0^{1/2}}{m^{1/2}R_0^{3/2}}\exp\left[-\frac{9}{2}\frac{r^2}{R_0^2}\right]\,. \tag{D.20}$$

The potential $\Phi_{N,i}$ of this configuration can be derived by solving the Poisson equation:

$$\Delta\Phi_{N,i} = 4\pi G m\phi_i\phi_i^*\,. \tag{D.21}$$

With our ansatz from Eq. (D.20) this can be done analytically. We find that

$$\Phi_{N,i}(z) = -\frac{(GM_0/R_0)\mathrm{Erf}[3z] + A}{z} + B\,, \tag{D.22}$$

with $z = r/R_0$. The constants A and B should be fixed by the boundary conditions. An obvious one is that the potential shpould vanish at infinity, i.e. $B = 0$. The constant A we can fix by demanding that at $r = R_0$, i.e. $z = 1$, the potential should read

$$\Phi_{N,i}(r = R_0) = -\frac{GM_0}{R_0}\,. \tag{D.23}$$

With $\mathrm{Erf}[3] \simeq 1$ we set $A = 0$ as well. Thus, we end up with

$$\Phi_{N,i}(r) = -\frac{GM_0}{R_0}\left(\frac{r}{R_0}\right)^{-1}\mathrm{Erf}\left[3\frac{r}{R_0}\right]. \tag{D.24}$$

With the form for the wave function and the Newtonian potential at hand, the intregrals in H_{kin}, H_{grav}, and H_{self} can be performed analytically. We find:

$$H_{\mathrm{kin}} = 0.7\frac{M_0}{m^2R_0^2}\,, \tag{D.25}$$

$$H_{\mathrm{grav}} = 0.1\frac{M_0^2}{M_{\mathrm{Pl}}R_0}\,, \tag{D.26}$$

$$H_{\mathrm{self}} = \frac{M_0^2}{f_{\mathrm{PQ}}^2m^2R_0^3}\,. \tag{D.27}$$

Appendix E.

Numerical Approach for Solving the Schrödinger-Poisson System

In the following, we discuss our scheme for numerically solving the Schrödinger-Poisson (SP) system discussed in Sec. V. We use a similar procedure as described in Refs. [118] and [164].

Time-dependent Schrödinger Equation

We start by considering the time-dependent Schrödinger equation.

$$\mathrm{i}\partial_t\psi = H\psi\,. \tag{E.1}$$

For simplicity, let us stick to one spatial dimension for the moment. Here, it is

$$H = \frac{1}{2m}\partial_x^2 + V(x)\,. \tag{E.2}$$

Recall that the time evolution of a wave function ψ following from Eq. (E.1) can be expressed via the time-evolution operator $U(t,t_0)$ as

$$\psi(x,t) = U(t,t_0)\psi(x,t_0) \tag{E.3}$$

For a time-independent Hamiltonian H, it is

$$U(t,t_0) = \exp[-\mathrm{i}H(t-t_0)]\,. \tag{E.4}$$

For a numerical treatment of Eq. (E.1) we have to discretize space and time, i.e. $t \to t_n = n\Delta t$ and $x \to x_j = x_0 + j\Delta x$. It is Δt and Δx the spacing of our grid in time and space, respectively, and in one spatial dimension x_0 correpsonds to the left boundary whereas for some $j = N$, x_N correpsonds the right boundary. Also the wave function in the discretized spacetime is only defined at specific gridpoints (t_n, x_j), therefore

$$\psi(x,t) \to \psi(x_j,t_n) \equiv \psi_j^n\,. \tag{E.5}$$

With Eq. (E.4) the time evolution from (t_n, x_j) to (t_{n+1}, j) is given by

$$\psi_j^{n+1} = U(\Delta t)\psi_j^n = \exp[-\mathrm{i}H\Delta t]\psi_j^n\,. \tag{E.6}$$

If we chose Δt small enough, we can try to Taylor expand the time evolution operator. But we have to be careful when doing so, since we have to preserve its unitarity. The naive ansatz $U(\Delta t) \simeq 1 - \mathrm{i}H\Delta t$ does not. A second order in space and time accurate and unitary conserving approximation of $U(\Delta t)$ is [226, 227]

$$U(\Delta t) \simeq \frac{1 - \mathrm{i}\frac{\Delta t}{2}H}{1 + \mathrm{i}\frac{\Delta t}{2}H}\,. \tag{E.7}$$

Plugging this back into Eq. (E.6), we end up with

$$\left(1+\mathrm{i}\frac{\Delta t}{2}H\right)\psi_j^{n+1}=\left(1-\mathrm{i}\frac{\Delta t}{2}H\right)\psi_j^n\,. \tag{E.8}$$

The spatial derivative in the kintetic term of the Hamiltonian becomes in discretized space

$$\frac{\partial^2}{\partial x^2}\psi(x)\to\frac{\psi_{j+1}-2\psi_j+\psi_{j-1}}{(\Delta x)^2} \tag{E.9}$$

using the centered time difference method. Thus, Eq. (E.8) now reads

$$\psi_j^{n+1}+\mathrm{i}\frac{\Delta t}{2}\left(-\frac{\psi_{j+1}^{n+1}-2\psi_j^{n+1}+\psi_{j-1}^{n+1}}{2(\Delta x)^2}+V_j\psi_j^{n+1}\right)=\psi_j^n-\mathrm{i}\frac{\Delta t}{2}\left(-\frac{\psi_{j+1}^{n}-2\psi_j^{n}+\psi_{j-1}^{n}}{2(\Delta x)^2}+V_j\psi_j^{n}\right) \tag{E.10}$$

with the potential $V(x)\to V(x_j)\equiv V_j$.

Defining the $N-$dimensional vectors

$$\vec{\psi}^{n+1,n}=(\psi_0^{n+1,n},\psi_1^{n+1,n},\dots,\psi_j^{n+1,n},\dots\psi_{N-1}^{n+1,n},\psi_N^{n+1,n})\,, \tag{E.11}$$

Eq. (E.10) can be written as a matrix equation

$$\mathcal{U}_1\vec{\psi}^{n+1}=\mathcal{U}_2\vec{\psi}^{n}\,. \tag{E.12}$$

The $N\times N$ matrices $\mathcal{U}_{1,2}$ read

$$\mathcal{U}_1=\begin{pmatrix}1+\beta_0 & -\alpha & 0 & \dots & & \\ -\alpha & 1+\beta_1 & -\alpha & 0 & \dots & \\ 0 & -\alpha & 1+\beta_2 & -\alpha & 0 & \dots \\ & & \ddots & \ddots & \ddots & \\ & & \dots & -\alpha & 1+\beta_{N-1} & -\alpha \\ & & \dots & 0 & -\alpha & 1+\beta_N\end{pmatrix}, \tag{E.13}$$

$$\mathcal{U}_2=\begin{pmatrix}1-\beta_0 & \alpha & 0 & \dots & & \\ \alpha & 1-\beta_1 & \alpha & 0 & \dots & \\ 0 & \alpha & 1-\beta_2 & \alpha & 0 & \dots \\ & & \ddots & \ddots & \ddots & \\ & & \dots & \alpha & 1-\beta_{N-1} & \alpha \\ & & \dots & 0 & \alpha & 1-\beta_N\end{pmatrix}, \tag{E.14}$$

with

$$\alpha=\mathrm{i}\frac{\Delta t}{4(\Delta x)^2}\,,\quad \beta_j=\mathrm{i}\frac{\Delta t}{2(\Delta x)^2}+\mathrm{i}\frac{\Delta t}{2}V_j\,. \tag{E.15}$$

We note that the matrices $\mathcal{U}_{1,2}$ are of a tridiagonal form. Naively we would exepct that Eq. (E.12) can be solved by inverting $\mathcal{U}_1$ to find an implicit equation for $\vec{\psi}^{n+1}$. In principle this is possible, but inverting a matrix is numerically as well as analytically very time consuming. Especially, when N becomes large. So it is much more reasonable to solve the linear system of equations in Eq. (E.12) for every time step $n+1$ and evolve the system forward in time starting with some initial $\vec{\psi}^0$.

A simple Example and How to deal with the Boundaries

Let us apply our method for solving the Schrödinger equation numerically to the simple example of a moving Gaussian wave packet. It should have the initial wave function

$$\psi(x, t=0) = \frac{1}{\sqrt{2\pi\sigma^2}} \exp\left[\mathrm{i}k_x(x - x_0) - \frac{(x-x_0)^2}{2\sigma^2} \right] . \tag{E.16}$$

and evolve with the free Hamiltonian. Its width is defined via σ, its initial position by x_0, and k_x is its momentum.

The algorithm to find the evolution of ψ can be summarized as following:

1. The initial wave function $\psi(x, t = 0)$ for a given σ, x_0, and k_x is discretized on lattice points $x_0, \ldots, x_N$ with parameters x_0, x_N and N. The lattice spacing is calculated from $\Delta x = |x_N - x_0|/N$.

2. The matrices $\mathcal{U}_{1,2}$ are calculated with the above formulas, using the explicit tridiagonal form.

3. The system of linear equations given in Eq. (E.12) is then subsequently be solved forward in time, starting with t_0 to some t_{N_t}. The spacing in the time domain is calculated via $\Delta t = |t_{N_t} - t|/N_t$.

The result of the procedure is shown in Fig E.1 for some initial Gaussian. A movie of the simulation can be found here [228]. Unfortunately, we observe a rather unintended result. Namely, the boundaries act as perfect mirrors, reflecting the wave package back and forth. This is a result of the Schrödinger equation conserving the normalization of the wave function in the volume we gave it. But this is not what we intend to see. In fact, the wave package should just leave the volume without any reflections. This we have to implement by hand via manipulating the boundaries.[1]

One way to do this is to apply so-called sponges at the boundaries. This means adding some imaginary potential close the boundaries of our spatial domain. See also Refs. [164, 166]. The idea is that the Schrödinger equation in fact only conserves probabitlity respectively the normalization of the wave function if the Hamiltonian is Hermitian. But if the potential is complex, then the continuity equation in fact reads

$$\partial_t |\psi|^2 - \nabla\psi = 2\mathfrak{Im}V|\psi|^2 . \tag{E.17}$$

This effect is also known as dissipation which is exactely what we want to have at our boundaries. If, for example, we consider the moving wave packet from before and we want it to leave our domain, i.e. the probability that it is inside the domain should vanish, we can artifically include an appropriate imaginary potential close to the boundaries. This is called then the sponge.

The question now is of course, what is an appropriate imaginary potential or sponge. A good guess, as always, is some kind exponential potential which vanishes when moving away from the boundaries. We found that such a potential can be effectively described via three parameters:

[1] Here [229] also a simulation of a non-moving Gaussian wave package can be found. We observe the expected dispersion of the package, but again the unphysical reflections at the boundaries.

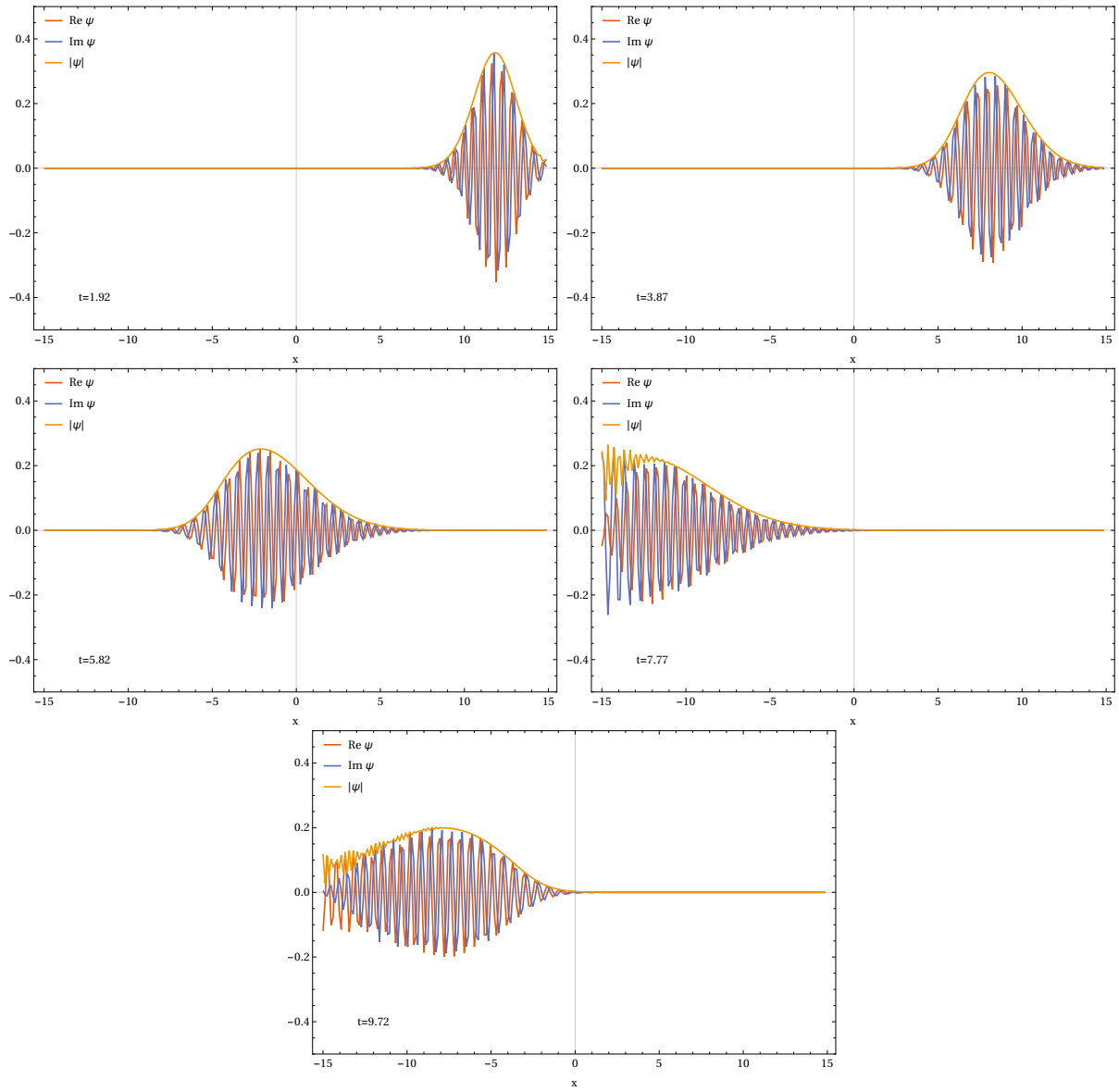

Figure E.1.: A moving Gaussian Wave Packet in a Box. Since the Schrödinger equation conserves the norm of the wave function, the bounadries of the box act as perfect mirrors.

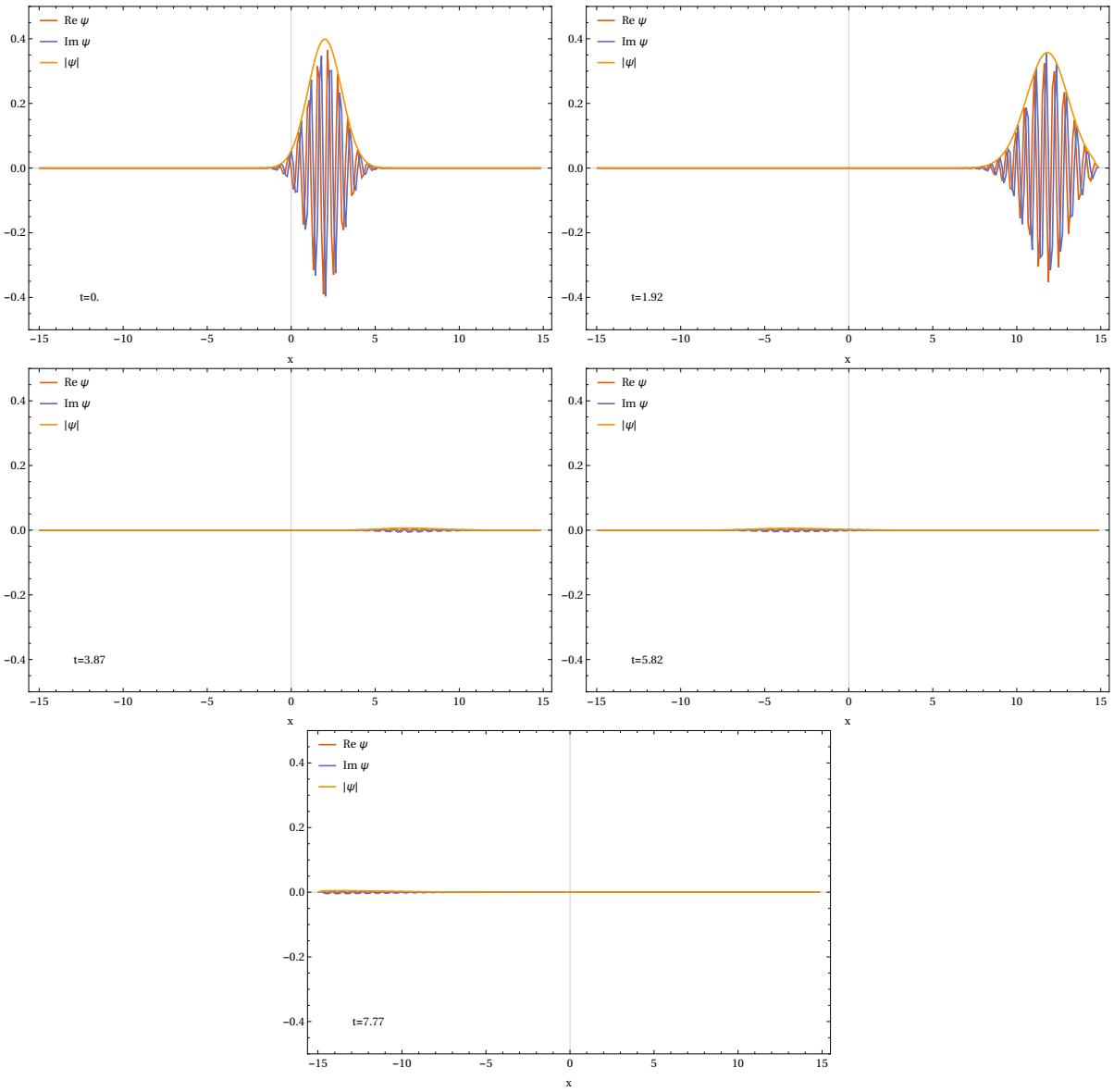

Figure E.2.: A moving Gaussian Wave Packet in a Box with absorbing Boundaries. Adding an imaginary potential, a so-called sponge, close to the boundaries allows for dispersion in the Schrödinger equation. Therefore, the wave packet can leave the box. For better illustration, the sponge is chosen such that some parts are still reflected.

a the amplitude, b the "steepness" of the exponential, and L the "thickness" of the sponge. A discretized version of the imaginary potential on the left boundary looks like this

$$V_{i,\mathrm{L}} = \begin{cases} \mathrm{i}a \exp\left[-bi\right] & \text{for } 1 < i < L \\ 0 & \text{else} \end{cases} \tag{E.18}$$

and on the right boundary it has the form

$$V_{i,\mathrm{R}} = -\begin{cases} \mathrm{i}a \exp\left[-b(1+i)\right] & \text{for } 0 < i < L-1 \\ 0 & \text{else} \end{cases} . \tag{E.19}$$

The sign of the potential must be different for left respectively right boundaries, see e.g. Refs. [226, 227] for an explanation even though a different kind of absorbing boundary condition is derived therein.

In Fig. E.2 we show the same moving wave package as before. But now we apply sponges at the boundaries. We observe how it nicely leaves the domain, cf. [230] for a movie of the simulation. For better illustration, we have chosen the sponges such that small parts of the wave are still reflected.

For the purpose of simulating the gravitational collapse, the sponges are important when some parts of the initial configuration are ejected. If they can escape the gravitational potential they should leave to infinity. Therefore, in the simulation we have to make sure that there are no unphysical reflections at the boundaries.

Schrödinger Equation for Spherical Symmetric Wave Functions

So far, we considered only one spatial dimension. When studying the minicluster collapse we will consider the spherical symmetric case in three plus one dimensions. This can basically maped onto the one-dimensional problem, when using an ansatz for the wave function of the form

$$\psi(r) = \frac{u(r)}{r} . \tag{E.20}$$

Then the spherically symmetric Schrödinger equation for u is simply

$$\mathrm{i}\partial_t u = -\frac{1}{2m}\partial_r^2 u + Vu . \tag{E.21}$$

The only important thing is to define sufficient boundary conditions for u to have a physically well behaved wave function ψ. This means for or large r, u should vanish. Thus, we set $u \to 0$ for $r \to \infty$. For $r = 0$, u must also vanish to have a finite ψ. Thus, u must be set to zero at the first spatial grid point.

Poisson Equation

The Poisson equation

$$\Delta\Phi_N = 4\pi G_N m\psi\psi^* \tag{E.22}$$

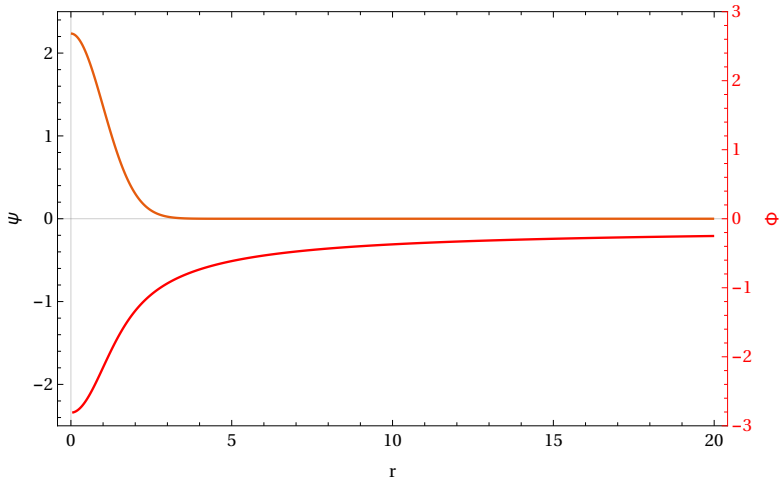

Figure E.3.: Gravitational Potential of a Gaussian Wave Packet. With the finite difference method described in the text we solve the Poisson equation for the Newtonian potential (red). The source is the Gaussian wave packet, displayed in orange. Both have arbitrary units.

might written as

$$\partial_r^2 U = r\tilde{\psi}\tilde{\psi}^* \tag{E.23}$$

when introducing the rescaled wave function $\tilde{\psi} \equiv \psi/\sqrt{4\pi G_N m}$ and making the ansatz

$$\Phi_N = \frac{U}{r} \tag{E.24}$$

for the potential. Equation (E.23) is in fact a boundary value problem (BVP) with

$$U = 0 \quad \text{for} \quad r = 0\,, \tag{E.25}$$

$$U = -M \quad \text{for} \quad r \to \infty\,. \tag{E.26}$$

In the second line we used that far away from the source, the Newtonian potential should take the form $\Phi_N = -G_N M/R$ and should be finite at $r = 0$.

These kind of BVPs can be solved either by shooting methods or a finite difference scheme. Since we used the latter also for solving the Schrödinger equation, we apply it to the Poisson equation too.

Using the Numerov method to put (E.23) on a grid, we find

$$U_{j-1} - 2U_j + U_{j+1} = \frac{(\Delta r)^2}{12}\left(r_{j+1}\psi_{j+1}\psi^*_{j+1} + 10 r_j \psi_j \psi^*_j + r_{j-1}\psi_{j-1}\psi^*_{j-1}\right)\,, \tag{E.27}$$

with the boundary values

$$U_0 = 0 \quad \text{and} \quad U_N = -M\,. \tag{E.28}$$

We can rewrite this as a system of linear equations a la

$$m\vec{U} = \vec{s}, \tag{E.29}$$

$$\vec{U} = (U_0, U_1, \ldots, U_{N-1}, U_N)^{\mathrm{T}} \,, \tag{E.30}$$

$$\vec{s} = (0, s_1, \ldots, s_j, \ldots, s_{N-1}, -M)^{\mathrm{T}} \,, \tag{E.31}$$

$$s_j = \frac{(\Delta r)^2}{12} \left(r_{j+1}\psi_{j+1}\psi^*_{j+1} + 10 r_j \psi_j \psi^*_j + r_{j-1}\psi_{j-1}\psi^*_{j-1} \right) \tag{E.32}$$

$$m = \begin{pmatrix} 1 & 0 & 0 & \ldots & & \\ 1 & -2 & 1 & 0 & \ldots & \\ 0 & 1 & -2 & 1 & 0 & \ldots \\ & & \ddots & \ddots & \ddots & \\ & & \ldots & 1 & -2 & 1 \\ & & \ldots & 0 & 0 & 1 \end{pmatrix} . \tag{E.33}$$

In Fig. E.3 we show the result Φ_N when we apply our method to a wave function ψ is of Gaussian shape.

Solving the Schrödinger-Poisson System

The SP system can be written in the dimensionless form

$$\mathrm{i}\partial_t \psi = -\frac{\Delta}{2}\psi + \Phi\psi + V\psi \tag{E.34}$$

$$\Delta\Phi = \psi\psi^* \,. \tag{E.35}$$

In case of spherical symmetry, we can express ψ and Φ_N via the functions u and U as discussed above. They are determined via the coupled system:

$$\mathrm{i}\partial_t u = -\frac{1}{2}\frac{d^2}{dr^2}u + \frac{U}{r}u + Vu \tag{E.36}$$

$$\frac{d^2}{dr^2}U = \frac{1}{r}|u|^2 \,. \tag{E.37}$$

In discretization scheme as the one described before it becomes

$$\begin{aligned} u_j^{n+1} + \mathrm{i}\frac{\Delta t}{2}\left(-\frac{u_{j+1}^{n+1} - 2u_n^{n+1} - u_{j-1}^{n+1}}{2(\Delta r)^2} + \frac{1}{r_j}U_j^{n+1}u_j^{n+1} + V_j u_j^{n+1} \right) \\ = u_j^n - \mathrm{i}\frac{\Delta t}{2}\left(-\frac{u_{j+1}^{n} - 2u_n^{n} - u_{j-1}^{n}}{2(\Delta r)^2} + \frac{1}{r_j}U_j^{n}u_j^{n} + V_j u_j^{n} \right) \end{aligned} \tag{E.38}$$

$$U_{j-1}^n - 2U_j^n + U_{j+1}^n = \frac{(\Delta r)^2}{12}\left[\frac{1}{r_{j+1}}\left(|u|^2_{j+1}\right)^n + 10\frac{1}{r_j}\left(|u|^2_j\right)^n + \frac{1}{r_{j-1}}\left(|u|^2_{j-1}\right)^n \right] . \tag{E.39}$$

Both equations are coupled in the sense that Eq. (E.38) depends on U^{n+1} which in turn depends on u^{n+1}. So the question is, how can we find u^{n+1}, if U^{n+1} is unknown? The answer is solving Eq. (E.38) and Eq. (E.39) alternatively to go from one time step n to $n+1$. The algorithm is the following [118, 164]:

1. Start with setting $U^{n+1} = U^n$ in the LHS of (E.38). Solve the linear system of equations to find $u^{n+1,0}$.
2. Feed $u^{n+1,0}$ in (E.39) to find an updated potental $U^{n+1,\mathrm{update}}$. Note that also the boundary conditions have to be updated, according to the mass inside the physical volume.
3. Put $U^{n+1,\mathrm{update}}$ in the LHS of (E.38) to find $u^{n+1,\mathrm{update}}$.

4. Compare $u^{n+1,0}$ and $u^{n+1,\text{update}}$. If $\max|u^{n+1,\text{update}} - u^{n+1,0}| < c$, with $c \in \mathbb{R}$ being the desired precission, terminate since we found the proper u^{n+1}.We can go on with step 1 to find u^{n+2}. If the desired precission is not reached, instead go to step 2 set $u^{n+1,0} \to u^{n+1,\text{update}}$ and start all over again, till the precission is reached.

Proof of Working

As a test setup to check if the numerics for solving the SP system are working, we chose a wave function a Gaussian of the form discussed in Sec. V.2, i.e.

$$\tilde{\phi} = \frac{\tilde{M}_0^{1/2}}{\pi^{3/4} X} \exp\left[-\frac{x^2}{2X^2}\right] \tag{E.40}$$

with the initial properties

$$\tilde{M}_0 = 30 \quad \text{and} \quad X = 3\,. \tag{E.41}$$

Note that for $m = 10^{-6}$ eV, this translates to

$$M_0 = \frac{\tilde{M}_0}{m G_N} \simeq 10^{-5} M_\odot \quad \text{and} \quad R_0 = \frac{9X}{m} \simeq 10^{-2} \text{ km}\,. \tag{E.42}$$

Hence, this initial configuration is far from where our minicluster distribution sit and in fact should be unstable in that sense that kinetic energy dominates over gravitational energy. Thus, we can expect a sudden explosion already at our beginning of our simulations.

As a brief side remark, we want to point out that if the particle mass would be $m = 10^{-22}$ eV then the chosen values correspond to

$$M_0 \simeq 10^{16} M_\odot \quad \text{and} \quad R_0 \simeq 10^{14} \text{ km} \sim 4 \text{ pc}\,. \tag{E.43}$$

This also nicely underlines why the case of ultralight axions is cosmologically much more relevant than that of "heavy" axions. Since we notet that the chosen paramters could, for example, easily correspond to the evolution of a galactic halo.

For our spacetime grid we set the outermost points to $R_N = 70$ and $T = 85$.[2] For both, space and time domain, we take $N_r = N_t = 650$ gridpoints. This results in a gridspacing $\Delta r = 0.12$ and $\Delta t = 0.13$. The spatial domain should be chosen as large as possible compared to the initial size avoid too much influence of the boundaries and the applied sponge. For the sponge we took an exponential potential of the form

$$V_{\text{sponge}}(r) = -\mathrm{i}a \exp\left[b(r - R_N)\right]\,, \tag{E.44}$$

where a tunes the height and b the steepness.

Further, we can define the physical volume, as the volume where it holds that

$$V_{\text{sponge}}(r < R_{\text{phys}}) < 1/\mathrm{e}\,. \tag{E.45}$$

This translates to

$$R_{\text{phys}} = \frac{bR_N - \log a - 1}{b} \quad \text{resp} \quad N_{\text{phys}} = \frac{bR_N - \log a - 1}{b\Delta r}\,. \tag{E.46}$$

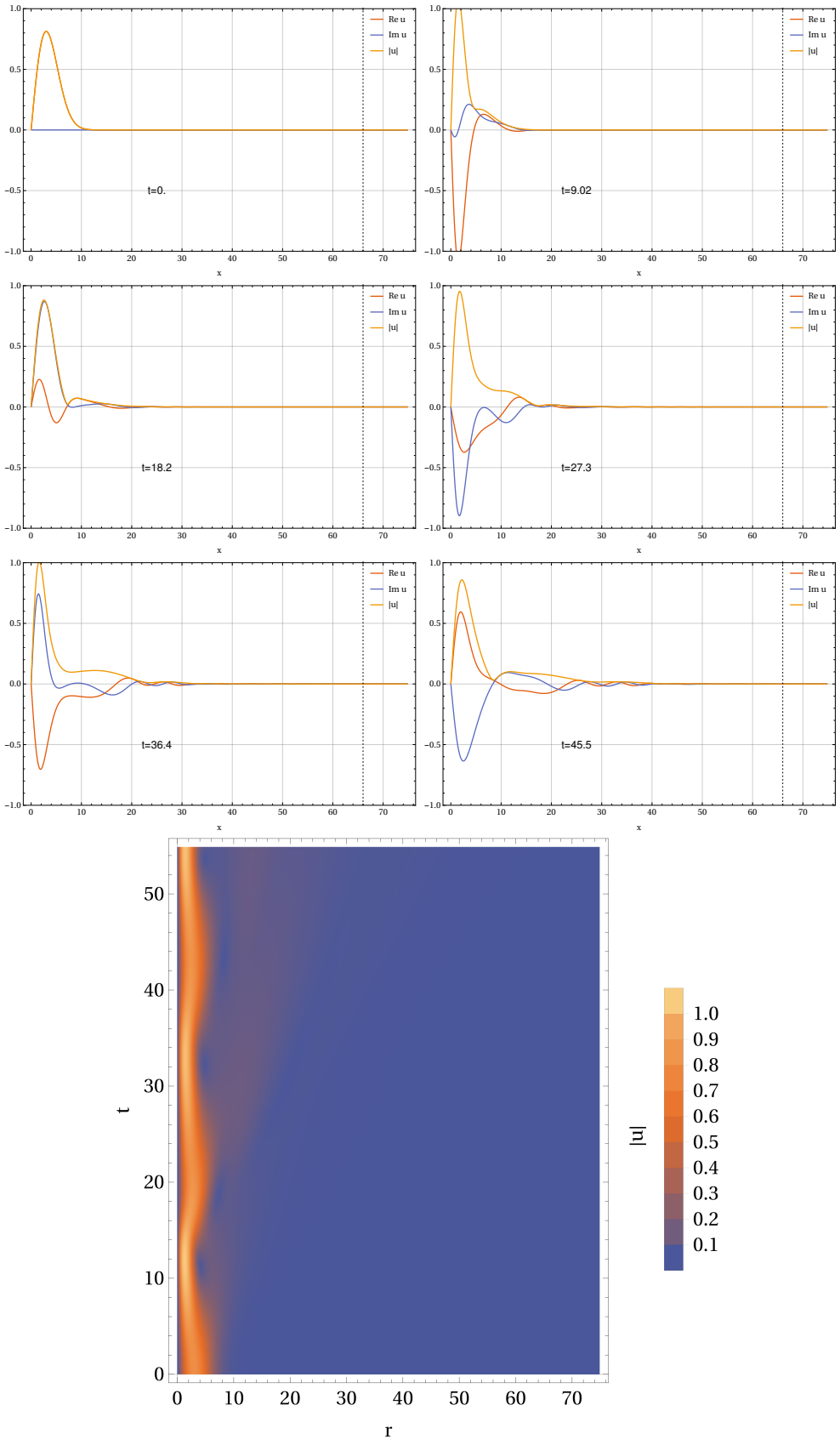

Figure E.4.: Evolution of Gaussian Wave Packet under the Schrödinger-Poisson System. We use the methods described in the text to determine the evolution of the Gaussian intial wave function. The last panel shows a projection of the absolute value of the wave function on the time-radius plane.

For our test run we set $a = 10$ and $b = 0.5$. It gives $R_{\rm phys} = 66$.

In Fig. E.4 we show different snapshots for the evolution of $u = r\psi$. The dotted line marks $R_{\rm phys}$. In the lowest panel we show a projection of the evolution of u on the time-radius plane. A movie file can be found here [231]. We observe that at the first moments of the simulation the peak seems to disperse away and parts are ejected towards infinity, as already anticipated. The initial coherence is quickly broken up. Real and imaginary part start to oscillate on some characteristic scale. The simulation time is too short as to see if the ejected parts are effectively soaked up by the sponge. However, runs where we simulate longer show that the sponge is quite effective. Further, it would be interesting to study if the oscillating peak close to $r = 0$ at some point completely vanishes. Also for that a longer running time would be needed. Note that our simulations show similar features as the results found by Seidel and Suen in Ref. [163].

[2]Note that expressing T in terms of $m = 10^{-6}$ eV, we find $T \sim 10^{-7}$ sec but for $m = 10^{22}$ eV it corresponds to $T \sim 10^{8}$ sec ~ 3 years.

Appendix F.
Madelung Transformation

The interpretation of the Schrödinger equation in terms of hydrodynamic quantities goes back to the work of Madelung in 1927 [168]. Here, we want to repeat the most important steps of the calculation and apply it to the case of the Schrödinger-Poisson (SP) system. The SP system is given by

$$\mathrm{i}\partial_t\phi = -\frac{1}{2m}\Delta\phi + m\Phi_N\phi \tag{F.1}$$

$$\Delta\Phi_N = 4\pi G m|\phi|^2\,, \tag{F.2}$$

where Φ_N is the gravitational potential.

We start with the ansatz for the wave function as in Ref. [168]

$$\phi = \alpha \mathrm{e}^{\mathrm{i}\beta}\,, \tag{F.3}$$

α, β being real functions. First, we note that

$$\Delta\phi = \Delta\alpha \mathrm{e}^{\mathrm{i}\beta} + 2\mathrm{i}\nabla\alpha\nabla\beta\mathrm{e}^{\mathrm{i}\beta} + \mathrm{i}\alpha\Delta\beta\mathrm{e}^{\mathrm{i}\beta} - \alpha\left(\nabla\beta\right)^2\mathrm{e}^{\mathrm{i}\beta} \tag{F.4}$$

and

$$\partial_t\phi = \dot{\alpha}\mathrm{e}^{\mathrm{i}\beta} + \mathrm{i}\alpha\dot{\beta}\mathrm{e}^{\mathrm{i}\beta}\,. \tag{F.5}$$

Thus, the real part of Eq. (F.1) with an ansatz of the form like in Eq. (F.3) gives

$$-\frac{1}{2m}\left[\Delta\alpha - \alpha\left(\nabla\beta\right)^2\right] + m\Phi_N\alpha = -\alpha\dot{\beta} \tag{F.6}$$

and the imaginary part yields

$$-\frac{1}{2m}\left[2\nabla\alpha\nabla\beta + \alpha\Delta\beta\right] = \dot{\alpha}\,. \tag{F.7}$$

Defining $\varphi = \beta/m$, Eq. (F.7) can be rewritten as

$$\nabla\left(\alpha^2\nabla\varphi\right) + \partial_t\alpha^2 = 0\,. \tag{F.8}$$

Now we can identify $\nabla\varphi = \mathbf{u}$ as the flow velocity of a fluid with density $\alpha^2 = \rho$ and Eq. (F.8) turns into the continuity equation

$$\nabla\left(\rho\mathbf{u}\right) + \partial_t\rho = 0\,. \tag{F.9}$$

Identifiying $\nabla\left(\beta/m\right) = \mathbf{u}$ as flow velocity becomes clear when we look at the current $\mathbf{j}$ which is defined as

$$\mathbf{j} = \frac{1}{2m\mathrm{i}}\left(\phi^*\nabla\phi - \phi\nabla\phi^*\right)\,. \tag{F.10}$$

With the ansatz $\phi = \alpha \exp[\mathrm{i}\beta]$, we find

$$\mathbf{j} = \alpha^2 \frac{\nabla\beta}{m} \,. \tag{F.11}$$

In quantum mechanics the current $\mathbf{j}$ can be interpreted as the flow of the propability density ρ with a certain velocity $\mathbf{u}$.

Using the definition of the velocity potential φ also in (F.6) we find

$$-\frac{\Delta\alpha}{2m^2\alpha} + \frac{1}{2}(\nabla\varphi)^2 + \Phi_N + \partial_t\varphi = 0 \,. \tag{F.12}$$

Taking the gradient of this equation, eventually leads to[1]

$$\partial_t\mathbf{u} + \underbrace{\mathbf{u}\cdot(\nabla\mathbf{u})}_{=(\mathbf{u}\cdot\nabla)\mathbf{u}} = -\nabla\left(\Phi_N - \frac{\Delta\sqrt{\rho}}{2m^2\sqrt{\rho}}\right) \tag{F.13}$$

which is nothing but the Euler equation of a perfect fluid. Besides the Newtonian potential Φ_N driving the gravitational collaps of the fluid, we can identfy the quantum potential $V_Q = \Delta\sqrt{\rho}/(2m^2\sqrt{\rho})$ which is basically a consquence of the uncertainty principle. It acts as an outward pressure which avoids a collaps of the fluid to a singularity.

Thus, we found that when describing the wave function ϕ by its density ρ and bulk velocity $\mathbf{u}$, it behaves like a fluid which dynamics are governed by the Euler-Poisson equations

$$\nabla(\rho\mathbf{u}) + \partial_t\rho = 0 \,, \tag{F.14}$$

$$\partial_t\mathbf{u} + (\mathbf{u}\cdot\nabla)\,\mathbf{u} = -\nabla\left(\Phi_N - \frac{\Delta\sqrt{\rho}}{2m^2\sqrt{\rho}}\right) \,, \tag{F.15}$$

$$\Delta\Phi_N = 4\pi G\rho \,. \tag{F.16}$$

As a short side remark: Note that this is a system of nonlinear differential equations. Recall that we started with the linear Schrödinger equation plus the Poisson equation wich is nonlinear in ϕ. So on first sight it looks like we made the system more complictated. On the other hand, it shows that a system of nonlinear differential equations can be rewritten in terms of a linear ones by applying an inverese Madelung transformation. This is sometimes used to bypass N-body simulation of the Euler-Poisson system and rather use a description via wave function in the Schrödinger-Poisson picture [170, 171].

[1] When taking the gradient one needs a known formula to compute $\nabla(\mathbf{u}\cdot\mathbf{u})$.

Bibliography

[1] F. Zwicky, "Die Rotverschiebung von extragalaktischen Nebeln," *Helv. Phys. Acta* **6** (1933) 110–127. [Gen. Rel. Grav.41,207(2009)]. 1

[2] S. Smith, "The Mass of the Virgo Cluster," *Astrophys. J.* **83** (1936) 23–30. 1

[3] G. Bertone, D. Hooper, and J. Silk, "Particle dark matter: evidence, candidates and constraints," *Physics Reports* **405** no. 5, (2005) 279 – 390. http://www.sciencedirect.com/science/article/pii/S0370157304003515. 1

[4] B. Carr, F. Kuhnel, and M. Sandstad, "Primordial Black Holes as Dark Matter," *Phys. Rev.* **D94** no. 8, (2016) 083504, arXiv:1607.06077 [astro-ph.CO]. 1

[5] M. Sasaki, T. Suyama, T. Tanaka, and S. Yokoyama, "Primordial black holes—perspectives in gravitational wave astronomy," *Class. Quant. Grav.* **35** no. 6, (2018) 063001, arXiv:1801.05235 [astro-ph.CO]. 1

[6] **MACHO** Collaboration, C. Alcock *et al.*, "The MACHO project: Microlensing results from 5.7 years of LMC observations," *Astrophys. J.* **542** (2000) 281–307, arXiv:astro-ph/0001272 [astro-ph]. 1

[7] T. D. Brandt, "Constraints on MACHO Dark Matter from Compact Stellar Systems in Ultra-Faint Dwarf Galaxies," *Astrophys. J.* **824** no. 2, (2016) L31, arXiv:1605.03665 [astro-ph.GA]. 1

[8] M. Zumalacárregui and U. c. v. Seljak, "Limits on stellar-mass compact objects as dark matter from gravitational lensing of type ia supernovae," *Phys. Rev. Lett.* **121** (Oct, 2018) 141101. https://link.aps.org/doi/10.1103/PhysRevLett.121.141101. 1

[9] M. Milgrom, "MOND theory," *Can. J. Phys.* **93** no. 2, (2015) 107–118, arXiv:1404.7661 [astro-ph.CO]. 1

[10] D. Clowe, M. Bradač, A. H. Gonzalez, M. Markevitch, S. W. Randall, C. Jones, and D. Zaritsky, "A direct empirical proof of the existence of dark matter," *The Astrophysical Journal Letters* **648** no. 2, (2006) L109. http://stacks.iop.org/1538-4357/648/i=2/a=L109. 1

[11] S. P. Martin, "A Supersymmetry primer," arXiv:hep-ph/9709356 [hep-ph]. [Adv. Ser. Direct. High Energy Phys.18,1(1998)]. 1

[12] J. Silk *et al.*, *Particle Dark Matter: Observations, Models and Searches*. Cambridge Univ. Press, Cambridge, 2010. http://www.cambridge.org/uk/catalogue/catalogue.asp?isbn=9780521763684. 1

[13] **PandaX-II** Collaboration, A. Tan *et al.*, "Dark Matter Results from First 98.7 Days of Data from the PandaX-II Experiment," *Phys. Rev. Lett.* **117** no. 12, (2016) 121303, arXiv:1607.07400 [hep-ex]. 1

[14] **XENON** Collaboration, E. Aprile *et al.*, "Dark Matter Search Results from a One Ton-Year Exposure of XENON1T," *Phys. Rev. Lett.* **121** no. 11, (2018) 111302, arXiv:1805.12562 [astro-ph.CO]. 1

[15] **ATLAS** Collaboration, G. Aad *et al.*, "Summary of the ATLAS experiment's sensitivity to supersymmetry after LHC Run 1 — interpreted in the phenomenological MSSM," *JHEP* **10** (2015) 134, arXiv:1508.06608 [hep-ex]. 1

[16] G. Arcadi, M. Dutra, P. Ghosh, M. Lindner, Y. Mambrini, M. Pierre, S. Profumo, and F. S. Queiroz, "The waning of the WIMP? A review of models, searches, and constraints," *Eur. Phys. J.* **C78** no. 3, (2018) 203, arXiv:1703.07364 [hep-ph]. 1

[17] R. D. Peccei and H. R. Quinn, "CP Conservation in the Presence of Instantons," *Phys. Rev. Lett.* **38** (1977) 1440–1443. [,328(1977)]. 1, 6

[18] S. Weinberg, "A New Light Boson?," *Phys. Rev. Lett.* **40** (1978) 223–226. 1

[19] F. Wilczek, "Problem of Strong P and T Invariance in the Presence of Instantons," *Phys. Rev. Lett.* **40** (1978) 279–282. 1

[20] A. Arvanitaki, S. Dimopoulos, S. Dubovsky, N. Kaloper, and J. March-Russell, "String Axiverse," *Phys. Rev.* **D81** (2010) 123530, arXiv:0905.4720 [hep-th]. 1, 9

[21] P. Arias, D. Cadamuro, M. Goodsell, J. Jaeckel, J. Redondo, and A. Ringwald, "WISPy Cold Dark Matter," *JCAP* **1206** (2012) 013, arXiv:1201.5902 [hep-ph]. 1

[22] T. W. Donnelly, S. J. Freedman, R. S. Lytel, R. D. Peccei, and M. Schwartz, "Do Axions Exist?," *Phys. Rev.* **D18** (1978) 1607. 1, 8

[23] M. Dine, W. Fischler, and M. Srednicki, "A simple solution to the strong cp problem with a harmless axion," *Physics Letters B* **104** no. 3, (1981) 199 – 202. http://www.sciencedirect.com/science/article/pii/0370269381905906. 2, 8

[24] A. R. Zhitnitsky, "On Possible Suppression of the Axion Hadron Interactions. (In Russian)," *Sov. J. Nucl. Phys.* **31** (1980) 260. [Yad. Fiz.31,497(1980)]. 2, 8

[25] J. E. Kim, "Weak-interaction singlet and strong CP invariance," *Phys. Rev. Lett.* **43** (Jul, 1979) 103–107. https://link.aps.org/doi/10.1103/PhysRevLett.43.103. 2, 8

[26] M. Shifman, A. Vainshtein, and V. Zakharov, "Can confinement ensure natural cp invariance of strong interactions?," *Nuclear Physics B* **166** no. 3, (1980) 493 – 506. http://www.sciencedirect.com/science/article/pii/0550321380902096. 2, 8

[27] M. Dine and W. Fischler, "The Not So Harmless Axion," *Phys. Lett.* **B120** (1983) 137–141. 2, 14

[28] J. Preskill, M. B. Wise, and F. Wilczek, "Cosmology of the Invisible Axion," *Phys. Lett.* **B120** (1983) 127–132. 2, 14

[29] M. S. Turner, "Coherent Scalar Field Oscillations in an Expanding Universe," *Phys. Rev.* **D28** (1983) 1243. 2, 14

[30] L. F. Abbott and P. Sikivie, "A Cosmological Bound on the Invisible Axion," *Phys. Lett.* **B120** (1983) 133–136. 2, 14

[31] L. Visinelli and P. Gondolo, "Dark matter axions revisited," *Phys. Rev. D* **80** (Aug, 2009) 035024. http://link.aps.org/doi/10.1103/PhysRevD.80.035024. 2, 21, 24

[32] C. J. Hogan and M. J. Rees, "AXION MINICLUSTERS," *Phys. Lett.* **B205** (1988) 228–230. 2, 91

[33] E. W. Kolb and I. I. Tkachev, "Femtolensing and picolensing by axion miniclusters," *Astrophys. J.* **460** (1996) L25–L28, arXiv:astro-ph/9510043 [astro-ph]. 2, 30, 41

[34] I. I. Tkachev, "Fast Radio Bursts and Axion Miniclusters," *JETP Lett.* **101** no. 1, (2015) 1–6, arXiv:1411.3900 [astro-ph.HE]. [Pisma Zh. Eksp. Teor. Fiz.101,no.1,3(2015)]. 2, 30

[35] R. RUFFINI and S. BONAZZOLA, "Systems of self-gravitating particles in general relativity and the concept of an equation of state," *Phys. Rev.* **187** (Nov, 1969) 1767–1783. https://link.aps.org/doi/10.1103/PhysRev.187.1767. 2, 30

[36] R. D. Peccei, "The Strong CP Problem," *Adv. Ser. Direct. High Energy Phys.* **3** (1989) 503–551. 5

[37] R. D. Peccei, "The Strong CP problem and axions," *Lect. Notes Phys.* **741** (2008) 3–17, arXiv:hep-ph/0607268 [hep-ph]. [,3(2006)]. 5, 6

[38] J. E. Kim and G. Carosi, "Axions and the Strong CP Problem," *Rev. Mod. Phys.* **82** (2010) 557–602, arXiv:0807.3125 [hep-ph]. 5

[39] M. Dine, "TASI lectures on the strong CP problem," in *Flavor physics for the millennium. Proceedings, Theoretical Advanced Study Institute in elementary particle physics, TASI 2000, Boulder, USA, June 4-30, 2000*, pp. 349–369. 2000. arXiv:hep-ph/0011376 [hep-ph]. 5, 6

[40] M. Dine, P. Draper, L. Stephenson-Haskins, and D. Xu, "Axions, Instantons, and the Lattice," arXiv:1705.00676 [hep-ph]. 5

[41] M. Kuster, B. Beltrán, and G. Raffelt, eds., *Axions : Theory, Cosmology, and Experimental Searches*. SpringerLink : Bücher. Springer Berlin Heidelberg, Berlin, Heidelberg, 2008. 5

[42] P. W. Graham, I. G. Irastorza, S. K. Lamoreaux, A. Lindner, and K. A. van Bibber, "Experimental Searches for the Axion and Axion-Like Particles," *Ann. Rev. Nucl. Part. Sci.* **65** (2015) 485–514, arXiv:1602.00039 [hep-ex]. 5

[43] I. G. Irastorza and J. Redondo, "New experimental approaches in the search for axion-like particles," *Prog. Part. Nucl. Phys.* **102** (2018) 89–159, arXiv:1801.08127 [hep-ph]. 5, 7, 9, 10, 12, 97

[44] P. Sikivie, "Axion Cosmology," *Lect. Notes Phys.* **741** (2008) 19–50, arXiv:astro-ph/0610440 [astro-ph]. [,19(2006)]. 5, 13, 14, 25

[45] L. D. Duffy and K. van Bibber, "Axions as Dark Matter Particles," *New J. Phys.* **11** (2009) 105008, arXiv:0904.3346 [hep-ph]. 5

[46] M. Kawasaki and K. Nakayama, "Axions: Theory and Cosmological Role," *Ann. Rev. Nucl. Part. Sci.* **63** (2013) 69–95, arXiv:1301.1123 [hep-ph]. 5

[47] A. Ringwald, "Alternative dark matter candidates: Axions," in *Neutrino Oscillation Workshop (NOW 2016): International Workshop on Neutrino and Astroparticle Physics (NOW 2016) Otranto (Lecce), Italy, September 4-11, 2016*. 2016. arXiv:1612.08933 [hep-ph]. http://inspirehep.net/record/1507050/files/arXiv:1612.08933.pdf. 5

[48] G. 't Hooft, "Symmetry Breaking Through Bell-Jackiw Anomalies," *Phys. Rev. Lett.* **37** (1976) 8–11. [,226(1976)]. 5

[49] R. Jackiw and C. Rebbi, "Vacuum Periodicity in a Yang-Mills Quantum Theory," *Phys. Rev. Lett.* **37** (1976) 172–175. 5

[50] A. J. Buras, "Flavor physics and CP violation," in *2004 European School of High-Energy Physics, Sant Feliu de Guixols, Spain, 30 May - 12 June 2004*, pp. 95–168. 2005. arXiv:hep-ph/0505175 [hep-ph]. http://doc.cern.ch/yellowrep/2006/2006-003/p95.pdf. 6

[51] **Particle Data Group** Collaboration, M. Tanabashi, K. Hagiwara, K. Hikasa, K. Nakamura, Y. Sumino, F. Takahashi, J. Tanaka, K. Agashe, G. Aielli, C. Amsler, M. Antonelli, D. M. Asner, H. Baer, S. Banerjee, R. M. Barnett, T. Basaglia, C. W. Bauer, J. J. Beatty, V. I. Belousov, J. Beringer, S. Bethke, A. Bettini, H. Bichsel, O. Biebel, K. M. Black, E. Blucher, O. Buchmuller, V. Burkert, M. A. Bychkov, R. N. Cahn, M. Carena, A. Ceccucci, A. Cerri, D. Chakraborty, M.-C. Chen, R. S. Chivukula, G. Cowan, O. Dahl, G. D'Ambrosio, T. Damour, D. de Florian, A. de Gouvêa, T. DeGrand, P. de Jong, G. Dissertori, B. A. Dobrescu, M. D'Onofrio, M. Doser, M. Drees, H. K. Dreiner, D. A. Dwyer, P. Eerola, S. Eidelman, J. Ellis, J. Erler, V. V. Ezhela, W. Fetscher, B. D. Fields, R. Firestone, B. Foster, A. Freitas, H. Gallagher, L. Garren, H.-J. Gerber, G. Gerbier, T. Gershon, Y. Gershtein, T. Gherghetta, A. A. Godizov, M. Goodman, C. Grab, A. V. Gritsan, C. Grojean, D. E. Groom, M. Grünewald, A. Gurtu, T. Gutsche, H. E. Haber, C. Hanhart, S. Hashimoto, Y. Hayato, K. G. Hayes, A. Hebecker, S. Heinemeyer, B. Heltsley, J. J. Hernández-Rey, J. Hisano, A. Höcker, J. Holder, A. Holtkamp, T. Hyodo, K. D. Irwin, K. F. Johnson, M. Kado, M. Karliner, U. F. Katz, S. R. Klein, E. Klempt, R. V. Kowalewski, F. Krauss, M. Kreps, B. Krusche, Y. V. Kuyanov, Y. Kwon, O. Lahav, J. Laiho, J. Lesgourgues, A. Liddle, Z. Ligeti, C.-J. Lin, C. Lippmann, T. M. Liss, L. Littenberg, K. S. Lugovsky, S. B. Lugovsky, A. Lusiani, Y. Makida, F. Maltoni, T. Mannel, A. V. Manohar, W. J. Marciano, A. D. Martin, A. Masoni, J. Matthews, U.-G. Meißner, D. Milstead, R. E. Mitchell, K. Mönig, P. Molaro, F. Moortgat, M. Moskovic, H. Murayama, M. Narain, P. Nason, S. Navas, M. Neubert, P. Nevski, Y. Nir, K. A. Olive, S. Pagan Griso, J. Parsons, C. Patrignani, J. A. Peacock, M. Pennington, S. T. Petcov, V. A. Petrov, E. Pianori, A. Piepke, A. Pomarol, A. Quadt, J. Rademacker, G. Raffelt, B. N. Ratcliff, P. Richardson, A. Ringwald, S. Roesler, S. Rolli, A. Romaniouk, L. J. Rosenberg, J. L. Rosner, G. Rybka, R. A. Ryutin, C. T. Sachrajda, Y. Sakai, G. P. Salam, S. Sarkar, F. Sauli, O. Schneider, K. Scholberg, A. J. Schwartz, D. Scott, V. Sharma, S. R. Sharpe, T. Shutt, M. Silari, T. Sjöstrand, P. Skands, T. Skwarnicki, J. G. Smith, G. F. Smoot, S. Spanier, H. Spieler, C. Spiering, A. Stahl, S. L. Stone, T. Sumiyoshi, M. J. Syphers, K. Terashi, J. Terning, U. Thoma, R. S. Thorne, L. Tiator, M. Titov, N. P. Tkachenko, N. A. Törnqvist, D. R. Tovey, G. Valencia, R. Van de Water, N. Varelas, G. Venanzoni, L. Verde, M. G. Vincter, P. Vogel, A. Vogt, S. P. Wakely, W. Walkowiak, C. W. Walter, D. Wands, D. R. Ward, M. O. Wascko, G. Weiglein, D. H. Weinberg, E. J. Weinberg, M. White, L. R. Wiencke, S. Willocq, C. G. Wohl, J. Womersley, C. L. Woody, R. L. Workman, W.-M. Yao, G. P. Zeller, O. V. Zenin, R.-Y. Zhu, S.-L. Zhu, F. Zimmermann, P. A. Zyla, J. Anderson, L. Fuller, V. S. Lugovsky, and P. Schaffner, "Review of particle physics," *Phys. Rev. D* **98** (Aug, 2018) 030001. https://link.aps.org/doi/10.1103/PhysRevD.98.030001. 6, 11, 12, 23, 82

[52] G. Grilli di Cortona, E. Hardy, J. Pardo Vega, and G. Villadoro, "The QCD axion, precisely," *JHEP* **01** (2016) 034, arXiv:1511.02867 [hep-ph]. 6, 7, 10

[53] A. E. Nelson, "Naturally Weak CP Violation," *Phys. Lett.* **136B** (1984) 387–391. 6

[54] S. M. Barr, "Solving the Strong CP Problem Without the Peccei-Quinn Symmetry," *Phys. Rev. Lett.* **53** (1984) 329. 6

[55] J. Schwichtenberg, P. Tremper, and R. Ziegler, "A Grand-Unified Nelson-Barr Model," `arXiv:1802.08109 [hep-ph]`. 6

[56] M. Dine and P. Draper, "Challenges for the Nelson-Barr Mechanism," *JHEP* **08** (2015) 132, `arXiv:1506.05433 [hep-ph]`. 6

[57] C. Vafa and E. Witten, "Parity Conservation in QCD," *Phys. Rev. Lett.* **53** (1984) 535. 7

[58] D. J. Gross, R. D. Pisarski, and L. G. Yaffe, "QCD and Instantons at Finite Temperature," *Rev. Mod. Phys.* **53** (1981) 43. 7

[59] O. Wantz and E. P. S. Shellard, "Axion Cosmology Revisited," *Phys. Rev.* **D82** (2010) 123508, `arXiv:0910.1066 [astro-ph.CO]`. 8, 24

[60] S. Borsanyi *et al.*, "Calculation of the axion mass based on high-temperature lattice quantum chromodynamics," *Nature* **539** no. 7627, (2016) 69–71, `arXiv:1606.07494 [hep-lat]`. 8, 21, 85

[61] E. Masso, "Axions and axion like particles," *Nucl. Phys. Proc. Suppl.* **114** (2003) 67–73, `arXiv:hep-ph/0209132 [hep-ph]`. [,67(2002)]. 9

[62] A. Ringwald, "Exploring the Role of Axions and Other WISPs in the Dark Universe," *Phys. Dark Univ.* **1** (2012) 116–135, `arXiv:1210.5081 [hep-ph]`. 9

[63] L. Di Luzio, F. Mescia, and E. Nardi, "Redefining the Axion Window," *Phys. Rev. Lett.* **118** no. 3, (2017) 031801, `arXiv:1610.07593 [hep-ph]`. 10

[64] P. Sikivie, "Experimental Tests of the Invisible Axion," *Phys. Rev. Lett.* **51** (1983) 1415–1417. [Erratum: Phys. Rev. Lett.52,695(1984)]. 11

[65] **ADMX** Collaboration, S. J. Asztalos *et al.*, "A SQUID-based microwave cavity search for dark-matter axions," *Phys. Rev. Lett.* **104** (2010) 041301, `arXiv:0910.5914 [astro-ph.CO]`. 11

[66] **ADMX** Collaboration, N. Du *et al.*, "A Search for Invisible Axion Dark Matter with the Axion Dark Matter Experiment," *Phys. Rev. Lett.* **120** no. 15, (2018) 151301, `arXiv:1804.05750 [hep-ex]`. 11

[67] M. Beutter, A. Pargner, T. Schwetz, and E. Todarello, "Axion-electrodynamics: a quantum field calculation," `arXiv:1812.05487 [hep-ph]`. 11, 97, 98

[68] G. G. Raffelt, *Astrophysical Axion Bounds*, pp. 51–71. Springer Berlin Heidelberg, Berlin, Heidelberg, 2008. `https://doi.org/10.1007/978-3-540-73518-2_3`. 11

[69] P. Gondolo and G. Raffelt, "Solar neutrino limit on axions and keV-mass bosons," *Phys. Rev.* **D79** (2009) 107301, `arXiv:0807.2926 [astro-ph]`. 11

[70] **CAST** Collaboration, K. Zioutas *et al.*, "First results from the CERN Axion Solar Telescope (CAST)," *Phys. Rev. Lett.* **94** (2005) 121301, `arXiv:hep-ex/0411033 [hep-ex]`. 11

[71] E. Armengaud *et al.*, "Conceptual Design of the International Axion Observatory (IAXO)," *JINST* **9** (2014) T05002, `arXiv:1401.3233 [physics.ins-det]`. 11

[72] A. Ayala, I. Domínguez, M. Giannotti, A. Mirizzi, and O. Straniero, "Revisiting the bound on axion-photon coupling from Globular Clusters," *Phys. Rev. Lett.* **113** no. 19, (2014) 191302, `arXiv:1406.6053 [astro-ph.SR]`. 11

[73] **H.E.S.S.** Collaboration, A. Abramowski *et al.*, "Constraints on axionlike particles with H.E.S.S. from the irregularity of the PKS 2155-304 energy spectrum," *Phys. Rev.* **D88** no. 10, (2013) 102003, arXiv:1311.3148 [astro-ph.HE]. 11

[74] **Fermi-LAT** Collaboration, M. Ajello *et al.*, "Search for Spectral Irregularities due to Photon–Axionlike-Particle Oscillations with the Fermi Large Area Telescope," *Phys. Rev. Lett.* **116** no. 16, (2016) 161101, arXiv:1603.06978 [astro-ph.HE]. 11

[75] A. Arvanitaki and A. A. Geraci, "Resonantly Detecting Axion-Mediated Forces with Nuclear Magnetic Resonance," *Phys. Rev. Lett.* **113** no. 16, (2014) 161801, arXiv:1403.1290 [hep-ph]. 11

[76] G. Raffelt, "Limits on a CP-violating scalar axion-nucleon interaction," *Phys. Rev.* **D86** (2012) 015001, arXiv:1205.1776 [hep-ph]. 11

[77] A. Sedrakian, "Axion cooling of neutron stars," *Phys. Rev. D* **93** (Mar, 2016) 065044. https://link.aps.org/doi/10.1103/PhysRevD.93.065044. 11

[78] D. Budker, P. W. Graham, M. Ledbetter, S. Rajendran, and A. Sushkov, "Proposal for a Cosmic Axion Spin Precession Experiment (CASPEr)," *Phys. Rev.* **X4** no. 2, (2014) 021030, arXiv:1306.6089 [hep-ph]. 11, 12

[79] E. W. Kolb and M. S. Turner, *The early universe*. Frontiers in Physics. Westview Press, Boulder, CO, 1990. https://cds.cern.ch/record/206230. 13, 14, 20, 21, 62, 73, 74, 75, 81, 102

[80] G. G. Raffelt, "Axions: Motivation, limits and searches," *J. Phys.* **A40** (2007) 6607–6620, arXiv:hep-ph/0611118 [hep-ph]. 13

[81] G. R. Blumenthal, S. M. Faber, J. R. Primack, and M. J. Rees, "Formation of Galaxies and Large Scale Structure with Cold Dark Matter," *Nature* **311** (1984) 517–525. [96(1984)]. 13

[82] D. J. E. Marsh, "Axion Cosmology," *Phys. Rept.* **643** (2016) 1–79, arXiv:1510.07633 [astro-ph.CO]. 14, 17, 21, 25, 81, 82

[83] **Planck** Collaboration, Y. Akrami *et al.*, "Planck 2018 results. I. Overview and the cosmological legacy of Planck," arXiv:1807.06205 [astro-ph.CO]. 17, 84

[84] E. Hardy, "Miniclusters in the Axiverse," arXiv:1609.00208 [hep-ph]. 18, 51, 52

[85] J.-c. Hwang and H. Noh, "Axion as a Cold Dark Matter candidate," *Phys. Lett.* **B680** (2009) 1–3, arXiv:0902.4738 [astro-ph.CO]. 19

[86] H. Noh, C.-G. Park, and J.-c. Hwang, "Axion as a Cold Dark Matter Candidate: Proof to Second order," *Phys. Lett.* **B726** (2013) 559–563, arXiv:1309.5692 [astro-ph.CO]. 19

[87] H. Noh, J.-c. Hwang, and C.-G. Park, "Axion as a cold dark matter candidate: Analysis to third order perturbation for classical axion," *JCAP* **1512** no. 12, (2015) 016, arXiv:1509.00937 [gr-qc]. 19

[88] H. Noh, J.-c. Hwang, and C.-G. Park, "Axion as a cold dark matter candidate: Proof to fully nonlinear order," *Astrophys. J.* **846** no. 1, (2017) 1, arXiv:1707.08568 [gr-qc]. 19

[89] P. J. E. Peebles, "Fluid dark matter," *The Astrophysical Journal Letters* **534** no. 2, (2000) L127. http://stacks.iop.org/1538-4357/534/i=2/a=L127. 19, 79

[90] W. Hu, R. Barkana, and A. Gruzinov, "Fuzzy cold dark matter: The wave properties of ultralight particles," *Phys. Rev. Lett.* **85** (Aug, 2000) 1158–1161. https://link.aps.org/doi/10.1103/PhysRevLett.85.1158. 19, 79

[91] L. Hui, J. P. Ostriker, S. Tremaine, and E. Witten, "Ultralight scalars as cosmological dark matter," *Phys. Rev. D* **95** (Feb, 2017) 043541. https://link.aps.org/doi/10.1103/PhysRevD.95.043541. 19

[92] P. W. Graham and A. Scherlis, "Stochastic axion scenario," *Phys. Rev.* **D98** no. 3, (2018) 035017, arXiv:1805.07362 [hep-ph]. 19, 82

[93] S. Hoof, F. Kahlhoefer, P. Scott, C. Weniger, and M. White, "Axion global fits with Peccei-Quinn symmetry breaking before inflation using GAMBIT," arXiv:1810.07192 [hep-ph]. 19

[94] M. S. Turner, "Cosmic and Local Mass Density of Invisible Axions," *Phys. Rev.* **D33** (1986) 889–896. 19, 20, 27

[95] R. Hlozek, D. Grin, D. J. E. Marsh, and P. G. Ferreira, "A search for ultralight axions using precision cosmological data," *Phys. Rev.* **D91** no. 10, (2015) 103512, arXiv:1410.2896 [astro-ph.CO]. 21, 78, 83

[96] S. Borsanyi *et al.*, "Lattice QCD for Cosmology," arXiv:1606.07494 [hep-lat]. 21, 22, 33, 102

[97] K. J. Bae, J.-H. Huh, and J. E. Kim, "Update of axion CDM energy," *JCAP* **0809** (2008) 005, arXiv:0806.0497 [hep-ph]. 24

[98] E. Di Valentino, E. Giusarma, M. Lattanzi, A. Melchiorri, and O. Mena, "Axion cold dark matter: status after Planck and BICEP2," *Phys. Rev.* **D90** no. 4, (2014) 043534, arXiv:1405.1860 [astro-ph.CO]. 24

[99] T. W. B. Kibble, "Topology of cosmic domains and strings," *Journal of Physics A: Mathematical and General* **9** no. 8, (1976) 1387. http://stacks.iop.org/0305-4470/9/i=8/a=029. 24, 32

[100] A. Vilenkin, "Cosmic strings and domain walls," *Physics Reports* **121** no. 5, (1985) 263 – 315. http://www.sciencedirect.com/science/article/pii/037015738590033X. 24

[101] M. B. Hindmarsh and T. W. B. Kibble, "Cosmic strings," *Rept. Prog. Phys.* **58** (1995) 477–562, arXiv:hep-ph/9411342 [hep-ph]. 24

[102] M. Gorghetto, E. Hardy, and G. Villadoro, "Axions from Strings: the Attractive Solution," *JHEP* **07** (2018) 151, arXiv:1806.04677 [hep-ph]. 24, 25

[103] V. B. Klaer and G. D. Moore, "The dark-matter axion mass," *JCAP* **1711** no. 11, (2017) 049, arXiv:1708.07521 [hep-ph]. 25

[104] R. L. Davis, "Goldstone Bosons in String Models of Galaxy Formation," *Phys. Rev.* **D32** (1985) 3172. 25

[105] D. Harari and P. Sikivie, "On the Evolution of Global Strings in the Early Universe," *Phys. Lett.* **B195** (1987) 361–365. 25

[106] R. A. Battye and E. P. S. Shellard, "Axion string constraints," *Phys. Rev. Lett.* **73** (1994) 2954–2957, arXiv:astro-ph/9403018 [astro-ph]. [Erratum: Phys. Rev. Lett.76,2203(1996)]. 25

[107] M. Kawasaki, T. Sekiguchi, M. Yamaguchi, and J. Yokoyama, "Long-term dynamics of cosmological axion strings," arXiv:1806.05566 [hep-ph]. 25

[108] A. Vaquero, J. Redondo, and J. Stadler, "Early seeds of of axion miniclusters," arXiv:1809.09241 [astro-ph.CO]. 25, 30, 38, 40, 41, 56, 76, 91

[109] P. Sikivie, "Of Axions, Domain Walls and the Early Universe," *Phys. Rev. Lett.* **48** (1982) 1156–1159. 25

[110] "Nasa asteroid fact sheet," November, 2018. https://nssdc.gsfc.nasa.gov/planetary/factsheet/asteroidfact.html. 29

[111] J. I. Read, "The Local Dark Matter Density," *J. Phys.* **G41** (2014) 063101, arXiv:1404.1938 [astro-ph.GA]. 29

[112] M. Fairbairn, D. J. E. Marsh, and J. Quevillon, "Searching for the QCD Axion with Gravitational Microlensing," *Phys. Rev. Lett.* **119** no. 2, (2017) 021101, arXiv:1701.04787 [astro-ph.CO]. 30, 50, 51

[113] M. Fairbairn, D. J. E. Marsh, J. Quevillon, and S. Rozier, "Structure formation and microlensing with axion miniclusters," *Phys. Rev.* **D97** no. 8, (2018) 083502, arXiv:1707.03310 [astro-ph.CO]. 30, 46, 47, 50, 51, 52

[114] H. Niikura, M. Takada, N. Yasuda, R. H. Lupton, T. Sumi, S. More, A. More, M. Oguri, and M. Chiba, "Microlensing constraints on primordial black holes with the Subaru/HSC Andromeda observation," arXiv:1701.02151 [astro-ph.CO]. 30

[115] P. Tinyakov, I. Tkachev, and K. Zioutas, "Tidal streams from axion miniclusters and direct axion searches," *JCAP* **1601** no. 01, (2016) 035, arXiv:1512.02884 [astro-ph.CO]. 30

[116] S. Davidson and T. Schwetz, "Rotating Drops of Axion Dark Matter," *Phys. Rev.* **D93** no. 12, (2016) 123509, arXiv:1603.04249 [astro-ph.CO]. 30, 55, 59

[117] L. Visinelli, S. Baum, J. Redondo, K. Freese, and F. Wilczek, "Dilute and dense axion stars," *Phys. Lett.* **B777** (2018) 64–72, arXiv:1710.08910 [astro-ph.CO]. 30, 55, 56

[118] E. D. Schiappacasse and M. P. Hertzberg, "Analysis of Dark Matter Axion Clumps with Spherical Symmetry," *JCAP* **1801** (2018) 037, arXiv:1710.04729 [hep-ph]. [Erratum: JCAP1803,no.03,E01(2018)]. 30, 55, 56, 57, 107, 114

[119] P.-H. Chavanis, "Phase transitions between dilute and dense axion stars," *Phys. Rev.* **D98** no. 2, (2018) 023009, arXiv:1710.06268 [gr-qc]. 30, 55

[120] D. G. Levkov, A. G. Panin, and I. I. Tkachev, "Gravitational Bose-Einstein condensation in the kinetic regime," *Phys. Rev. Lett.* **121** no. 15, (2018) 151301, arXiv:1804.05857 [astro-ph.CO]. 30

[121] J. Veltmaat, J. C. Niemeyer, and B. Schwabe, "Formation and structure of ultralight bosonic dark matter halos," *Phys. Rev.* **D98** no. 4, (2018) 043509, arXiv:1804.09647 [astro-ph.CO]. 30, 62, 79

[122] E. W. Kolb and I. I. Tkachev, "Axion miniclusters and Bose stars," *Phys. Rev. Lett.* **71** (1993) 3051–3054, arXiv:hep-ph/9303313 [hep-ph]. 30, 38, 56

[123] E. W. Kolb and I. I. Tkachev, "Nonlinear axion dynamics and formation of cosmological pseudosolitons," *Phys. Rev.* **D49** (1994) 5040–5051, arXiv:astro-ph/9311037 [astro-ph]. 30, 38, 56

[124] K. M. Zurek, C. J. Hogan, and T. R. Quinn, "Astrophysical Effects of Scalar Dark Matter Miniclusters," *Phys. Rev.* **D75** (2007) 043511, arXiv:astro-ph/0607341 [astro-ph]. 30, 38, 56

[125] J. Eby, M. Leembruggen, P. Suranyi, and L. C. R. Wijewardhana, "Collapse of Axion Stars," *JHEP* **12** (2016) 066, arXiv:1608.06911 [astro-ph.CO]. 30

[126] D. G. Levkov, A. G. Panin, and I. I. Tkachev, "Relativistic axions from collapsing Bose stars," *Phys. Rev. Lett.* **118** no. 1, (2017) 011301, arXiv:1609.03611 [astro-ph.CO]. 30

[127] J. Enander, A. Pargner, and T. Schwetz, "Axion minicluster power spectrum and mass function," *JCAP* **1712** no. 12, (2017) 038, arXiv:1708.04466 [astro-ph.CO]. 30, 31, 38, 39, 44, 45, 46, 47, 48, 49

[128] A. R. Zentner, "The Excursion Set Theory of Halo Mass Functions, Halo Clustering, and Halo Growth," *Int. J. Mod. Phys.* **D16** (2007) 763–816, arXiv:astro-ph/0611454 [astro-ph]. 37, 43, 44

[129] M. E. Peskin and D. V. Schroeder, *An introduction to quantum field theory*. The advanced book program. Westview Pr., Boulder, Colo. [u.a.], [nachdr.] ed., 2006. 37

[130] E. W. Kolb and I. I. Tkachev, "Large amplitude isothermal fluctuations and high density dark matter clumps," *Phys. Rev.* **D50** (1994) 769–773, arXiv:astro-ph/9403011 [astro-ph]. 42, 43, 47, 53

[131] W. H. Press and P. Schechter, "Formation of galaxies and clusters of galaxies by selfsimilar gravitational condensation," *Astrophys. J.* **187** (1974) 425–438. 43

[132] J. R. Bond, S. Cole, G. Efstathiou, and N. Kaiser, "Excursion set mass functions for hierarchical Gaussian fluctuations," *Astrophys. J.* **379** (1991) 440. 43

[133] J. A. Peacock and A. F. Heavens, "Alternatives to the Press-Schechter cosmological mass function," *Mon. Not. Roy. Astron. Soc.* **243** (1990) 133–143. 43

[134] M. Maggiore and A. Riotto, "The Halo Mass Function from Excursion Set Theory. I. Gaussian fluctuations with non-Markovian dependence on the smoothing scale," *Astrophys. J.* **711** (2010) 907–927, arXiv:0903.1249 [astro-ph.CO]. 43, 44

[135] V. Springel *et al.*, "Simulating the joint evolution of quasars, galaxies and their large-scale distribution," *Nature* **435** (2005) 629–636, arXiv:astro-ph/0504097 [astro-ph]. 43, 62

[136] T. Yano, M. Nagashima, and N. Gouda, "Limitation of the press-schechter formalism," *Astrophys. J.* **466** (1996) 1, arXiv:astro-ph/9504073 [astro-ph]. 47

[137] J. Frank, "Axion-like particle miniclusters (working title, in preparation)," Master's thesis, Karlsruhe Institue of Technology, 2019. 51, 52, 76, 91, 102

[138] J. L. Feng, H. Tu, and H.-B. Yu, "Thermal Relics in Hidden Sectors," *JCAP* **0810** (2008) 043, arXiv:0808.2318 [hep-ph]. 52

[139] L. F. Abbott and M. B. Wise, "Constraints on Generalized Inflationary Cosmologies," *Nucl. Phys.* **B244** (1984) 541–548. 52, 78, 85

[140] A. Caputo, A. Pargner, and T. Schwetz, "*In preparation*,". 53

[141] S. Weinberg, *Cosmology*. Cosmology. OUP Oxford, 2008. https://books.google.de/books?id=nqQZdg020fsC. 53, 55, 73, 82, 103

[142] T. Helfer, D. J. E. Marsh, K. Clough, M. Fairbairn, E. A. Lim, and R. Becerril, "Black hole formation from axion stars," *JCAP* **1703** no. 03, (2017) 055, arXiv:1609.04724 [astro-ph.CO]. 54

[143] J. Y. Widdicombe, T. Helfer, D. J. E. Marsh, and E. A. Lim, "Formation of Relativistic Axion Stars," *JCAP* **1810** no. 10, (2018) 005, arXiv:1806.09367 [astro-ph.CO]. 54

[144] F. Michel and I. G. Moss, "Relativistic collapse of axion stars," *Phys. Lett.* **B785** (2018) 9–13, arXiv:1802.10085 [gr-qc]. 54

[145] Y. Nambu and M. Sasaki, "Quantum treatment of cosmological axion perturbations," *Phys. Rev. D* **42** (Dec, 1990) 3918–3924. https://link.aps.org/doi/10.1103/PhysRevD.42.3918. 54

[146] E. Braaten, A. Mohapatra, and H. Zhang, "Classical Nonrelativistic Effective Field Theories for a Real Scalar Field," arXiv:1806.01898 [hep-ph]. 54

[147] J. J. Sakurai, *Modern quantum mechanics; rev. ed.* Addison-Wesley, Reading, MA, 1994. https://cds.cern.ch/record/1167961. 54

[148] P. Sikivie and Q. Yang, "Bose-einstein condensation of dark matter axions," *Phys. Rev. Lett.* **103** (Sep, 2009) 111301. https://link.aps.org/doi/10.1103/PhysRevLett.103.111301. 54

[149] S. Davidson, "Axions: Bose Einstein Condensate or Classical Field?," *Astropart. Phys.* **65** (2015) 101–107, arXiv:1405.1139 [hep-ph]. 54

[150] P. Sikivie and E. M. Todarello, "Duration of classicality in highly degenerate interacting Bosonic systems," *Phys. Lett.* **B770** (2017) 331–334, arXiv:1607.00949 [hep-ph]. 54

[151] F. Dalfovo, S. Giorgini, L. P. Pitaevskii, and S. Stringari, "Theory of bose-einstein condensation in trapped gases," *Rev. Mod. Phys.* **71** (Apr, 1999) 463–512. https://link.aps.org/doi/10.1103/RevModPhys.71.463. 55

[152] G. Dvali and S. Zell, "Classicality and Quantum Break-Time for Cosmic Axions," *JCAP* **1807** no. 07, (2018) 064, arXiv:1710.00835 [hep-ph]. 55

[153] G. Dvali, C. Gomez, and S. Zell, "Quantum Break-Time of de Sitter," *JCAP* **1706** (2017) 028, arXiv:1701.08776 [hep-th]. 55

[154] E. Braaten and H. Zhang, "Axion Stars," arXiv:1810.11473 [hep-ph]. 55

[155] P.-H. Chavanis, "Mass-radius relation of Newtonian self-gravitating Bose-Einstein condensates with short-range interactions. I. Analytical results," *Phys.Rev.D* **84** no. 4, (Aug., 2011) 043531, arXiv:1103.2050. 56

[156] P.-H. Chavanis and L. Delfini, "Mass-radius relation of Newtonian self-gravitating Bose-Einstein condensates with short-range interactions. II. Numerical results," *Phys.Rev.D* **84** no. 4, (Aug., 2011) 043532, arXiv:1103.2054 [astro-ph.CO]. 56

[157] W. Wang, J. Han, A. P. Cooper, S. Cole, C. Frenk, and B. Lowing, "Estimating the dark matter halo mass of our Milky Way using dynamical tracers," *Mon. Not. Roy. Astron. Soc.* **453** no. 1, (2015) 377–400, arXiv:1502.03477 [astro-ph.GA]. 57

[158] L. Diósi, "Gravitation and quantummechanical localization of macroobjects," *Phys. Lett.* **A105** (1984) 199–202, arXiv:1412.0201 [quant-ph]. 58

[159] H. Lange, B. Toomire, and P. Zweifel, "An overview of schrödinger-poisson problems," *Reports on Mathematical Physics* **36** no. 2, (1995) 331 – 345. http://www.sciencedirect.com/science/article/pii/0034487796836299. Proceedings of the XXVI Symposium on Mathematical Physics. 58

[160] I. M. Moroz, R. Penrose, and P. Tod, "Spherically symmetric solutions of the Schrodinger-Newton equations," *Class. Quant. Grav.* **15** (1998) 2733–2742. 58

[161] P. Tod and I. M. Moroz, "An analytical approach to the schrödinger-newton equations," *Nonlinearity* **12** no. 2, (1999) 201. http://stacks.iop.org/0951-7715/12/i=2/a=002. 58

[162] E. Seidel and W.-M. Suen, "Dynamical Evolution of Boson Stars. 1. Perturbing the Ground State," *Phys. Rev.* **D42** (1990) 384–403. 58

[163] E. Seidel and W.-M. Suen, "Formation of solitonic stars through gravitational cooling," *Phys. Rev. Lett.* **72** (1994) 2516–2519, arXiv:gr-qc/9309015 [gr-qc]. 58, 117

[164] R. Harrison, I. Moroz, and K. P. Tod, "A numerical study of the Schrödinger–Newton equations," *Nonlinearity* **16** no. 1, (2003) 101. http://stacks.iop.org/0951-7715/16/i=1/a=307. 58, 61, 107, 109, 114

[165] F. S. Guzmán and L. A. Ureña López, "Newtonian collapse of scalar field dark matter," *Phys. Rev. D* **68** (Jul, 2003) 024023. https://link.aps.org/doi/10.1103/PhysRevD.68.024023. 58

[166] F. S. Guzman and L. A. Urena-Lopez, "Evolution of the Schrodinger-Newton system for a selfgravitating scalar field," *Phys. Rev.* **D69** (2004) 124033, arXiv:gr-qc/0404014 [gr-qc]. 58, 61, 109

[167] F. S. Guzmán and L. A. Ureña-López, "Gravitational cooling of self-gravitating bose condensates," *The Astrophysical Journal* **645** no. 2, (2006) 814. http://stacks.iop.org/0004-637X/645/i=2/a=814. 58

[168] E. Madelung, "Quantentheorie in hydrodynamischer form," *Zeitschrift für Physik* **40** no. 3, (Mar, 1927) 322–326. https://doi.org/10.1007/BF01400372. 61, 119

[169] P. Mocz, L. Lancaster, A. Fialkov, F. Becerra, and P.-H. Chavanis, "Schrödinger-Poisson Vlasov-Poisson correspondence," *Phys. Rev.* **D97** no. 8, (2018) 083519, arXiv:1801.03507 [astro-ph.CO]. 61

[170] L. M. Widrow and N. Kaiser, "Using the Schrodinger equation to simulate collisionless matter," *Astrophys. J.* **416** (1993) L71–L74. 62, 120

[171] M. Garny and T. Konstandin, "Gravitational collapse in the Schrödinger-Poisson system," *JCAP* **1801** no. 01, (2018) 009, arXiv:1710.04846 [astro-ph.CO]. 62, 120

[172] "Evolution of a gaussian wave packet following the schrödiner poisson equation. toy model.," 2018. https://youtu.be/hU9C3GcupsE. 64

[173] "Evolution of the current density.," 2018. https://youtu.be/y9g92hz2Kic. 67

[174] E. R. Arriola and J. Soler, "A variational approach to the schrödinger–poisson system: Asymptotic behaviour, breathers, and stability," *Journal of Statistical Physics* **103** no. 5, (Jun, 2001) 1069–1105. https://doi.org/10.1023/A:1010369224196. 69

[175] M. Feix, J. Frank, B. M. Schaefer, A. Pargner, R. Reischke, and T. Schwetz, "Testing post-inflation axion dark matter using cmb observations (working title, in preparation),". 73, 82, 84

[176] G. Efstathiou and J. R. Bond, "Isocurvature cold dark matter fluctuations," *Monthly Notices of the Royal Astronomical Society* **218** no. 1, (1986) 103–121. http://dx.doi.org/10.1093/mnras/218.1.103. 74, 81

[177] A. R. Liddle and D. H. Lyth, *Cosmological Inflation and Large-Scale Structure*. Cambridge Univ. Press, Cambridge, 2000. https://cds.cern.ch/record/452061. 73, 75, 76

[178] D. S. Gorbunov and V. A. Rubakov, *Introduction to the theory of the early universe: cosmological perturbations and inflationary theory*. World Scientific, Singapore, 2011. https://cds.cern.ch/record/1354521. 73

[179] S. Dodelson, *Modern cosmology*. Academic Press, San Diego, CA, 2003. https://cds.cern.ch/record/1282338. 77

[180] D. Parkinson, S. Riemer-Sørensen, C. Blake, G. B. Poole, T. M. Davis, S. Brough, M. Colless, C. Contreras, W. Couch, S. Croom, D. Croton, M. J. Drinkwater, K. Forster, D. Gilbank, M. Gladders, K. Glazebrook, B. Jelliffe, R. J. Jurek, I. h. Li, B. Madore, D. C. Martin, K. Pimbblet, M. Pracy, R. Sharp, E. Wisnioski, D. Woods, T. K. Wyder, and H. K. C. Yee, "The WiggleZ Dark Energy Survey: Final data release and cosmological results," *prd* **86** (Nov., 2012) 103518, arXiv:1210.2130 [astro-ph.CO]. 78

[181] L. Amendola and R. Barbieri, "Dark matter from an ultra-light pseudo-Goldsone-boson," *Phys. Lett.* **B642** (2006) 192–196, arXiv:hep-ph/0509257 [hep-ph]. 79

[182] D. J. E. Marsh and P. G. Ferreira, "Ultra-Light Scalar Fields and the Growth of Structure in the Universe," *Phys. Rev.* **D82** (2010) 103528, arXiv:1009.3501 [hep-ph]. 79

[183] D. J. E. Marsh, E. Macaulay, M. Trebitsch, and P. G. Ferreira, "Ultra-light Axions: Degeneracies with Massive Neutrinos and Forecasts for Future Cosmological Observations," *Phys. Rev.* **D85** (2012) 103514, arXiv:1110.0502 [astro-ph.CO]. 79

[184] R. Hlozek, D. J. E. Marsh, and D. Grin, "Using the Full Power of the Cosmic Microwave Background to Probe Axion Dark Matter," *Mon. Not. Roy. Astron. Soc.* **476** no. 3, (2018) 3063–3085, arXiv:1708.05681 [astro-ph.CO]. 79

[185] H.-Y. Schive, T. Chiueh, and T. Broadhurst, "Cosmic Structure as the Quantum Interference of a Coherent Dark Wave," *Nature Phys.* **10** (2014) 496–499, arXiv:1406.6586 [astro-ph.GA]. 79

[186] G. Gilmore, M. I. Wilkinson, R. F. G. Wyse, J. T. Kleyna, A. Koch, N. W. Evans, and E. K. Grebel, "The Observed properties of Dark Matter on small spatial scales," *Astrophys. J.* **663** (2007) 948–959, arXiv:astro-ph/0703308 [ASTRO-PH]. 79

[187] V. Iršič, M. Viel, M. G. Haehnelt, J. S. Bolton, and G. D. Becker, "First constraints on fuzzy dark matter from lyman-α forest data and hydrodynamical simulations," *Phys. Rev. Lett.* **119** (Jul, 2017) 031302. https://link.aps.org/doi/10.1103/PhysRevLett.119.031302. 79, 80

[188] T. Kobayashi, R. Murgia, A. De Simone, V. Iršič, and M. Viel, "Lyman-α constraints on ultralight scalar dark matter: Implications for the early and late universe," *Phys. Rev.* **D96** no. 12, (2017) 123514, arXiv:1708.00015 [astro-ph.CO]. 79

[189] K.-H. Leong, H.-Y. Schive, U.-H. Zhang, and T. Chiueh, "Testing extreme-axion wave dark matter using the BOSS Lyman-Alpha forest data," arXiv:1810.05930 [astro-ph.CO]. 79, 83

[190] D. J. E. Marsh and J. C. Niemeyer, "Strong Constraints on Fuzzy Dark Matter from Ultrafaint Dwarf Galaxy Eridanus II," arXiv:1810.08543 [astro-ph.CO]. 79, 80

[191] B. Bar-Or, J.-B. Fouvry, and S. Tremaine, "Relaxation in a Fuzzy Dark Matter Halo," *ArXiv e-prints* (Sept., 2018) , arXiv:1809.07673. 79

[192] Y. B. Zel'Dovich, "Generation of Waves by a Rotating Body," *ZhETF Pisma Redaktsiiu* **14** (Aug., 1971) 270. 79

[193] R. Brito, V. Cardoso, and P. Pani, "Superradiance," *Lect. Notes Phys.* **906** (2015) pp.1–237, arXiv:1501.06570 [gr-qc]. 79, 80

[194] S. Detweiler, "Klein-gordon equation and rotating black holes," *Phys. Rev. D* **22** (Nov, 1980) 2323–2326. https://link.aps.org/doi/10.1103/PhysRevD.22.2323. 80

[195] M. J. Stott and D. J. E. Marsh, "Black hole spin constraints on the mass spectrum and number of axionlike fields," *Phys. Rev.* **D98** no. 8, (2018) 083006, arXiv:1805.02016 [hep-ph]. 80

[196] A. Arvanitaki, M. Baryakhtar, and X. Huang, "Discovering the QCD Axion with Black Holes and Gravitational Waves," *Phys. Rev.* **D91** no. 8, (2015) 084011, arXiv:1411.2263 [hep-ph]. 80

[197] V. Cardoso, O. J. C. Dias, G. S. Hartnett, M. Middleton, P. Pani, and J. E. Santos, "Constraining the mass of dark photons and axion-like particles through black-hole superradiance," arXiv:1801.01420 [gr-qc]. 80

[198] H. Yoshino and H. Kodama, "Bosenova collapse of axion cloud around a rotating black hole," *Prog. Theor. Phys.* **128** (2012) 153–190, arXiv:1203.5070 [gr-qc]. 80

[199] A. Arvanitaki and S. Dubovsky, "Exploring the String Axiverse with Precision Black Hole Physics," *Phys. Rev.* **D83** (2011) 044026, arXiv:1004.3558 [hep-th]. 80

[200] D. J. E. Marsh and J. Silk, "A Model For Halo Formation With Axion Mixed Dark Matter," *Mon. Not. Roy. Astron. Soc.* **437** no. 3, (2014) 2652–2663, arXiv:1307.1705 [astro-ph.CO]. 80

[201] **Planck** Collaboration, P. A. R. Ade *et al.*, "Planck 2013 results. XXII. Constraints on inflation," *Astron. Astrophys.* **571** (2014) A22, arXiv:1303.5082 [astro-ph.CO]. 81

[202] **Planck** Collaboration, Y. Akrami *et al.*, "Planck 2018 results. X. Constraints on inflation," arXiv:1807.06211 [astro-ph.CO]. 81, 82

[203] M. P. Hertzberg, M. Tegmark, and F. Wilczek, "Axion Cosmology and the Energy Scale of Inflation," *Phys. Rev.* **D78** (2008) 083507, arXiv:0807.1726 [astro-ph]. 81, 82

[204] M. Beltran, J. Garcia-Bellido, and J. Lesgourgues, "Isocurvature bounds on axions revisited," *Phys. Rev.* **D75** (2007) 103507, arXiv:hep-ph/0606107 [hep-ph]. 81

[205] D. H. Lyth and E. D. Stewart, "Constraining the inflationary energy scale from axion cosmology," *Phys. Lett.* **B283** (1992) 189–193. 81

[206] J. Garcia-Bellido, "Bounds on isocurvature perturbations from CMB and LSS," arXiv:astro-ph/0406488 [astro-ph]. [PoSAHEP2003,041(2003)]. 81

[207] **Planck** Collaboration, N. Aghanim *et al.*, "Planck 2018 results. VI. Cosmological parameters," arXiv:1807.06209 [astro-ph.CO]. 81, 82, 83

[208] D. H. Lyth, "A Limit on the Inflationary Energy Density From Axion Isocurvature Fluctuations," *Phys. Lett.* **B236** (1990) 408–410. 82

[209] D. Seckel and M. S. Turner, ""isothermal" density perturbations in an axion-dominated inflationary universe," *Phys. Rev. D* **32** (Dec, 1985) 3178–3183. https://link.aps.org/doi/10.1103/PhysRevD.32.3178. 82

[210] **CMB-S4** Collaboration, K. N. Abazajian *et al.*, "CMB-S4 Science Book, First Edition," arXiv:1610.02743 [astro-ph.CO]. 82, 84

[211] B. S. Acharya, K. Bobkov, and P. Kumar, "An M Theory Solution to the Strong CP Problem and Constraints on the Axiverse," *JHEP* **11** (2010) 105, arXiv:1004.5138 [hep-th]. 82

[212] A. Lewis, A. Challinor, and A. Lasenby, "Efficient computation of CMB anisotropies in closed FRW models," *Astrophys. J.* **538** (2000) 473–476, arXiv:astro-ph/9911177 [astro-ph]. 83

[213] J. Lesgourgues, "The Cosmic Linear Anisotropy Solving System (CLASS) I: Overview," *ArXiv e-prints* (Apr., 2011) , arXiv:1104.2932 [astro-ph.IM]. 83

[214] A. Lewis and S. Bridle, "Cosmological parameters from CMB and other data: A Monte Carlo approach," *Phys. Rev.* **D66** (2002) 103511, arXiv:astro-ph/0205436 [astro-ph]. 83

[215] D. Foreman-Mackey, D. W. Hogg, D. Lang, and J. Goodman, "emcee: The MCMC Hammer," *Publications of the Astronomical Society of the Pacific* **125** (Mar., 2013) 306, arXiv:1202.3665 [astro-ph.IM]. 83

[216] M. Tegmark, A. Taylor, and A. Heavens, "Karhunen-Loeve eigenvalue problems in cosmology: How should we tackle large data sets?," *Astrophys. J.* **480** (1997) 22, arXiv:astro-ph/9603021 [astro-ph]. 84

[217] L. Husdal, "On Effective Degrees of Freedom in the Early Universe," *Galaxies* **4** no. 4, (2016) 78, arXiv:1609.04979 [astro-ph.CO]. 85

[218] M. Beutter, "Interactions with an axion background field (working title, in preparation)," Master's thesis, Karlsruhe Institue of Technology, 2019. 97

[219] L. S. Brown and G. Gabrielse, "Geonium Theory: Physics of a Single Electron or Ion in a Penning Trap," *Rev. Mod. Phys.* **58** (1986) 233. 97

[220] J. Ouellet and Z. Bogorad, "Solutions to Axion Electrodynamics in Various Geometries," arXiv:1809.10709 [hep-ph]. 98, 99

[221] Y. Kim, D. Kim, J. Jung, J. Kim, Y. C. Shin, and Y. K. Semertzidis, "Effective Approximation of Electromagnetism for Axion Haloscope Searches," arXiv:1810.02459 [hep-ph]. 98, 99

[222] M. E. Tobar, B. T. McAllister, and M. Goryachev, "Modified Axion Electrodynamics through Oscillating Vacuum Polarization and Magnetization and Low Mass Detection using Electric Sensing," arXiv:1809.01654 [hep-ph]. 98, 99

[223] J. Hong and J. E. Kim, "A new method for the detectability of oscillating theta," *Physics Letters B* **265** no. 1, (1991) 197 – 200. http://www.sciencedirect.com/science/article/pii/037026939190040W. 98

[224] C. T. Hill, "Axion Induced Oscillating Electric Dipole Moments," *Phys. Rev.* **D91** no. 11, (2015) 111702, arXiv:1504.01295 [hep-ph]. 98

[225] C. T. Hill, "Axion Induced Oscillating Electric Dipole Moment of the Electron," *Phys. Rev.* **D93** no. 2, (2016) 025007, arXiv:1508.04083 [hep-ph]. 98

[226] F. L. DUBEIBE, "Solving the time-dependent schrödinger equation with absorbing boundary conditions and source terms in mathematica 6.0," *International Journal of Modern Physics C* **21** no. 11, (2010) 1391–1406. https://www.worldscientific.com/doi/abs/10.1142/S0129183110015919. 107, 112

[227] T. Shibata, "Absorbing boundary conditions for the finite-difference time-domain calculation of the one-dimensional schrödinger equation," *Phys. Rev. B* **43** (Mar, 1991) 6760–6763. https://link.aps.org/doi/10.1103/PhysRevB.43.6760. 107, 112

[228] "A moving gaussian wave packet in a box.," 2018. https://youtu.be/EAy2eJZRQO8. 109

[229] "Dispersion of a non-moving gaussian," 2018. https://youtu.be/icjZM6NHZek. 109

[230] "A moving gaussian wave packet in a box with absorbing boundaries," 2018. https://youtu.be/ANQca-Ugc4E. 112

[231] "Evolution of wave packet following the schrödinger-poisson system.," 2018. https://youtu.be/7otfToGnukI. 117

Acknowledgments

First of all, I have to thank Prof. Thomas Schwetz-Mangold for being more than just a supervisor in the last three years. Foremost, I have to thank him for letting me develop my own ideas, my own understanding of things, and most importantly my own opinions.

Further, I thank Prof. Guido Drexlin for being the second supervisor of this dissertation.

Of course, I want to thank all my collaborators, campanions and friends (in no specific order): Alvaro Hernandez, Andrea Caputo, Oliver Fischer, Elisa Todarello, Martin Feix, Robert Reischke, Bjoern-Malte Schafer, Marc Beutter, Yannick Müller, Johann Frank, Claus-Robert Ziegahn, Alexander Schmid, Daniel Reis, Dr. Norman Mechau, Jakob Schwichtenberg, Hendrik Seitz-Moskaliuk, and Ruben Betz.

Finally, I thank my family and my beautiful wife for taking this journey with me.